Studies of hexafluorophosphate, tetrafluoroborate, and perchlorate Electro-intercalation into Graphitic Carbon

By
Jennifer Ann Seel

Submitted in partial fulfillment of
the requirements for the degree of
Doctor of Philosophy

at

Dalhousie University
Halifax, N.S.
July, 2004

Your file Votre référence
ISBN: 0-612-94056-X
Our file Notre référence
ISBN: 0-612-94056-X

DALHOUSIE UNIVERSITY

To comply with the Canadian Privacy Act the National Library of Canada has requested that the following pages be removed from this copy of the thesis:

Preliminary Pages

Examiners Signature Page (pii)

Dalhousie Library Copyright Agreement (piii)

Appendices

Copyright Releases (if applicable)

Table of Contents

List of Figures

List of Tables

Abstract

There has been some interest in using carbon materials as both working electrodes in electrochemical cells and rechargeable batteries [1-6]. This would result in the intercalation of not only of lithium ions into one carbon electrode but the anion component of the lithium salt, such as PF_6^-, into the other carbon electrode. The intercalation of the anion component of the salt into carbon electrodes has not been studied extensively and it is not completely understood. The work presented here will expand on this rarely touched subject through electrochemical cycling as well as *in-situ* and *ex-situ* X-ray diffraction experiments. The anions that will be studied are: PF_6^-, BF_4^- and ClO_4^-. It will be shown that anion intercalation occurs for various types of soft carbons and that the process can be greatly affected by the amount of turbostratic disorder present in the carbon material as well as by the specific anion used.

It was discovered that using ethyl methyl sulfone, EMS, as the solvent component of the electrolyte resulted in more stable electrochemical cells than ethylene carbonate/diethyl carbonate, a more common solvent, at the high potentials required for anion intercalation. It was also discovered that PF_6 and BF_4 formed staged phases during electrochemical cycling whereas ClO_4 did not. The amount of disorder present in the carbon electrode did affect the intercalation of the anion. The samples with a greater amount of disorder present had a larger amount of capacity loss between charge and discharge capacities. It was also found that purer and more distinct staged phases occurred in the more ordered carbon samples. The turbostratically disordered carbon layers may rotate to accommodate PF_6 and therefore become slightly more ordered.

X-ray diffraction evidence suggests that intercalated PF_6 molecules may be free-rotating between the carbon layers. However, the orientation of BF_4 molecules between the carbon layers could not be determined. There may also be some co-intercalation of the solvent, mainly with ClO_4 and to a lesser extent BF_4 and PF_6. It is thought that a large amount of solvent co-intercalation occurs with ClO_4 and this is the most probable reason why staged phases were not observed.

An unfortunate aspect of this study is that dual carbon cells are not at all viable as commercial cells. The energy densities of dual carbon cells are much lower than the currently available lithium-ion cells. For dual carbon cells to become viable new inexpensive salts and solvents that can operate at high potentials and high concentrations must be discovered. With further investigation, combinations of different anions and solvents may result in higher specific capacities that would also make dual carbon cells more viable.

List of Symbols and Abbreviations

A	cross-sectional area
$a_{inplane}$	in-plane lattice constant
a, b	the width and length of footprint of the X-ray beam
a_i,b_i,c	parameters for determining the atomic scattering factor for the *i*th atom
$A_{that\ hits\ sample}$	surface area of the sample
A_{beam}	surface area covered by the X-ray beam
A_{hkl}, B_{hkl}	components of the geometric structure factor
AN	acetonitrile
α	angular divergence of the slit
c	lattice constant
C	circumference
d	distance between two adjacent layers
d_A	spacing between two carbon layers that have an intercalated PF_6 between them
DEC	diethyl carbonate
e	magnitude of the charge on the electron
EC	ethylene carbonate
EMS	ethyl methyl sulfone
f	atomic scattering factor
f_i	atomic scattering factor for the *i*th atom
$\|F_{hkl}\|$	magnitude of the geometric structure factor for the (hkl) reflection

FPMS	trifluoropropylmethyl sulfone
ΔG	free energy
GIC	graphite intercalation compound
h	height of ring
H	position of ring within the sphere
i	current
I	measured intensity
I_o	calibrated or corrected measured intensity
$I_{hk\ell}$	measured intensity of the (hkℓ) reflection
φ_s	porosity of the separator
$[Li^+]$	concentration of lithium ions in solution
l	length of the side of the ring
L	distance between the X-ray tube and the sample
L_{factor}	Lorentz factor
L_a	coherence length
λ	wavelength of the incident X-ray radiation
k	a general scale factor
m	an integer
m_a	active mass
m_{total}	total mass of cell
M_c	molarity at the end of charge
M_d	molarity at the end of discharge
MCMB	mesocarbon microbeads

MeOH	methanol
μ	absorption factor
μ_{Li}^{-}	chemical potential of a lithium ion in lithium metal electrode
μ_{Li}^{+}	chemical potential of a lithium ion in carbon electrode
μ^{Li}	chemical potential of a lithium ion in lithium metal
$\mu^{Li+}{}_{sol}$	chemical potential of a lithium ion in solution
μ^{A}	chemical potential of an anion/molecule in the carbon electrode
$\mu^{A-}{}_{sol}$	chemical potential of an anion in solution
μ_{1M}	chemical potential of lithium ion in a one molar solution
Δn	number of transferred electrons
N	total number of layers in sphere of fluorine atoms
p	probability of that two adjacent sheets will be turbostratically misaligned
p_{factor}	polarization factor
PC	propylene carbonate
Q	specific capacity
dQ/dV	differential capacity
q_a and q_b	specific capacities of the electrodes
Q_a and Q_b	charge stored in the electrodes
Q_{total}	total charge
θ	incident angle or Bragg angle
θ_s	angle between H and r_s
θ_n	angle of (00n) diffraction peak

θ_{n+1}	angle of (00 n+1) diffraction peak
r	radius of the sample
r_s	radius of sphere
R	conversion factor equal to 26.8 AhL/M
ρ	bulk density of graphite
ρ_c	bulk density of the electrolyte
ρ_s	bulk density of the separator
t	time
t_{be}	thickness of the beryllium window
t_a and t_b	thicknesses of the electrodes
t_e	thickness of the separator
TBA	tetrabutyl ammonium
V	potential or potential difference
Vol	volume
W	work
X	radius of ring

Acknowledgements

I would first like to thank Jeff, my supervisor especially for his patience and guidance throughout my degree.

Secondly, my parents for allowing me to live at home so that I wouldn't have to worry about room and board and the like.

Thirdly, my fellow lab mates both past and present, especially Dave and Luc, for being there to bounce ideas off and, well, just to listen and give encouragement. I would also like to thank the support staff, mostly present but a few past: Barb, Judy, Bridget, Gloria, Anne-Marie, Anne, Jim, Andy, Simon and Alex. Without their help, life in the Dunn building would have been more difficult.

I would also like to thank my internal committee, Daniel Labrie and Jurgen Kreuzer for their insight and their enthusiasm especially when I gave them their copies of this thesis. I would especially like to thank Richard Wang for his calculations and useful information used in various parts of this work.

I would like to thank 3M for supplying Jeff and therefore myself with funding as well as the Walter C. Sumner Foundation for the scholarships that I received.

Thanks also goes out to my friends for being there when I needed them and giving me space when I needed it. I would especially like to mention Janya, Liz, Bonny and my other dancer friends like Belinda and Andrea.

And last, but certainly by no means least, my cat Imp. She reminds me not to take myself too seriously and would always remind me when I spent too much time in front of the computer and it was high time to take a break and give her some attention.

Chapter 1 Introduction

With growing populations, demand on existing natural resources such as oil, coal, and natural gases, has increased. This in turn has depleted existing resources. The emission of harmful gases and other products into the environment has also increased and will continue to do so if nothing is done. As more of the population has become aware of these things, the interest in renewable energies has grown. With this added interest in renewable energy sources for increasingly more and more applications, there is an abundant and growing amount of research trying to improve the quality, efficiency and lifetime of such sources.

One of the more common uses for rechargeable batteries is for portable electronics, from laptops to phones to personal entertainment devices. Rechargeable batteries can also have larger applications such as powering various modes of transportation. They may also be used as storage devices. Hydro, solar and wind power are primary sources of energy, ones that can be used over and over, i.e. renewable. If these power sources are to become the primary source of energy for general use, energy storage devices will be required. This would allow excess energy to be stored over a period of time for use at a later time when, perhaps, the primary sources are not available, for example, when there is insufficient wind or when the sun has set. If the world is to become more dependent on renewable energy sources, then rechargeable batteries will most likely play a very important role.

Some examples of rechargeable batteries are Nickel-Cadmium, nickel-metal hydride and lithium ion cells. With the growing interest in rechargeable batteries, research groups around the world are constantly trying to improve the energy density, efficiency and lifetime of these devices without comprising safety or cost.

There is some interest in rechargeable batteries to be comprised of electrochemical cells that have both the negative electrode and the positive electrode made from carbon materials [1-6]. One of the main reasons is simply for ease of production, possible lower cost and, perhaps, the relative safety of the cell. Unfortunately such cells have not been studied sufficiently and more work is required.

Lithium-ion cells use a carbon electrode as the negative electrode. In such cells, lithium atoms are cycled between a positive electrode, usually a lithium transition metal oxide, and a carbon negative electrode. In a dual carbon cell, where carbon electrodes act as both the negative electrode and the positive electrode, the intercalation of not only lithium atoms but also the corresponding anion from the lithium salt is needed.

This phenomenon of the anion being inserted into carbon has not been studied to nearly the same extent as lithium insertion into carbon. Once the anion from solution intercalates into the carbon material it is no longer an anion, its charge is now neutral. For the lack of a better term, this type of intercalation shall be referred to as anion intercalation throughout this thesis. The reader should keep in mind that it is an anion within the solution and a molecule once it has intercalated into the carbon electrode. In order to fully understand dual-carbon electrochemical cells, electrochemical cells where the anion is intercalating into the carbon electrode should be studied first. In these types of cells, a carbon material would naturally be used as the electrode under investigation

and lithium metal would generally be used as the counter electrode. The work presented here will hopefully fill part of the lack of understanding of anion intercalation (rather than lithium intercalation) and prove useful in the future.

Since lithium intercalation is dependent on the structure of the carbon [7,8] it would be interesting to see how carbon structure affects anion intercalation. It would also be interesting to see if and how different anions intercalate into a carbon material. The work presented here will investigate these aspects of anion intercalation into carbon.

Chapter 2 Background

This chapter will discuss the general operation of electrochemical cells for lithium and anion intercalation into carbon electrodes. Various works by other researchers concerning anion insertion into carbon materials as well as electrochemical cycling using anions as the source of the current will also be discussed.

Section 2.1 Lithium and Anion Electrochemical Cells

Before discussing how anion intercalation works, the more common process of lithium intercalation in an electrochemical cell will be briefly discussed. There are numerous reviews available if the reader is interested in reading further [9,10]

As with all batteries, there are positive and negative electrodes. In this example, the positive electrode is a carbon, C, material and the negative electrode is lithium, Li, metal. These electrodes are placed in a container and surrounded by an electrolyte. The electrolyte contains, usually, a lithium salt, LiA, and a solvent. A schematic of such a cell is shown in Figure 2.1.1.

If the electrodes were simply connected electrons would spontaneously travel from the lithium electrode to the carbon electrode. Electrons from the lithium electrode would travel through the wire to the carbon electrode at the same time as lithium ions from the lithium electrode enter into solution. Simultaneously, the electrons combine with other lithium ions from solution at the carbon electrode. Ultimately, enough lithium atoms will intercalate into the carbon electrode so that there will be one lithium atom for

every six atoms of the graphite form of carbon. This process can be reversed by applying a current in the opposite direction, i.e. force the electrons to travel from the positive electrode to the negative electrode. During this charging process, the lithium ions within the carbon electrode are ionized and the electrons travel through the wires to the lithium electrode, and the lithium ions diffuse back into solution. At the lithium electrode the electrons and lithium ions recombine to form more lithium.

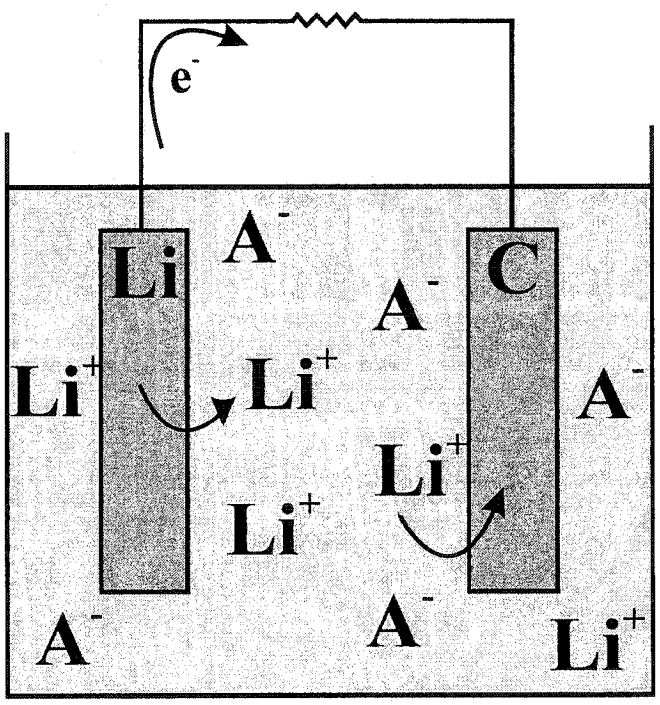

Figure 2.1.1 A schematic of a lithium cell.

The half-cell reactions for this cell, as depicted above, are as follows:

for the lithium negative electrode: $x\ Li \Leftrightarrow x\ Li^+ + x\ e^-$

and for the carbon positive electrode: $C + x\ e^- + x\ Li^+ \Leftrightarrow Li_xC$ (2.1)

The overall cell reaction would therefore be:

$$x\,Li + C \Leftrightarrow Li_xC\,. \tag{2.2}$$

The work, W, performed by the cell is defined by the number of electrons transferred, Δn, and the potential difference, V, through which they move

$$W = \Delta n\, eV. \tag{2.3}$$

This work is also equal to the change in the free energy, ΔG, of the cell which is proportional to the difference of the chemical potentials of lithium atoms within the lithium metal, μ_{Li}^{-} , and the carbon electrode, μ_{Li}^{+}.

$$\Delta G = \left(\mu_{Li}^{-} - \mu_{Li}^{+}\right) \Delta n. \tag{2.4}$$

By combining equations (2.3) and (2.4) the cell potential of a lithium ion cell is given by the change in the chemical potential of the lithium atom in the cathode and in the anode

$$eV = \left(\mu_{Li}^{-} - \mu_{Li}^{+}\right). \tag{2.5}$$

It is possible to start the current flowing in the direction opposite to that of the natural flow. This means that the electrons would initially be removed from the carbon electrode and would travel to the lithium electrode through the wire. In this case the carbon electrode is acting as the formal cathode, and the lithium electrode is acting as the formal anode. As electrons are being removed from the carbon electrode the anion, A^-, from solution replaces those electrons and intercalates into the carbon electrode. At the same time, the electrons combine with lithium ions from solution at the lithium electrode. This process is demonstrated in Figure 2.1.2.

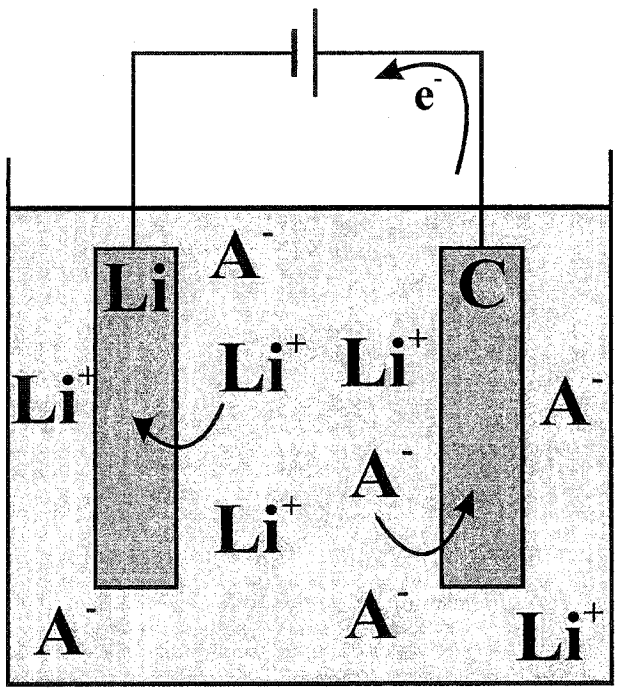

Figure 2.1.2 A schematic of an anion cell.

During this process the half-cell reactions are as follows:

for the lithium electrode: $x\,Li + \delta\,Li^+_{sol} + \delta\,e^- \Leftrightarrow (x+\delta)\,Li$

and at the carbon electrode: $A_yC + \delta\,A^-_{sol} \Leftrightarrow A_{(y+\delta)}C + \delta\,e^-$ (2.6)

The overall cell reaction would therefore be:

$$A_yC + x\ Li + \delta\ Li^+_{sol} + \delta\ A^-_{sol} \Leftrightarrow (x+\delta)\ Li + A_{(y+\delta)}C \qquad (2.7)$$

As with lithium ion intercalation into carbon, the work performed by the cell is defined by the number of electrons transferred and the cell potential. This work is also given by the free energy of the cell. Therefore, the cell potential is given by:

$$n\ eV = n\ (\mu^{Li} - \mu^{Li+}_{sol}) + n(\mu^{A} - \mu^{A-}_{sol}) \qquad (2.8)$$

where n is the number of electrons, e the magnitude of the charge of an electron, V the cell potential, μ^{Li} and μ^{Li+}_{sol}, are, respectively, the chemical potentials for the lithium atoms within the metal and for the lithium ion in solution, i.e. in the electrolyte. Similarly, μ^{A} and μ^{A-}_{sol}, are the chemical potentials for the intercalated A molecule and the anion within the electrolyte.

In the dilute limit the chemical potential for the ions in solution can be expressed in terms of the chemical potential at 1M, μ_{1M}, and the concentration of the ion. Since, in most electrolytes' salts, the anion and the cation are in a one to one ratio, the concentration of the anion is the same as the cation, $[Li^+]$ in this case. Hence, the chemical potentials for the ions in solution can be given by:

$$\mu^{Li+}_{sol} = \mu^{Li+}_{1M} + kT\ ln[Li+] \text{ and } \mu^{A-}_{sol} = \mu^{A-}_{1M} + kT\ ln[Li^+] \qquad (2.9)$$

Using these equations and equation (2.8), the following is obtained for the cell potential:

$$eV = \mu^{Li} + \mu^{A} - (\mu^{Li+}_{1M} + \mu^{A-}_{1M} + 2kT\ ln[Li^+]) \qquad (2.10)$$

Since the cell potential depends on the chemical potential of the ions within the solvent, it may very well depend on the type of solvent used. This is not at all like lithium-ion cells that show no real dependence on the type of solvent used. Also, unlike

Li-ion cells, the anion chosen will most likely affect the potential of this type of cell. Also, the concentration of the electrolyte may have an affect on the potential of an electrochemical cell for anion intercalation. These possibilities, among other things, should be kept in mind when studying anion intercalation into carbon materials.

Section 2.2 Anion Insertion

Various groups have investigated anion insertion over the years. Among the various anions and molecules that have been studied are BF_4^- [11,12], PF_6^- [12], MoF_6^- [13], $InCl_3$ [14], $SbCl_4F$ [15,16,17], SbF_5 [16], SbF_6^- [12], and, $SbCl_5$ [16,18,19], as well as various chlorides [20] .

There are several techniques available to insert a guest species into carbon. Most of these techniques involve heating of either, or both, the carbon material and the guest species, sometimes in a controlled environment. One of these techniques is the two-zone method, or the two-zone vapour transport method [21]. In this method the carbon material is heated to a temperature generally higher than the temperature of the guest species. The temperature difference controls the amount of the guest species that goes into the carbon material. The smaller this difference, the more of the guest species is inserted into the carbon. Generally, for this type of insertion, the carbon is held at a constant temperature and the temperature of the guest species is varied to achieve ranges of concentration of the guest species. Often the molecular guest species are prepared under high vapour pressure conditions. Once the insertion is complete, the guest species is quenched and sealed off from the carbon material. This helps to prevent areas within the carbon material of mixed concentrations of the guest species. Another way is to limit the amount of the inserted species is, of course, simply to limit the amount available.

Other methods include the liquid intercalation method [21] and simply heating the carbon material in solutions that contain the desired molecular species and annealing, at a high temperature, the appropriate amounts of the guest species and the carbon material,

(for example see references 16 and 18). The solutions and temperatures, of course, vary with the desired guest species and concentration desired.

A summary of various anions and the stages reached along with other information such as the repeat distance of the layers are given in Table 2.1. (Staging is explained in Chapter 4 Section 4). It can be easily seen that for the mixtures that achieved stage 1, where each carbon layer is separated by the guest compound, the distance between the layers or the c-axis repeat distance, is about 8 or 9 Å.

As an example, $SbCl_5$ shall be discussed in a little more detail. Priess, et al., [16] prepared stage 2 and stage 3 graphite intercalated compounds, or GIC's, by using the two-zone method with a vapour of $SbCl_5$ and natural graphite. Melin and Herold [18] also studied antimony pentachloride and prepared stages 1 through 4 by heating either a liquid or a gas containing $SbCl_5$ along with natural graphite in a closed glass container in an inert environment. The reactions were optimally completed in the range of 160 to 200°C. X-ray diffraction measurements were used by both groups to determine the staging and other parameters of the intercalated graphite compounds.

Both groups' findings for the c-axis repeat distances agree reasonably well with each other for stages 2 and 3. Stage 1 was found to have a c-axis spacing of 9.42 Å; stage 2, 12.72 to 12.78 Å; stage 3, 16.08 to 16.10 Å; and stage 4, 19.45 Å. The composition of the intercalated compound was found to be $C_{12n}SbCl_5$, where n represents the stage number. Preiss et al. found that the antimony atom was not in the center of the occupied layer but rather that the chlorine atoms were equidistant from the carbon layers. This is illustrated in Figure 2.2.1. Other work by Streeifinger et al. [22] and Herold [23] found similar values for the layer spacings for stages 1 through 4.

These works show that molecular insertion/intercalation into carbon is certainly possible. What remains to be seen is whether these anions can be used in electrochemical cells containing carbon electrodes.

Anion or Molecule	Stage(s) reached	Repeat distances (Å)	n in C_nA	Reference number(s)
BF_4^-	2	11.13		11
BF_4^-	2 3	11.25 14.58		12
PF_6^-	2 3	11.10 14.44	48	12
MoF_6^-	1	8.4		13
$InCl_3$	2	12.8	17.6	14
$InCl_3$	1	9.53		20
$SbCl_4F$	1 2 3	9.30 12.72 16.06		15
$SbCl_4F$	1 2 3 4	9.33 12.72 16.06 19.40		16,17
SbF_5	2 3	11.70 14.90		16
$SbCl_5$	2 3	12.78 16.10		16
$SbCl_5$	1 2 3 4	9.42 12.72 16.08 19.45	12 24 36 48	18
$SbCl_5$	1	9.45		19
SbF_6^-	1 2	8.05 11.38		12
$CdCl_2$	1	9.52		20
$BiCl_3$	2	13.05		20
$HgCl_2$	2	12.95		20
$HgCl_3$	3	16.4		20

Table 2.1 Summary of graphite intercalation compounds and their corresponding c-axis repeat distances.

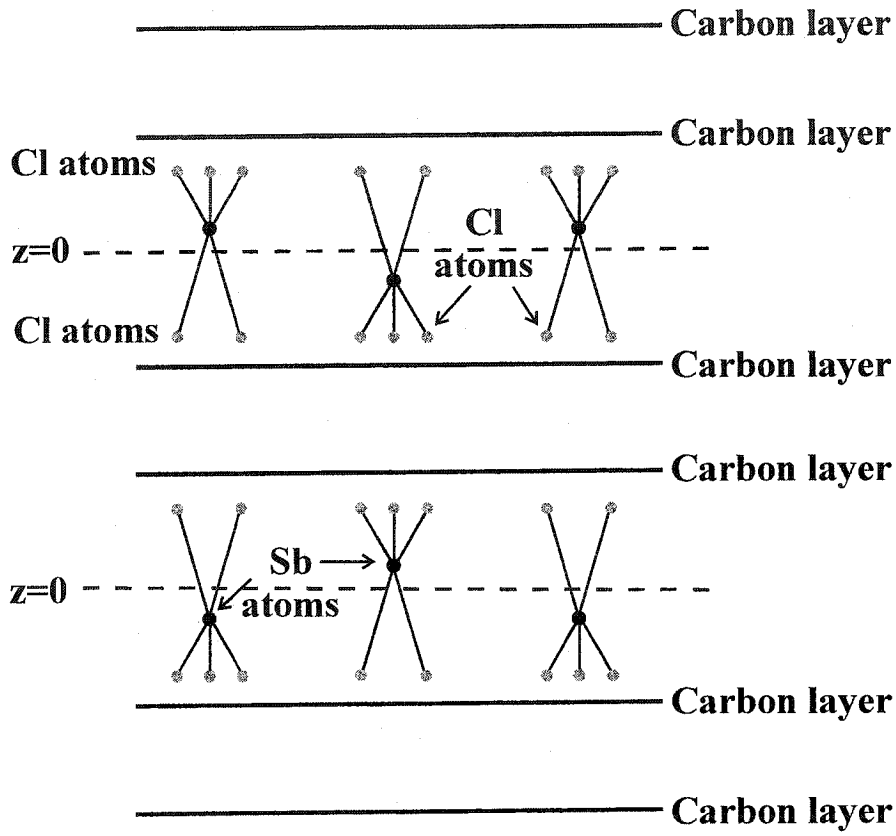

Figure 2.2.1 A schematic showing $SbCl_5$ intercalated into graphite as a stage 2 compound which illustrates the positions of the chlorine and the antimony atoms within the layered structure. (Adapted from reference 16)

Section 2.3 Electrochemical Anion Insertion

This section will briefly discuss experiments performed by various groups over the years in which different anions were intercalated electrochemically into a form of graphite. One has to keep in mind that not every article published will be included here but that it is hoped that the reader obtains a good overview of the possibilities for electrochemical anion insertion.

Early work on anion insertion into graphite was performed by Rudorff and Hoffman [24] where they discovered that HSO_4^-, PO_4^{-3} and $P_2O_7^{-4}$ could be intercalated into graphite. The c-axis repeat distance for HSO_4^- was found to be 7.84 Å as a stage 1 compound. The resulting composition was $C_{24}HSO_4$. Stage 2 compounds for both PO_4^{-3} and $P_2O_7^{-4}$ were obtained with c-axis repeat distances of 11.3 Å and 11.5 Å, respectively.

Dunning et al. [25] studied secondary, nonaqueous solvent batteries with a graphite compound positive electrode. The electrolyte they used was comprised of $LiClO_4$ in dimethyl sulfide. The electrolyte appeared to be stable up to 4.5 V. The authors suggested staging did not occur but rather a lamellar compound formed with the composition $C_{89}ClO_4$.

Besenhard and Fritz [26] confirmed the results of the Dunning group and performed similar experiments using propylene carbonate instead of dimethyl sulfide. They found that staging formed and that propylene carbonate seemed to be more stable at higher potentials than dimethyl sulfide. They also determined a stoichiometry of C_nClO_4. A pure stage was observed with $n = 24$. Stages with $n > 24$ were observed but were not

but the exact n could not be determined. No stages were observed that had n < 24. Besenhard and Fritz have also studied acidic solutions such as $HClO_4$ and H_2SO_4 [27, 28] where they showed that co-intercalation of the solvent occurred during the anion intercalation. That is to say, some of the $HClO_4$ (or H_2SO_4) would intercalate into the graphite foil along with the ClO_4^- (or HSO_4^-) ions. The cycling potential for this experiment ranges between 0 V and approximately 2.5 V. As Rudorff et al. discovered, for every 24 carbon atoms one anion would intercalate. Similarly, cells constructed using electrolytes consisting of propylene carbonate as the solvent and $LiClO_4$, $NaBF_4$ or KPF_6 as the salt also had a composition of C_nA where n>24 and A represents the intercalation molecule.

Beck, et al. [29] studied the intercalation of HSO_4^-, ClO_4^-, and BF_4^- into natural graphite. The source of these anions were aqueous acidic solutions at various molarities from rather low values, 0.1 M, to rather high ones, 12 M. These cells were operated up to potentials of 1.9 V vs. nhe[1]. If this potential was measured with respect to a lithium metal electrode, the potential would be approximately 5 V. The intercalation process was found to be reversible in a potential range of about 200 mV. The highest stage reached for each anion, A, resulting in a composition $C_{24}A$. They also reported cycling efficiencies of over 80% by the third cycle.

Billaud et al. investigated electrochemical insertion of $LiAsF_6$ [30, 31] and BF_4^- and PF_6^- [31] into pyrographite. It was discovered that there was co-intercalation of the solvent, CH_3NO_2. Stages 5 through 1 were achieved and with X-ray diffraction the

[1] nhe stands for the normal hydrogen electrode which is the 0 V thermodynamic reference point for potential measurements.

interlayer spacings were found. For AsF_6^-, the interlayer spacing of stage 5 was 21.39 Å; for stage 4 it was calculated to be 18.05 Å; stage 3 had a value of 14.69 Å; the spacing for stage 2 turned out to be 11.34 Å; and for stage 1 it was 8.00 Å. They determined a formula of $C_{24n}X(CH_3NO_2)_2$ where n represents the stage number and X the anion. The authors assumed that the distance between two carbon layers without an intercalant between them was 3.35 Å which resulted in an anion layer thickness of 8.00 Å. Stage 1 was achieved at a potential of 4.7 to 5 V. The potential for stage 2 was approximately 4.7 V.

Touzain et al. [32] studied PF_6^-, AsF_6^-, and SbF_6^- in a lithium salt propylene carbonate electrolyte. They found that four propylene carbonate molecules (PC) would co-intercalate into the carbon along with the anions resulting in a fairly large spacing between the carbon layers: 10.6 Å for PF_6^-+4(PC), 10.9 Å for AsF_6^-+4(PC). Through these experiments it was found that the composition was $C_{24n}X(PC)_4$ with n being the stage number and X the anion. Touzain et al. [33] also found that TaF_6^- would intercalate into graphite in the potential range between 3.5 V and 4.2 V. The composition of the intercalated graphite was found to be $C_{24n}TaF_6(PC)_4$, where n represents the stage number and PC is the solvent part of the electrolyte, propylene carbonate. Stage 3 and stage 2 were found to give c-axis spacings of about 21 Å and 17.3 Å, respectively. This suggests an anion layer spacing of about 14 Å. At first this seems rather large, but considering the fact that the solvent co-intercalates, the value is not so large. In fact, stage 1 was not achieved because of this co-intercalation.

Most of the work with electrochemical anion intercalation involves relatively small ions. It is possible for larger anions to intercalate into graphite as well. Boehm et

al. studied intercalation of perfluorobutanesulfonic acid, $C_4F_9SO_3H$, [34, 35] and other perfluoroalkanesulfonic, $C_nF_{2n+1}SO_3H$, and alkanesulfonic acids, $C_nH_{2n+1}OSO_3H$, [36]. Stages 1 through 3 were observed for $C_4F_9SO_3H$ with an intercalant layer spacing of about 20 Å and a formula of $C_x(C_4F_9SO_3)$ where for stage 1 x = 24 to 28, x = 48 to 70 for stage 2 and x = 85 to 94 for stage 3. By comparing various perfluoroalkanesulfonic acids, $C_nF_{2n+1}SO_3H$ where n = 4, 6 or 8, it was discovered that the potential curve for oxidation was more structured for n = 4 than for n = 6 and n = 8. Stage 2 compounds were achieved for all three perfluoroalkanesulfonic acids all with very large intercalant layers, greater than 20 Å. Stage 1 was not achieved for n = 8. It was found that CH_3OSO_3H and $C_4H_9OSO_3H$ both obtained an intercalant layer spacing of about 7.9 Å and a stage 2 repeat axis distance of about 11.3 Å both of which are very similar to smaller intercalant species such as PF_6^-.

Sanathanam and Noel [37] worked with $LiClO_4$, $(TBA)ClO_4$, and $(TBA)BF_4$. TBA represents tetrabutyl ammonium. The concentration of these salts were 0.25M in three different solvents: propylene carbonate, PC; acetonitrile, AN; and methanol, MeOH. The cells were charged to a potential of 2.5 V, and the reference electrode was a saturated calomel electrode. The efficiency of these cells was found to be better for the PC electrolyte. Both $LiClO_4$ and $(TBA)BF_4$ had higher efficiencies than $(TBA)ClO_4$. Overall the $LiClO_4$ cell performed the best. If the concentrations of the cells, constructed with $LiClO_4$ and $(TBA)BF_4$, were increased, the efficiencies of the BF_4^- cells are higher than the ClO_4^- anions, ~90% versus ~75% at ~1 M. X-ray diffraction measurements were also performed. Results show a d-spacing of 5.27 Å and 5.21 Å for ClO_4^- and BF_4^-, respectively. One cannot say if this is the intercalated molecule layer spacing or not,

since no mention is given to the staging of the graphite electrode or what angles the X-ray diffraction patterns were taken, the first (00ℓ) peak may not have been scanned.

Leng et al. [38] studied the electrochemical synthesis and characterization of formic acid graphite intercalation compounds. In this case, the formic acid solution served as both the electrolyte and the intercalant source. They were able to from stages 3, 4 and 5 with c-axis spacings of 14.41 Å, 17.75 Å and 21.11 Å, respectively. This resulted in an intercalant layer spacing of 7.7 Å. Stage 2 and 1 did not form. This is most likely due to exfoliation of the graphite material when charged beyond the potential plateau of 1.9 V versus Hg/Hg_2SO_4.

Yan and Lerner [39] have shown that $N(SO_2CF_3)_2^-$ can intercalate into graphite. Two different electrolytes were used: 0.33M $LiN(SO_2CF_3)_2$ in CH_3NO_2 and 0.66M $LiN(SO_2CF_3)_2$ in ethyl methyl sulfone, EMS. The carbon electrodes were prepared by making a slurry of a carbon powder and the reference electrodes were lithium foils. The electrochemical experiments were performed in glass cells under an Argon atmosphere. The cell cut-off potential for the discharge was 2.4 V where as the upper cut-off potential for charge was approximately 5.4 V. Their work shows the presence of staging during intercalation and has a capacity of ~450 mAh/g in CH_3NO_2 which is higher than the value for lithium, 372 mAh/g. However, the discharge capacity is much lower, barely 100 mAh/g, an efficiency of 22%. It was found that the anion layer spacing was 8.12 Å. In EMS, a capacity of ~300 mAh/g was achieved at approximately 5.9 V in a pulse-charge experiment. The cycling efficiency was not reported for this particular experiment. The composition of the intercalated stage 1 compound, for the experiments with CH_3NO_2 as the solvent, was found to be $C_{23.1}N(SO_2CF_3)_2 \cdot 0.6\ CH_3NO_2$.

Section 2.4 Structure Determination

The structure of intercalated graphite compounds has been seldom determined. There are various ways to determine the structure of these compounds. A few different intercalated species and the methods used to determine their structure by various groups shall be discussed in this section.

It seems that there is more work involving larger species that form into chains such as hexafluorobutanesulfonic acid, as opposed to smaller species such as perfluorophosphate and copper chloride.

Perfluorobutanesulfonic acid was studied by Ruisinger and Boehm [34, 35]. They discovered that once intercalated, the acid forms a bilayer structure between two carbon layers and that as more of $C_4F_9SO_3H$ is intercalated into the carbon material the spacing increases from 17.7 Å to 21.0 Å for stage 1. This suggests that there is a change in the orientation of $C_4F_9SO_3H$. The SO_3 group of the acid is closer to the carbon later with the C_4F_9 chains pointing toward the center at an angle, see Figure 2.4.1. The angle shifts from 40° to 58° from the plane of the graphite layers as more $C_4F_9SO_3H$ enters into the layer.

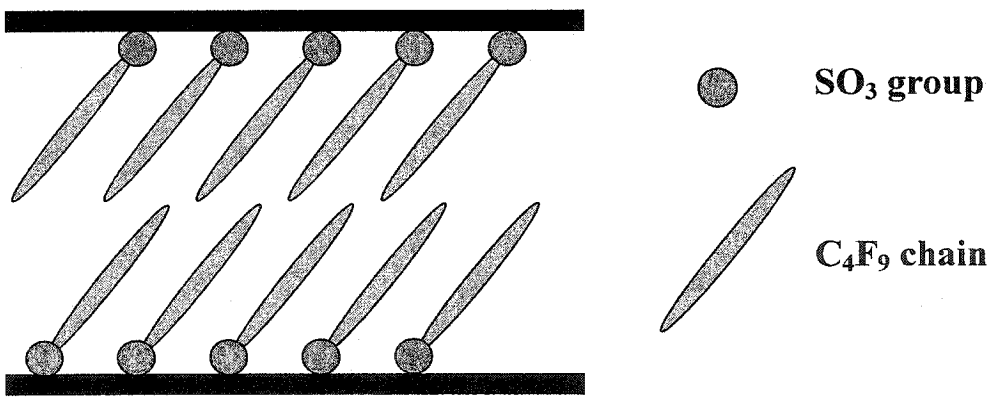

Figure 2.4.1 Illustrating the orientation of $C_4F_9SO_3^-$, adapted from reference 34.

Ruisinger and Boehm also studied other perfluoroalkanesulfonic, $C_nF_{2n+1}SO_3H$, and alkanesulfonic acids [36]. Both $C_6F_{13}SO_3H$ and $C_8F_{17}SO_3H$ formed a bilayer structure as $C_3F_7SO_3H$ did but no re-orientation occurred. The alkanesulfonic acids however in general did not form a bilayer structure. The only alkanesulfonic acid to form a bilayer structure was $C_5H_{11}OSO_3H$ with a spacing of ~25 Å. The other acids assumed a "flat" position, see Figure 2.4.2 with a layer spacing of approximately 7.9 Å. They thought that the flat position of $C_4H_9OSO_3^-$ was due to the fact that this is the only arrangement that would allow all four oxygen atoms to be near the carbon layers. The bilayer forms when the space between the SO_4^- groups is not large enough to accommodate the alkyl chains as for $C_5H_{11}OSO_3H$.

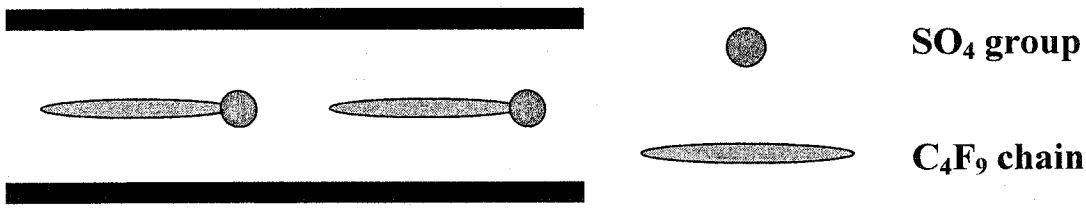

Figure 2.4.2 Illustrating the "flat" position of $C_4H_9OSO_3^-$.

Perfluorooctanesulfonic acids, $C_8F_{17}SO_3H$, were also studied by Lerner et al. [40,41,42]. They discovered as Ruisinger and Boehm did that a bilayer structure was formed with an ~ 60° inclination angle. Lerner's group also discovered that the anions nestle by 2 to 3 Å at the center of the intercalated layer, see Figure 2.4.3, which is fairly significant. They prepared $C_8F_{17}SO_3H$ intercalated graphite by both chemical and electrochemical means [41]. It was found that the compounds obtained by the chemical route have anion layer spacings about 3 Å smaller than the electrochemically prepared compounds. This suggests that there is a smaller inclination angle for the chemically

prepared compounds. They also found that the distance from the carbon layer to the sulfonate oxygen plane was ~ 3 Å.

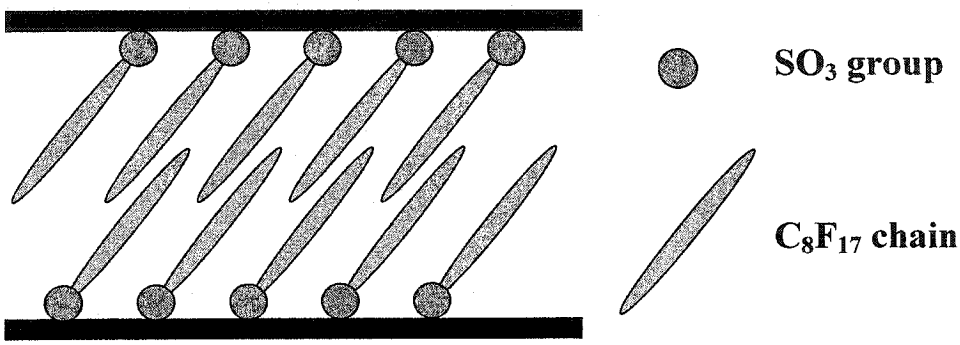

Figure 2.4.3 Illustrating the nestling of $C_8F_{17}SO_3^-$, adapted from reference 41.

Lerner et al. also tried to determine the exact structure of the intercalated $C_8F_{17}SO_3H$ using both a helical and linear model for the anion and one-dimensional electron density maps [42]. The results between the two models were fairly similar although the helical model resulted in a better fit to experimental values. The fitted parameters were the inclination angle, 60° and 58.8° for the helical and linear models, respectively; the carbon to SO_4^- plane distance, 2.95 Å and 3.05 Å for the helical and linear models, respectively; and the twist angle: 16° for the helical model and 0° for the linear model, naturally.

Graphite $B[OC(CF_3)_2C(O)O]_2^-$ intercalation compounds were also studied by Yang and Lerner [43]. It was discovered that the intercalated layer thickness was about 10 Å which suggests that the anion has a "standing up" orientation between the graphite layers, see Figure 2.4.4. The observed and calculated 1-D electron density maps for this particular orientation matched quite well. By structure refinement it was found that for every anion there were 44 carbon atoms.

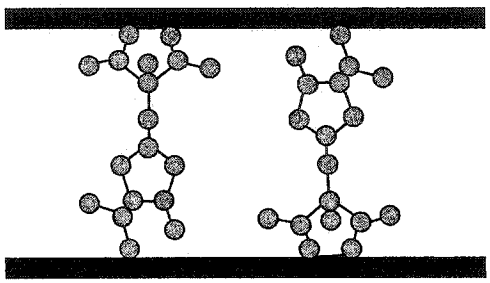

Figure 2.4.4 Illustrating the standing up orientation of $B[OC(CF_3)_2C(O)O]_2^-$, adapted from reference 43.

Some of the smaller intercalants that have been studied and it's intercalated structure determined are $MoCl_5$ and potassium-ammonia by Depondt et al. [44]. They used a simple maximum entropy model to determine the stacking profile. It was found that molybdenum lies in the center of the intercalated layer. Unfortunately, it is not mentioned where the chlorine atoms are situated. They found that both the potassium and the ammonia were located in the middle of the intercalated layer. It was determined that there were two possible orientations for the ammonia which are illustrated in Figure 2.4.5.

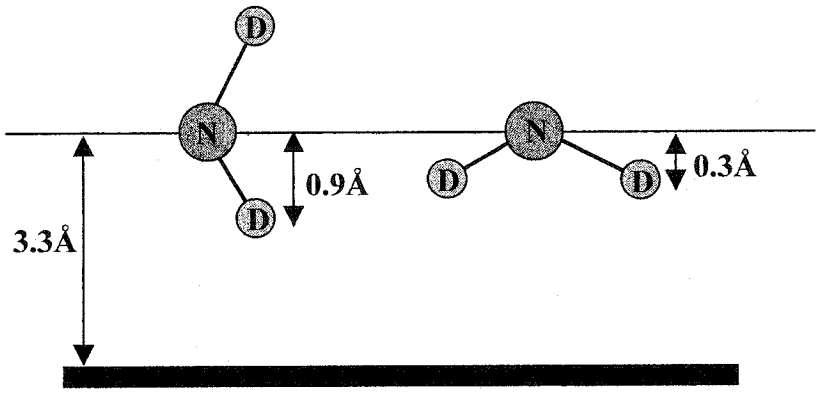

Figure 2.4.5 Illustrating the two different orientations of ammonia, adapted from reference 44.

Copper chloride intercalated graphite has also been studied. Schlögl et al. [45] found that the orientation of $CuCl_2$ between graphite layers is anisotropic and that there is short range ordering within the layer. The in-plane structure of the intercalated material

corresponded very well to the standard configuration of the space group C2/m. They were unable to analytically determine the exact atom positions due to the disorder present in the samples studied. However, the copper atoms were located in the center of the intercalated layer and the chlorine atoms were located above and below the copper atom at a distance approximately equal to ⅙ of the distance between two graphite layers with $CuCl_5$ in between them.

As with most research areas there is always room for more investigation. Anion intercalation into graphitic carbon is no exception. The work presented in this thesis will, hopefully, fill some gaps in the understanding of anion intercalation and provide useful information for future researchers.

Chapter 3 Experimental Procedures

As with any scientific study, numerous procedures and equipment were used. The equipment that was used in this thesis includes an X-ray diffractometer and electrochemical testing equipment. These apparati will be discussed here. The procedures used to prepare and study the electrodes and the electrochemical cells will also be discussed.

Section 3.1 Sample Analysis

The various carbon materials studied were first characterized by obtaining an X-ray diffraction pattern of each sample. Several types of carbon were investigated including fibers, fabrics, graphite, meso-carbon micro-beads (MCMB) and cokes.

The X-ray diffraction patterns were mainly obtained with a Siemens D5000, although other X-ray machines were sometimes used if the main machine was not available. Generally speaking, X-ray diffraction patterns are obtained by measuring radiation scattered from a sample. The appearance of a diffraction pattern depends greatly on the position of the atoms within a material. Suppose a sample with lattice planes such as depicted in Figure 3.1.1, is placed in an X-ray diffractometer and a scan is performed. The incident radiation will be scattered from atoms within the sample. For constructive interference, the path difference between rays reflected from neighbouring planes must be an integral number of wavelengths of the incident beam. This condition is known as Bragg's Law and is given by the equation

$$m\lambda = 2d\sin\theta \qquad (3.1.1)$$

where m is an integer, λ is the wavelength of the X-rays, d is the distance between the two adjacent planes and θ is the incident angle. It is fairly common to plot X-ray diffraction patterns with respect to twice the incident angle, 2θ. This angle is known as the scattering angle. An example of an X-ray diffraction pattern is shown in Figure 3.1.2.

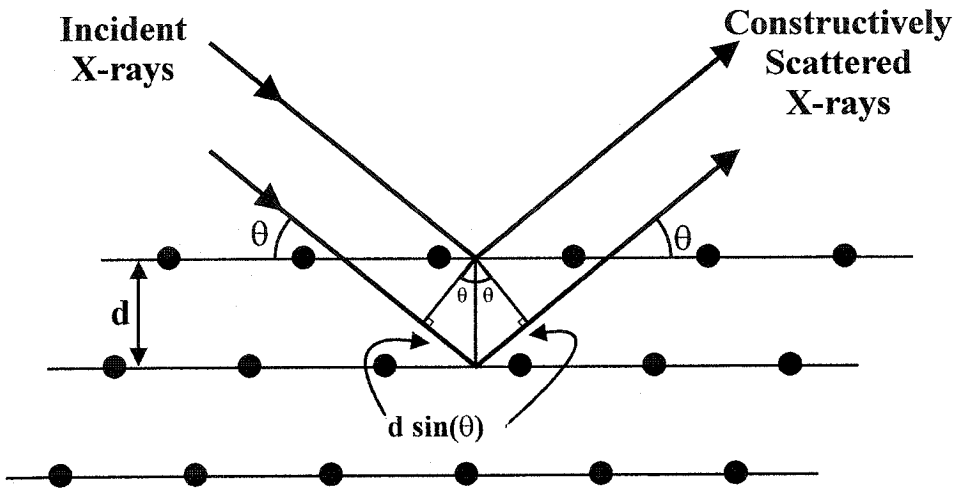

Figure 3.1.1 An illustration of a Bragg reflection.

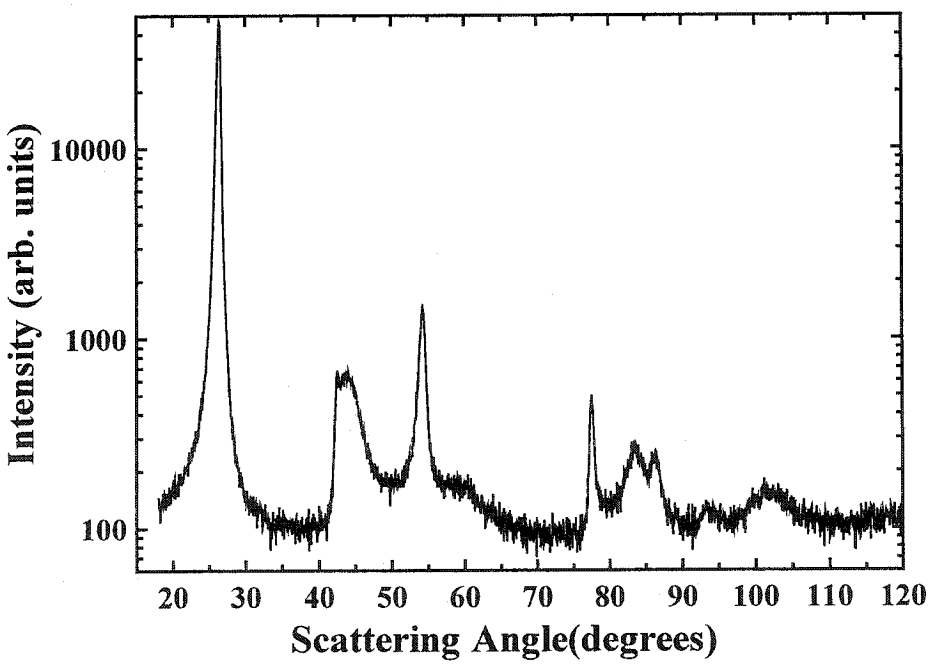

Figure 3.1.2 An example of an X-ray diffraction pattern.

The main difference between X-ray apparati is the orientation of the X-ray tube, the counter and sample, some or all of which can rotate with respect to the other components. Since the main type of machine used was a Siemens D5000 θ-θ diffractometer, its orientation and general operation shall be discussed briefly. This type of machine has a fixed sample holder and a moveable copper X-ray tube and detector. The tube and detector rotate at the same angle, with respect to the sample, while data is being collected. This is illustrated in Figure 3.1.3. The X-rays are emitted from the tube and travel through the divergence slits before striking the sample. These slits limit the size of the X-ray beam so that most, if not all of the beam, strikes the sample. After striking the sample, the reflected X-rays then travel through anti-scatter and receiving slits and then are collected in the detector. The receiving slits eliminate stray X-rays by counting only those that are diffracted from the sample, at an angle equal to that of the incident X-rays. The size of the receiving slit controls the angular resolution of the measurement as well as the signal to noise ratio.

Once the X-ray diffraction patterns were obtained they were analyzed using various fitting programs. Some of the parameters that were determined using these programs are the c-(or z-)axis repeat distance as well as an ordering factor. These shall be discussed in more detail in Chapter 4.

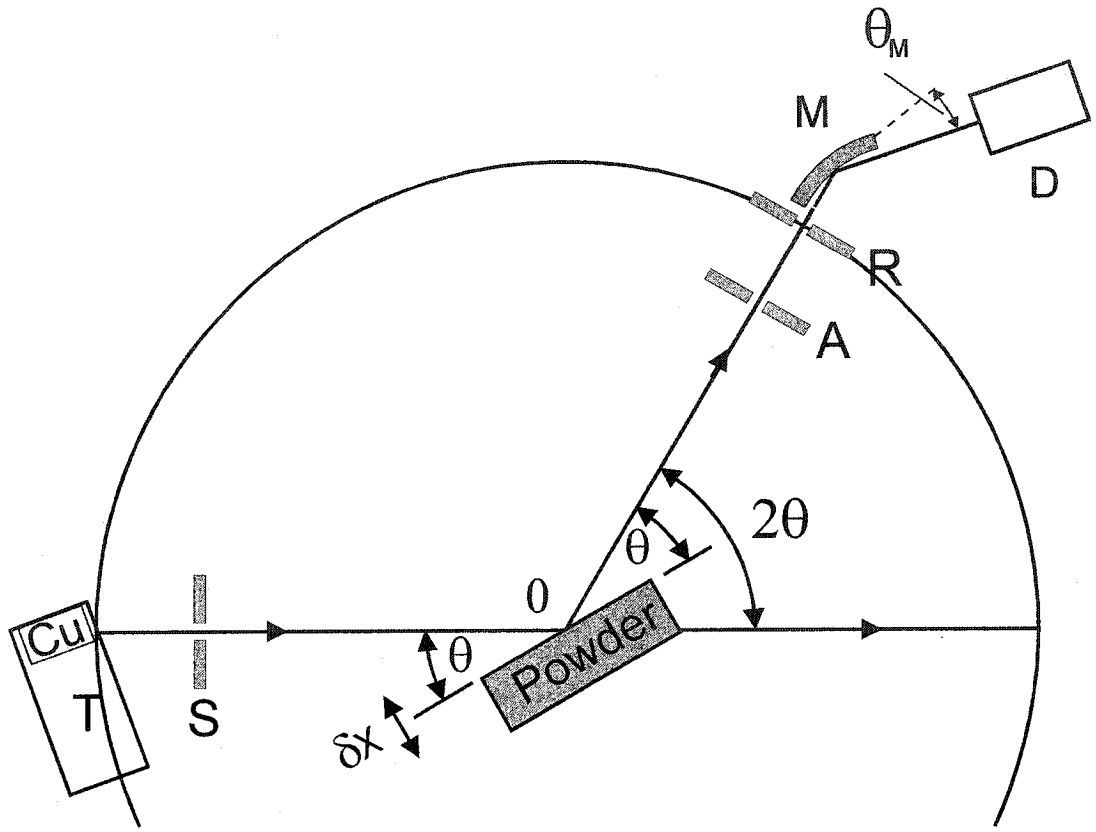

Figure 3.1.3 A schematic of the Siemens D5000 diffractometer.

Section 3.2 Electrode and Electrolyte Preparation

Once the carbon materials were characterized, they were then made into electrodes. These electrodes were made using the following recipe: about 12% by weight consisted of the active material, ~2.7% Super S black, ~6.0% Kynar Polymer (VdF-HFP), ~9.3% Ethylene Carbonate/Propylene Carbonate (EC/PC), and ~69.5% acetone. These substances are mixed under very low heat, at about 40-60°C, for about three hours before being spread over a glass plate using a notch bar to achieve a consistent thickness. The thickness could range between 0.006 inches to 0.026 inches (0.15 mm to 0.66 mm). The 0.026" notch bar was primarily used. The acetone was then allowed to evaporate.

The Super S black is a form of carbon black. Carbon black is a component of most rechargeable battery electrodes. Its main purpose is to aid in keeping the various particles of active material electrically connected, see Figure 3.2.1. The acetone is present to dissolve the polymer and to aid in spreading the electrode material into a film.

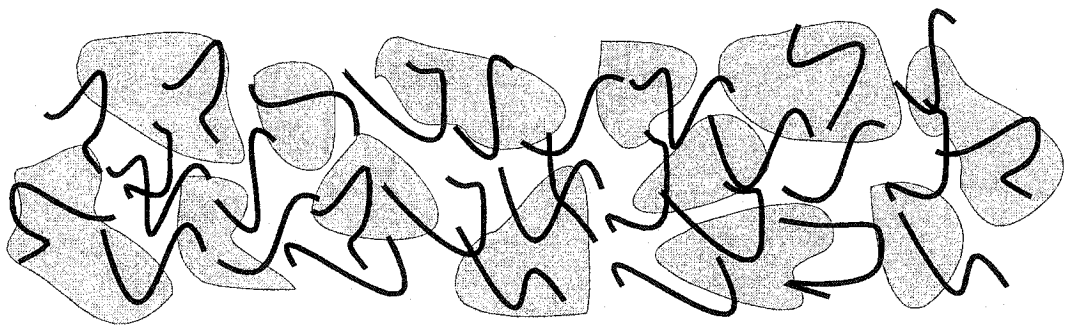

Figure 3.2.1 A schematic of the structure of an electrode demonstrating the usefulness of Super S black, represented by strings. The dark shapes represent the active material. Please note that the size of Super S Black is exaggerated.

Once prepared, the electrode material is then cut into the desired electrode shape, in this case, a circular disc, about 13 mm in diameter. These electrodes are then soaked

in diethyl ether a couple of times. The first for about 10 –20 minutes, the second for at least a 12 hour period. This soaking will remove most, and hopefully all, of the EC/PC. This will leave microscopic openings/holes in the electrodes that will be filled by the electrolyte once the cells are made.

Some of the electrolytes used in this work were bought commercially while others were prepared in house. The 1M $LiPF_6$ in ethylene carbonate / diethyl carbonate (EC/DEC) was purchased from Merck, Germany. The electrolytes that used ethyl methyl sulfone (EMS) as the solvent were made in house. EMS comes in solid form and was purchased from TCI America. If EMS is heated to about 60°C, it melts. After adding the desired amount of $LiPF_6$, $LiBF_4$ or $LiClO_4$, to make 3 M solutions, the solutions remain liquid at room temperature. It has been suggested [46] that these solutions may be supersaturated.

Section 3.3 Cell Construction, Different Types

Once the electrodes have been prepared, the cell parts are placed inside an argon-filled glove box to prevent contamination, mainly from water. The cell parts consist of a stainless steel can, top and bottom, a stainless steel spring and spacer, a polypropylene gasket, the lithium electrode, separator, and the carbon electrode.

Before assembling the cell, for certain electrolytes, the electrodes and separators are pressured-wetted. The electrodes and separators are placed in a vial and then covered with the electrolyte. The vial is then placed in a container that can be sealed. After closing, the pressure inside this container is increased to approximately 200 psi. It is left at this pressure for about thirty minutes. This procedure ensures that the viscous electrolyte enters the pores of the electrode and the separator and does not just lie on the surface. The high pressure is then released and the electrodes and separators are ready for use.

The cell assembly is shown in Figure 3.3.1. The cell is assembled upside down. The cell top in placed upside down and the carbon electrode is placed inside, in the center. The separator and any electrolyte, if needed, are added. A lithium foil disc is then placed on top of the separator. The purpose of the separator is to prevent direct contact between the two electrodes which would short the cell. The separator is a woven polypropylene material, cut into circles. The typical thickness of the separator is 0.002", but with these experiments a much greater thickness was used, 0.007" to 0.015" per separator. The number of separators used depended on the mass of the active material in the electrode. A spacer and spring are then added to fill the rest of the cell and to provide good electrical contact with the cell can. To prevent shorting and to provide a seal, a

gasket is then added as well as the cell can bottom. The whole assembly is then placed in a crimper which applies high pressure to the cell, crimping the edges of the cell can top into the gasket which seals the cell. Once finished and removed from the glove box, stainless steel tabs are attached to the bottom and top of the can to facilitate the insertion of the electrochemical cells into the testing equipment.

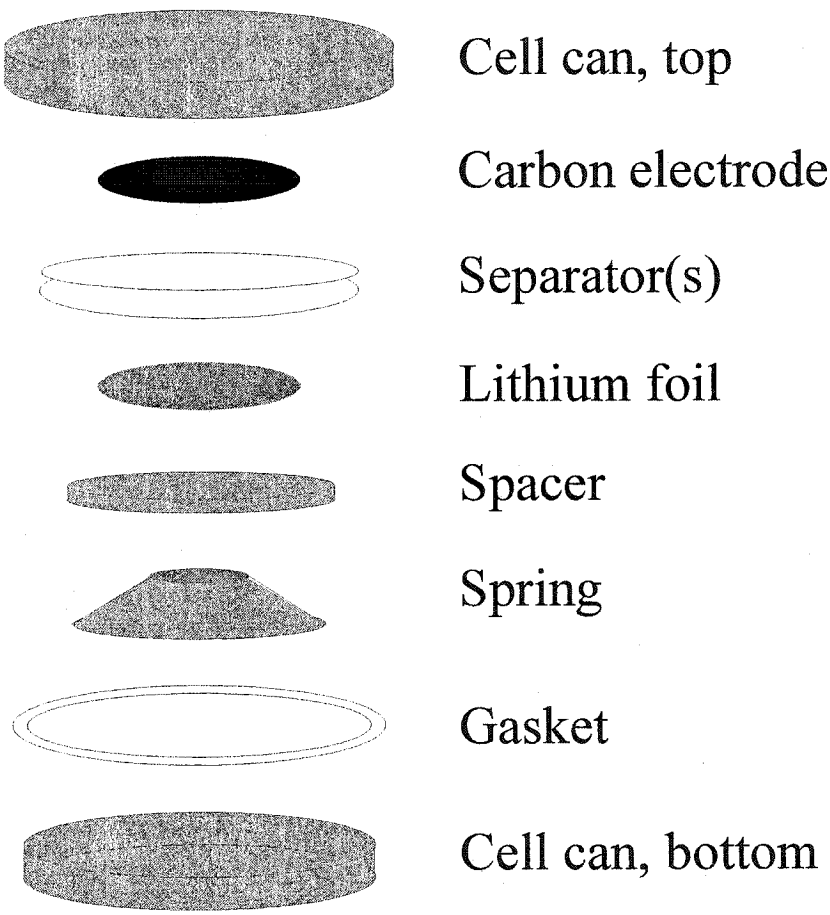

Figure 3.3.1 The assembly of a typical coin cell.

The cell assembly described above was the main type used, however for certain experiments, another type of cell was required. For some experiments it was desirable to obtain X-ray diffraction patterns of the electrode while cycling the cell, referred to as an

in-situ X-ray diffraction experiment. The assembly is very similar to that of a normal cell, except for the addition of a beryllium (Be) window and an aluminum ring, see Figure 3.3.2. The cell can top has had a hole cut into it to allow the X-rays to pass through. The Be window is glued to the cell can, and after assembly, it is sealed using Torr Seal™. The aluminum ring was placed between the Be window and the electrode to help prevent the electrolyte from reacting with the beryllium.

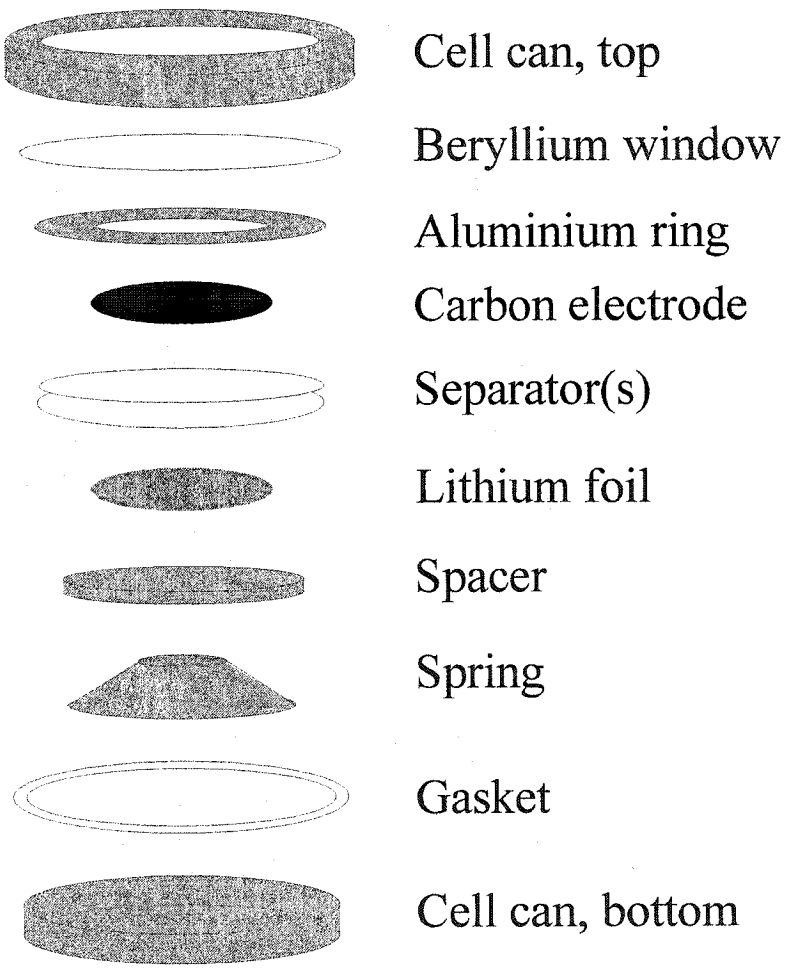

Figure 3.3.2 The cell assembly used for *in-situ* X-ray diffraction experiments.

Section 3.4 Electrochemical Testing

Once the cells were constructed, the electrochemical properties of the electrode material could be tested. For this, a computer controlled testing system was used. There are numerous ways to test the performance of a cell. Two of the most common ways are: 1) holding the cell at a constant current while measuring the potential, and 2) cyclic voltammetry where the cell's current is measured while its potential is varied between two values. The method used here is the constant current method.

In the constant current method, values for charge and discharge currents are input into the computer as well as two cutoff potentials. For example, suppose the potential range that is desired is 1.0 to 4.5 V. Also suppose that the currents are +/- 0.1 mA. Suppose that the cell is charged first. The 0.1 mA current will be applied until the potential that is measured reaches, or surpasses 4.5 V. At this point the current will then switch to the discharge current, in this case –0.1 mA. The cell will be discharged until the lower cutoff potential of 1.0 V is reached. The cell then begins to be charged again using the specified charge current. This cycle will repeat until the desired number of cycles is reached. Note that a complete cycle is considered to be a set of one charge and discharge sequences.

Section 3.5 *In-situ* X-ray Diffraction Experiments

Sometimes it is desirable to investigate what happens to the structure of the electrode while it is cycling. Generally, this can lead to information that may explain why, perhaps, a cell fails, or succeeds, and can eventually lead to improvements. More specifically, especially in terms of this thesis, it will provide information about the physics of the intercalation process.

In order to perform these types of tests, an electrochemical cell placed in an X-ray diffractometer is desirable. For a description of this cell, refer to Chapter 3 Section 3. The cell is placed into a holder specifically designed to hold the cell and be able to fit into the X-ray diffractometer. A schematic of one of these holders is shown in Figure 3.5.1.

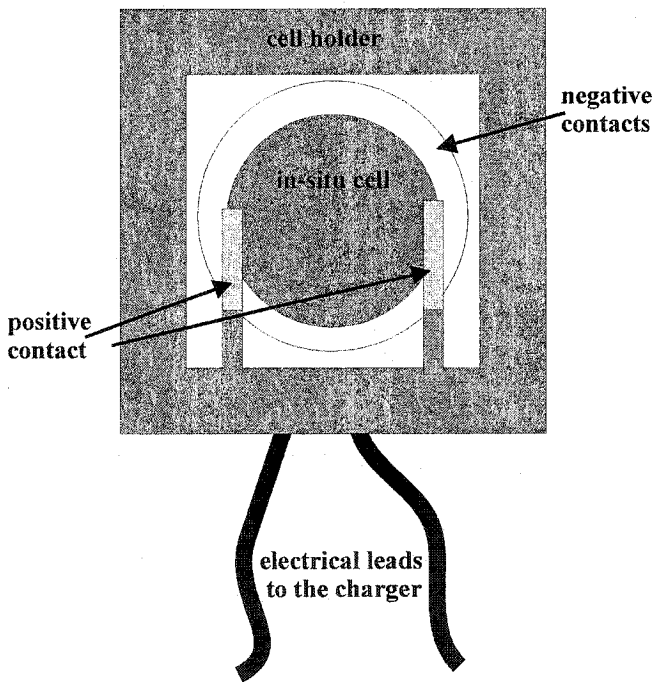

Figure 3.5.1 A schematic of the cell holder for *in-situ* X-ray diffraction experiments.

Once the cell and holder are placed in the X-ray diffractometer, a run is setup so that once one X-ray scan is completed, another immediately begins. While the X-ray diffractometer is running, the cell is being cycled. This type of experiment is referred to as an *in-situ* X-ray diffraction experiment. An example of the data obtained from this type of experiment is shown in Figure 3.5.2. The total length of time for an *in-situ* X-ray diffraction experiment could be a couple of days to almost a week but the actual length of time for a particular X-ray scan was usually about two hours.

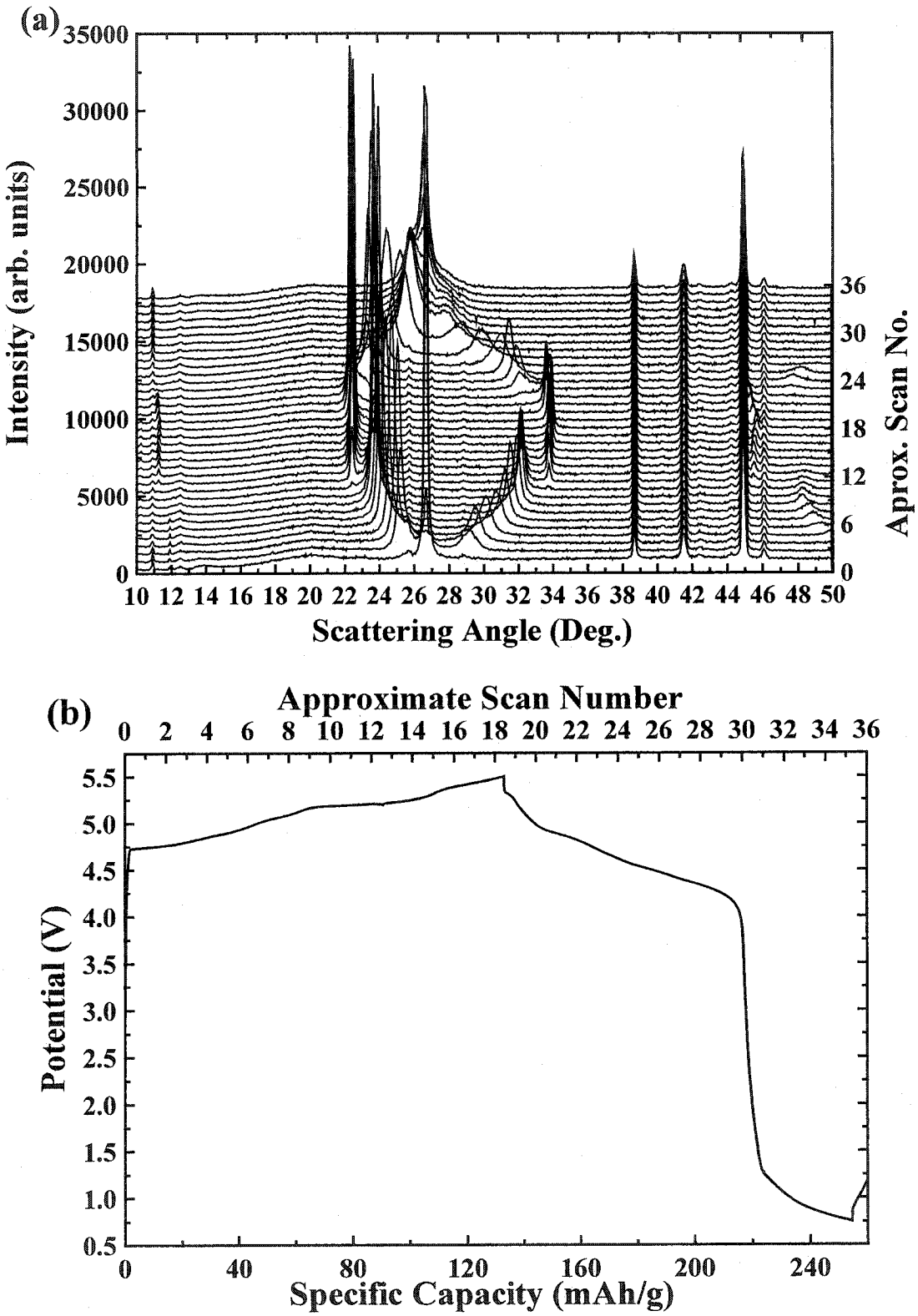

Figure 3.5.2 *In-situ* X-ray diffraction data. (a) Diffraction patterns obtained from the X-ray diffractometer. (b) Cell potential versus specific capacity obtained from the charger system.

Section 3.6 *Ex-situ* X-ray Diffraction Experiments

During *in-situ* X-ray diffraction experiments it is sometimes difficult to distinguish peaks from the electrode and peaks from the holder and other components of the cell. The range of angle is also limited. In order to scan a wider range of angle and eliminate some of the background peaks an *ex-situ* X-ray diffraction experiment is performed.

A normal cell is constructed and charged to the desired potential and removed from the charger. The cell is then taken into an argon filled glove box where it is dismantled. The electrode is placed in an *ex-situ* holder, which is air tight, preventing contamination from the environment. This holder is illustrated in Figure 3.6.1. The holder is then placed in the X-ray diffractometer and data is collected.

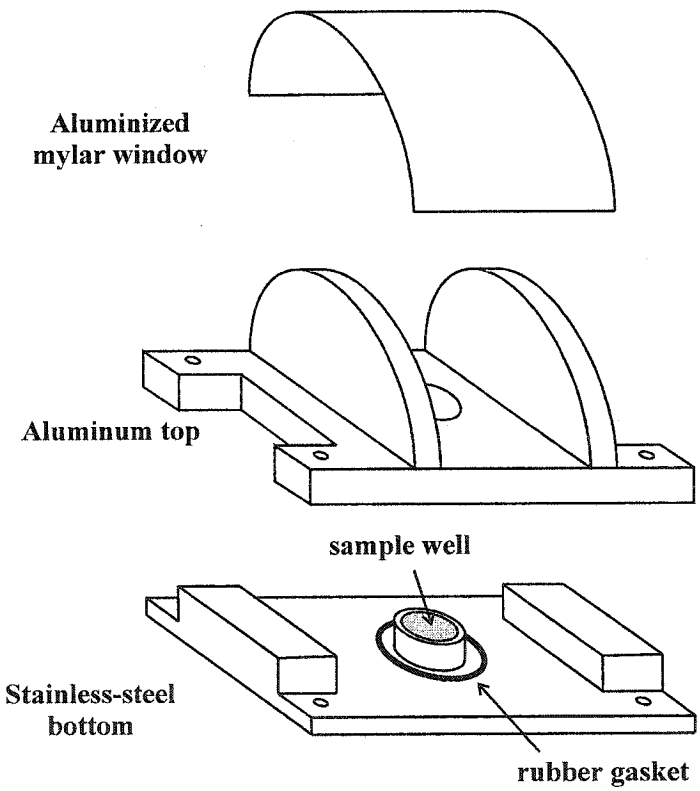

Figure 3.6.1 A schematic of an *ex-situ* holder.

An example of the difference between an X-ray pattern obtained during an *in-situ* and an *ex-situ* X-ray diffraction experiment is shown in Figure 3.6.2. It can be easily seen that the background in the *ex-situ* X-ray diffraction experiment is much lower than that of the *in-situ* X-ray diffraction experiment. As well, there are several peaks not present in the *ex-situ* scan that are present in the *in-situ* one. These peaks are due to components of the cell other than the carbon electrode itself. With the removal of these components it is easier to distinguish important peaks from the background. For instance, the peak just above 45° is surrounded by other peaks in the *in-situ* X-ray diffraction experiment whereas it is not in the *ex-situ* X-ray diffraction experiment and therefore easier to see.

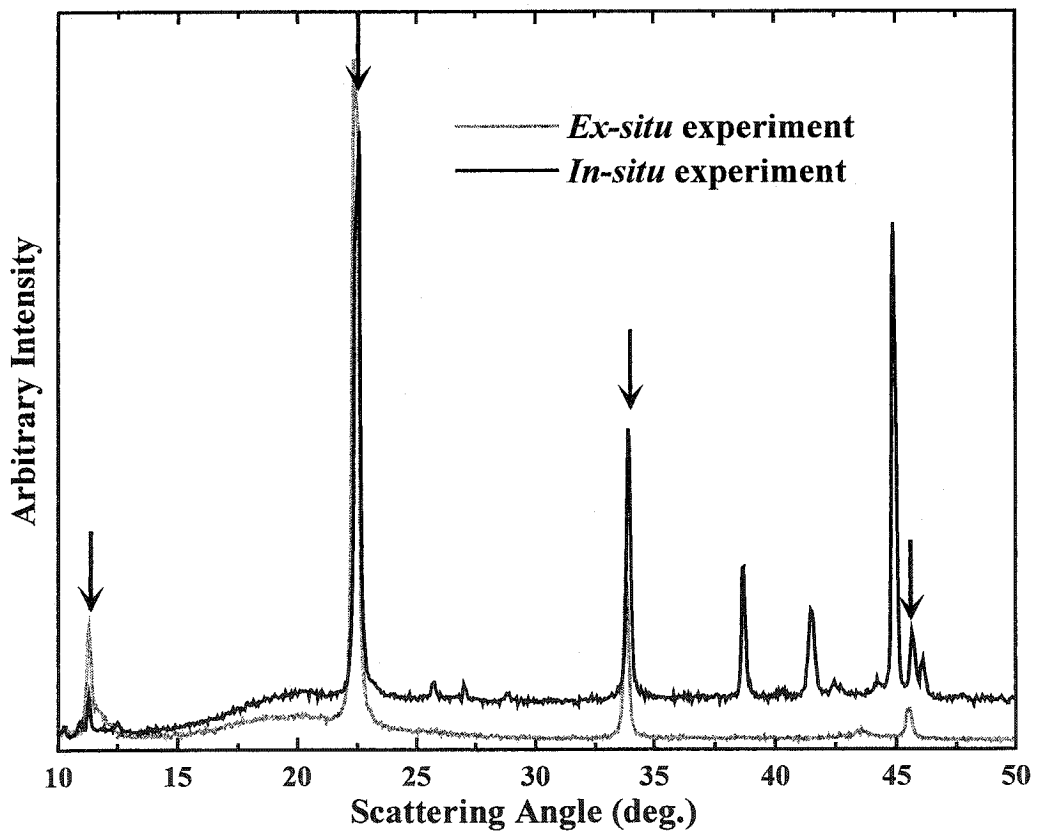

Figure 3.6.2 Comparison between *in-situ* and *ex-situ* X-ray diffraction data.

Chapter 4: Analysis Programs

As in most theses, there are always several programs that are used for the analysis of any data. Some of the various programs that were used will be discussed here.

Section 4.1 Carbonxs

A previous member of the group originally developed a program called carbonxs [47], which is used to determine various properties of a carbon material. Among the parameters that can be determined are: the average spacing between carbon layers, the fraction of layers that are in the typical ABAB graphite structure, the average number of the carbon layers within a graphite particle, the a-axis parameter, an ordering factor, etc.

Carbon generally forms into sheets with a honeycomb structure. Graphitic carbon typically has an ABAB structure, where the A(B) represents a particular orientation of a carbon sheet, see Figure 4.1.1(a). The carbon atoms are represented by black circles. Suppose that the layer given in 4.1.1(a) is an A layer, then the carbon atoms in a B layer, given by the smaller gray circles, are shifted so that all centers of the rings in one layer are occupied by a carbon atom in the other, see 4.1.1(b). These layers would then alternate in a perfectly ordered system.

As with many materials there is usually some amount of disorder. In graphitic carbons this disorder, most commonly, is given by rotations and/or translations of a carbon layer from the typical AB stacking. The probability that two adjacent carbon layers will be turbostratically misaligned is given by p. A sample with a small amount of

disorder would only have a few layers that would not be in the ABAB stacking arrangement and would have a low p. Likewise a carbon material with a large amount of disorder will have a high p and will have very few layers with ABAB stacking. In Figure 4.1.2(a) the black and light gray layers are the same as in Figure 4.1.1(b), and they are in AB stacking. A third carbon layer, the dark gray one, has been translated from the AB stacking arrangement. It can been seen easily that the three layers in Figure 4.1.2(b) have been rotated and/or translated from the AB stacking arrangement and that there is a large amount of disorder present.

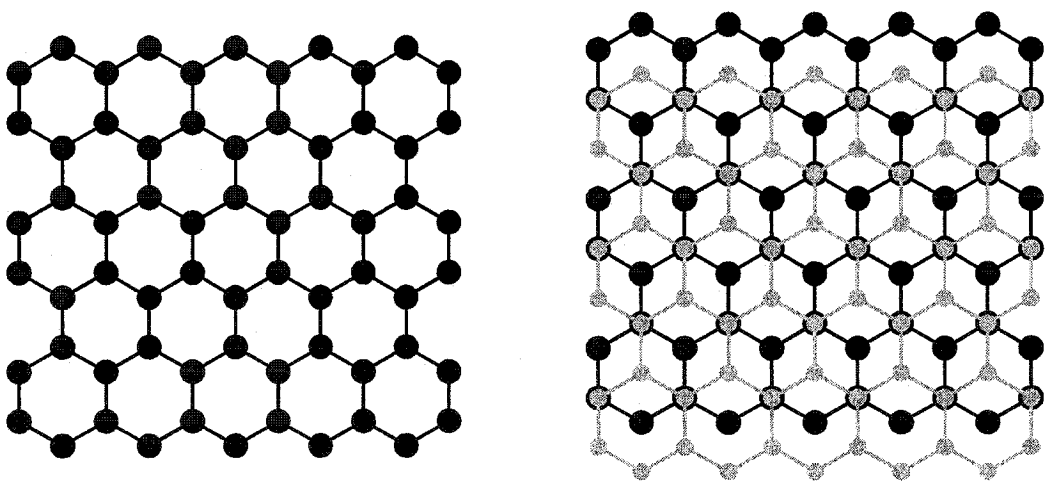

Figure 4.1.1 (a) The honeycomb structure of graphitic carbon. (b) Two layers of graphitic carbon in the AB stacking arrangement.

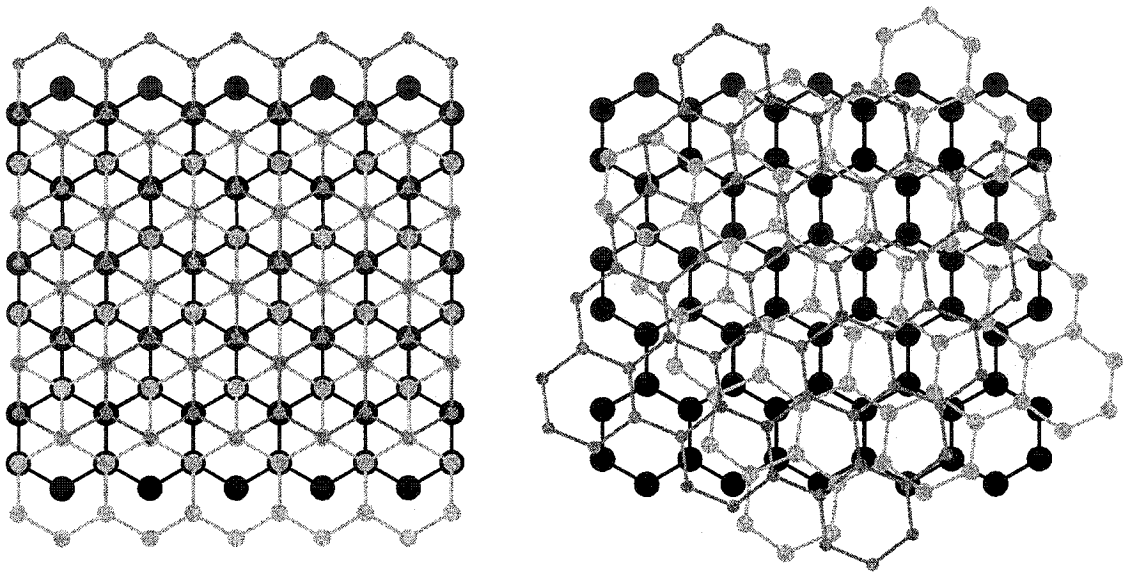

(a) (b)

Figure 4.1.2 Illustrating disorder within a carbon structure. (a) a material which is highly ordered, a low p. (b) a material which is highly disordered, a high p.

Section 4.2 Gfit

In order to determine the exact positions and intensities of the peaks in the X-ray diffraction patterns obtained from *in-situ* and *ex-situ* X-ray diffraction experiments a program called gfit is used. By using initial guesses for the position, width, intensity, and shape of various peaks, any X-ray diffraction pattern can be fit. The program uses both Guassian and Lorenztian peak shapes to fit the diffraction peaks. The information obtained with this program that is the most useful are the intensity and position of the peaks due to the active material being investigated.

Section 4.3 CAPV

A program called CAPV was used to convert the raw data obtained from the charger into useful formats such as data files that contain the potential, specific capacity and differential capacity of the electrochemical cell being investigated.

For constant current experiments, the potential, V, is measured with respect to time, t. A schematic of this type of data is shown in Figure 4.3.1. It can be seen that there are regions where there is a changing potential which signifies that for this potential range only one phase of the material exists. There are also regions where the potential barely changes which means that the electrode is changing from one phase to another, there is a co-existence of two phases. These phases are representative of a different form of the electrode.

To convert this data to specific capacity, the active mass, m_a, of the electrode is entered into the program. Specific capacity, Q, is given by the following equation

$$Q = \frac{i * t}{m_a} \tag{4.1}$$

where i is the input current and the units are Ah/g. An example of experimental data obtained from the charger with respect to time and after conversion to specific capacity is shown in Figure 4.3.2. In general the experimental data is not displayed as it is in Figure 4.3.2(b). The data would be displayed slightly differerntly, as it is in Figure 4.3.3. The only difference is that the discharge part of the curves are displayed with an increasing specific capacity as opposed to a decreasing one.

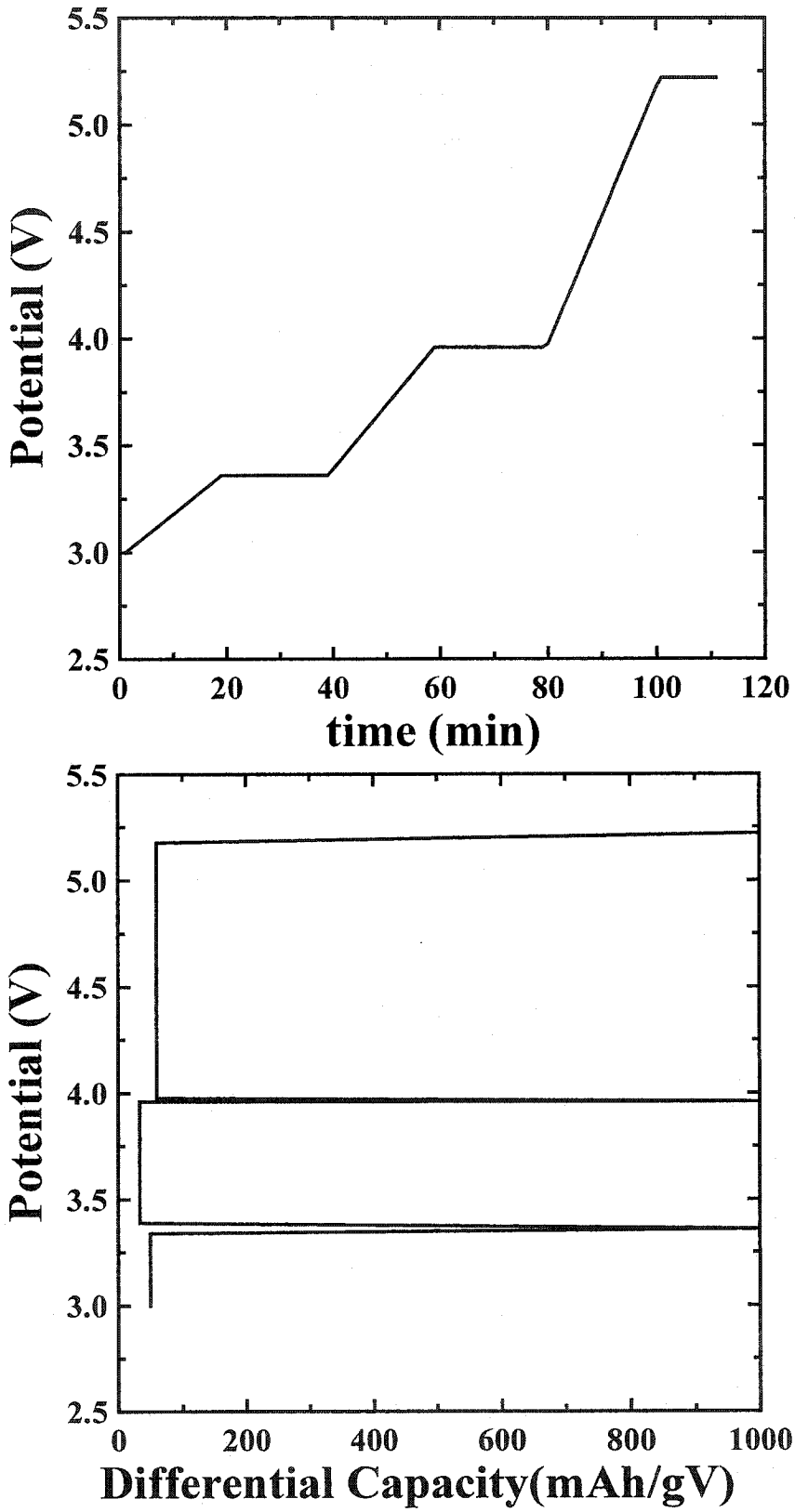

Figure 4.3.1 (a) Potential as a function of time. (b) Potential versus the differential capacity.

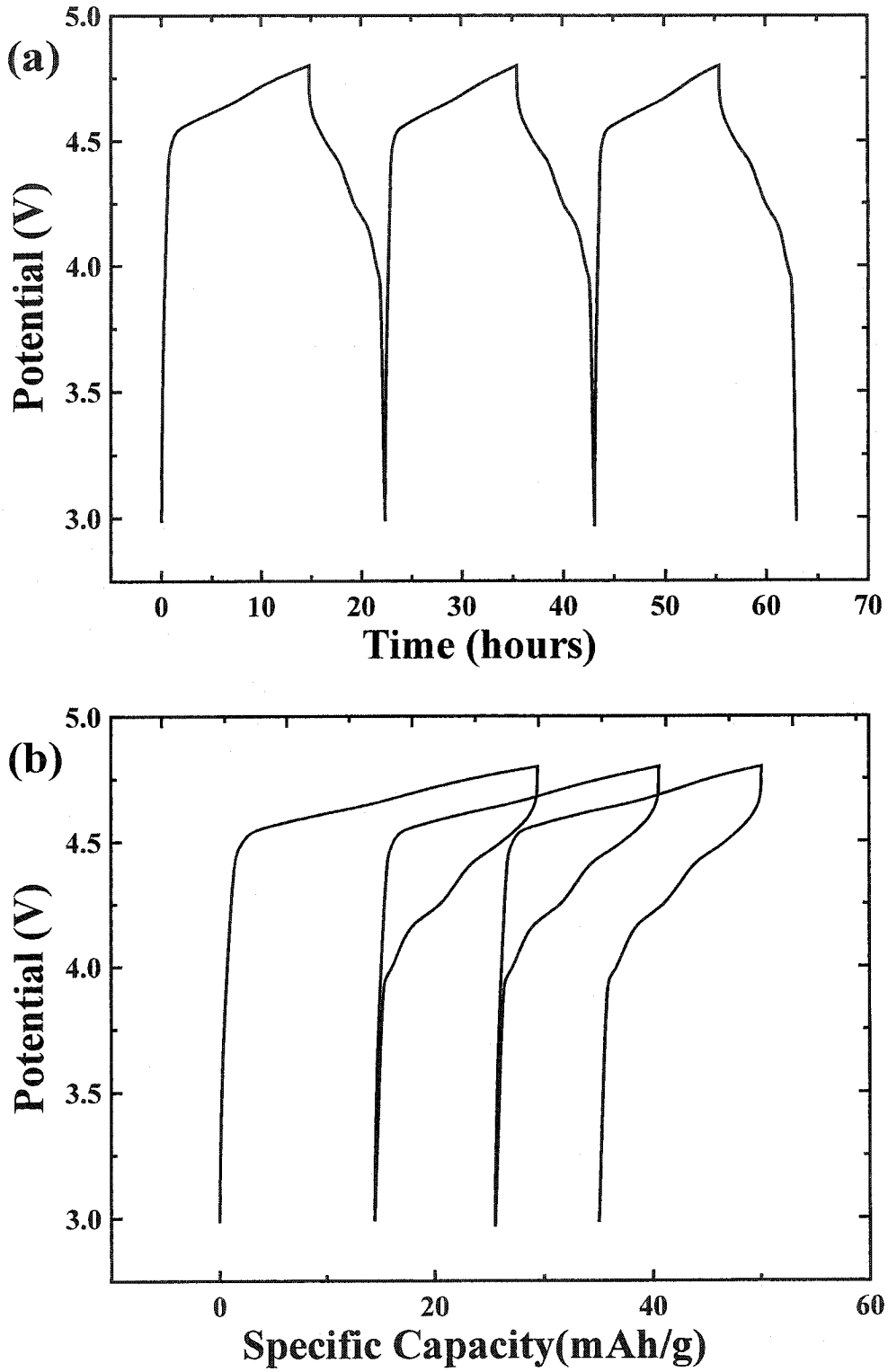

Figure 4.3.2 (a) An example of collected electrochemical data, cell potential with respect to time. (b) The same data converted to cell potential versus specific capacity.

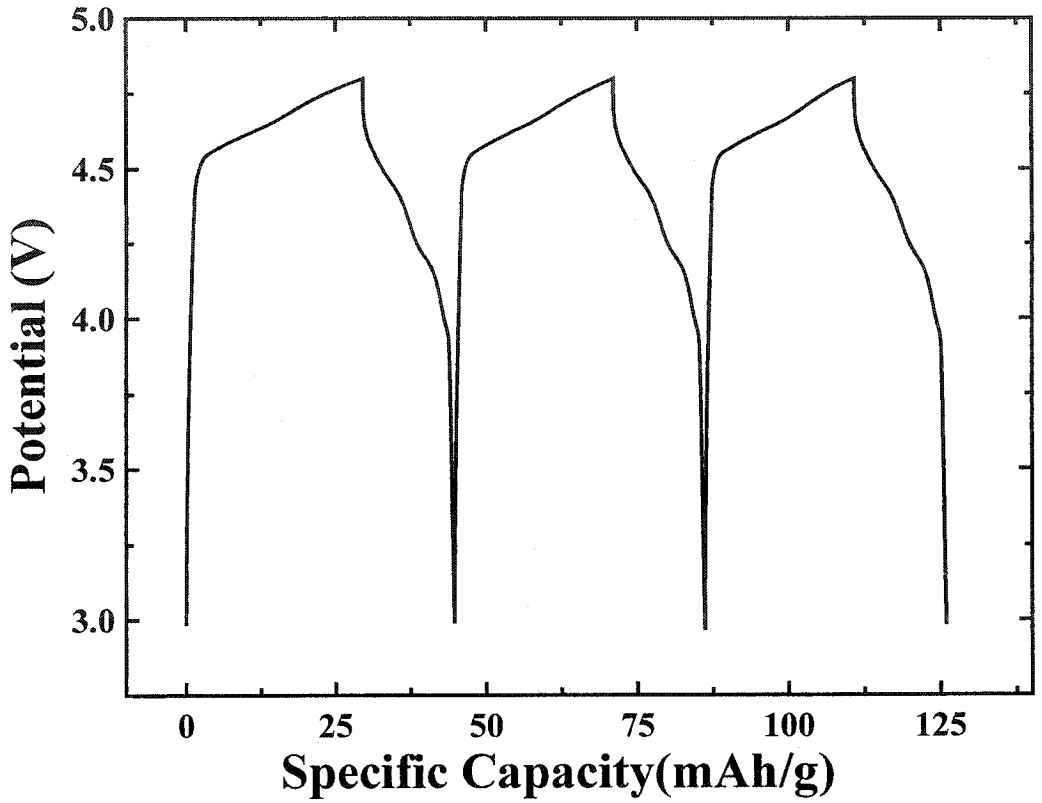

Figure 4.3.3 Potential versus specific capacity as it will be displayed throughout this thesis.

Sometimes it is easier to see changes in the potential curve if it is converted into a differential capacity versus cell potential curve. The differential capacity, dQ/dV, is obtained by taking the derivative of the specific capacity with respect to the voltage. The differential capacity versus potential curve of the potential schematic shown in Figure 4.3.1(a) is shown in Figure 4.3.1(b). The regions that are flat signify that there is only one phase in existance whereas the locations with a sharp spike are the regions in which two phases co-exist. An example of actual experimetnal data is given in Figure 4.3.4(a). In general the data is not displayed in this way but the two axes would be switched and the data would be displayed as it is in Figure 4.3.4(b). Here the peaks represent that regions in which there is a co-existence of two phases and the valleys would be regions in which there is only one phase present.

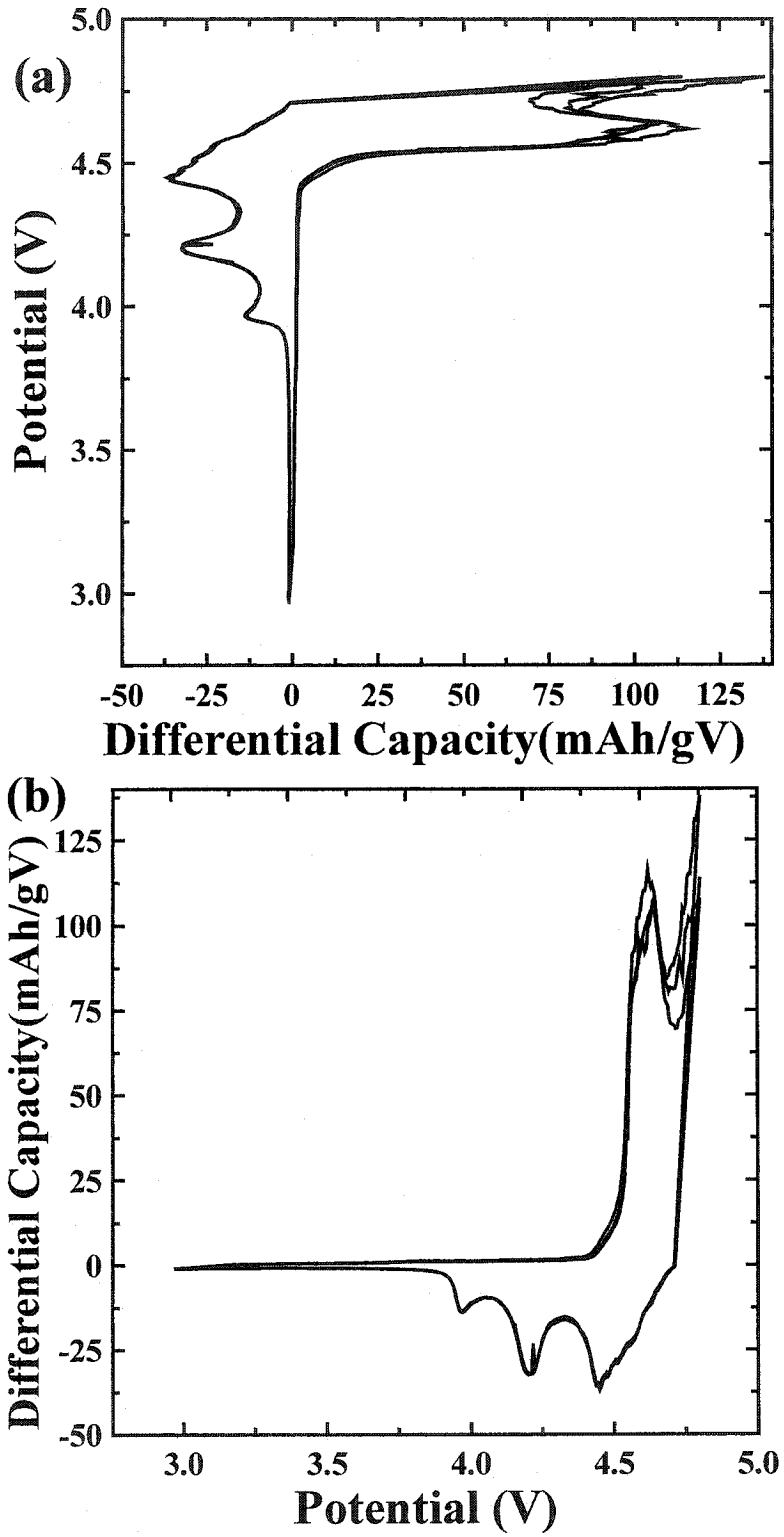

Figure 4.3.4 (a) Potential versus differential capacity for the data shown in Figure 4.3.2.(b) Differential capacity versus cell potential for the same data displayed as it will be shown throughout this thesis.

Section 4.4 Intensity Calculations

The X-ray diffraction patterns obtained during *in-situ* and *ex-situ* experiments showed evidence of staging. In order to determine the stage number as well as the layer spacing of the intercalated molecule layer, the z-axis repeat distance and the z-axis distance between the components of the intercalated molecule itself, a program was written.

Before the program itself is discussed, staging will be explained. Since graphitic carbon consists of sheets, there are spaces between the layers where the intercalated molecules can be accommodated. Suppose that every carbon layer is separated by a layer of intercalated molecules. This would be called stage 1, i.e. there is only one carbon layer between the layer of intercalated molecules. If there was a layer of carbon followed by another layer of carbon before an intercalated molecule layer and this repeated itself, this would be stage 2. For stage 2 materials, there are two carbon layers between every layer of intercalated molecules. This is shown in Figure 4.4.1. This can be carried even further, if there are n carbon layers between each intercalated molecule layer, this would be stage n.

Several research groups hae studied and formulated how and/or why staged phases in graphite and other compounds occurs. For instance, please refer to Safran [48,49], Dahn et al. [50], and Millman et al. [51,52]. The main reasons for the existence of staging will be briefly discussed.

Simply put staging is a result of net attractive interactions between the intercalants within a single layer and net repulsive interactions between layers of intercalants. The intercalant must overcome the cohesive energy between two adjacent layers. Once this is

done, further intercalation of the intercalant between those two layers becomes easier, hence a net attractive interaction between the intercalant particles within the same layer [51,52]. It was proposed by Safran [48,49] that the electrostatic repulsions between the intercalant layers must be the cause for staging.

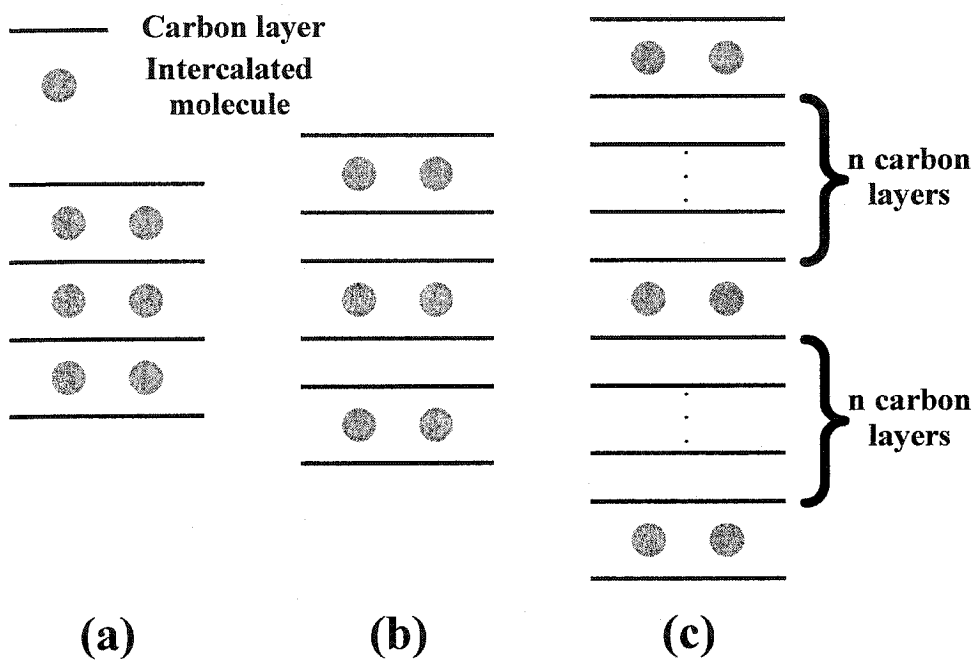

Figure 4.4.1 Illustrating staging. (a) Stage 1; (b) Stage 2; and (c) Stage n

To calculate the intensity of an X-ray diffraction pattern, several factors must be considered including the arrangement of the atoms, their atomic scattering and geometric factors, the Lorentz and polarization factors, absorption of X-rays by the beryllium window, etc.

Every type of atom will scatter X-rays differently since they all have a different number of electrons. This scattering of X-rays by an atom is described in terms of the atomic scattering factor, *f*. This scattering factor is the ratio of the amplitude of the

radiation scattered by the atom itself to the amplitude of the radiation scattered by a single electron [53,54].

If it is assumed that atoms are spherical in nature, then the scattering power depends simply on the type of atom, i.e., the number of electrons, the Bragg angle, θ, and the wavelength, λ, of the incident X-rays. It is interesting to note that the position of the atom within the material does not play a role in determining the atomic scattering factor. The atomic scattering factor for a particular atom is given by

$$f = \sum_{i=1}^{4} a_i \exp\left[-b_i\left(\frac{\sin\theta}{\lambda}\right)^2\right] + c \tag{4.2}$$

where a_i, b_i and c depend on the particular atom and can be found in the International Tables for X-ray Crystallography [54].

The value of this scattering factor is near the number of electrons for a given atom for low values of $(\sin\theta/\lambda)$ and diminishes as $(\sin\theta/\lambda)$ increases. Examples of this behaviour are given in Figure 4.4.2.

The position of the atom within the material being studied will, of course, affect the intensities of the diffracted radiation. The intensity of this radiation, or geometric structure factor, denoted $|F_{hk\ell}|$ is given by

$$|F_{hk\ell}| = \left(A_{hk\ell}^2 + B_{hk\ell}^2\right)^{1/2} \tag{4.3}$$

where

$$A_{hk\ell} = \sum f_i \cos 2\pi(hx_i + ky_i + \ell z_i) \tag{4.4}$$

and

$$B_{hk\ell} = \sum f_i \sin 2\pi(hx_i + ky_i + \ell z_i) \tag{4.5}$$

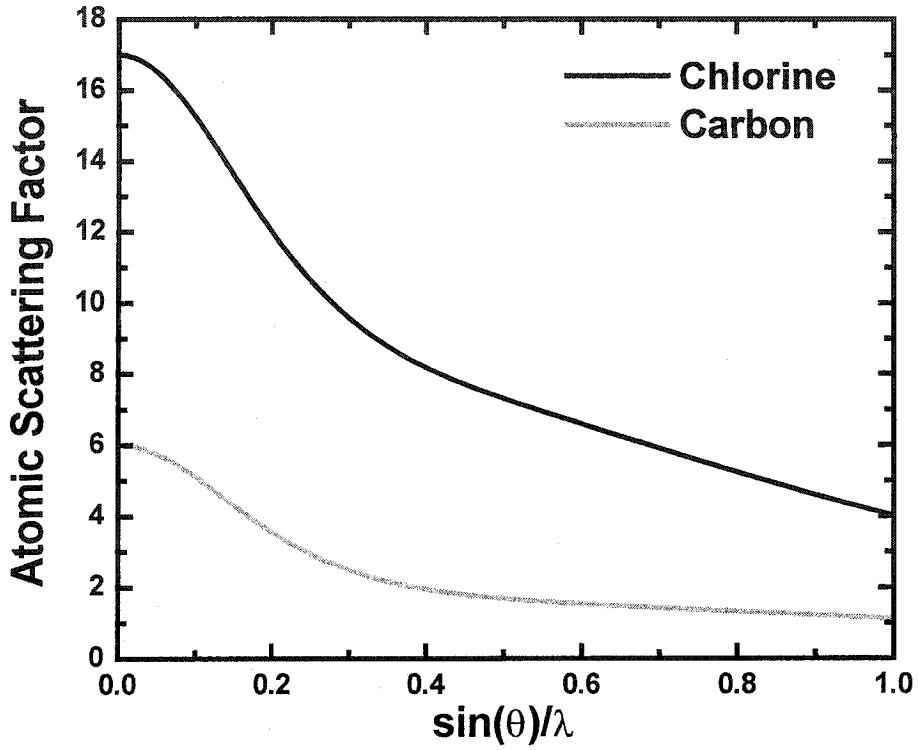

Figure 4.4.2 The atomic scattering factors of carbon and chlorine versus (sinθ)/λ.

where f_i is the atomic scattering factor for the ith atom and x_i, y_i, and z_i are the co-ordinates of the atom in fractions of the unit cell edges. Also, (hkℓ) is a particular reflection. The summations would be performed over the total number of atoms within the unit cell. For this thesis, the reflections of interest are the (00ℓ) reflections so equations (4.4) and (4.5) reduce to

$$A_{hk\ell} = \sum f_i \cos 2\pi(\ell z_i) \quad \text{and} \quad B_{hk\ell} = \sum f_i \sin 2\pi(\ell z_i) \tag{4.6}$$

The actual intensity, I, obtained during an X-ray diffraction experiment is not equal to $|F|^2$, although it is proportional. The relationship between these two intensities depends on such factors as the actual angle of the measurement, i.e., the individual

reflection, and to the actual apparatus used. Two such factors are the polarization factor, p_{factor}, given by,

$$p_{factor} = \frac{1+\cos^2 2\theta}{2} \tag{4.7}$$

and the Lorentz factor, L_{factor}, given by

$$L_{factor} = \frac{1}{\sin 2\theta}. \tag{4.8}$$

Keeping these factors in mind, F and I can be equated:

$$|F_{hkl}| = \left(k \frac{I_{hkl}}{L_{factor} p_{factor}} \right)^{1/2} \tag{4.9}$$

where k is basically a scale factor which depends on a number of things including crystal size and the beam intensity. This factor is generally constant.

This results in the calculated intensity, I_{hkl}, being given by

$$I_{hk\ell} = L_{factor} p_{factor} \left(A_{hk\ell}^2 + B_{hk\ell}^2 \right) \tag{4.10}$$

where $A_{hk\ell}$ and $B_{hk\ell}$ are given by equation (4.6).

Before the experimental data could be compared with the calculated intensities it was corrected for various elements which would change the relative ratio of the (00ℓ) peaks. Two such corrections were performed.

The first correction to keep in mind is that the beryllium window that is part of the electrochemical cell will absorb some of the radiation and this amount changes as the angle of the incident radiation changes. The measured intensity, I, would have been greater if the beryllium window was not present, so the "true" intensity, I_o, is given by

$$I = I_0 \exp\left(-\mu \frac{2t_{be}}{\sin\theta} \right) \tag{4.11}$$

where μ is the absorption factor of beryllium and is equal to 1.863 cm^{-1}, θ is the angle of the radiation to the sample, and t_{be} is the thickness of the beryllium window which is equal to 0.25 mm.

The other correction to keep in mind is the fact that for some angles a good portion of the X-ray beam may not be hitting the sample therefore reducing the intensity of the measured X-rays. This reduction in intensity is proportional to the ratio of the areas of the actual sample and the beam spread:

$$I = I_0 \frac{A_{that\ hits\ sample}}{A_{beam}} \tag{4.12}$$

The sample itself is a circle with radius, r, and it is constant. In contrast the cross-sectional area of the beam is a rectangular and it is not constant. The width changes with the scattering angle. There are three cases to consider which are illustrated in Figure 4.4.3. The first case to consider is that the area of the beam is sufficiently large that there are two areas, two arcs, shaded dark gray in Figure 4.4.(a), to either side of the beam that are not hit by the sample. There is a significant amount of the beam that does not hit the sample. This occurs for small angles up to θ_1, which shall be defined in a moment. For intermediate angle, θ_1 to θ_2, the areas that were not hit by the sample for angle below θ_1 are still present and are the same size. There are two additional areas that are no longer hit by the beam. These occur ahead and behind the beam, shaded light gray in Figure 4.4.3(b). After this point, Figure 4.4.3(c), for angles above θ_2, the beam completely hits the sample and this correction is no longer required.

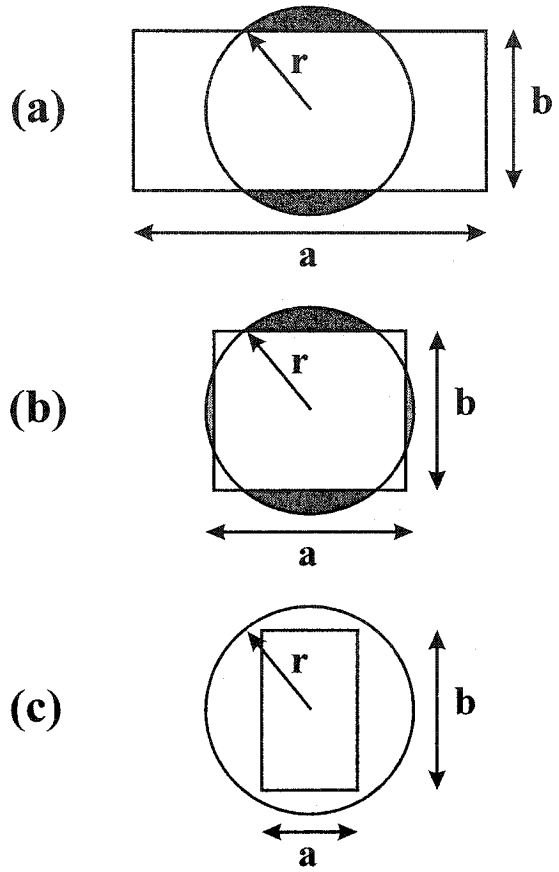

Figure 4.4.3 Illustrating the beam footprint on the sample for the three cases described in the text.

Assume that the width of the beam is given by a. This parameter depends on the scattering angle and is given by

$$a = \frac{L\alpha(\pi/180)}{\sin\theta}, \tag{4.13}$$

where L is the distance from the emitter to the sample, 2θ is the scattering angle and α is the divergence angle usually either 0.4° or 0.6°. Also assume that the length of the beam is constant and is given by b. Therefore the area of the beam is given by

$$A_{beam} = \frac{L\alpha(\pi/180)}{\sin\theta} b \ . \tag{4.14}$$

The area of the sample that is not hit by the beam in both the first and second case described above is given by

$$A = 2\left[\frac{r^2}{2}\left\{2\arccos\left(\frac{\frac{1}{2}b}{r}\right) - \sin\left(2\arccos\left(\frac{\frac{1}{2}b}{r}\right)\right)\right\}\right] \tag{4.15}$$

where r is the radius of the sample and b is the length of the sample, both are constant.

For the first case described above, the area of the beam that hits the sample is given by

$$A_{\textit{that hits sample}} = \pi r^2 - A \tag{4.16}$$

This equation is valid up to the point where a = 2r which occurs at 8.57°, this is θ_1.

For the second case described above, the area of the beam that beam that hits the sample is very similar to that of the above but it would have an additional term which would be area B, the light gray area in Figure 4.4.3. Area B is given by

$$B = 2\left[\frac{r^2}{2}\left\{2\arccos\left(\frac{\frac{1}{2}a}{r}\right) - \sin\left(2\arccos\left(\frac{\frac{1}{2}a}{r}\right)\right)\right\}\right] \tag{4.17}$$

where a is given by equation (4.13). The area that hits the sample is now:

$$A_{\textit{that hits sample}} = \pi r^2 - A - B \tag{4.18}$$

This equation is only valid from θ_1 up to the point where $a = 2\sqrt{\left(r^2 - \left(\frac{1}{2}b\right)^2\right)}$. This results in $\theta_2 = 22.79°$. After this point no correction is needed, as far as the beam area is concerned.

Using the corrections for the equations above the intensity, I , when correcting for the beam area only, would be

$$I = \frac{I_0\left(\pi r^2 - A\right)}{\left(\frac{L\alpha(\pi/180)}{\sin\theta}b\right)} \tag{4.19a}$$

for angles below 8.57° and

$$I = \frac{I_0\left(\pi r^2 - A - B\right)}{\left(\frac{L\alpha(\pi/180)}{\sin\theta} b\right)} \tag{4.19b}$$

for angles between 8.57° and 22.79°. For angles above 22.79° $I = I_0$. In equation (4.19), A is given by (4.15) and B is given by (4.17). The distance between the sample and the emitter, L, is 185 mm, the length of the beam, b is 12 mm and the radius of the sample was 6.5 mm.

To ensure that I is indeed continuous at the transitions between the various cases, I versus θ was graphed and it is shown in Figure 4.4.4. It was assumed that I_o was equal to 1 for this plot. It can be seen easily that it is indeed continuous.

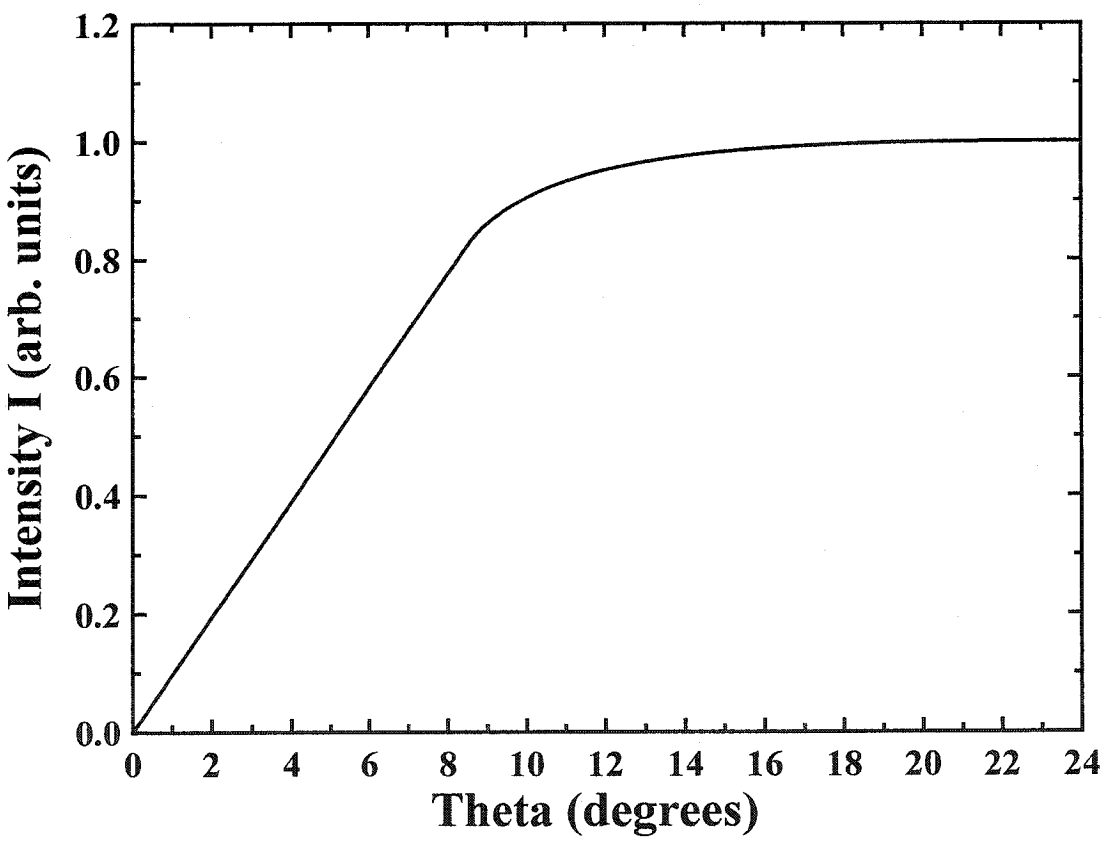

Figure 4.4.4 The calibrated intensity, I, described by equation (4.19) versus theta.

If a correction for beryllium absorption is required then equations (4.19) would be multiplied by an additional term, $\exp(-\mu * 2 * t_{be} / \sin\theta)$ where θ is half the scattering angle, μ is the absorption factor of beryllium and t_{be} is the thickness of the beryllium window. For angles above 22.79° the intensity would be given by equation 4.11. This corrected measured intensity, I_o, given by equations (4.19) and (4.11) is the intensity which will be compared to the calculated intensity given by equation (4.10).

A program was created to determine the z-axis positions of the atoms of the intercalated molecule between two layers of carbon by comparing the calculated intensities with the corrected experimental values. It was initially assumed that for PF_6, the phosphorous atom would be located at z = 0 and the fluorine would be equi-distant from the phosphorous atom at a value that would be determined. For stages higher than stage 1, the intercalated molecule layer thickness would also be determined.

The input parameters include the c-axis spacing obtained from the X-ray diffraction measurements, the maximum number of (00ℓ) peaks and the stage number. Other values, some of which are allowed to vary depending on the stage, include the specific capacity reached by the electrochemical cell, an initial value for the distance between two carbon layers where no intercalated molecule is present (for stage 2 and higher), an initial value for the phosphorous to fluorine distance. The intensities of the (00ℓ) peaks obtained from experiments are also included in the input file.

For clarity an example will now be illustrated. Suppose there is a data set that is suspected to be a stage 2 compound with a z-axis repeat distance of 11 Å. A possible input file is given below:

11, 6, 2
180, 0.0, 91
2.9, 0.01, 91
0.1, 0.01, 251
100,70
100
0.001
1562
482
50
100

In the first line, the c-axis spacing, the number of (00ℓ) peaks and the stage number are given. The second line gives the capacity, its increment and the total number of capacity points desired. In this example, the capacity increment is zero, signifying that the capacity is actually fixed. The third line is the C-C empty layer distance, its increment and the number of points. In this case the range would be from 2.9 Å to 3.8 Å. The fourth, gives the distance from the fluorine atom to z=0 along the z-axis, its increment and number of points. The range given here, is 0.1 Å to 2.6 Å. The fifth line of the input file contains two numbers which will create an output file of the intensities, both calculated and normalized, of the point specified. In this case, the 100^{th} A-X distance and the 70^{th} C-C distance, 1.1 Å and 3.6 Å respectively. The second number in the first line determines the number of lines remaining. In this case that number was six so there are six more lines in the input file. These lines contain the intensities of the (00ℓ) peaks obtained from experiment.

Several possible orientations of the PF_6 anion were investigated which shall be discussed in Chapter 7. These different orientations would change the fluorine's z-distances and in turn change the relative intensities of the (00ℓ) peaks. It is interesting to note that for PF_6, it was discovered that the anion is probably rotating about the

phosphorous atom. This was treated as a phosphorous atom surrounded by a shell of evenly distributed fluorine atoms. The sphere would then be divided horizontally into equal pieces and then the geometric structure factors would be calculated. These horizontal slices of the sphere each share an equal number of fluorine atoms. If the sphere were divided into one hundred slices and all share the six fluorine atoms, then each slice would contain 0.06 fluorine atoms. This may not be clear to the reader so it shall be explained. The fluorine atoms are distributed across the surface of a sphere of radius r_s. Suppose the sphere is divided into 2N layers. The surface area of one of these slices is basically the surface area of a ring, see Figure 4.4.5. Suppose we have a ring at height H. The resulting radius, x, of this ring would be equal to $r_s \sin\theta_s$. The length of the side of the ring, l, is proportional to the height of the ring, h. In this case $l = h/\sin\theta_s$. The surface area of the ring is given by simply multiplying its circumference by the height of the ring and it is $C*l = 2\pi(r_s \sin\theta_s)*h/\sin\theta_s$. Since the sphere has been divided

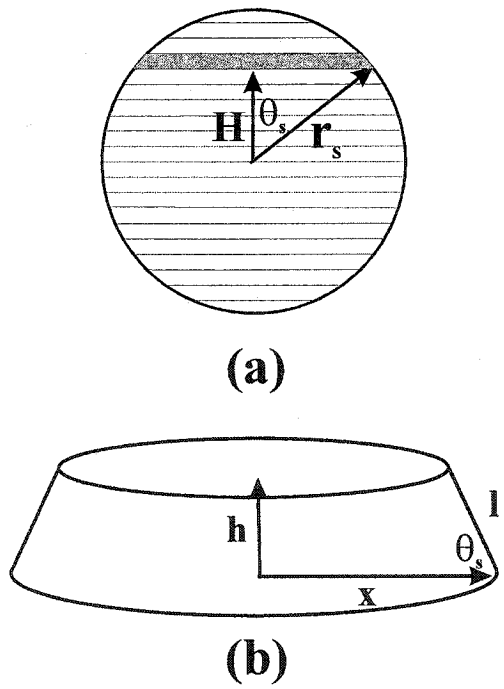

Figure 4.4.5 (a) Sphere divided into several rings, (b) a particular ring.

horizontally in equal parts, $h = r_s/N$, the resulting surface area of each sphere is the same, $SA = 2\pi r_s^2/N$. Since the fluorine atoms are distributed evenly over the sphere and each layer has the same area each layer will have 6/N fluorine atoms spread across the surface. These results are discussed in great detail in Chapter 7.

After calculating the intensities, they are normalized to the largest measured intensity, i.e., in the input file above, the (003) peak has the maximum intensity in the measured data. The calculated (003) peak would be normalized to this value and the other calculated peaks would be scaled accordingly.

To compare the calculation to the measured values, a goodness of fit was determined using the following formula

$$goodness of\ fit = \sqrt{\sum_{(00l)\,peaks} \left(\log(normalized) - \log(measured)\right)^2} \qquad (4.3.2)$$

Naturally, the closer the goodness of fit is to zero the better. The goodness of fit was calculated for all the various C-C and fluorine distances. The resulting data would then be plotted in a contour plot for easy viewing. An example is given in Figure 4.4.6.

It may be asked why a non-linear least squares fitting program was not used. The answer is simple and can be illustrated with the aide of Figure 4.4.6. It can be easily seen in the figure that there are several local minima and a least squares fitting program may get trapped one of these local minima which may not be the true minimum. By determining the fit in the way illustrated above several local minima could be investigated to determine which was actually the true minimum and therefore result in the lowest goodness of fit possible and hopefully realistic values for the various parameters involved.

A similar program was written for BF_4. Its possible orientations shall be discussed in Chapter 8.

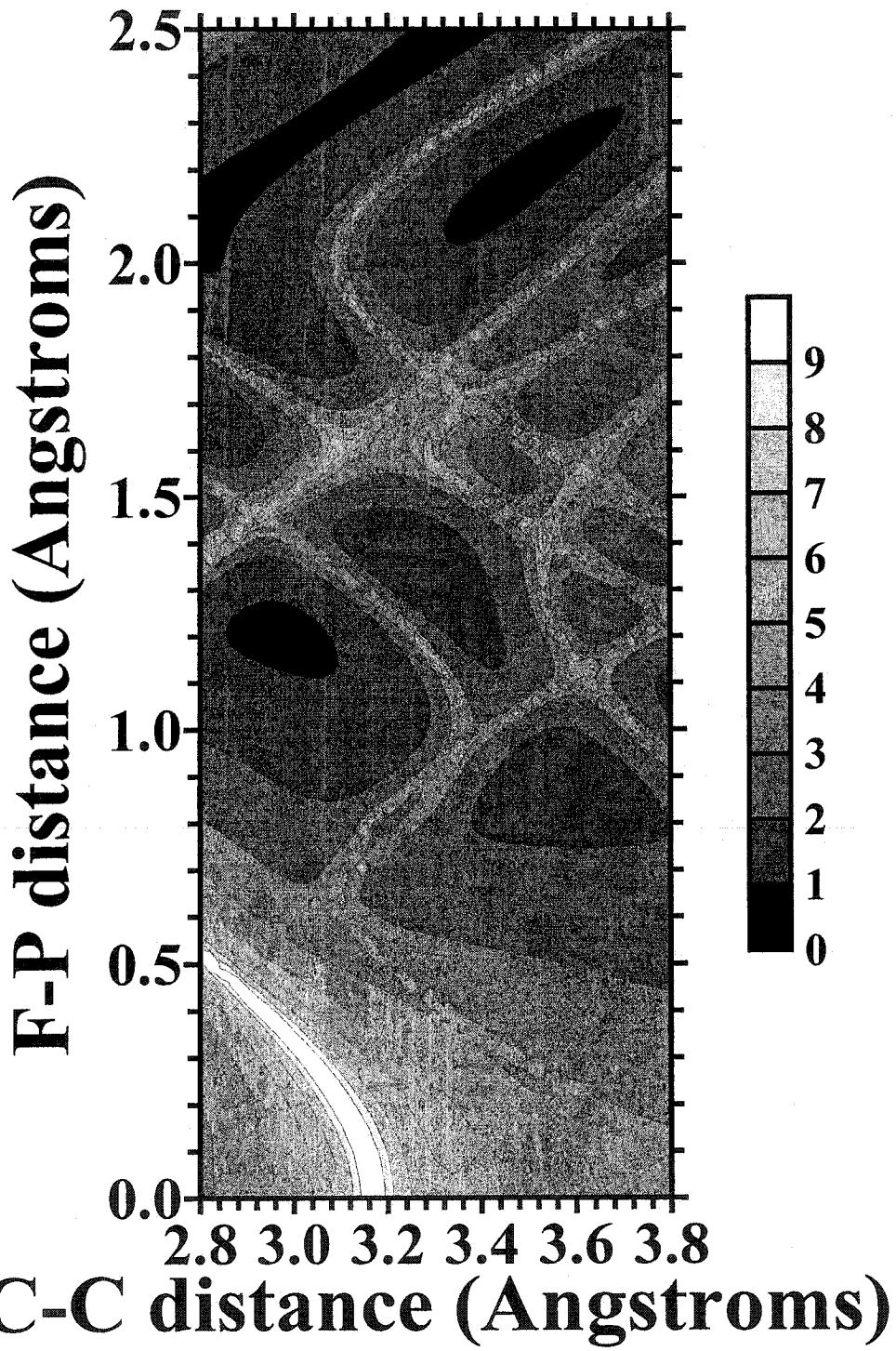

Figure 4.4.6 A contour plot showing the goodness of fit for a range of F-P distances (x-axis) and C-C distances (y-axis).

Chapter 5 Initial Results

Various carbon materials, including some carbon fabrics, fibers and powders were tested to see which types of carbon material would be a good candidate for anion intercalation, i.e. for intercalation of the non-lithium component of the lithium salt. A selection of these materials is characterized here.

Section 5.1 Primary Sample Analysis

In the first stages of this work, several different types of carbon were analyzed from powders to fibers to fabrics. The following figure, Figure 5.1.1, shows the X-ray diffraction patterns obtained for three different carbons: a meso-carbon micro-bead powder heated to 2800°C, MCMB2800, a carbon fiber, denoted TA-1F, and a carbon fabric, PW-03. It can be seen easily that there are peaks located at ~27°, ~44°, ~54° and ~80° which are present in all three samples. However, these peaks become harder to distinguish from other peaks for the fabric in particular. The fiber has more and narrower peaks than the fabric and, likewise, the MCMB sample has more and narrower peaks than the fiber. This implies that although the basic structure of these carbons is the same or at least very similar there are still major differences. The number of peaks and the sharpness of those peaks are related to the amount of disorder in the sample. Since these three carbon samples all have a varying number of peaks present with different peak widths, all have a different amount of disorder. From simply looking at the pattern, the MCMB sample would be the most ordered sample whereas the fabric, PW-03, would be the least ordered sample.

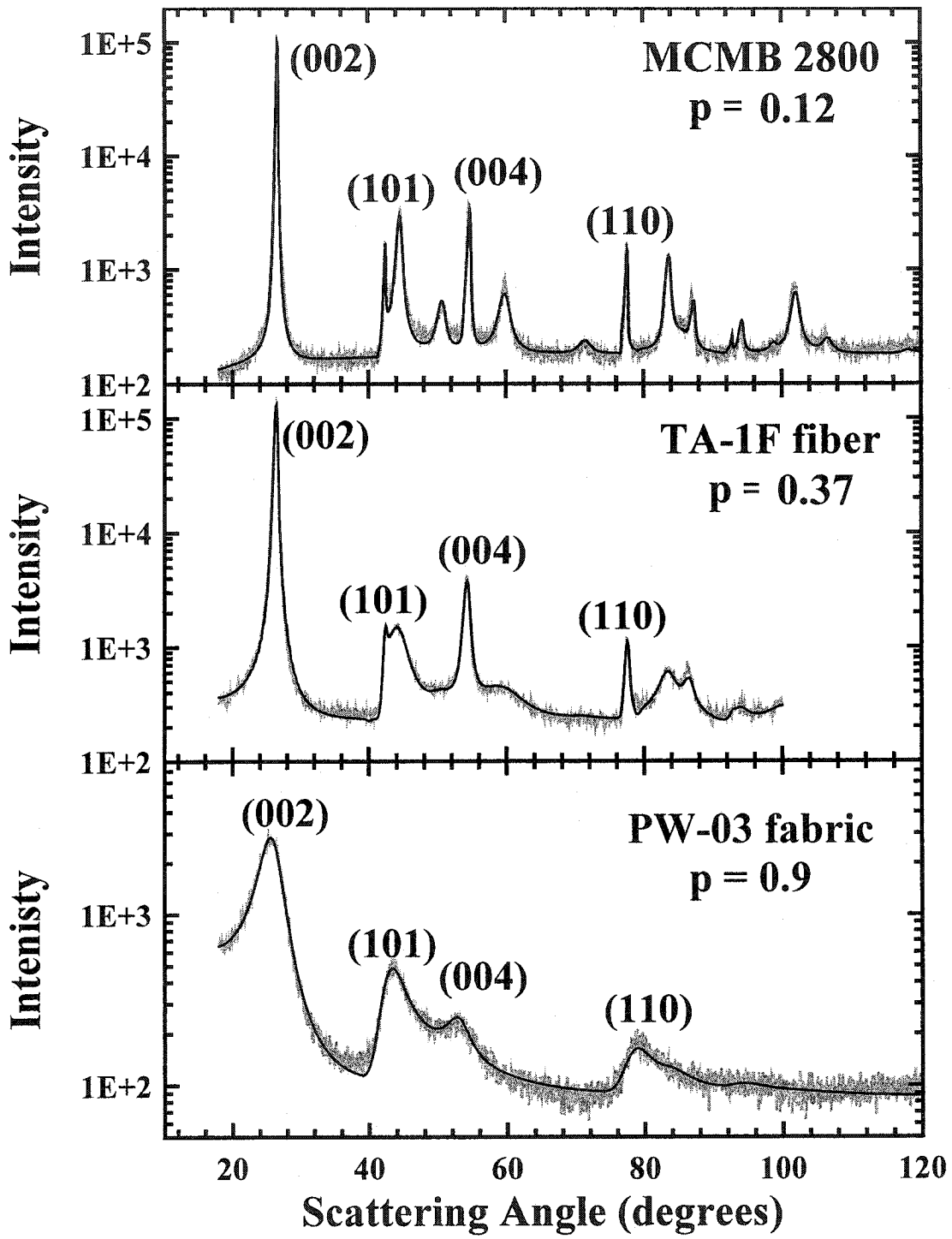

Figure 5.1.1 X-ray diffraction patterns for (a) MCMB 2800°C powder, (b) TA-1F fiber and (c) PW-03 fabric.

A fitting program, carbonxs[1], was used to fit these patterns. A summary of these results can be found in Table 5.1. Some of the parameters listed in the table are illustrated in Figure 5.1.2. The first parameter listed in the table, the in-plane lattice constant, is the distance between two atoms separated by one atom within the carbon ring structure of a graphite sheet and is approximately the same for all samples. This parameter is labeled a in Figure 5.1.2. The interlayer spacing, labeled c, is the distance between two adjacent carbon layers. This value increases slightly from the MCMB sample (3.347 Å) to the fabric sample (3.440 Å). The coherence length in the AB plane is the measure of how far the honeycomb lattice structure is intact. This number is much larger for the MCMB sample than the other two suggesting that it is more ordered. The fiber also has a larger value than the fabric. The MCMB sample also has a greater number of carbon sheets (or layers) within a grain of carbon. The fiber and the fabric are comparable. The final parameter, p, is the probability that two adjacent layers are turbostratically misaligned. As suspected, the MCMB sample has the lowest value, $p = 0.12$, i.e., the most ordered. The fiber is the next with $p = 0.37$ and the fabric is the most disordered sample with $p = 0.90$. This gives a quantitative way to compare the disorder of various carbon samples.

The next step is to see how these different carbons perform electrochemically.

---

[1] For details on carbonxs, please refer to Chapter 4, Section 1.

Parameter	MCMB 2800°C	Fiber, TA-1F	Fabric, PW-03
In-plane, a-axis (Å)	2.457	2.457	2.436
Interlayer spacing, c-axis (Å)	3.347	3.367	3.440
Coherence length in AB plane(Å)	2690	197	27
Average number of layers	209	62	89
Amount of disorder, p	0.12	0.37	0.90

Table 5.1 Structural parameters for MCMB2800, TA-1F and PW-03.

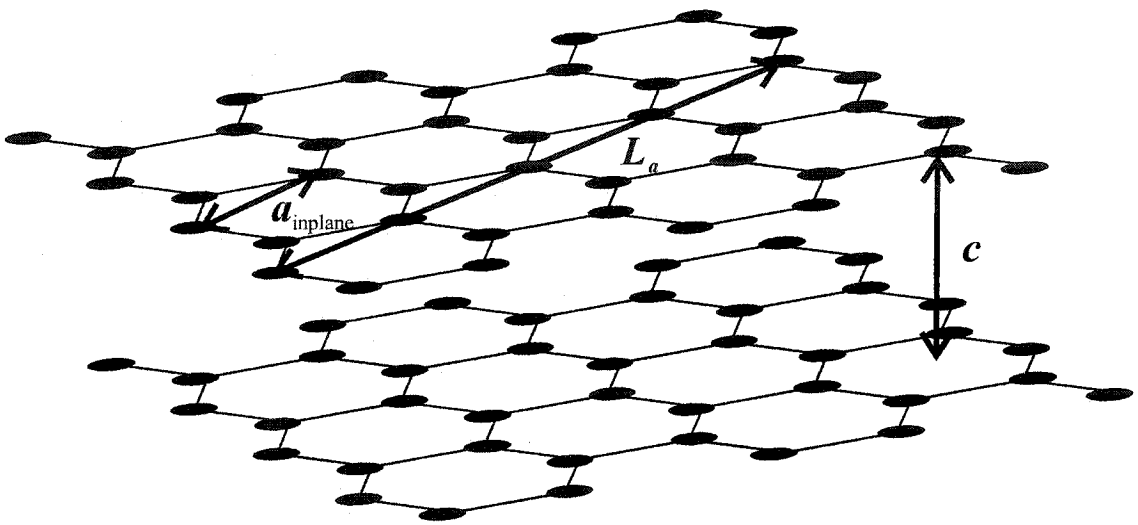

Figure 5.1.2 Illustrating some of the parameters described in Table 5.1. The in-plane lattice constant is given by $a_{inplane}$, the interlayer spacing by c, and the coherence length by L_a.

Section 5.2 Electrochemical Results

The carbons discussed in the previous section were used to make coin-type cells, this procedure is discussed in Chapter 3, Section 3. The electrolyte used in these cells was 1M $LiPF_6$ in ethylene carbonate/diethyl carbonate, EC/DEC, at a one to two volumetric ratio. These cells were charged up to a potential of 5.0 V and discharged down to 3.0 V. The results can be found in Figure 5.2.1.

It can be seen easily that the TA-1F fiber does not cycle well since it only has a charge capacity of 20 mAh/g which dies off fairly quickly to less than 10 mAh/g. The discharge capacity is also very low at a value of ~5 mAh/g. The PW-03 fabric has a much higher charge capacity of 50 mAh/g. However, this charge capacity is also much larger than the discharge capacity which is under 10 mAh/g. This suggests that the anions that are going into the carbon electrode during charge but most of the anions are not being removed during discharge. It is also noticeable that the subsequent charges have lower and lower capacities falling from 50 to 30 mAh/g in one cycle and to ~10 mAh/g by the seventh cycle. This is not very desirable for a practical cell.

By far the best performing cell from these samples is the MCMB 2800°C. It has a charge capacity slightly above 50 mAh/g. This capacity decreases to ~40 mAh/g where is stays constant for the next several cycles. The discharge capacity remains constant at about 30 mAh/g and, although, it is still lower than the charge capacity, it is closer to the charge capacity than the fiber and the fabric where both decreased by at least 50%.

Since the more ordered sample, MCMB 2800°C, was discovered to be more reliable than the other samples, this material, or a similarly ordered carbon, would be used for the next phase of experiments.

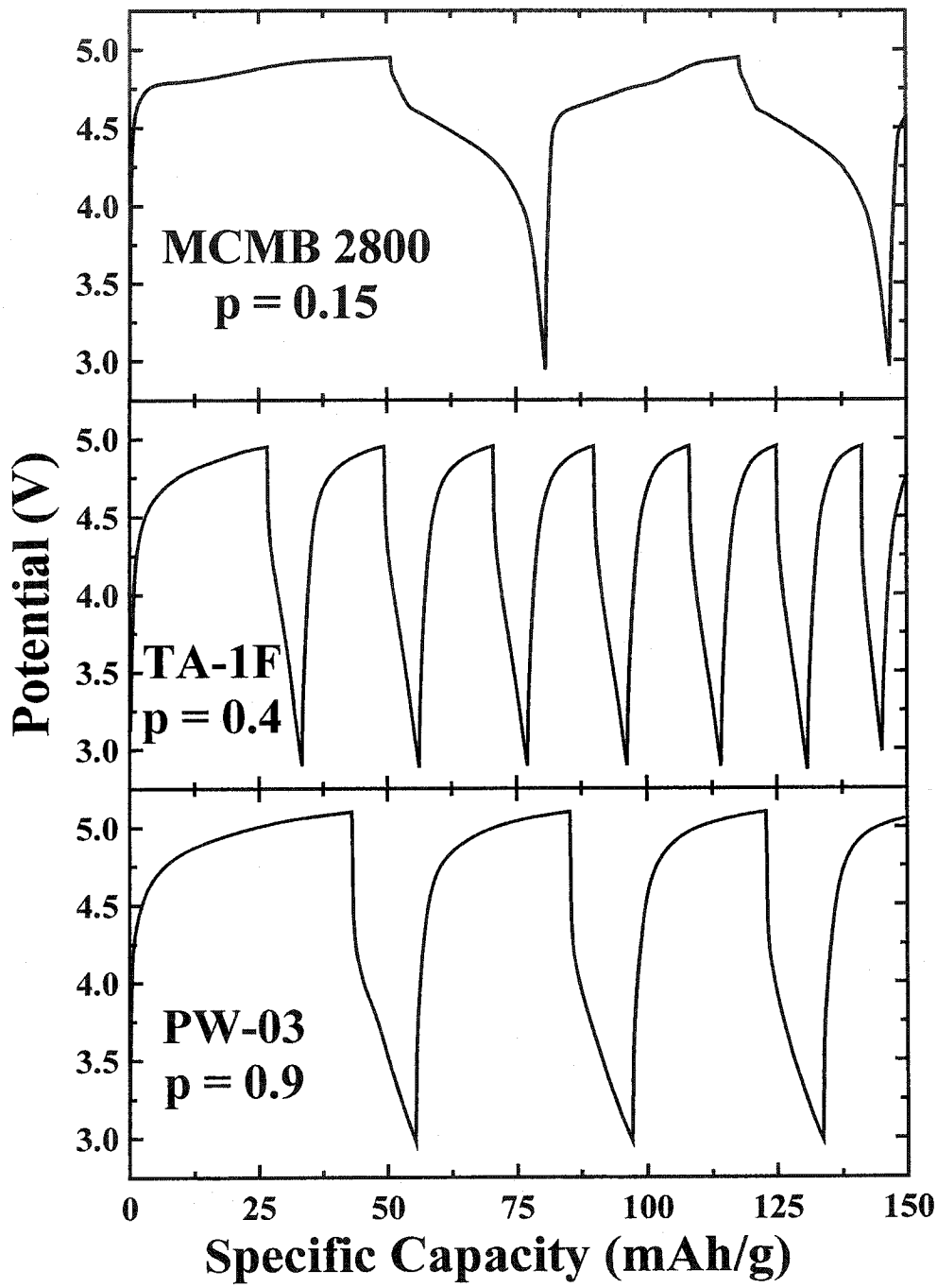

Figure 5.2.1 Cell potential versus specific capacity for MCMB 2800°C powder (upper panel), TA-1F fiber (middle panel) and PW-03 fabric (lower panel).

Chapter 6 EC/DEC vs. EMS in Graphite

When constructing electrochemical cells (and rechargeable batteries in general), the solvent component in the electrolyte can play a major role. It may react with the other components of the cell or may even decompose at high potentials [see for example references 55, 56 and 57]. This chapter will compare two electrolytes: 1) 1M $LiPF_6$ in ethylene carbonate/diethyl carbonate (EC/DEC) in a one to two ratio and 2) 2M $LiPF_6$ in ethyl methyl sulfone (EMS). The electrochemical cells used in these experiments consist of a lithium metal anode and a graphite cathode.[1]

Section 6.1 Electrochemical Testing

The graphite used in the following experiments was obtained from Fluka. The interlayer spacing was found to be 3.35 Å and the intralayer spacing (a-axis spacing) was found to be 2.46 Å indicating a well graphitized sample. In fact, the disorder factor, p was found to be 0.11.

The electrolyte that was initially chosen was 1M $LiPF_6$ /EC+DEC simply because it was commercially available and no pressure wetting during cell construction was necessary. Several experiments were performed with various cycling parameters. Two typical scans are shown in Figure 6.1.1. In Figure 6.1.1(a), the upper cutoff potential was 4.9 V and the lower cutoff potential was 3.0 V. The specific capacity reached during charge was only about 34 mAh/g and the subsequent discharge had a specific capacity of

[1] Some of the results presented in this chapter have been previously reported [58].

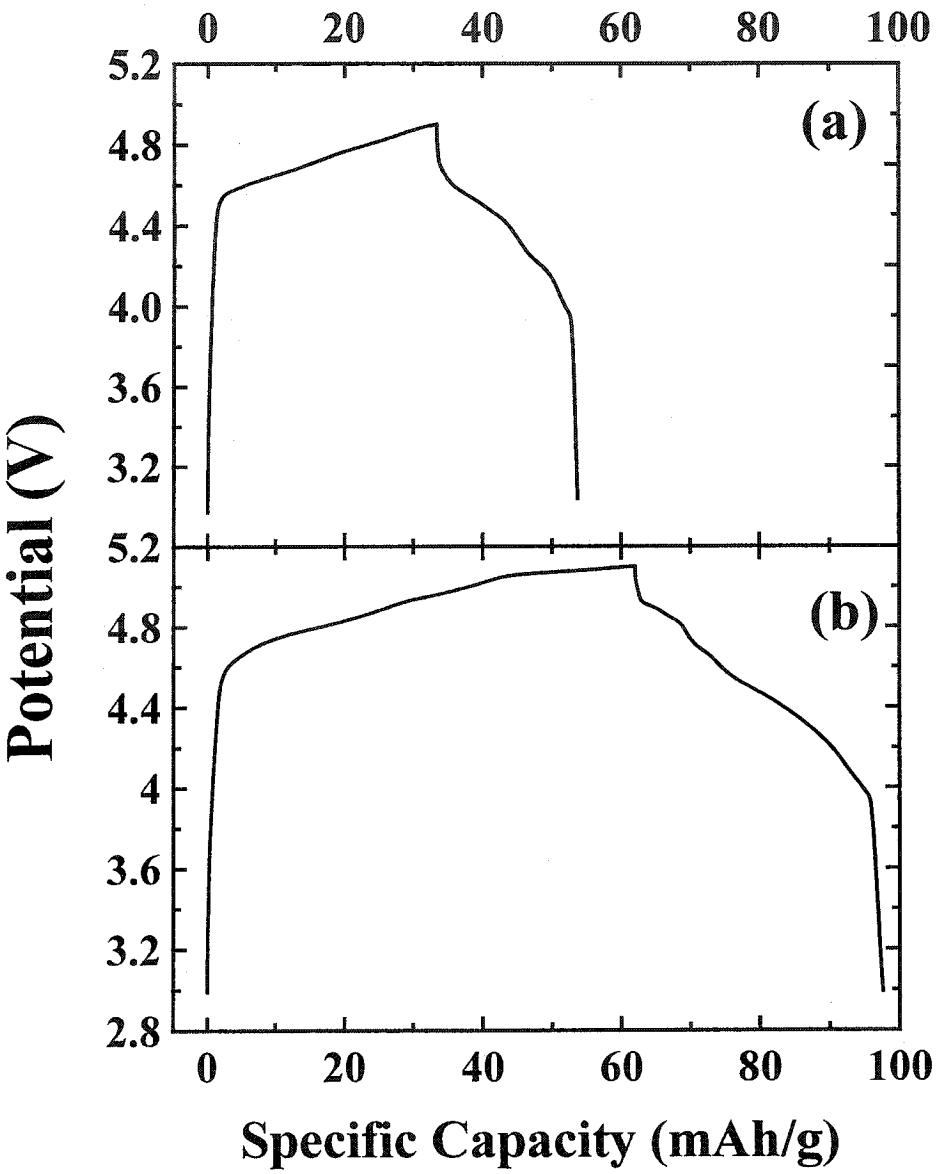

Figure 6.1.1 Potential versus specific capacity for graphite in 1M $LiPF_6$/EC+DEC with a maximum cutoff potential of (a) 4.9 V and (b) 5.1 V.

20 mAh/g, a loss of one third. A charge with a higher cutoff potential of 5.1 V is shown in Figure 6.1.1(b). The added 0.2 V gives an additional 28 mAh/g, for a charge capacity of 62 mAh/g. The discharge capacity is 36 mAh/g. This time the loss is almost 50%. Needless to say, neither of these two results are very good since the capacity loss is so large.

Another experiment was performed using EC+DEC as the solvent in the electrolyte. This time, however, the salt concentration was increased to 3M. The upper cutoff potential was 5.0 V and the lower cutoff potential was about 1 V. This resulted in a charge capacity of 85 mAh/g and a discharge capacity of 64 mAh/g. This is a decrease of 25%. If the charge and discharge capacities were measured at 3 V, as in Figure 6.1.1, then they would be 75 mAh/g and 40 mAh/g, respectively. This suggests that not only does the increase in the potential range increase the specific capacity but that the increase in molarity also increases the specific capacity at least for the charge part of the cycle. This makes sense since the anion within the electrolyte is the source of charge.

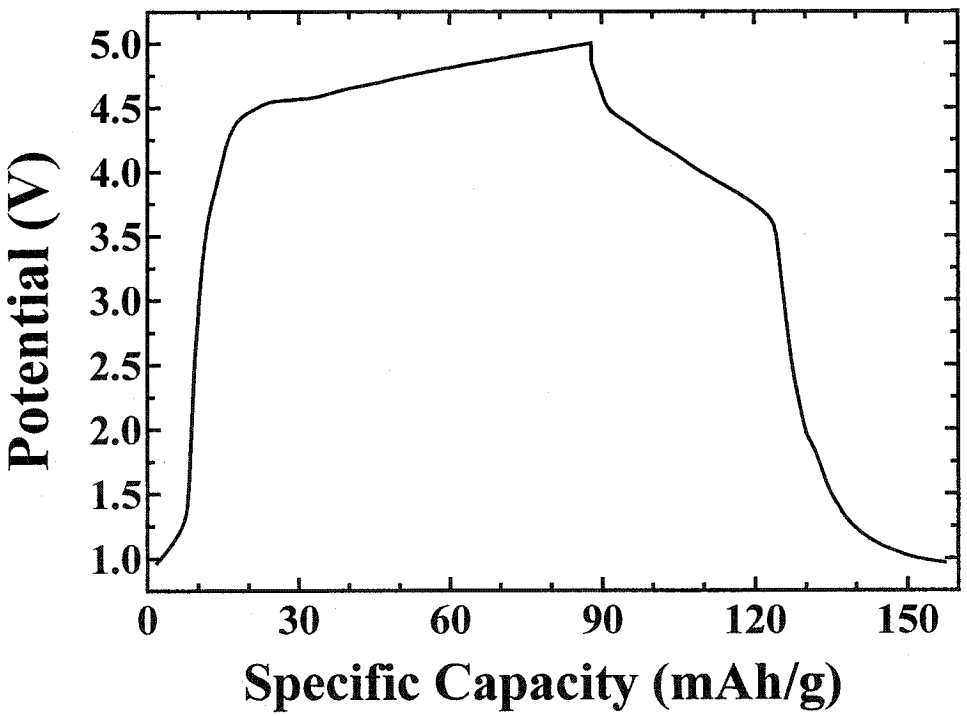

Figure 6.1.2 Potential versus specific capacity for graphite in 3M $LiPF_6$/EC+DEC with a cutoff of 5.0 V.

To see if there were any differences between solvents, similar charging experiments were performed using 2M $LiPF_6$/ethyl methyl sulfone (EMS). These results are shown in Figure 6.1.3. Figure 6.1.3(a) shows potential versus specific capacity with

an upper cutoff potential of 5.3 V and a lower cutoff potential of 1.5 V. The charge capacity is approximately 135 mAh/g and the discharge capacity is about 115 mAh/g, a loss of about 15%. The potential versus specific capacity plot with a cutoff potential of 5.4 V is shown Figure 6.1.3(b). Here the charge capacity is approximately 180 mAh/g and the discharge capacity is 140 mAh/g, a loss of about 20%.

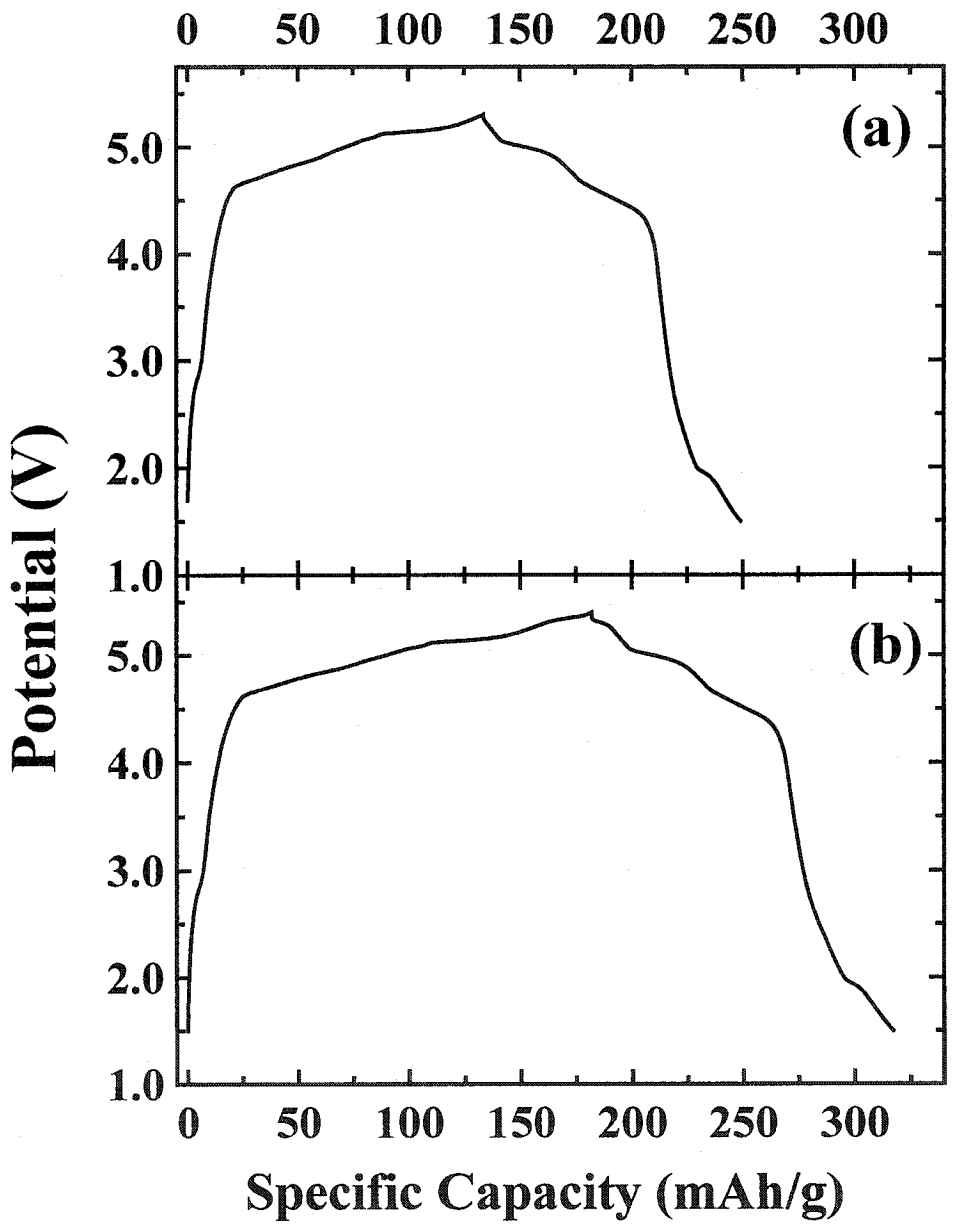

Figure 6.1.3 Potential versus specific capacity for graphite in 2M $LiPF_6$/EMS with maximum cutoff potentials of (a) 5.3 V and (b) 5.4 V.

The discrepancies between the charge and the discharge capacities can be accounted, most likely, by the fact that not all of the hexafluorophosphate has been removed from the carbon electrode. Another possibility is co-intercalation of the solvent molecule itself.

Overall, the performance of the electrochemical cells that use EMS as the solvent is better than the performance of the cells that use EC+DEC in terms of the reversibility. Perhaps the differences in performance between these two types of electrolytes can be seen more easily in a differential capacity versus potential curve. Such a plot is shown in Figure 6.1.4. It can be easily seen that when the electrochemical cell which uses 1M $LiPF_6$/EC+DEC as the electrolyte, is pushed to 5.1 V, there are definite problems. The differential capacity curve becomes rather noisy. Above 5.0 V, the value of the differential capacity is becoming quite large which indicates that the cell is no longer cycling well. At such a high potential the electrolyte itself is most likely starting to decompose. The cells constructed using 2M $LiPF_6$/EMS have more stable behaviour at higher potentials. The numerous peaks and valleys in the differential capacity plots versus potential do not seem to be "running away" to large values. The peaks and valleys present in all the differential capacity versus potential curves give an indication of staging and perhaps other phase transitions that may be occurring within the carbon electrode.

Another indication that EMS is more stable and therefore more suitable for our studies, is that the profile of the differential capacity curve change does not change depending on the upper cutoff potential where the profile for EC+DEC changes with different cutoff potentials. In Figures 6.1.4 (a) and (b), it can be easily seen that the

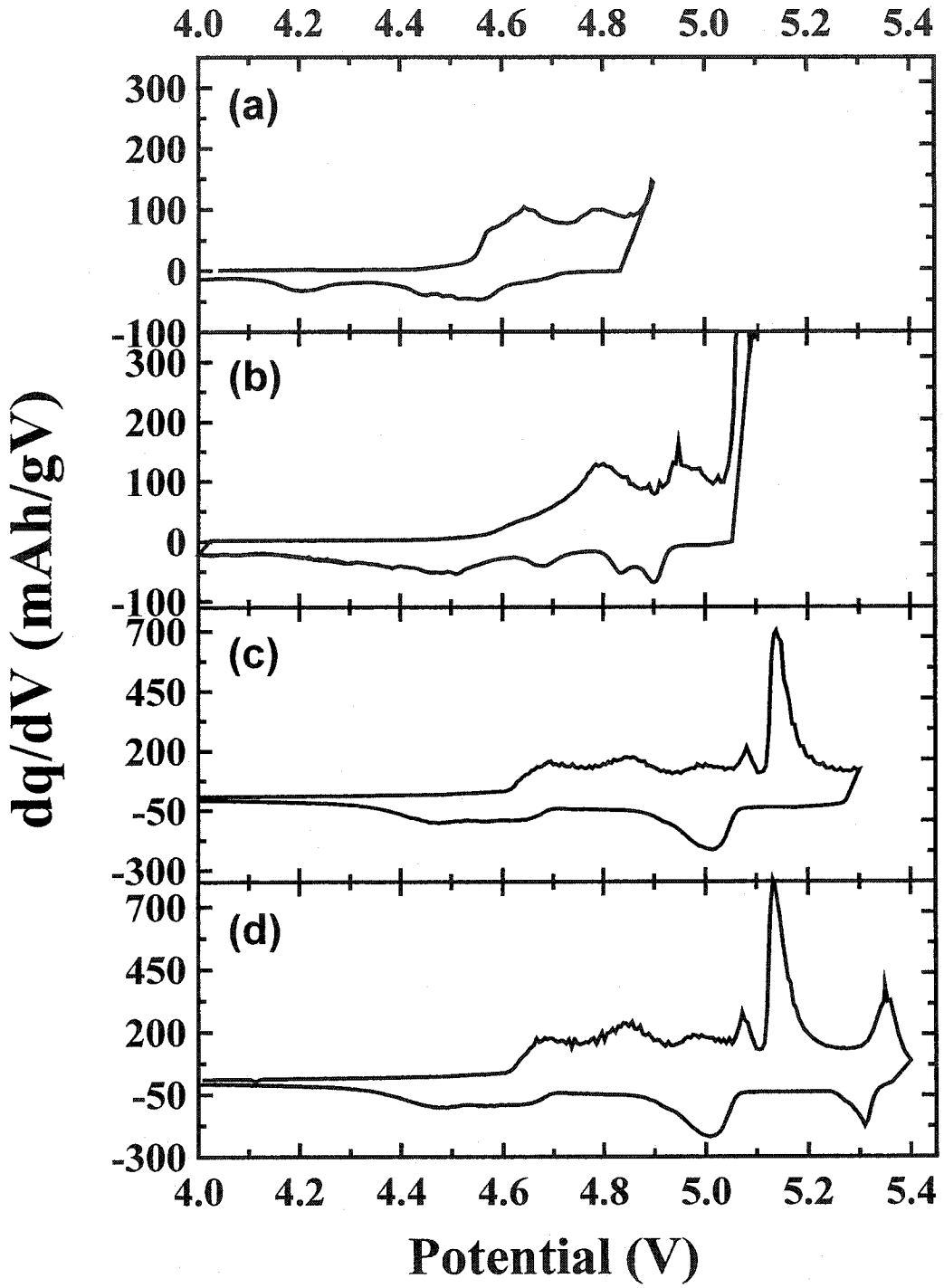

Figure 6.1.4 Differential capacity versus potential for graphite in (a) 1M $LiPF_6$/EC+DEC with a maximum cut off potential of 4.9 V, (b) 1M $LiPF_6$/EC+DEC with a maximum cut off potential of 5.1 V, (c) 2M $LiPF_6$/EMS with a maximum cut off potential of 5.3 V, and (d) 2M $LiPF_6$/EMS with a maximum cut off potential of 5.4 V.

peaks (and valleys) during charge are in different locations. For example, in Figure 6.1.4 (a), there is a slow rise in dQ/dV until about 4.5 V where there is a steep rise which is followed by three peaks. These peaks are occur approximately at 4.55 V, 4.62 V and 4.75 V. These peaks do not occur at the same positions in the curve shown in Figure 6.1.4(b). Each peak has shifted to a higher potential: ~4.6 V, 4.78 V and 4.95 V. Clearly the upper cutoff potential effects the performance of the cell. In contrast, the peaks present in Figure 6.1.4(c) are also present in Figure 6.1.4(d) at the same positions, suggesting using EMS as the solvent results in a more stable electrochemical cell, at the very least, a more reliable one.

To determine the maximum upper cutoff potential of an electrochemical cell using EMS as the solvent component of the electrolyte, an experiment was started with a high upper cutoff potential of 5.6 V. If this cell was still found to be stable, then a new and higher upper cutoff potential would be used. Figure 6.1.5(a), shows the capacity plot for an electrochemical cell with a cutoff potential of 5.63 V. The charge capacity is approximately 235 mAh/g and the discharge capacity, to 1.0 V, is about 150 mAh/g. This is a loss of approximately 36%, not as good as previous results. The differential capacity versus potential is shown in Figure 6.1.5(b). The large increase in the value of the differential capacity around 5.6 V is an indication that the cell is having difficulties cycling. Most likely this is where the electrolyte is decomposing. Other work has shown that EMS is stable up to very high potentials. In fact, Xu and Angell showed that EMS was stable up to 5.8 V [57]. This indicates that experiments using EMS as the solvent component of the electrolyte up to about 5.5 V should not have any problems, at least ones that are due to the electrolyte.

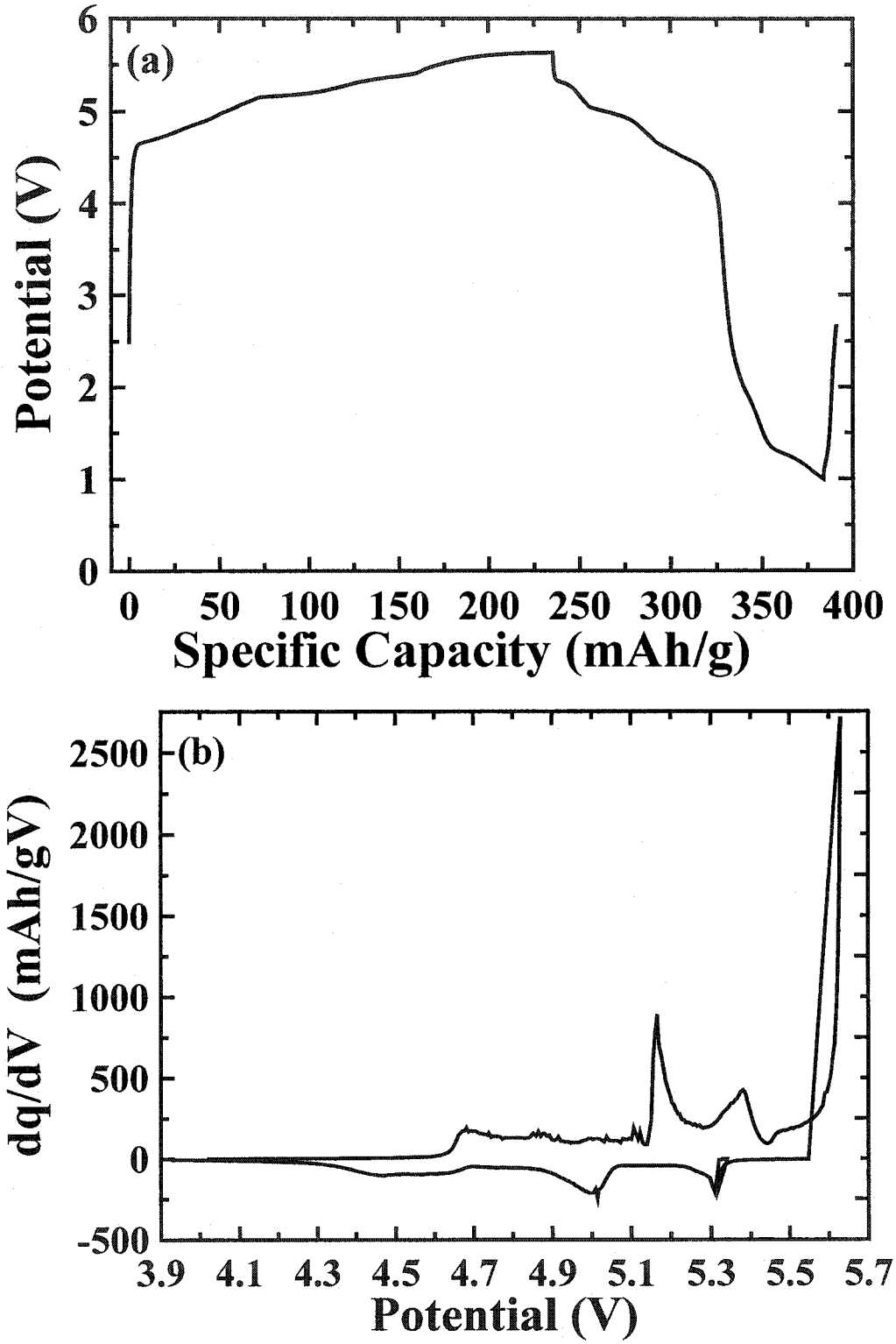

Figure 6.1.5 (a) Potential versus specific capacity for graphite in 2M $LiPF_6$/EMS with a cutoff potential of 5.63V. (b) Differential capacity versus potential for the same cell.

Section 6.2 *In-situ* X-ray Diffraction Experiments

To understand what is happening to the structure of the carbon electrode, *an in-situ* X-ray diffraction experiment was performed using 2 M $LiPF_6$/EMS as the electrolyte. This particular experiment had an upper cutoff potential of 5.5 V and a lower cutoff potential of 1.0 V. The capacity plot is shown in Figure 6.2.1, along with a time scale to give an idea how long the experiment actually took. Figure 6.2.2 shows the X-ray diffraction patterns obtained during the course of the experiment. It can be seen easily that as the cell is charged and discharged, there is a definite structure change within the carbon electrode.

As the potential is increased, the (002) peak of graphite at ~26.7°, in the first scan, disappears quickly. Two new peaks form at lower and higher angles. Generally speaking, these peaks continue to shift to lower and higher angles as the potential is increased. As the potential is increased further these peaks diminish in size as new peaks form, near scan 19, again at lower and higher angles. These peaks also shift in angle before the current is switched and the cell discharged. The opposite process occurs as the cell's potential is decreased. The (002) peak of graphite reappears at the bottom of the discharge, although it is much broader.

The formation and deformation of peaks is due to the fact that PF_6 is entering into the graphite structure. As the first few PF_6 molecules enter into the electrode, the ABAB structure is altered by these anions being inserted between the carbon sheets. As more PF_6 is added, i.e. as the potential is increased, an ordering occurs. Layers of PF_6 will form and areas where these layers are separated by n carbon sheets also begin to form. Locally, regions of stage n will form. This is illustrated, by using stage 3 as an example,

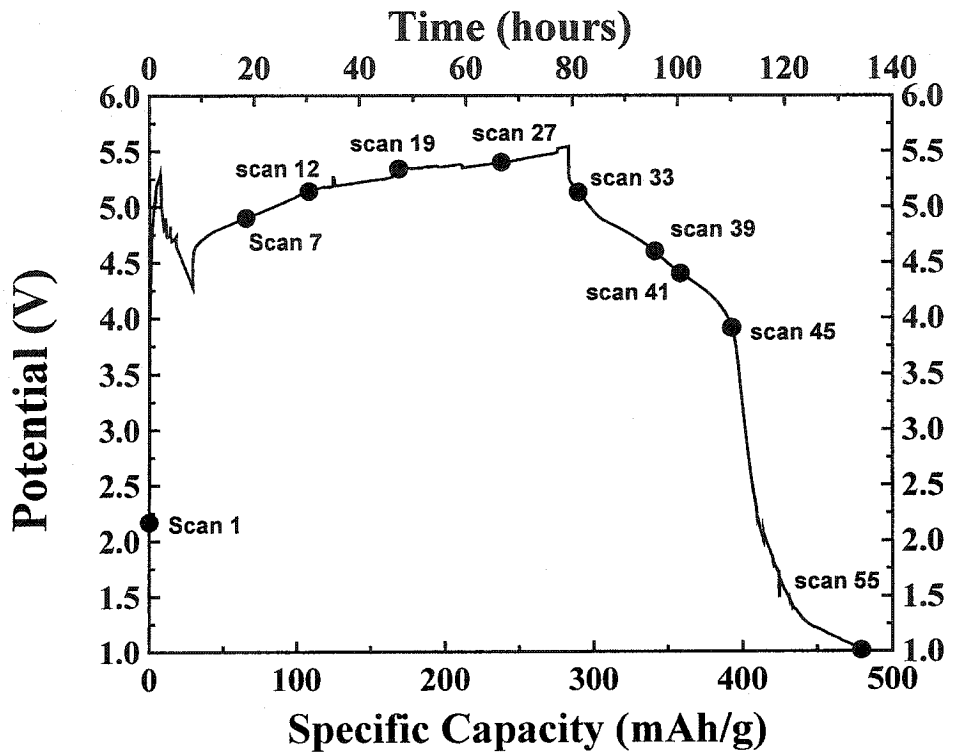

Figure 6.2.1 Potential versus specific capacity (top x-axis) and versus time (bottom x-axis) for an *in-situ* X-ray diffraction experiment of graphite with 2M $LiPF_6$/EMS as the electrolyte.

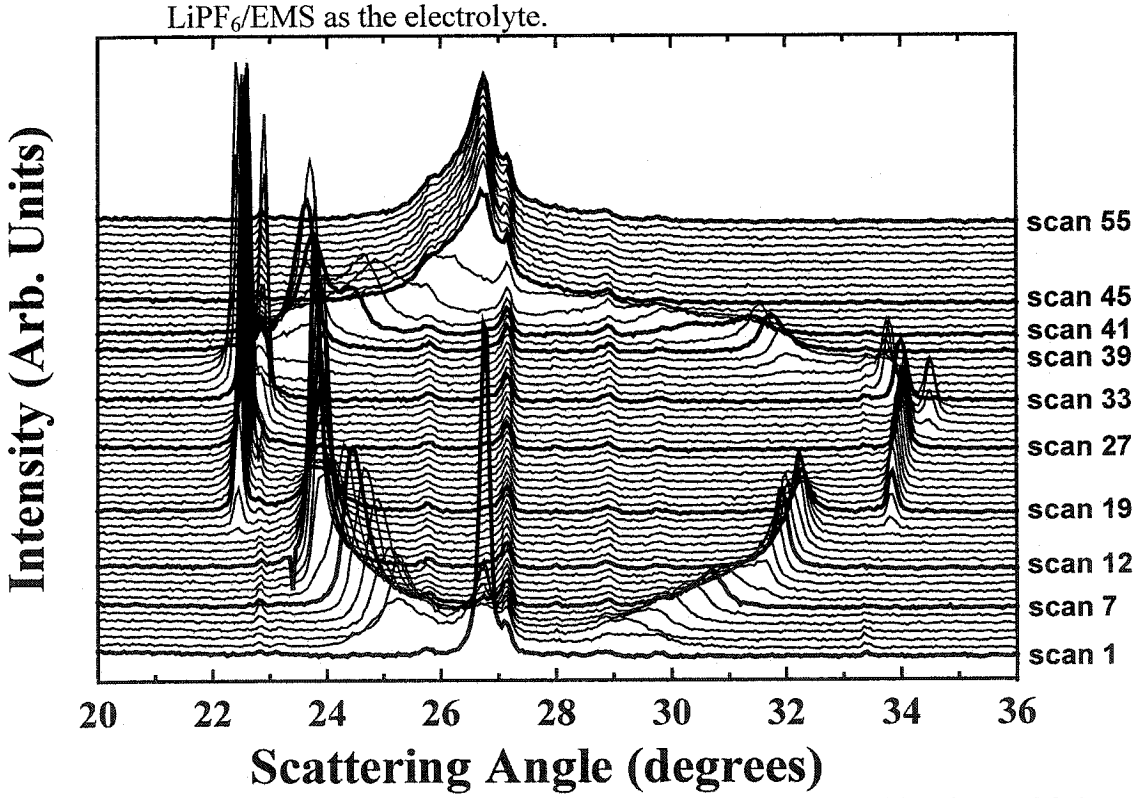

Figure 6.2.2 *In-situ* X-ray diffraction patterns for the cell described in Figure 6.2.1.

in Figure 6.2.3 [59]. One of these pure stages occurs by scan 12 at about 5.1 V. The two main peaks for this stage occur at 23.79° and 31.93°. Using the Bragg equation and setting m=3 and m=4, respectively, the average c-axis spacing for this stage is 11.21 Å. This stage is either stage 2 or stage 3. If it is assumed that the distance between two carbon layers that are not separated by an anion remains the standard 3.35 Å of normal graphite, then for stage 2 the anion layer spacing would be 7.86 Å and for stage 3 this spacing would be 4.51 Å. If this is actually stage 3, then the anion layer spacing seems quite small. However, by simply using bond-length arguments, the PF_6 anion would actually fit within this layer. The 7.86 Å spacing obtained if this is stage 2 seems much more reasonable and this agrees well with values obtained by other groups for PF_6 and similarly sized anions [11,12,16,30]. Stage 2 is the more likely stage for these peaks.

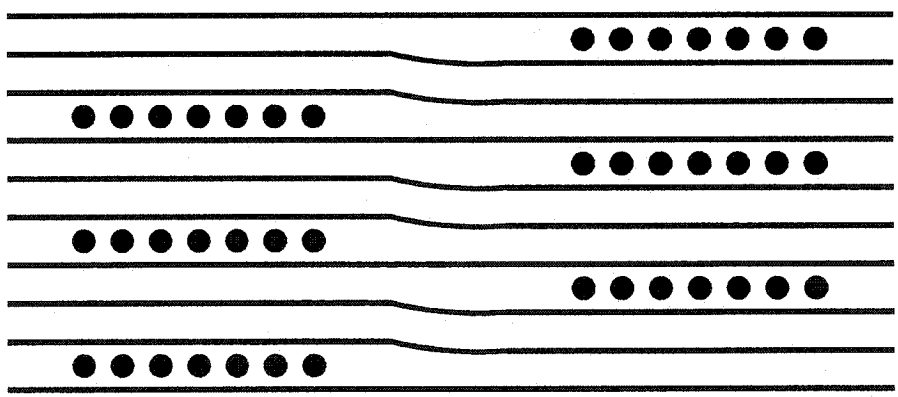

Figure 6.2.3 Illustrating local regions of stage 3. The black circles represent anions and the black lines represent the carbon layers.

As the potential is increased even further, the two peaks for stage 2 shift to slightly higher values from 23.79° (scan 12) to 23.92° (scan 16) and 31.93° to 32.24°. This results in a lower c-axis spacing of 11.13 Å and therefore an anion-layer spacing of 7.78

Å. This suggests that the PF_6 anion reorients within the layer as the concentration increases.

Once the potential reaches approximately 5.25 V, scan 17, the peaks for stage 2 start to disappear and the (002) peak and the (003) peak of stage 1 start to form. By scan 24, the stage 2 peaks are no longer present. As with the peaks for stage 2, the ones for stage 1 also shift from 27.52° to 27.62° (scan 28) and 33.94° to 34.07°. The corresponding c-axis spacings, or the PF_6-layer spacings, for this stage 1 are 7.91 Å and 7.88 Å. As with stage 2, the c-axis spacing has decreased, suggesting that a similar reorientation is taking place.

As the potential nears 5.55 V, new peaks at 22.6° and 34.5° form suggesting a transition from the present stage 1 to another stage 1 with the PF_6 oriented differently. This stage 1′ has a c-axis spacing of 7.79 Å, which is even smaller than the previous value.

During discharge the transitions occur in reverse order and occur much more rapidly. This is presumably due to the beginning of electrolyte decomposition that has occurred during charge. The peaks for stage 1 shift to lower angle before becoming smaller and stage 2 peaks form. Stage 2 peaks also shift to lower angles before higher staged phases form, at approximately 4.4 V (scan 41).

The (002) peak of graphite starts to reform just above 3.9 V (scan 45). At about 3.7 V this peak no longer changes in shape or intensity, even when the potential is decreased to 1.0 V. The integrated intensity of the initial (002) peak is actually smaller than the integrated intensity of the final (002) peak. This discrepancy can be accounted for by the fact that some PF_6 probably remains within some of the carbon layers.

Similar experiments were performed with 3 M $LiPF_6$/EC+DEC with an upper cutoff potential of 5.0 V and a lower cutoff potential of 0.90 V. Stage 1 was not achieved and the original peak of graphite did return. To see if stage 1 could be achieved, the upper cutoff potential was increased to 5.25 V. The potential versus specific capacity plot, with a time scale, in shown is Figure 6.2.4. This resulted in the destruction of the graphite layered structure as can be seen in the *in-situ* X-ray diffraction patterns shown in Figure 6.2.5. Not only can stage 1 not be achieved but the structure of the intercalated graphite is not as well defined for EC+DEC as for EMS since the main peaks are not as narrow and the higher angle peaks are barely noticeable. During subsequent discharges, the higher stages are no longer obtainable. This suggests that the electrolyte may be decomposing and no longer able to transfer the anions as efficiently as before. A significant amount of decomposition would have to occur to greatly effect the transport of ions. More likely the solvent is co-intercalating along with PF_6 resulting in the destruction of the graphite layered structure which would mean that staging would no longer occur.

These experiments have shown that ethyl methyl sulfone is a much more promising solvent than ethylene carbonate/diethyl carbonate for anion intercalation into graphitic carbon. EMS will be used as the solvent in the rest of this thesis.

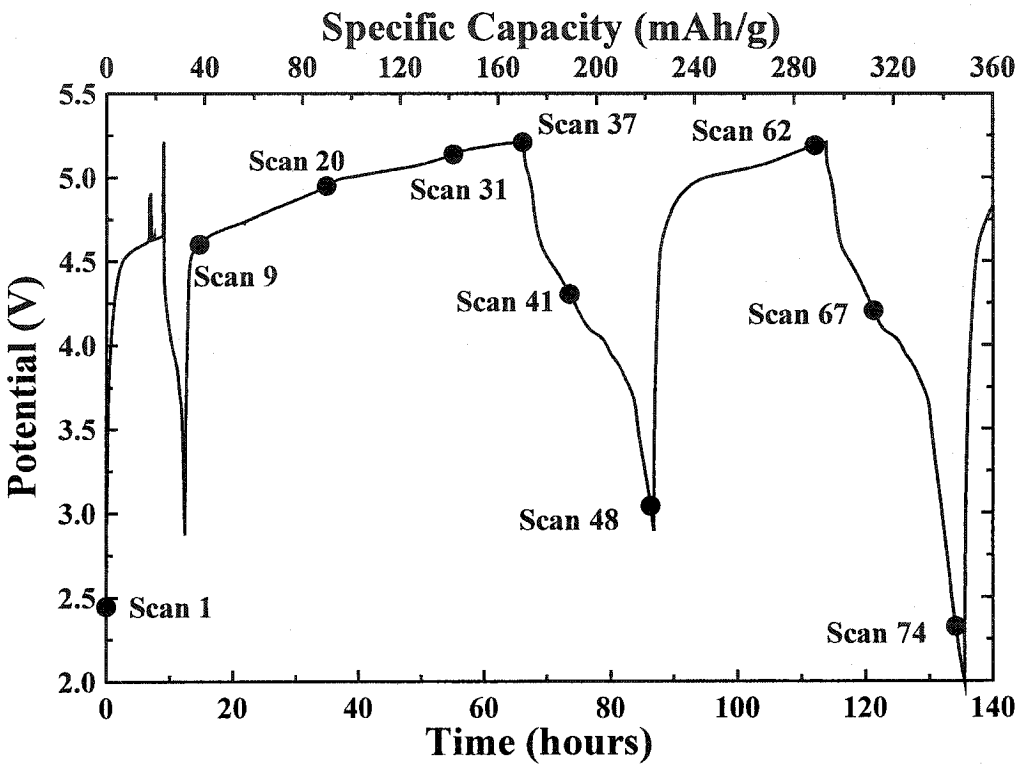

Figure 6.2.4 Potential versus time (bottom x-axis) and versus specific capacity (top x-axis) for an *in-situ* X-ray experiment of graphite with 3 M $LiPF_6$/EC+DEC as the electrolyte.

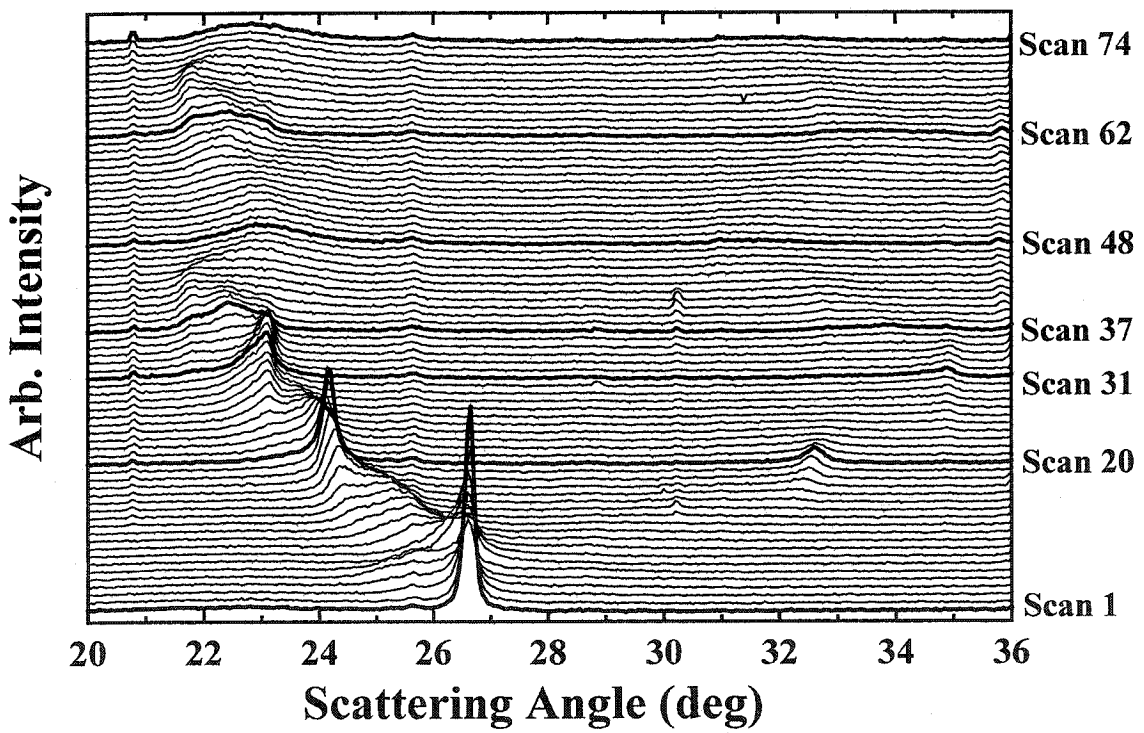

Figure 6.2.5 *In-situ* X-ray diffraction patterns for the cell described in Figure 6.2.4.

Chapter 7 Effect of Ordering

As the preliminary results showed in Chapter 5, the amount of disorder present within the carbon electrode plays a role in to what extent PF_6 will intercalate into the carbon. To study how the presence of disorder affects the intercalation of the PF_6 molecule, similar carbon materials should be used as the active material. XP3 Coke is a soft carbon material that can be heated to various temperatures to prepare samples with different values of p. Four such cokes were tested: XP3 2600°C, XP3 2300°C, XP3 1800°C, and XP3 1500°C. All samples were obtained from Conoco.

Section 7.1 Sample Analysis

The first step in determining the effects of disordered graphitic carbon on anion intercalation is to determine the amount of disorder present within the various XP3 Coke samples. For a discussion of disorder please refer to Chapter 4 Section 1.

The X-ray diffraction patterns for the four XP3 Coke samples are shown in Figure 7.1.1. It can be seen easily that the higher the temperature, the greater number of peaks present in the X-ray diffraction pattern. The XP3 Coke sample heated to 2600°C, Figure 7.1.1(a), has numerous peaks present. The sample heated to 2300°C, Figure 7.1.1(b) has the same number of peaks present, however, all but the (002), (004) and (006) peaks are much broader. Figure 7.1.1(c) shows the pattern for the sample heated to 1800°C. Even though the (002), (004), and (006) peaks are still easily distinguishable they are much broader. The other peaks have become even broader and some have become

indistinguishable, such as (100) and (101) peaks. The peaks are broader still for the sample prepared at 1500°C, Figure 7.1.1(d). Carbonxs was used to fit these samples. These fitted curves are shown as the solid gray lines in Figure 7.1.1. The important information that can be obtained from carbonxs is shown in Table 7.1. Generally speaking, for these four samples, the higher temperature samples have a lower $\mathbf{d}_{002}$ spacing, which is the spacing between adjacent carbon sheets, and a lower p, the probability of turbostratic disorder between adjacent graphene sheets.

XP3 Coke Sample Temperature	$\mathbf{d}_{002}$ spacing	P
2600°C	3.36 Å	0.15
2300°C	3.37 Å	0.32
1800°C	3.42 Å	0.94
1500°C	3.43 Å	1.0

Table 7.1 The $\mathbf{d}_{002}$ spacings and p values for the XP3 Coke samples.

These four samples, with a wide range of p, from 0.15 to 1.0, will give a good indication of how disorder within the carbon material effects anion intercalation.

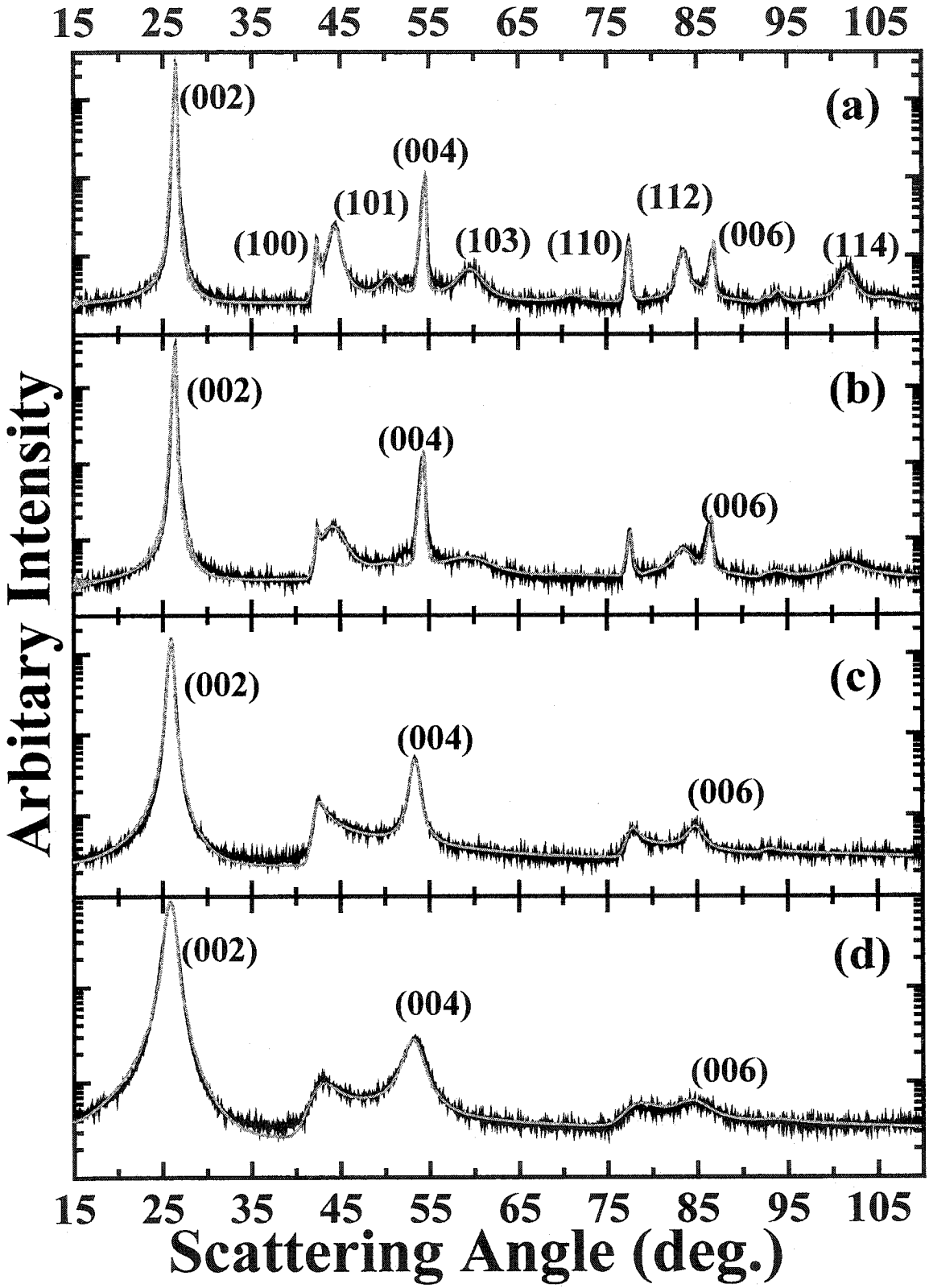

Figure 7.1.1 X-ray diffraction patterns for XP3 coke heated to (a) 2600°C, (b) 2300°C, (c) 1800°C and (d) 1500°C. The smooth gray lines in the plot are the fitted X-ray diffraction curves.

Section 7.2 Electrochemical Testing

Electrochemical cells were constructed using the four XP3 coke samples as positive electrodes. All cells used lithium metal as the counter electrode and the electrolyte was 2M $LiPF_6$/ethyl methyl sulfone. The cells were cycled at approximately a C/40 or C/45 rate which means that it should take approximately 40 or 45 hours to reach the top of charge. This resulted in currents between 50 and 75 μA. The upper and lower cutoff potentials were 5.5 V and 2.0 V, respectively, for all except the sample heated to 2300°C which had upper and lower cutoff potentials of 5.6 V and 1.5 V, respectively.

The specific capacity plots are shown in Figure 7.2.1. It can be easily seen that the specific capacities are approximately the same for both charge and discharge for the various samples. The lowest specific capacity for charge was about 108 mAh/g for the XP3 2600°C sample and the highest was 130 mAh/g for the XP3 1500°C sample. For discharge, the lowest capacity was ~92 mAh/g for both XP3 1500°C and 1800°C and the highest was ~100 mAh/g for XP3 2300°C. If the discharge capacity for XP 2300°C was taken only to 2 V, the capacity would be ~91 mAh/g instead. These results are summarized in Table 7.2.

XP3 Coke Sample Temperature	Charge Capacity (mAh/g)	Discharge Capacity (mAh/g)	Percentage Loss
2600°C	108	95	12%
2300°C	111(104)	100(91)	10%(13%)
1800°C	121	92	24%
1500°C	130	92	29%

Table 7.2 Charge and discharge capacities for the four XP3 Coke samples where 3 M $LiPF_6$/EMS was used as the electrolyte.

The percentage loss shown in Table 7.2 is determined by taking the difference between the charge and discharge capacities and dividing by the charge capacity. The

values in brackets for the 2300°C sample, are the values that are obtained if the specific capacities were taken with a lower cutoff potential of 2.0 V. It can be seen easily that the higher temperature samples have a lower capacity loss.

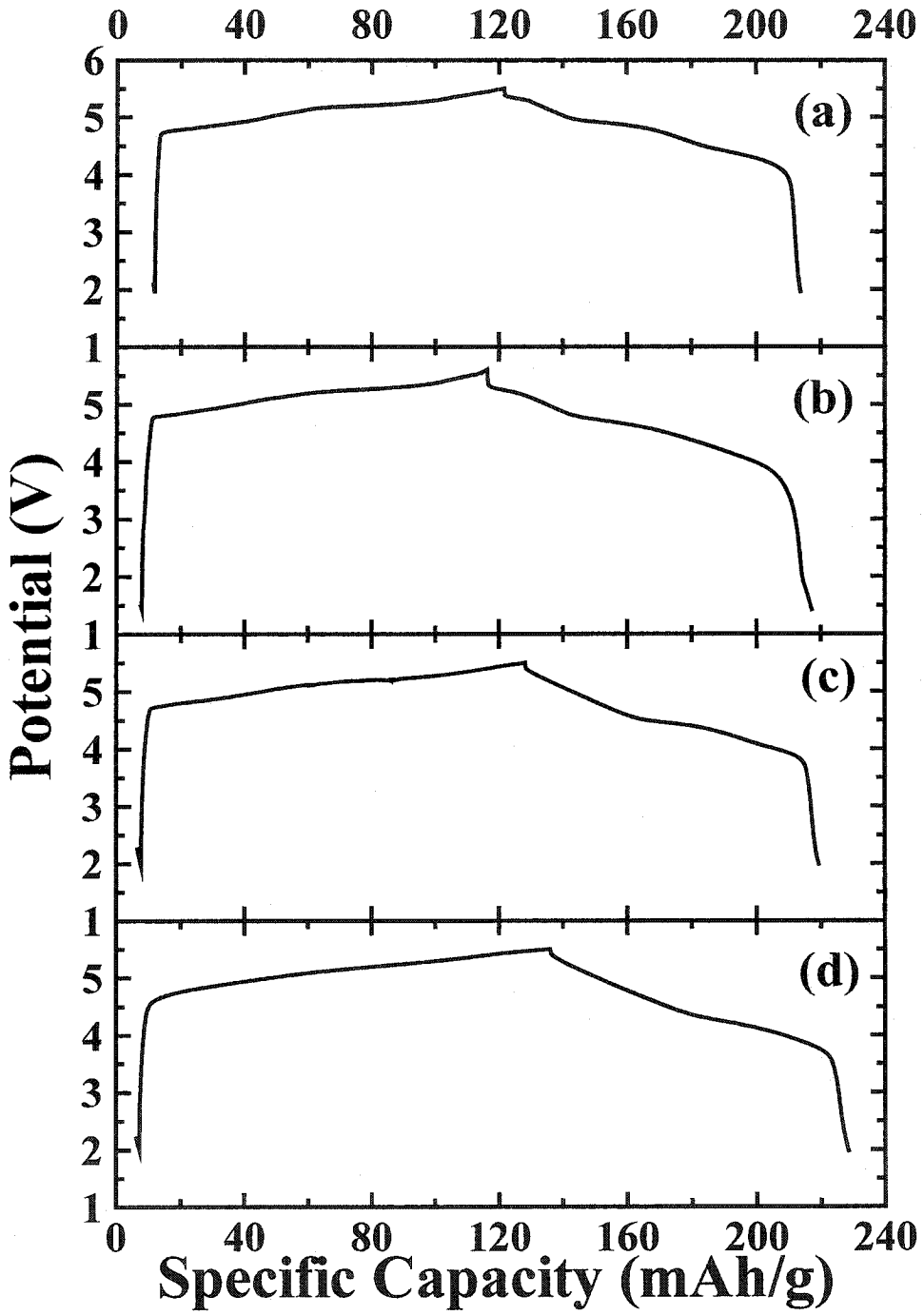

Figure 7.2.1 Potential versus capacity for XP3 Coke heated to (a) 2600°C, (b) 2300°C, (c) 1800°C and (d) 1500°C.

If the specific capacity plots are viewed qualitatively there appear to be subtle differences in the shapes of these curves. To see these differences more easily, a differential capacity versus potential plot is shown in Figure 7.2.2. In this figure it can be easily seen that there are more features in the curves for the more ordered samples than for the more disordered ones. However, there are still similarities. In all of the plots during charge (the upper part of the curves) and discharge (the lower part of the curves) there are locations that have been marked with squares and with circles. It is thought that these locations denote pure stages. The square represents stage (n+1) and the circle or double arrow line represents stage n. During charge, stage (n+1) occurs at approximately 5.1 V for all scans, with 1500°C being slightly lower. Stage n also occurs at approximately the same potential, around 5.4 V. During discharge there is a great difference in the potential for which stage (n+1) occurs; it decreases with increasing amounts of disorder. Also, the range, represented by the doubleheaded arrow in the figure, in which stage n is present during discharge increases with increasing disorder. It is interesting to note that the XP3 2600°C and 2300°C samples seem to have an extra transition.

To really understand what is occurring during charge and discharge and why there are differences between these XP3 Cokes, *in-situ* X-ray diffraction experiments on all samples must be performed.

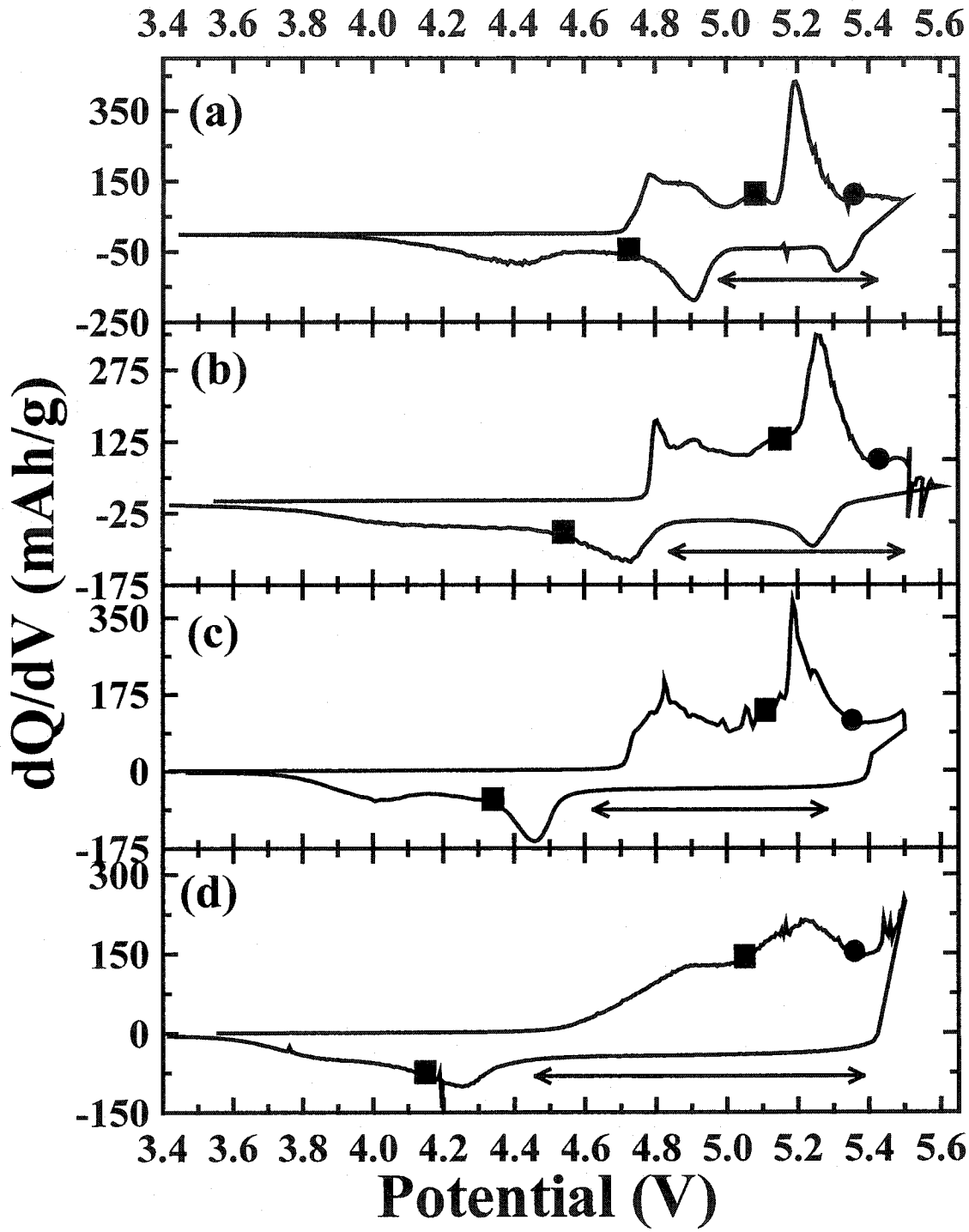

Figure 7.2.2 Differential capacity versus potential for XP3 Coke heated to (a) 2600°C, (b) 2300°C, (c) 1800°C and (d) 1500°C.

Section 7.3 *In-situ* X-ray Diffraction Experiments

In-situ X-ray diffraction experiments were performed using the method described in Chapter 3, Section 5. All four XP3 coke samples were studied using similar cutoff potentials.

Figure 7.3.1 shows the potential versus specific capacity curve as well as the X-ray diffraction patterns obtained for the XP3 1500°C samples. The cycling range during this experiment was up to 5.45 V and down to 1.5 V. The charge capacity for this experiment was quite large, ~370 mAh/g. This value is unrealistic and resulted from the very long time in which the experiment was performed. The time for the charge curve was about 96 hours. The noise present during charge may be due to electrolyte decomposition or just the fact the current was very low and therefore the error in this current very high resulting in a noisy profile. Discharge occurred much more rapidly, about 30 hours, that resulted in a realistic capacity of about 86 mAh/g.

In order to distinguish the peaks from the background in the 28° to 36° range, this part of the patterns was multiplied by a factor of five, see Figure 7.3.1(b). This sometimes resulted in a drastic change in intensity as in the final few scans. The initial (002) peak of graphite initially increases, scan 1 to scan 5, before new peaks at lower and higher angles appear. These new peaks slowly shift, the lower peak shifts to lower angles and the higher peak shifts to higher angles. This trend continues until the cell is switched to discharge at scan 44. There is a still slight shift in these peaks as during charge for the first few scans of discharge. As the potential is decreased further, the lower peak shifts to higher angles and the higher peak shifts to lower angles. The (002) peak present in the first scans did not reform.

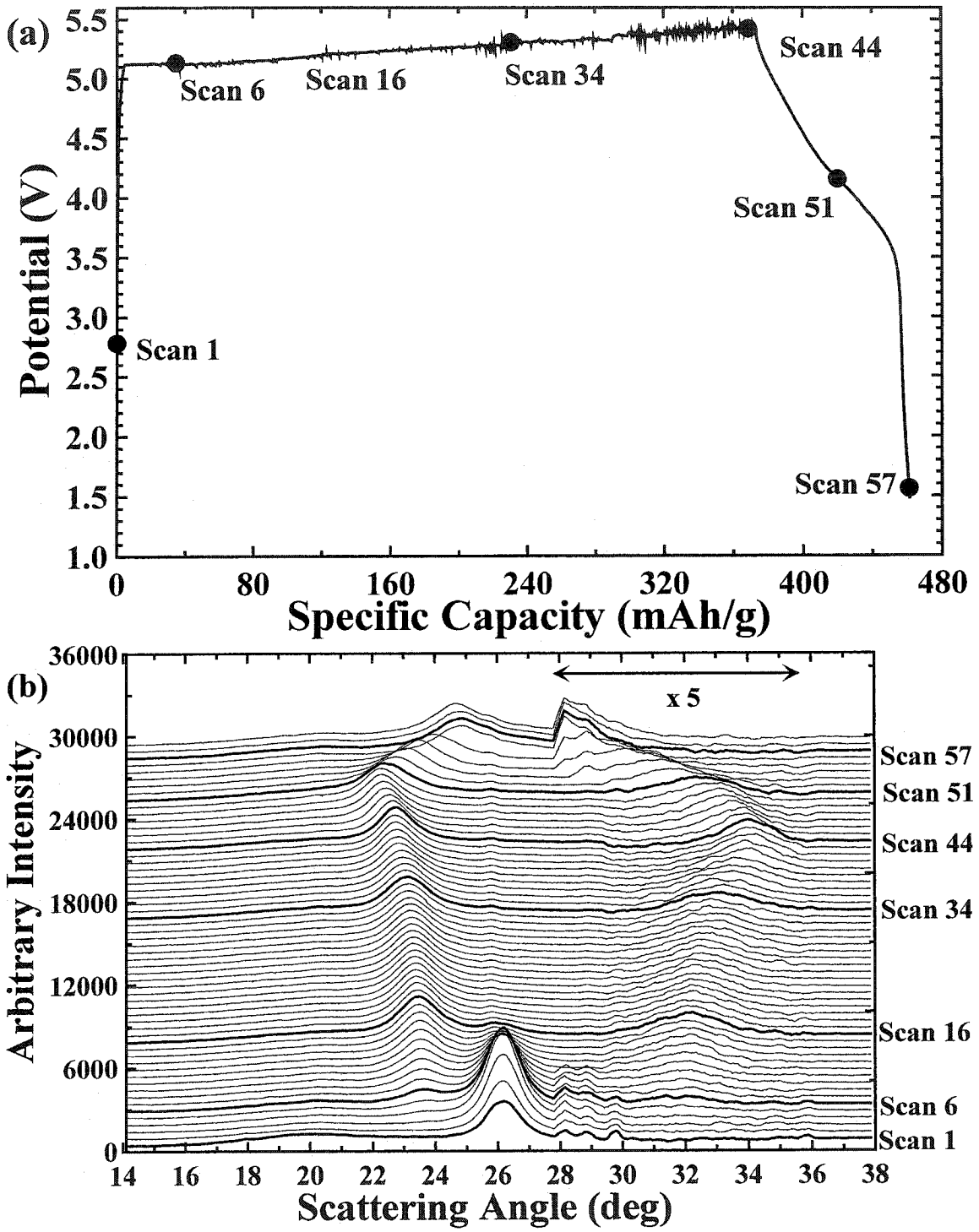

Figure 7.3.1 (a) Potential versus specific capacity and (b) X-ray diffraction patterns for an *in-situ* X-ray diffraction experiment for XP3 Coke heated to 1500°C.

It is hard to say whether pure stages are reached during this experiment, especially since the peaks are so broad. If it is assumed that a pure stage is reached just before discharge begins, at scan 44 or 5.45 V, then the corresponding angles for the peaks present for this stage are 22.8° and 34.0°. These would correspond to the (002) and (003) peaks respectively, giving an average c-axis spacing of 7.86 Å. This "pure" stage would correspond to stage 1 and has a c-axis spacing very similar to that of Fluka graphite which was determined in Chapter 6.

XP3 1800°C was studied next and its *in-situ* X-ray diffraction experiment is shown in Figure 7.3.2. The upper and lower cutoff potentials for this particular experiment were 5.5 V and 0.82 V respectively. It can be seen easily that there is a great deal more structure present in this experiment than the *in-situ* X-ray diffraction experiment for XP3 1500°C.

The initial (002) peak of graphite initially diminishes as the potential is increased. Peaks on either side of the (002) peak can be seen even by scan 2, but certainly more clearly by scan 3. These peaks shift and become more defined as the potential is increased further. Very well defined peaks occur at scan 10 or 5.19 V. The two peaks are at 23.5° and 31.9°. These two peaks are the (003) and (004) peaks and result in a c-axis spacing of 11.30 Å, which corresponds to stage 2. Assuming that the empty layer between two carbon sheets remains the same as the pure carbon sample then the anion layer spacing is 7.88 Å. At scan 11 and scan 12, about 5.22 V, a low angle shoulder begins to form near the (003) peak and a high angle shoulder appears on the (004) peak. The next few scans are a transition between these new peaks forming and the old peaks disappearing. By scan 19, 5.41 V, the old peaks are no longer present. The peaks present

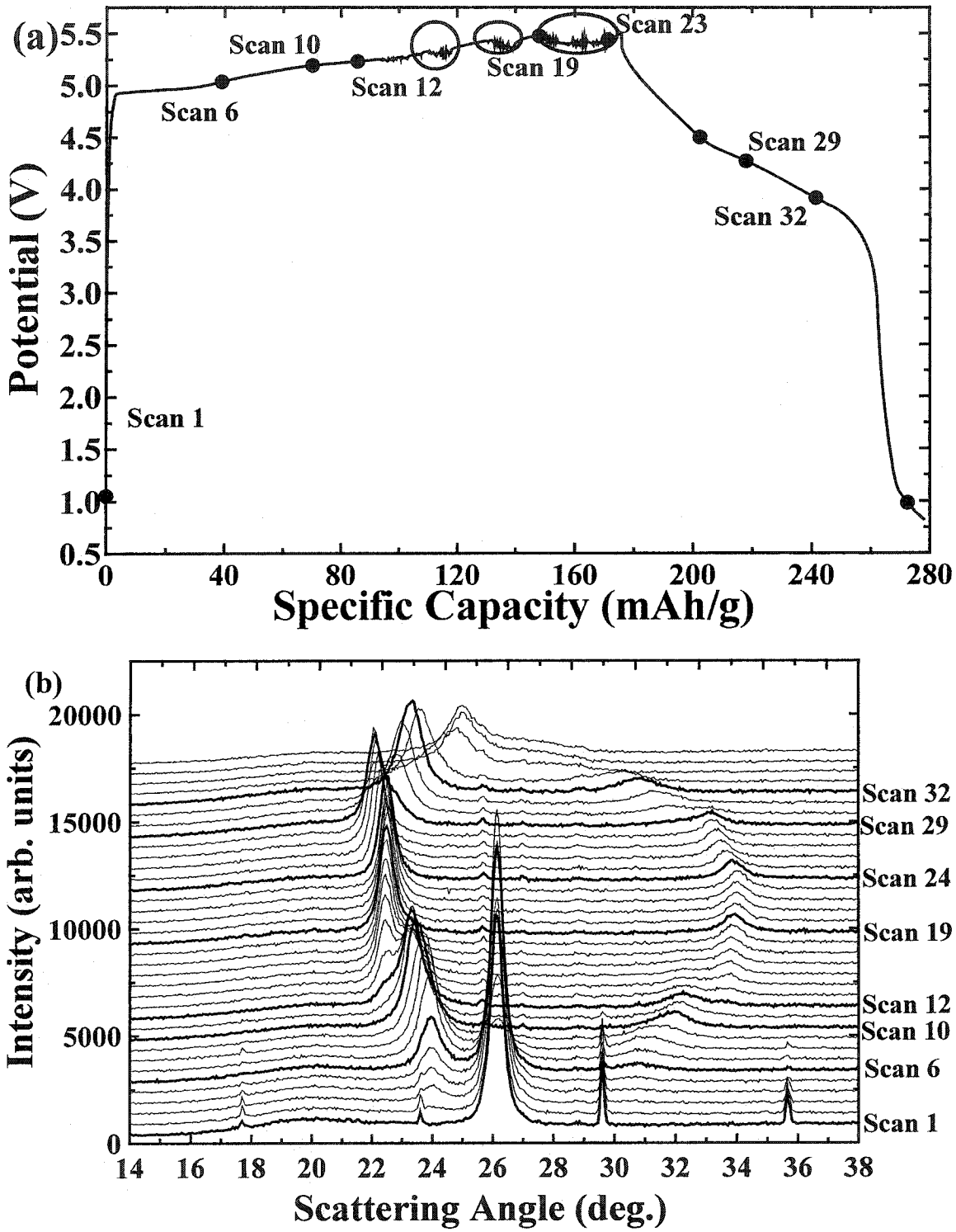

Figure 7.3.2 (a) Potential versus specific capacity and (b) X-ray diffraction patterns for an *in-situ* X-ray diffraction experiment for XP3 Coke heated to 1800°C.

at this potential are the (002) peak located at 22.48° and the (003) peak at 33.91°. These correspond to a c-axis spacing of 7.92 Å. The last scan before discharge is scan 23, 5.44 V, and this is still considered to be the same stage, in this case stage 1. The peaks are located at 22.53° and 34.04°. This is only a slight shift and results in a very similar c-axis spacing of 7.91 Å.

The opposite process occurs during discharge, and as with XP3 1500°C, it occurs more rapidly. It is interesting to note that the sample remains in stage 1, for several scans, after discharge begins and the (00ℓ) peaks shift to lower angles. The shift in angle is about 0.6°. This means that the c-axis spacing is increasing slightly from 7.92 Å to about 8.1 Å. This suggests that perhaps the PF_6 molecule is changing its orientation within the carbon electrode. Stage 2 begins to return by scan 29, 4.27 V, and stage 1 peaks are no longer present by scan 32, 3.91 V. The original (002) peak of graphite does not return by the time the experiment was terminated, at 0.82 V.

The charge capacity for this experiment was approximately 175 mAh/g which is about 55 mAh/g more than the experiment discussed in section two of this chapter. The main reason for this difference is the fact that in order to obtain X-ray diffraction patterns that minimize the background noise, a long period of time is required to conduct the experiment. This experiment had a very low current which causes the experiment to take a long time. This particular experiment took fifty hours during charge and thirty hours during discharge. If the current is too high, the amount of PF_6 that intercalates into the carbon electrode at a particular potential may not be optimized. This particular cell had a problem with dendrites. Dendrites form, in this case, on the lithium electrode as the cell is cycled. Instead of plating evenly onto the surface of the electrode, lithium particles

attach to the electrode surface into chains which may form away from the electrode surface and may eventually protrude through the separator shorting the cell. This can be seen by the noisiness in the charge part of the curve, especially the dips around 110 mAh/g, 140 mAh/g and 160 mAh/g. These regions are circled in Figure 7.3.2 (a). If these regions were removed, the corresponding specific capacity would be approximately 135 mAh/g which is more comparable with 121 mAh/g. The discharge capacity is about 113 mAh/g, approximately 10 mAh/g higher than in Section 7.2. This slight difference is due to the fact that the lower cutoff potential is lower.

The *in-situ* X-ray diffraction experimental results for XP3 2300°C are shown in Figure 7.3.3. The upper and lower cutoff potentials were 5.6 V and 1.5 V respectively. The charge and discharge capacities are ~135 mAh/g and ~90 mAh/g which agree reasonably well with the results discussed in section two of this chapter.

Visually, the patterns shown in Figure 7.3.3(b) appear very similar of that of Fluka graphite discussed in Chapter 6. As charging begins and PF_6 intercalates into the carbon electrode, the (002) peak of graphite begins to diminish and peaks on either side of this peak begin to form. As with XP3 1800°C, the lower angle peak shifts to lower angles and the higher angle peak shifts to higher angles. A pure stage appears at scan 9 or 5.11 V. There are three easily visible peaks which are located at 23.80°, 32.09° and 48.2°. These correspond to the (003), (004) and (006) peaks and a d-spacing of 11.23 Å. This particular stage is most likely stage 2 which would give an anion layer spacing of 7.86 Å. These peaks shift slightly as the potential is increased further. By scan 12, 5.24 V, new peaks start to form. These would be stage 1 peaks. Stage 2 peaks are completely gone by scan 19, 5.54 V. Four (00ℓ) peaks are actually visible at this scan. These peaks

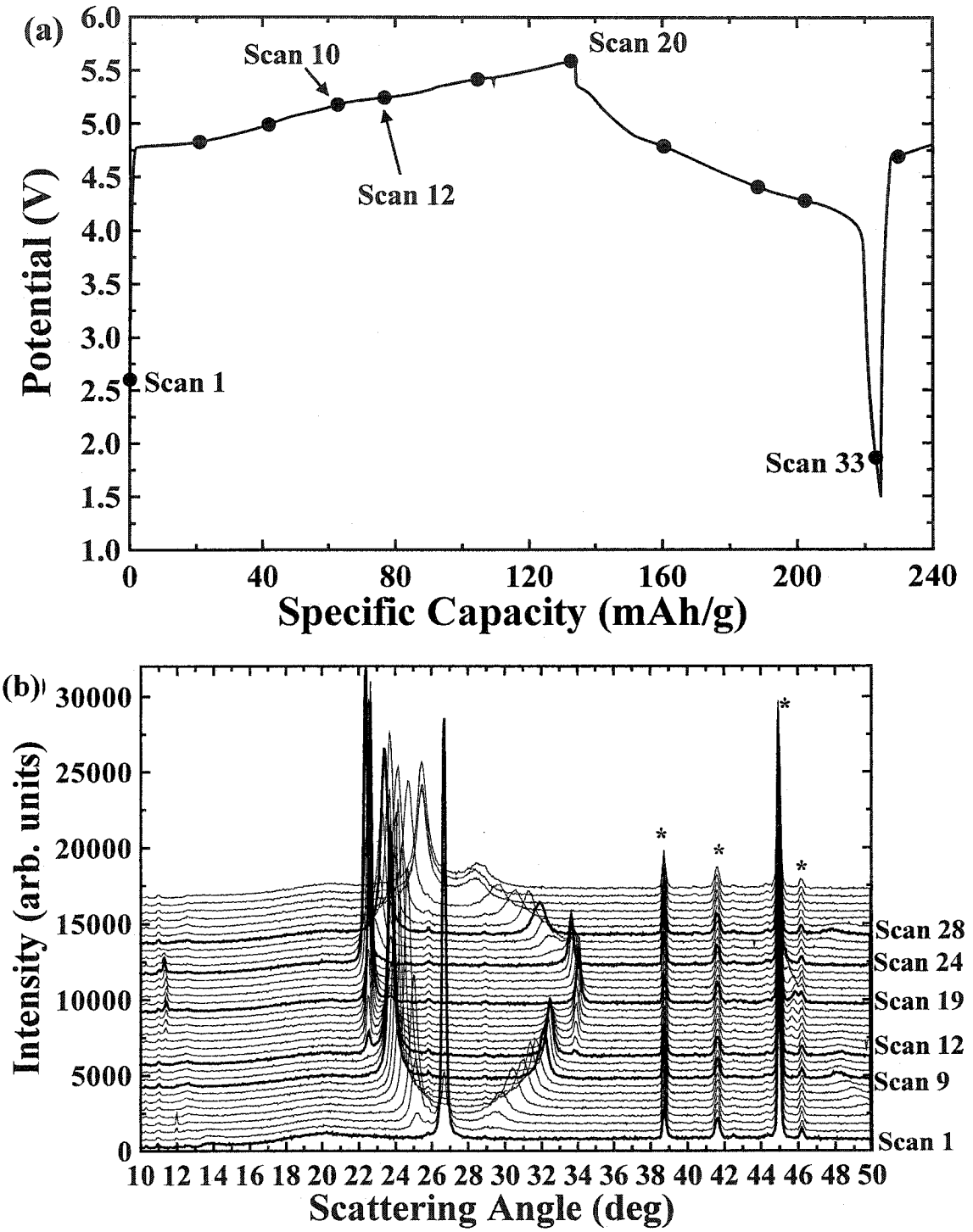

Figure 7.3.3 a) Potential versus specific capacity and (b) X-ray diffraction patterns for an *in-situ* X-ray diffraction experiment for XP3 Coke heated to 2300°C. The asterisks denote background peaks from components of the electrochemical cell not caused by the carbon electrode.

correspond to the (001), (002), (003), and (004) peaks, and are 11.41°, 22.63°, 34.06°, and 45.85°, respectively. This results in a c-axis spacing of 7.86 Å.

Discharge begins near the end of scan 20. As with the XP3 1800°C sample, the (00l) peaks shift to lower angles, resulting in a lattice expansion of the carbon material. Stage 2 peaks begin to reappear at scan 24, or 4.78 V. Pure stage 2 is reached at scan 28 or 4.35 V, although the peaks are slightly broader. The original (002) peak of graphite did not return by the end of the experiment at 1.5 V.

Figure 7.3.4 shows the *in-situ* X-ray diffraction experiment for XP3 2600°C. The upper and lower cutoff potentials for this experiment were 5.5 V and 0.75 V, respectively. The charge and discharge capacities are approximately 135 mAh/g and 120 mAh/g, respectively, a loss of about 11%.

Qualitatively, the X-ray diffraction patterns shown in Figure 7.3.4(b) are very similar to that of Fluka graphite discussed in Chapter 6. This is reasonable since the amount of disorder present for both samples is about the same. These patterns are also visually similar to the results for XP3 2300°C.

As the potential is increased, the (002) peak of graphite diminishes and new peaks at ~25° and ~29° begin to form. These peaks shift until about scan 8, 5.07 V. The peaks here are the peaks for stage 2. The (003) peak is present at 23.94°, the (004) peak is located at 31.51° and the (006) peak is located at 48.56°. This corresponds to a d-spacing of 11.25 Å and an anion layer spacing of 7.89 Å. Stage 1 peaks begin to form at scan 11, around 5.19 V. Pure stage 1 is present at scan 19, just before discharge, at 5.48 V. The (001), (002), (003) and (004) peaks are located at 11.3°, 22.51°, 33.93° and 45.68°, respectively. This results in an intercalated PF_6 layer spacing of 7.90 Å.

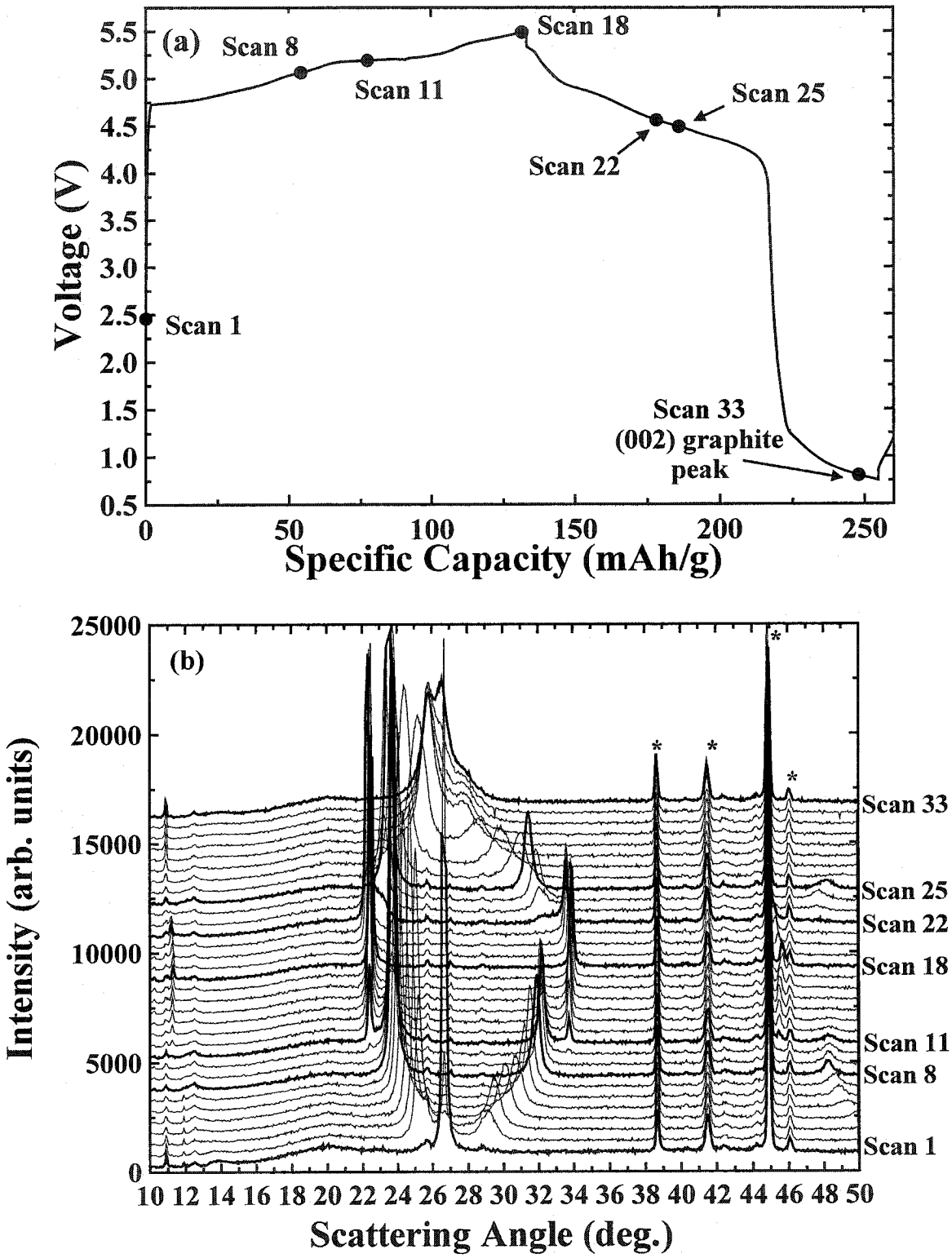

Figure 7.3.4 (a) Potential versus specific capacity and (b) X-ray diffraction patterns for an *in-situ* X-ray diffraction experiment for XP3 Coke heated to 2600°C. The asterisks denote background peaks from components of the electrochemical cell not caused by the carbon electrode.

Upon discharge the stage 1 peaks diminish as stage 2 peaks reform as PF_6 is removed. Stage 2 is reached at scan 25, 4.5 V. The peaks continue to shift back towards the location of the (002) peak of graphite. In fact the (002) peak begins to reform around scan 32 or 0.88 V but it is not well formed before the experiment was completed at 0.75 V. This suggests that a fair amount of PF_6 or perhaps EMS remains in the carbon electrode.

It is interesting to note for the two samples with $p < 0.5$, i.e. the more ordered samples, there are distinct and clear transitions between stage 2 and stage 1. The peaks corresponding to each stage are clearly distinguishable with no overlap. This does not occur for the two samples with $p > 0.5$. There are still separate peaks for stage 1 and stage 2 for the XP3 1800°C sample but they overlap. These peaks are no longer distinguishable for the XP3 1500°C sample, since the peaks are extremely broad in comparison.

There are a few interesting things to note about the more disordered samples. It can be seen quite easily in the first few scans of the XP3 1500°C *in-situ* X-ray diffraction patterns that the intensity of the initial (002) peak increases at the beginning of charge. It is thought that as a few of the PF_6 molecules intercalate in between two turbostratically disordered layers that one of the layers shifts so that the preferable AB stacking of graphite is achieved, hence causing a more intense (002) peak. These small packets of AB stacking which have turbostratically disordered layers between them become more filled as more PF_6 is intercalated and eventually staging begins.

This interesting phenomenon might be explained by the following. There may be a few locations between two turbostratically disordered layers that can accommodate a

PF_6 molecule. Naturally, these locations would be filled first. As more PF_6 is intercalated between the carbon layers these spots would fill up and one of these layers may locally shift or rotate to the standard AB stacking arrangement and more PF_6 molecules would then intercalate into the carbon material and then begin to form stages.

But is this really possible? Consider three turbostratically stacked layers, see Figure 7.3.5. Suppose the top layer, the A layer in black, and the bottom layer, layer C in light gray, are rotated about the origin by 30° as an example, marked with a large black dot. Both of these layers have a carbon at the origin and if the angle was zero instead then the two would have exactly the same orientation. The middle layer, layer B in dark gray, was rotated from A and its energy was calculated [60]. Note that this layer does not have a carbon at the origin. This calculated energy is shown in Figure 7.3.6.

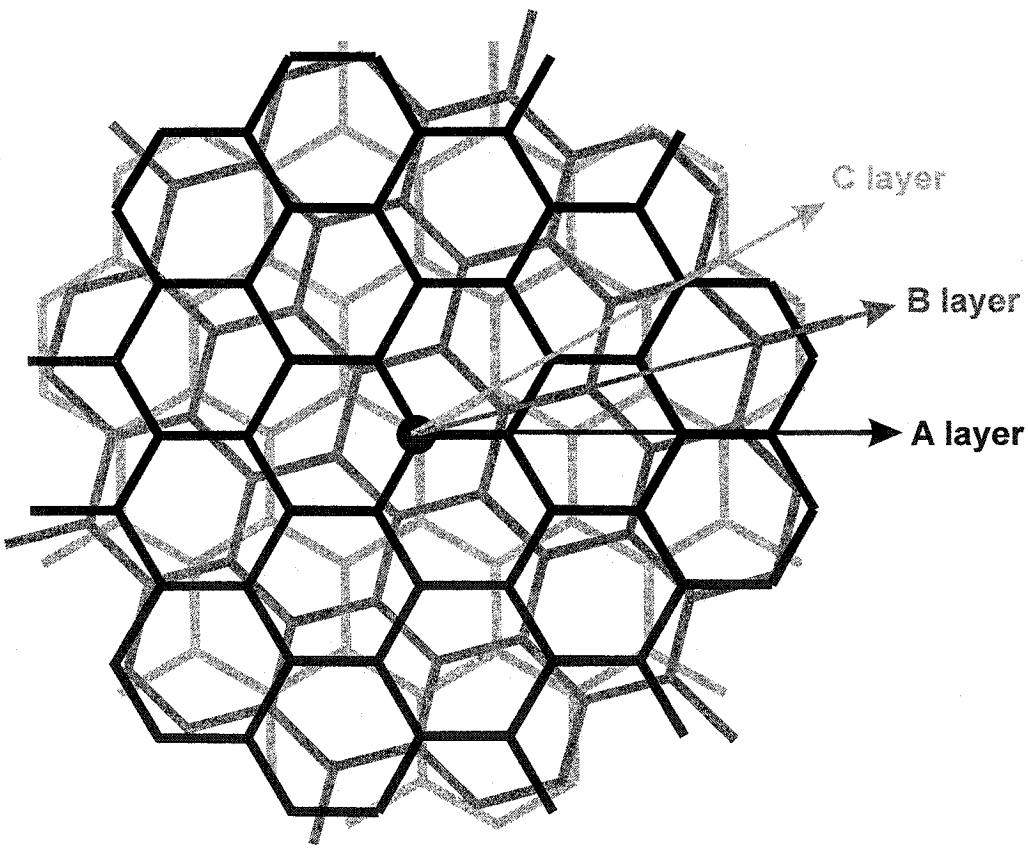

Figure 7.3.5 Illustrating three turbostratically misaligned layers.

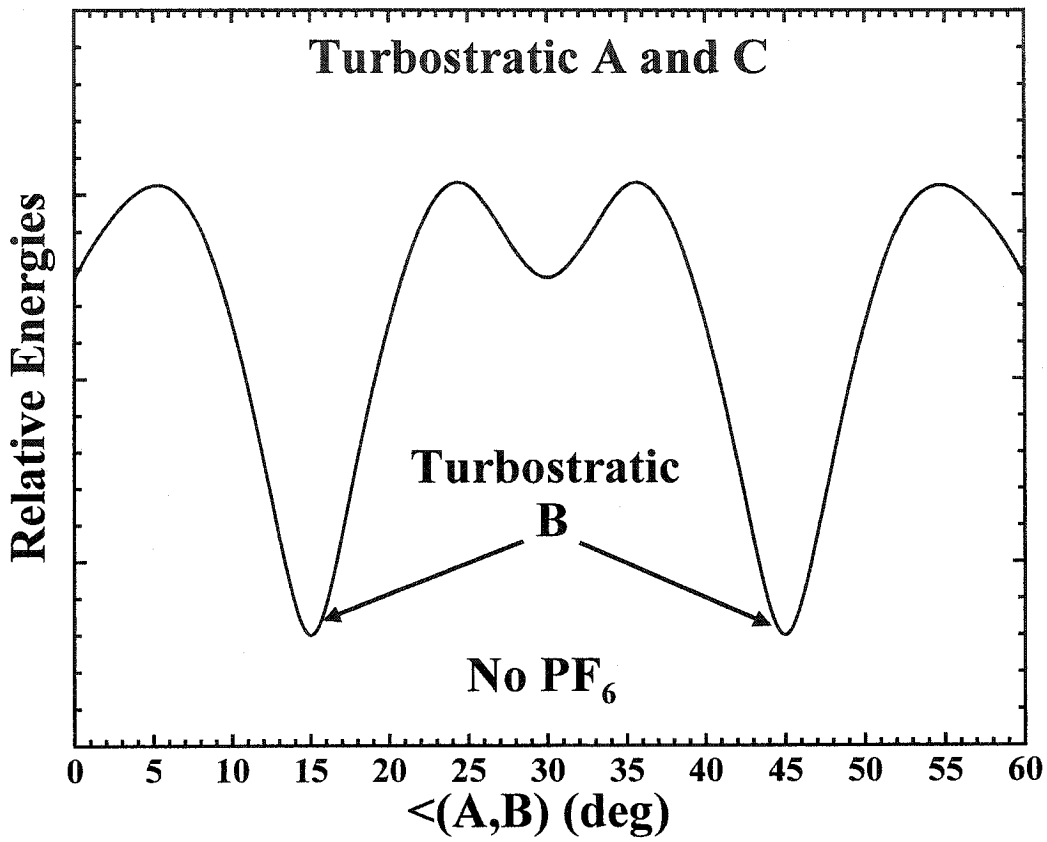

Figure 7.3.6 Relative energy versus the angle between sheets A and B without PF_6 present.

It can be seen easily that there is a local minimum at 30°. At this point layer C and B are in the AB stacking arrangement. Similarly at 0° and 60°, A and B are in AB stacking. However, the true minimum energy occurs at 15° and 45°. The middle layer, layer B, has situated itself between the other two layers resulting in this set of layers being turbostratically disordered. The central layer prefers to be turbostratically disordered when the surrounding layers are turbostratically disordered [60].

What will occur if the PF_6 molecule intercalates between these layers? If the PF_6 molecule intercalates between the A and B layers, the B layer would rotate to accommodate the PF_6 molecule. In fact, it would rotate to 0°. Similarly, if PF_6 molecule intercalates between the C and B layers, the B layer would rotate to 30° to accommodate

the PF_6 molecule. If the energy of the B layer was now calculated these angles would be located at a minimum [60]. This is illustrated in Figure 7.3.7.

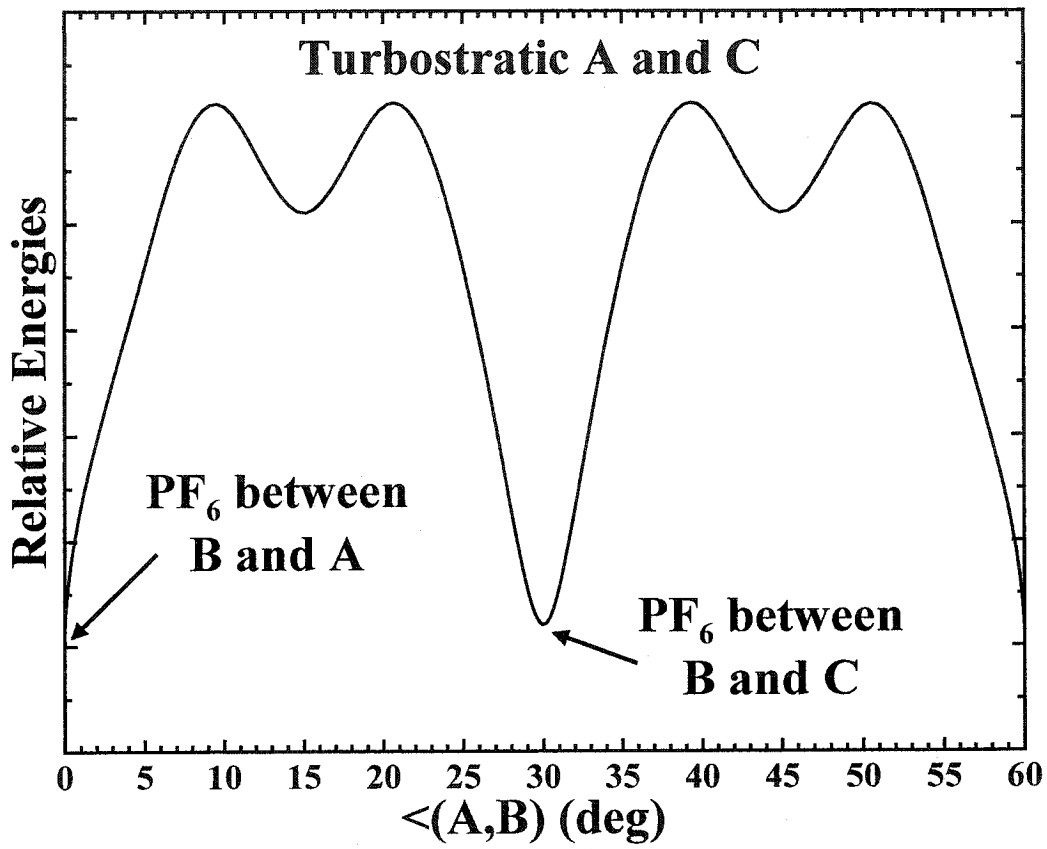

Figure 7.3.7 Relative energy of layer B versus the angle between sheets A and B with PF_6 present.

Another interesting feature, which is more readily seen in the disordered samples, is that even after discharge has begun, the sample remains in stage 1 for an extended period of time, as previously mentioned. This suggests that the PF_6 has become trapped in stage 1. Since AB stacking is preferred when the PF_6 is between two carbon sheets, the sample tries to retain this stacking arrangement as the PF_6 is removed. However, once enough of the PF_6 has been removed from the intercalant layer, the anion can no longer keep the carbon layers in the AB arrangement. In other words, the energy of the

AB arrangement is higher than that of the disordered state so the sample jumps back to its original disordered state.

This perhaps can be seen more easily in phase diagrams that show where the staged phases occur with respect to the potential of the cell and with respect to its specific capacity. The stage index, m, was determined using the following equation:

$$d = d_A + (m-1)*3.35 = \frac{n\lambda}{2\sin\theta_n} \tag{7.1}$$

where d_A is the spacing between two carbon layers that have an intercalated PF_6 between them and

$$n = \frac{\sin\theta_n}{\sin\theta_{n+1} - \sin\theta_n} \tag{7.2}$$

and where $2\theta_n$ is the position of the (00n) peak, the most intense peak of the X-ray diffraction pattern being studied, $2\theta_{n+1}$ is the position of the (00 n+1) peak, and λ is the wavelength of the X-rays.

In each of the following figures the solid circles and the open circles represent the stages reached during the charge and discharge part of the cycle, respectively. The phase diagram for the XP3 1500°C sample is shown in Figure 7.3.8. It can be easily seen that PF_6 remains trapped in stage 1 after discharge begins. It remains in stage 1 until the potential drops below ~4.3 V. At this point enough PF_6 has been removed from the electrode so higher stages begin to form.

Similarly, the XP3 1800°C sample also remains in stage 1 until about 4.5 V where stage 2 is beginning to form. It can be seen in Figure 7.3.9 that there is a region where one stage is forming as another is diminishing in both the charge and discharge part of the cycle.

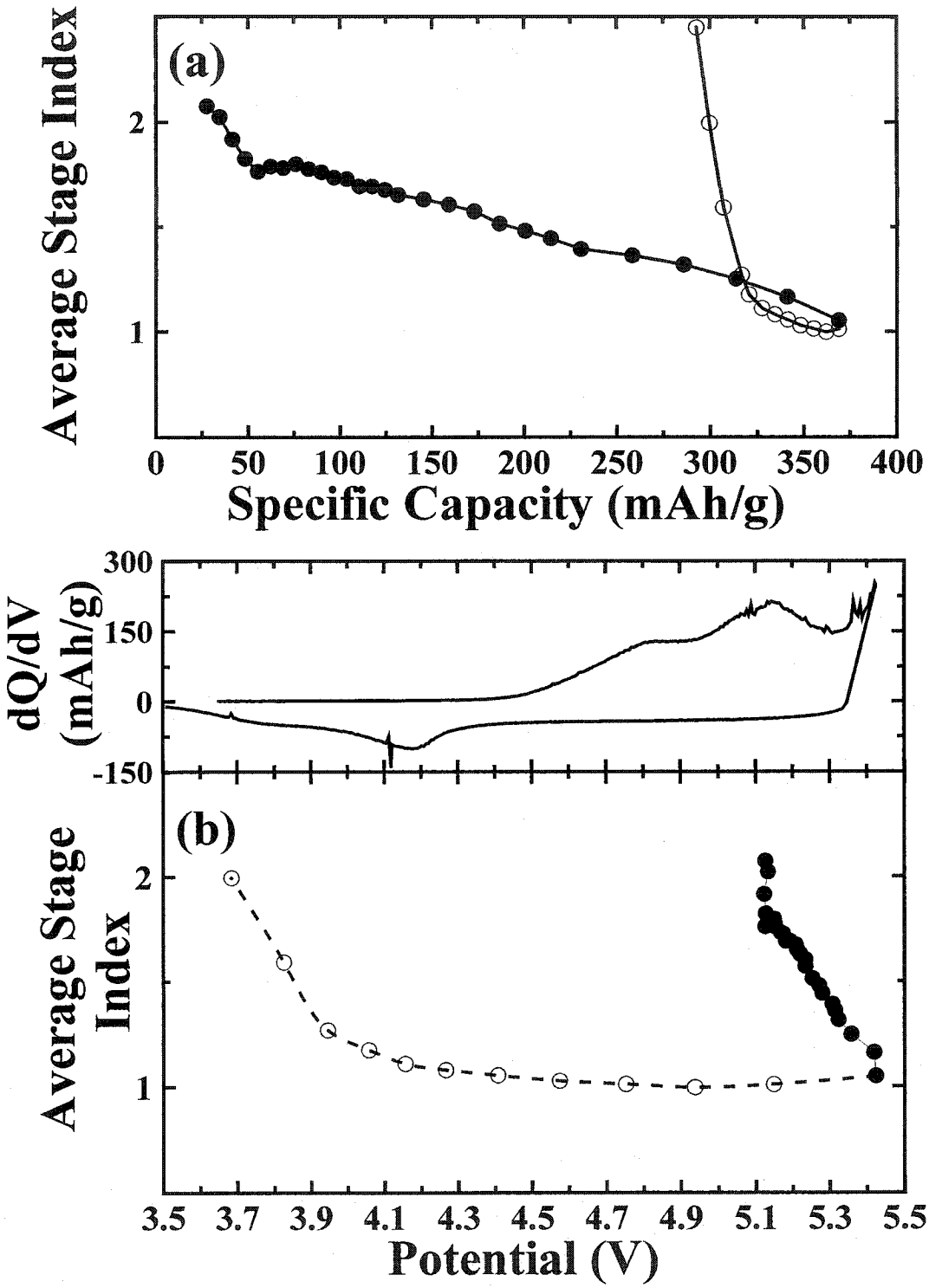

Figure 7.3.8 (a) Average stage number versus specific capacity and (b) top panel: dQ/dV versus potential and bottom panel: average stage number versus potential for the *in-situ* X-ray diffraction experiment of XP3 Coke heated to 1500°C. The solid circles represent the charging process and the open circles represent the discharge process.

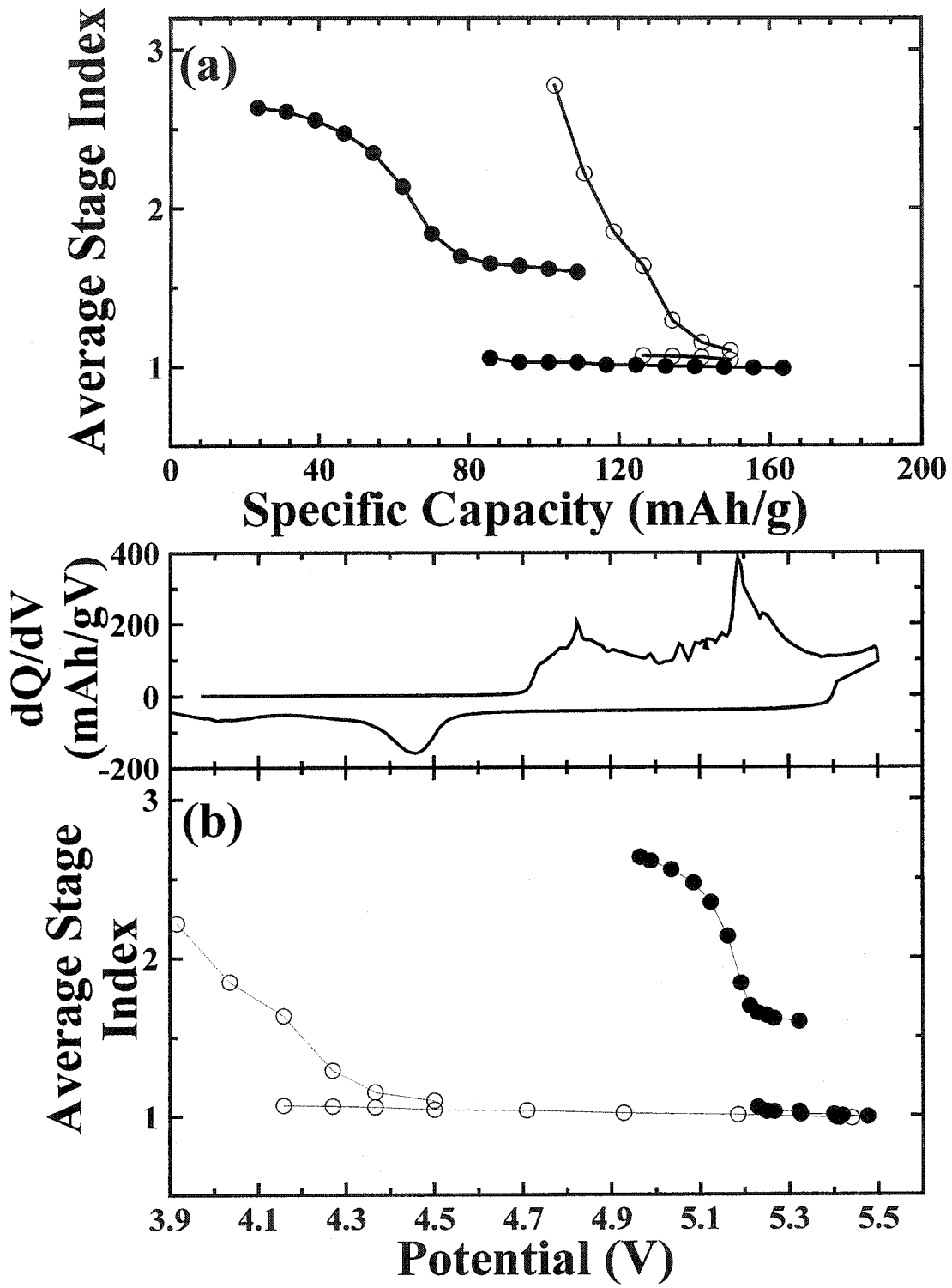

Figure 7.3.9 (a) Average stage number versus specific capacity and (b) top panel: dQ/dV versus potential and bottom panel: average stage number versus potential for the *in-situ* X-ray diffraction experiment of XP3 Coke heated to 1800°C. The solid circles represent the charging process and the open circles represent the discharge process.

Figure 7.3.10 shows the average stage number versus the specific capacity and versus potential for the XP3 2300°C sample. Even with this fairly ordered sample, the sample remains in stage 1 until ~4.8 V during discharge where a region of co-existing stages begins to form. Figure 7.3.11 show the same phase diagrams for XP3 2600°C. Even with this very ordered sample PF_6 remains in stage 1 until about 4.8 V. As with the 2300°C sample, there are regions where one stage is forming while another is disappearing both during charge and discharge.

Upon close inspection of the phase diagrams for all but the XP3 1500°C sample, it is evident that what had been referred to as stage 2 does not seem to have a stage index of 2. Instead the stage index is lower. The XP3 1800°C sample has m = 1.6, XP3 2300°C has m = 1.7 and XP3 2600°C has m = 1.8. It was first thought that the equations were perhaps incorrect, however, this is not the case. Next it was thought that perhaps there was an off-axis shift that was greatly effecting m. This was investigated and it was found that an off-axis shift of nearly 1° did not effect m sufficiently enough to be the cause of the large shift that was present in m. The most probable explanation of what is occurring is that as more PF_6 intercalated into the carbon electrode only a few PF_6 enter into the empty layers resulting in a average stage index of instead of 2. In Figure 7.3.12(a) a region of pure stage 2 is shown. If only a few layers with a stage 2 region are being filled with more PF_6 then there might be a region with mostly every other layer filled with PF_6 with an infrequent adjacent layers being filled with more PF_6, see Figure 7.3.12(b). As the potential is increased further these regions of an average stage index of less than 2 become smaller and eventually only stage 1 remains.

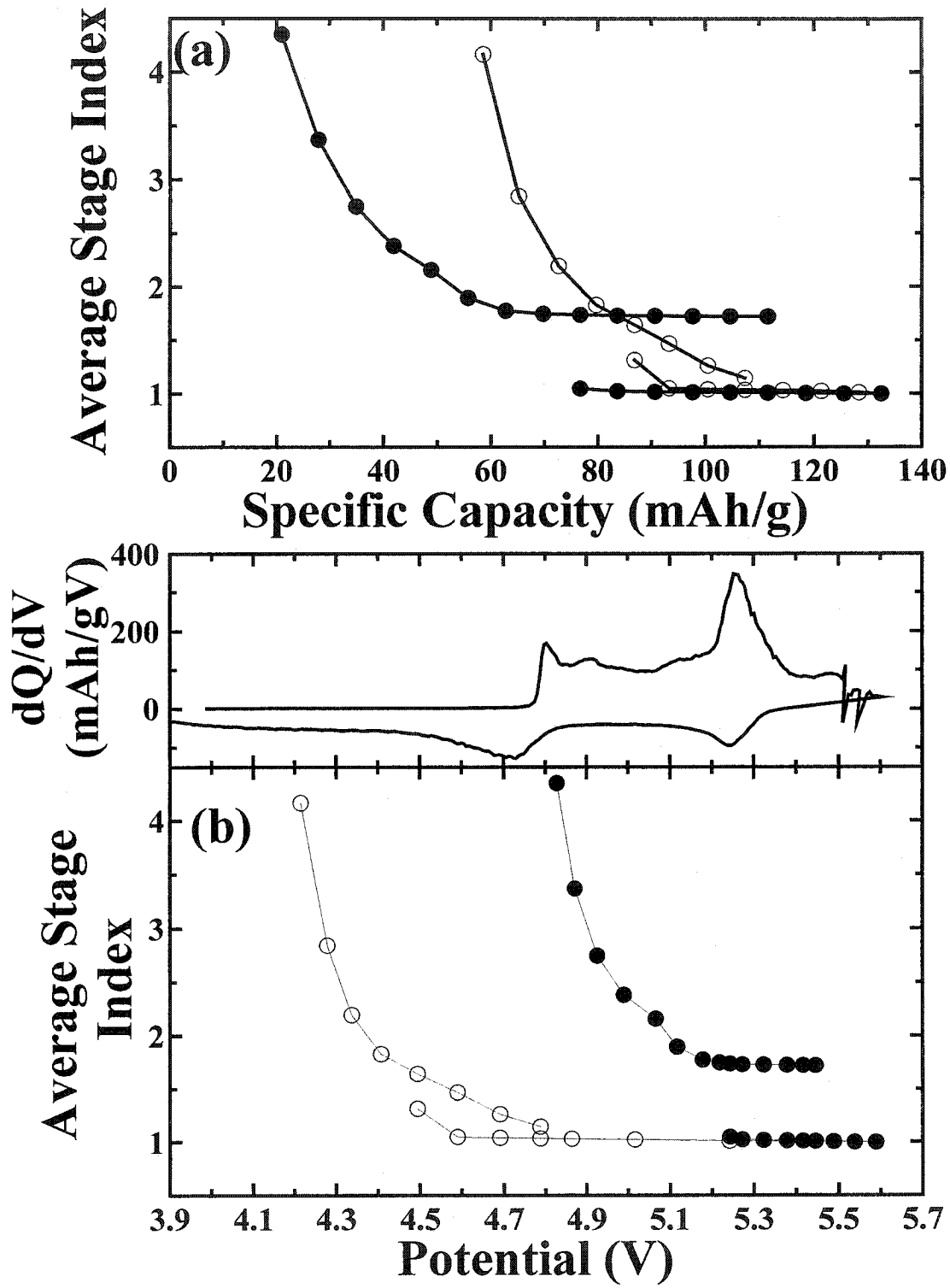

Figure 7.3.10 (a) Average stage number versus specific capacity and (b) top panel: dQ/dV versus potential and bottom panel: average stage number versus potential for the *in-situ* X-ray diffraction experiment of XP3 Coke heated to 2300°C. The solid circles represent the charging process and the open circles represent the discharge process.

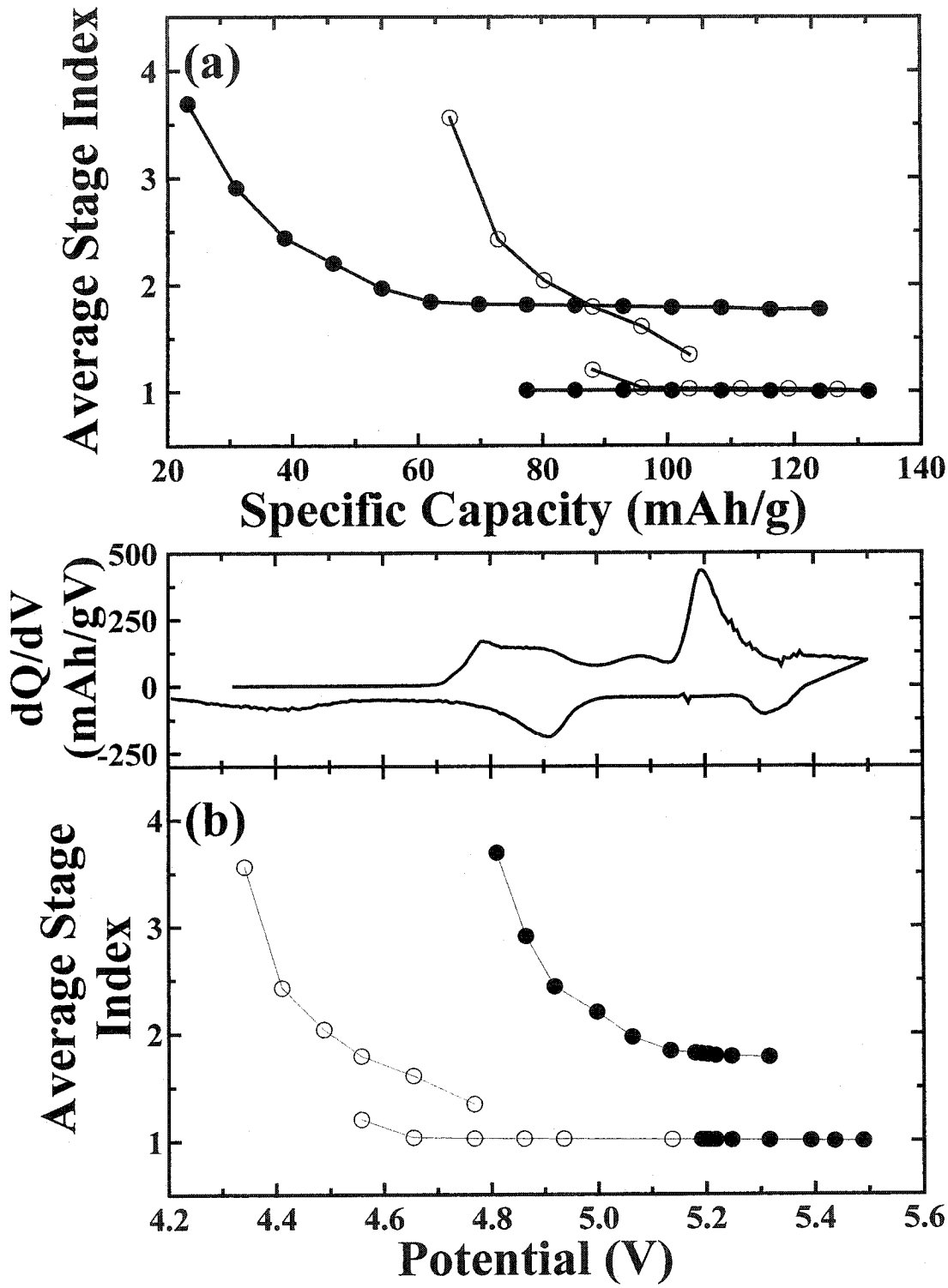

Figure 7.3.11 (a) Average stage number versus specific capacity and (b) top panel: dQ/dV versus potential and bottom panel: average stage number versus potential for the *in-situ* X-ray diffraction experiment of XP3 Coke heated to 2600°C. The solid circles represent the charging process and the open circles represent the discharge process.

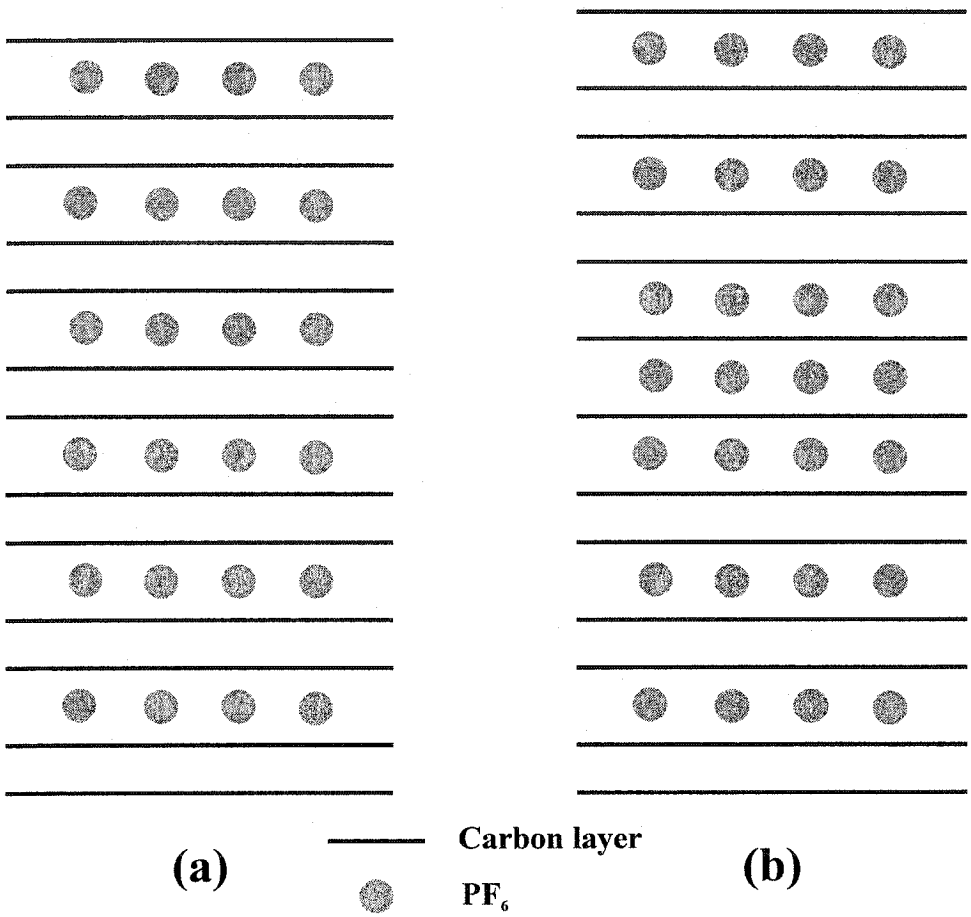

Figure 7.3.12 (a) Illustrating stage 2; (b) illustrating an average stage index slightly less than 2.

These phase diagrams also illustrate the, sometimes, wide range in which more than one stage is present, specifically the potential and specific capacity range where stage 1 and stage 2 co-exist. These results are summarized in Table 7.3. It can be seen fairly easily that the ranges for this co-existence of stages is very similar for the two more ordered samples, XP3C 2600°C and 2300°C. This is not surprising since, visually, the *in-situ* X-ray diffraction patterns were very similar. The less ordered sample has potential and specific capacity ranges during charge that are very similar to those of the more ordered samples. The main difference comes with the discharge ranges, the potential range is not only lower in value but also broader, from about 0.20 V for the

more ordered samples to 0.35 V for the XP3 1800°C sample. The discharge capacity range for XP3 1800°C is higher in value, most likely due to some electrolyte decomposition. The width of these ranges increases slightly as the disorder of the sample increases, from about 17 mAh/g for XP3 2600°C to 24 mAh/g for XP3 1800°C. However, this is not a huge difference. There is no definite correlation between how ordered the sample is and the range in which both stage 1 and stage 2 co-exist during charge. During discharge the sample remains in stage 1 until lower potentials are reached for more disordered samples.

XP3 sample	Charge		Discharge	
	Potential range (V)	Capacity range (mAh/g)	Potential range (V)	Capacity range (mAh/g)
2600°C	5.19-5.32	77-108	4.77-4.55	105-88
2300°C	5.24-5.45	77-111	4.79-4.49	107-87
1800°C	5.22-5.32	88-116	4.5-4.15	150-126

Table 7.3 Summarizing the results for the potential and capacity ranges in which both stage 1 and stage 2 are present.

Table 7.4 shows the minimum discharge potential at which PF_6 remains trapped in stage 1. How ordered the sample is effects the potential range at which PF_6 remains trapped in stage 1 after discharge has begun. The potential at which it no longer remains trapped decreases as p increases.

XP3 sample	p	Minimum potential at which PF_6 remains trapped
2600°C	0.15	4.77
2300°C	0.32	4.79
1800°C	0.94	4.5
1500°C	1.0	4.3

Table 7.4 Summarizing the results for the minimum potential for trapping PF_6.

The c-axis spacings for stage 2 and stage 1 and the corresponding PF_6 layer spacing for the four samples studied and shown in Table 7.5. There is no distinct trend in the average PF_6 layer spacing for these samples. The space between the two carbon layers occupied by PF_6 does not seem to be dependent on the amount of disorder present in the carbon sample. Since there is not a huge difference between the PF_6 layer distances for the four samples, this gives support to the rotating carbon layers to accommodate PF_6 suggested earlier in this chapter. If the layers did not rotate, the PF_6 layer distance could be significantly larger for the more disordered samples than for the more ordered ones. This is not in fact the case which suggests that the layers rotate in the more disordered samples, especially, making them more like the ordered samples, at least locally around PF_6.

XP3 sample (°C)	**d_{002} spacing (Å)**	**stage 2 d-spacing (Å)**	**stage 2 anion layer spacing (Å)**	**stage 1 d-spacing (Å)**	**average anion layer (Å)**
2600	3.36	11.25	7.89	7.90	7.89
2300	3.37	11.23	7.86	7.86	7.85
1800	3.42	11.30	7.88	7.92	7.90
1500	3.43	N/A	N/A	7.86	7.86

Table 7.5 The d-spacings for the four XP3 samples intercalated with PF_6.

The three different XP3 coke samples achieved stage 1 and stage 2 at different potentials and different specific capacities. From this information the amount of PF_6 that has intercalated per carbon atom of the material can be determined or likewise the number of carbon atoms per intercalated PF_6 can be obtained. If the number of carbons per PF_6 is known the theoretical specific capacity can be determined by using the following equation:

$$\text{Theorecitcal spec. cap.} = \frac{96500 \frac{C}{mole}}{3.6 \frac{C}{mAh} * 12 \frac{g}{mole} * \text{number of C}} \tag{7.3}$$

For instance if there were 12 carbons per PF_6 then the expected specific capacity would be 186 mAh/g. The exact expected number of carbons is not known but these can be calculated from the experimental specific capacities. Table 7.6 shows the specific capacities and the number of carbons required for stage 1 and stage 2 for the XP3 coke samples studied.

XP3 Coke Sample	Stage 1		Stage 2	
	Spec. Cap. (mAh/g)	x in PF_6C_x	Spec. Cap. (mAh/g)	x in PF_6C_x
1800°C	135	16.5	70	31.9
2300°C	125	17.9	56	39.9
2600°C	140	16.0	55	40.6

Table 7.6 Number of carbons per PF_6 required to obtain the experimental specific capacities for the three higher temperature XP3 Coke samples.

For stage 1 if the composition of the stage was to be expressed as $(PF_6)_xC$ then all samples would have $x \approx 0.06$, and for stage 2, $x \approx 0.03$. The amount of PF_6 present in stage 1 for the XP3 1800°C sample is about twice that present in stage 2 which is expected. However, for the two higher temperature samples, stage 1 holds slightly more than twice the amount of PF_6 that stage 2 holds. This may be due to a reordering within an intercalated layer to accommodate more PF_6.

Section 7.4 Determining the Stage

It has been assumed that the stage with a c-axis spacing of ~8 Å is stage 1 and that with a c-axis spacing of ~11.4 Å is stage 2. In order to show that this is indeed a correct assumption, *ex-situ* X-ray diffraction experiments were performed. The data was analyzed and then the intensity calculation program discussed in Chapter 4, Section 4, was used to determine the actual stage number and various parameters of the intercalated compound.

The XP3 coke sample heated to 2600°C was used in these experiments. The electrolyte was 2M $LiPF_6$/EMS and the counter electrode was lithium metal. Two *ex-situ* X-ray diffraction experiments were performed. The stage 1 experiment shall be discussed first.

The stage 1 electrochemical cell was charged to a potential of 5.5 V and removed from the charging system. This resulted in a specific capacity of approximately 140 mAh/g. The potential versus specific capacity plot is shown in Figure 7.4.1(a). The carbon electrode was placed in an *ex-situ* X-ray holder and the resulting X-ray diffraction pattern is shown in Figure 7.4.1(b). There are six distinct (00ℓ) peaks. The positions and $d_{00\ell}$ spacings and the layer spacings, $d_{00\ell} * \ell$, are shown in Table 7.7. These values have been corrected for an off-axis discrepancy which was found to be 480 microns. The average layer spacing for this stage is 8.024 ± 0.002 Å.

There are several different possible orientations of the PF_6 molecule, which are illustrated in Figure 7.4.2. These orientations, considering only the z-axis distances, are: (a) three fluorine atoms above and below the phosphorous atom, denoted 3F-P-3F; (b)

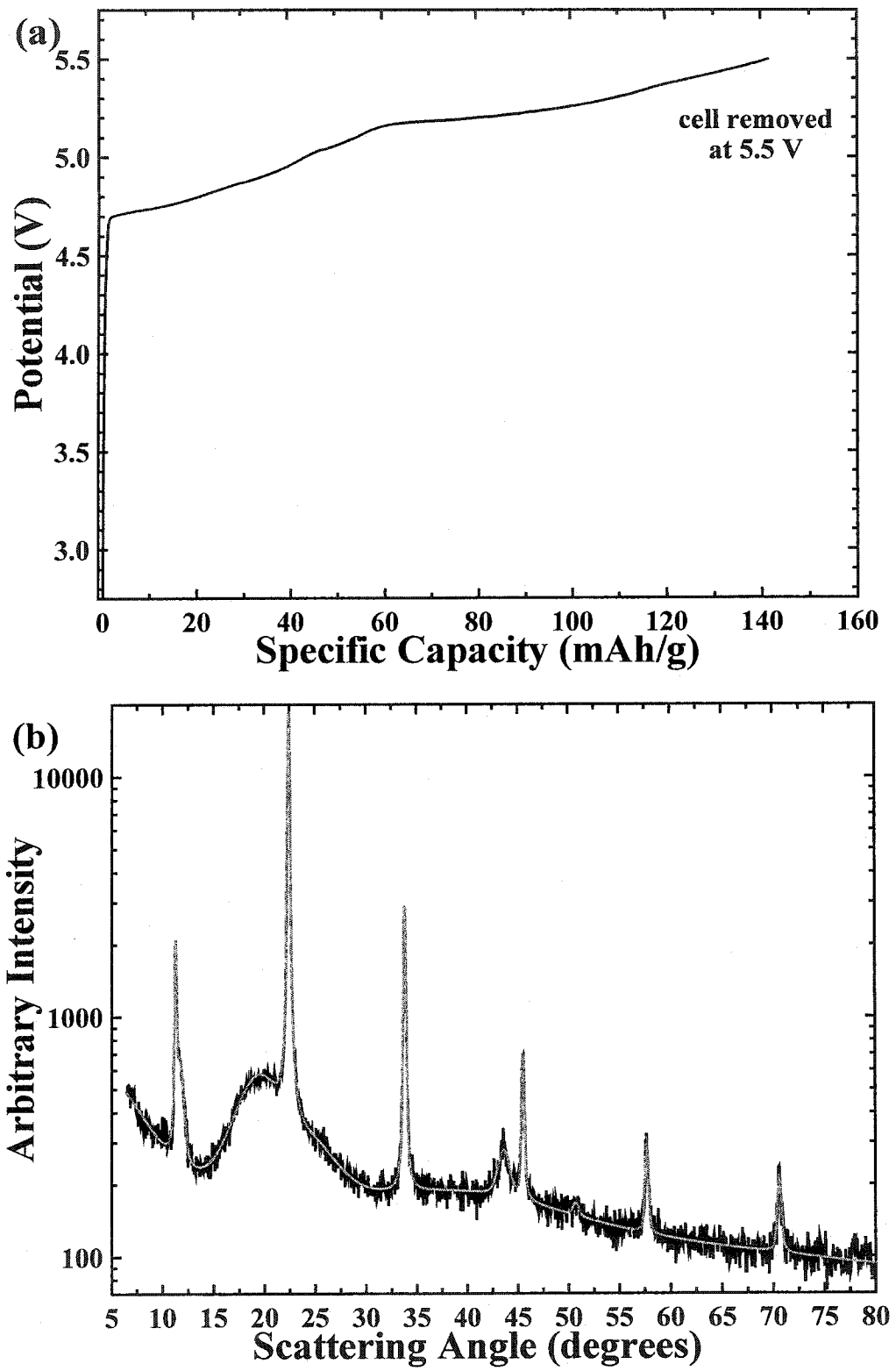

Figure 7.4.1 (a) Potential versus specific capacity; and (b) *ex-situ* X-ray diffraction pattern for XP3 Coke heated to 2600°C in 2M $LiPF_6$/EMS.

two fluorine atoms above and below the phosphorous atom as well as two fluorine atoms along z = 0, 2F-P+2F-2F; (c) one fluorine atom above and below the phosphorous atom and four fluorine atoms at z = 0, F-P+4F-F; and (d) a rotating PF_6 molecule with the fluorine atoms evenly distributed around the outer edge of the sphere, a rotating PF_6.

peak	Position	$d_{00\ell}$ spacing (Å)	$d_{00\ell}*\ell$ (Å)
(001)	11.027°	8.0234	8.0234
(002)	22.157°	4.0118	8.0237
(003)	33.504°	2.6746	8.0237
(004)	45.201°	2.0059	8.0238
(005)	57.421°	1.6047	8.0237
(006)	70.404°	1.3373	8.0237

Table 7.7 (00ℓ) peak information from the *ex-situ* X-ray diffraction pattern for the data shown in Figure 7.4.1.

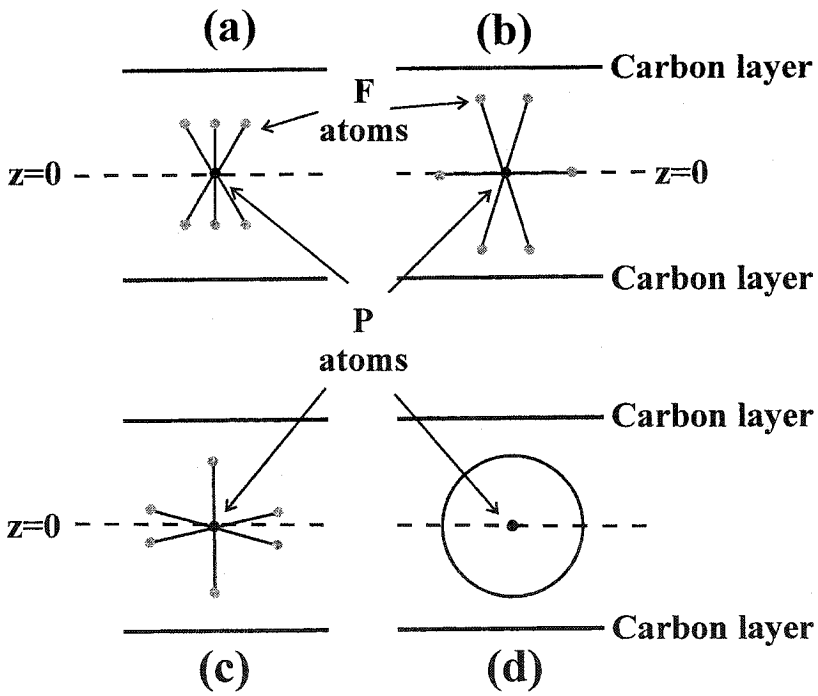

Figure 7.4.2 Different orientations for PF_6. (a) 3F-P-3F, (b) 2F-P+2F-2F, (c) F-P+4F-4; and (d) a rotating PF_6.

The first orientation that will be tried is the 3F-P-3F orientation. A sample contour plot, as described in Chapter 4, is given in Figure 7.4.3. This particular plot assumes that our stage 1 is in fact stage 1. It can be easily seen that there are two regions in which a minimum goodness of fit occurs. Naturally, a fit of zero would be perfect.

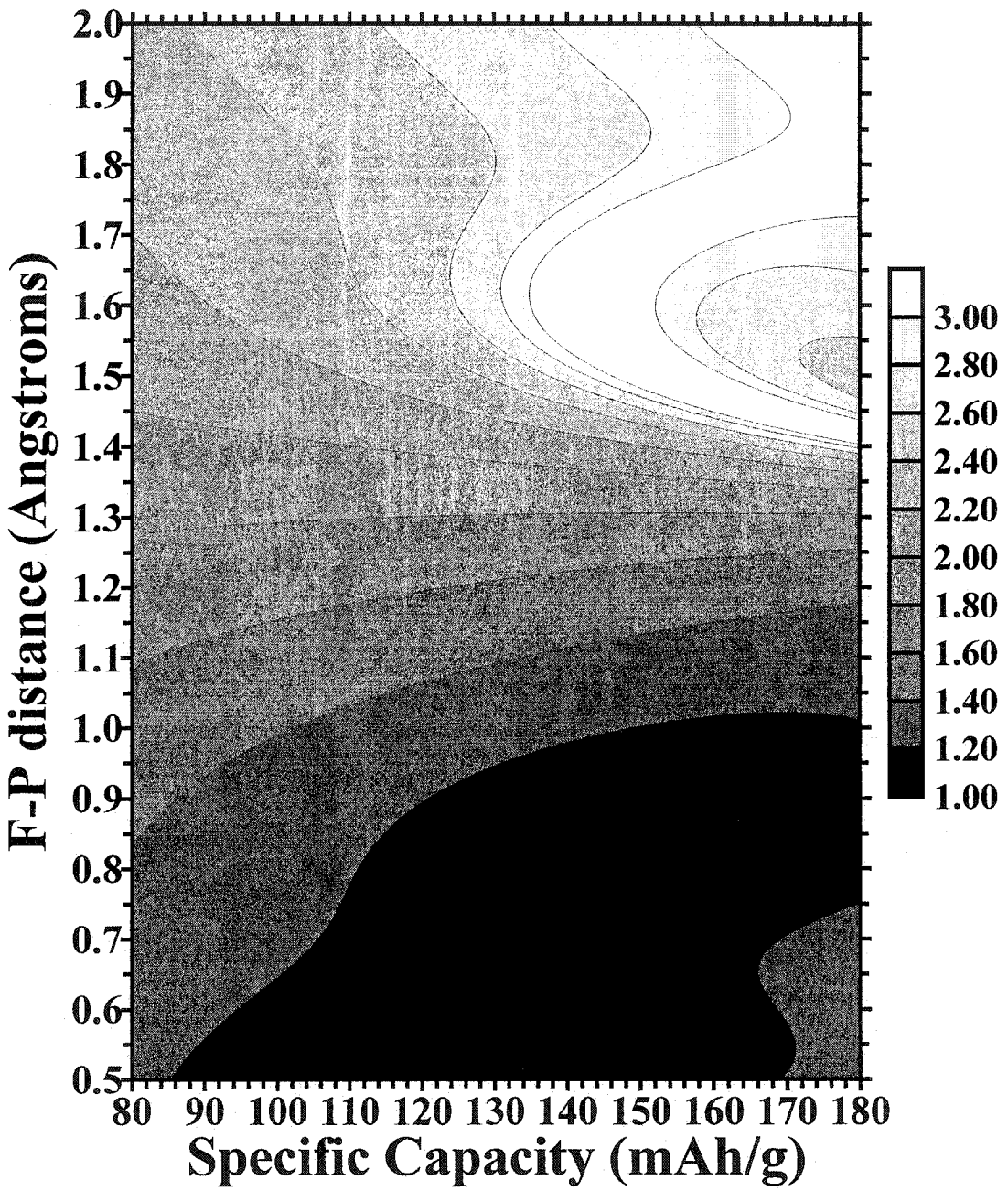

Figure 7.4.3 Initial contour plot of goodness of fit for various values of the specific capacity and the F-P distance for 3F-P-3F, stage 1 as stage 1.

The minimum area was analyzed further to determine the P-F z-axis distance and the specific capacity. The resulting minimum goodness of fit was found to be 1.001 with a P-F z-axis distance of 0.857 Å and a specific capacity of 135 mAh/g. This possibility does not seem very likely since the P-F distance is so small. The X-ray diffraction pattern from this calculation, the gray line, is shown in Figure 7.4.4. The black line in these and all following X-ray diffraction patterns is the experimental data with the background removed. It can be easily seen the (001) peak is too large and the (003) and (006) peaks are too small. This orientation is most likely not the orientation of PF_6, if it is indeed stage 1.

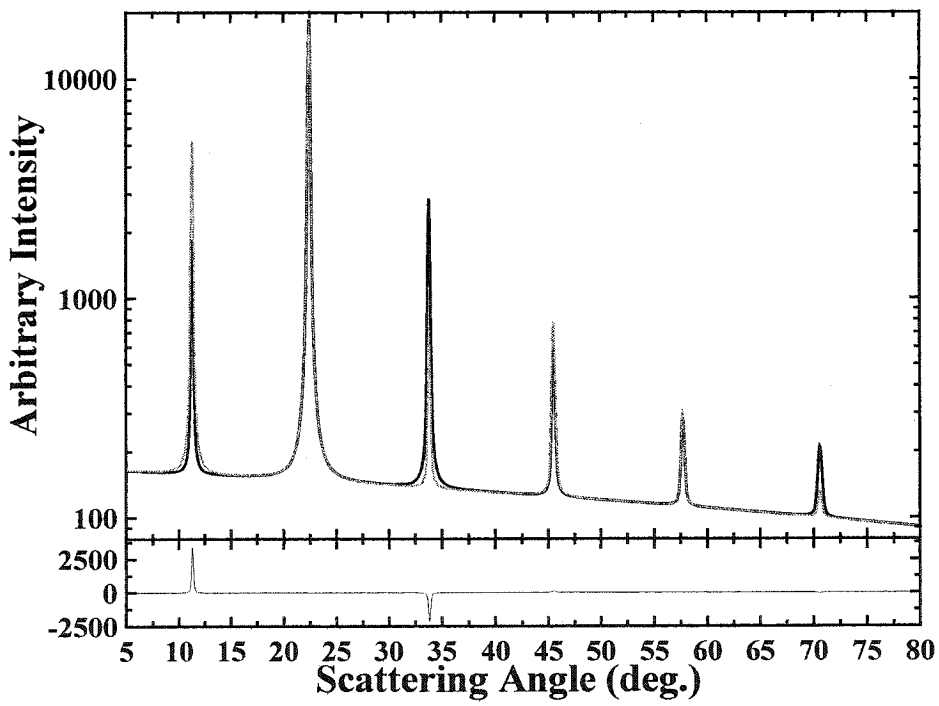

Figure 7.4.4 (top panel) Intensity versus scattering angle for calibrated experimental data, black line, and normalized calculated data, gray line, and (bottom panel) the difference between the experimental and calculated data, for 3F-P-3F, stage 1 as stage 1.

It is possible that this orientation is still valid if it is stage 2 rather than stage 1. The overall c-axis spacing will be the same, of course, but the layer occupied by PF_6 would be smaller, see Figure 7.4.5.

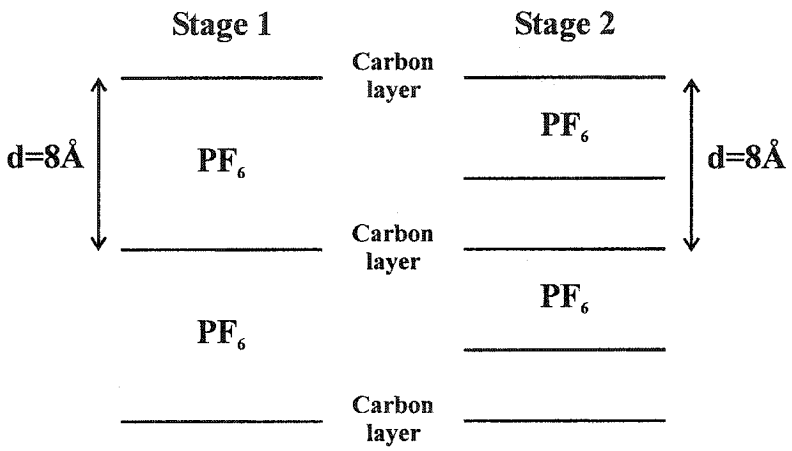

Figure 7.4.5 Illustrating the difference between the stage 1 and stage 2 possibility with the same c-axis spacing.

If the staged phase with a d-spacing of ~8 Å is in fact stage 2, this would mean that the anion layer spacing, assuming a C-C spacing of about 3.4 Å would be about 4.6 Å. This value is quite small. If one considers the geometry of PF_6, the known C-C bond length (~1.4 Å), the P-F bond length(~1.6 Å), and the appropriate ionic radii, it can be determined whether PF_6 can indeed fit between two graphite layers that ~4.6 Å apart [58]. If the intercalated PF_6 is orientated such that three fluorine atoms are above and below the phosphorous atom, it does indeed fit in between two carbon layers with the fluorine atoms nesting into the empty carbon rings, see Figure 7.4.6 [58]. It is interesting to note that the two graphite layers are in the standard AB stacking arrangement of graphitic carbon.

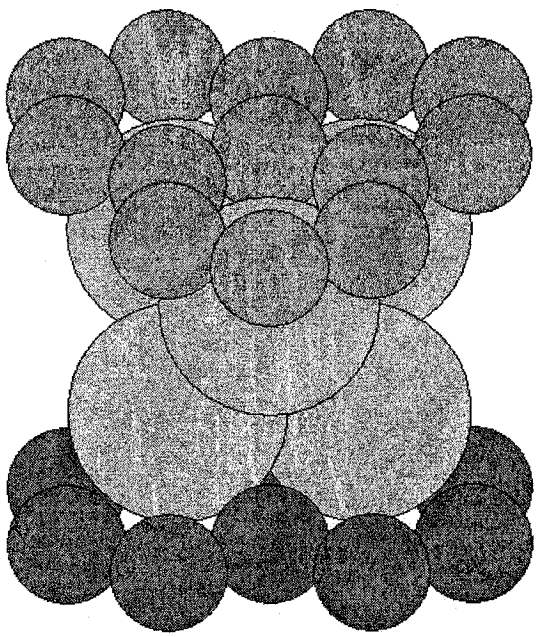

Figure 7.4.6 A view of the PF_6 molecule located between carbon planes (AB stacking) spaced 4.6 Å apart. The small dark and medium gray spheres represent the carbon atoms and the large light gray spheres represent the fluorine atoms. Note that the phosphorous atom is not visible.

For comparison with stage 1, a contour plot of a stage 2 calculation with the capacity fixed at 140 mAh/g is shown in Figure 7.4.7. There are various minimum areas, some with much lower values than others. This contour plot has a different topographical layout than the one for stage 1.

After minimizing the goodness of fit, the specific capacity was found to be 200 mAh/g and the distance parameters were 1.779 Å for the F-P distance and 2.661 Å for the C-C z-axis distance. The fit in this case was 0.2936. The X-ray diffraction pattern is shown in Figure 7.4.8. There are still several peaks, which are not in good agreement with the experimental ones. However, the overall goodness of fit is much better for stage 2 than stage 1. Although the (001) peak has a better fit, the (003) peak is still too small as

is the (004) peak. Even though the fit is better suggesting that 3F-P-3F may be the orientation of PF_6, the fact that the C-C distance is so small means that it is most likely not possible. Some compression of the experimental C-C distance, of 3.36 Å is possible but a compression of over 20% is not very likely.

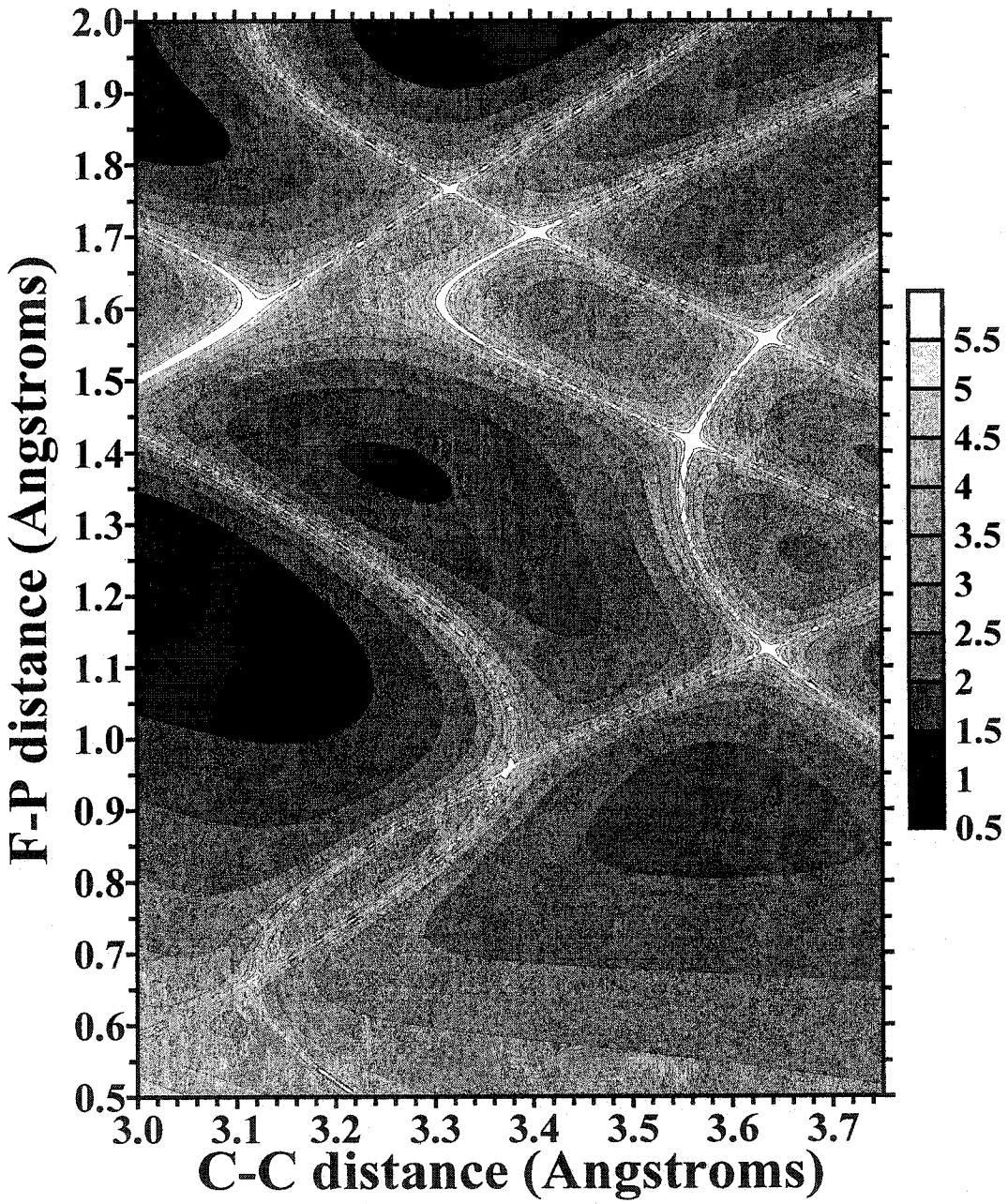

Figure 7.4.7 Initial contour plot of goodness of fit for various values of the C-C distance and the F-P distance for 3F-P-3F, stage 1 as stage 2.

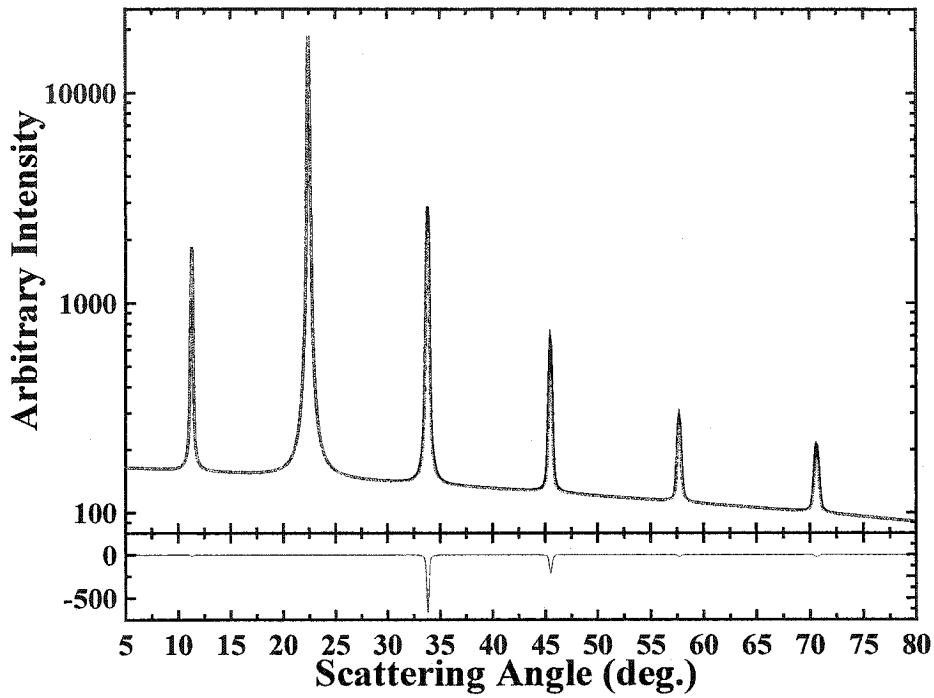

Figure 7.4.8 (top panel) Intensity versus scattering angle for calibrated experimental data, black line, and normalized calculated data, gray line, and (bottom panel) the difference between the experimental and calculated data, for 3F-P-3F, stage 1 as stage 2.

The X-ray diffraction patterns for stage 1 and stage 2 fits for 2F-P+2F-2F are shown in Figures 7.4.9 and 7.4.10, respectively. For stage 1 the goodness of fit obtained was 0.3213 with a specific capacity of 178.5 mAh/g which is higher than the experimental value of 140 mAh/g. The F-P distance was determined to be 0.968 Å. The goodness of fit for stage 2 was 0.2070 which is better. The C-C distance was 3.331 Å and the F-P distance was 1.326 Å. Both distances are reasonable; however, the specific capacity needed for this particular fit was only 90 mAh/g. This value is substantially lower than the experimental value. Although some loss of capacity during the removal of the electrode from the cell and placement into the *ex-situ* holder can be expected, a loss of nearly 35% is not.

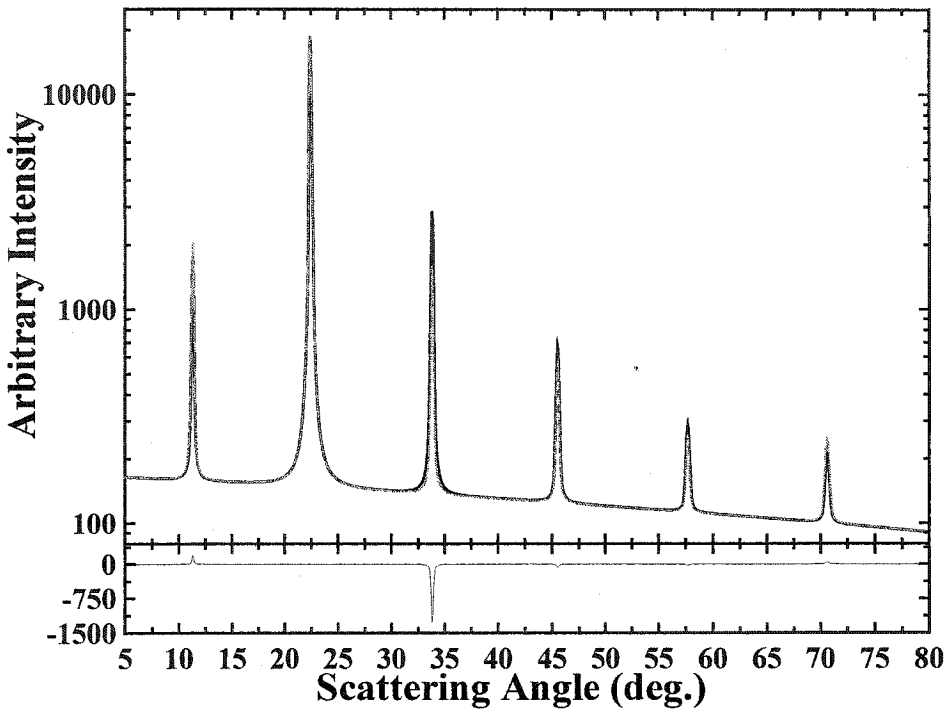

Figure 7.4.9 (top panel) Intensity versus scattering angle for calibrated experimental data, black line, and normalized calculated data, gray line, and (bottom panel) the difference between the experimental and calculated data, for 2F-P+2F-2F, stage 1 as stage 1.

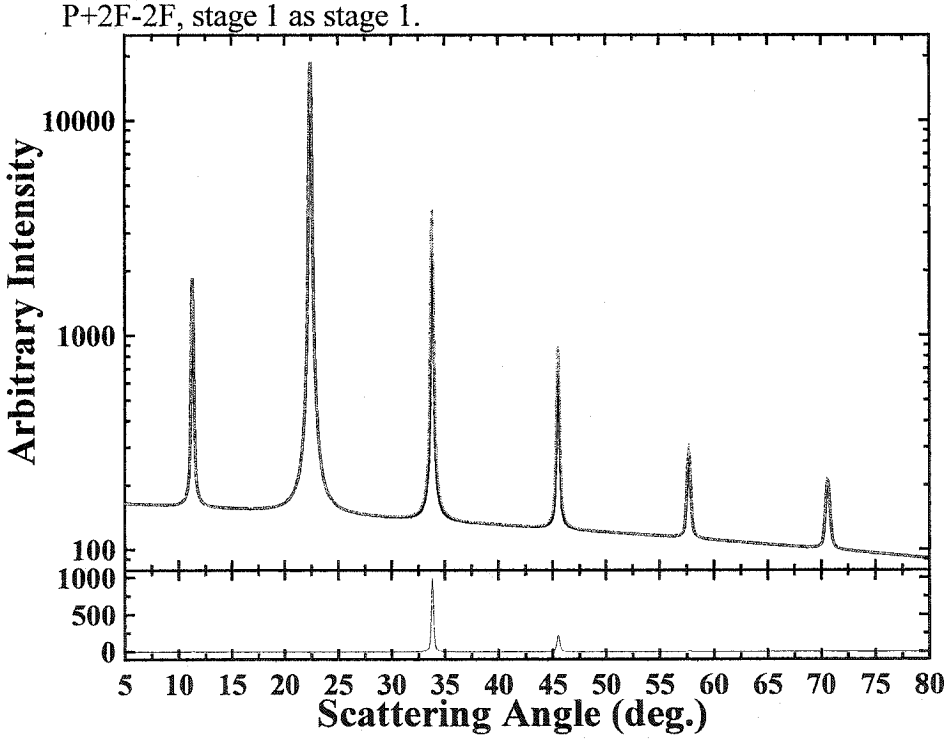

Figure 7.4.10 (top panel) Intensity versus scattering angle for calibrated experimental data, black line, and normalized calculated data, gray line, and (bottom panel) the difference between the experimental and calculated data, for 2F-P+2F-2F, stage 1 as stage 2.

The differences between these two calculations can be seen qualitatively in Figures 7.4.9 and 7.4.10. With the stage 1 calculation, there is one peak, the (003) peak, which has a very poor fit. With stage 2, this (003) peak is fit slightly better but the (004) peak does not agree with experiment as well as it did with stage 1.

The next orientation tested was F-P+4F-F. The X-ray diffraction pattern for the stage 1 calculation is shown in Figure 7.4.11. It can be seen quite easily that this is not a good fit. The fit of the (001) peak is particularly poor. In fact, the best goodness of fit determined was 1.12 with a specific capacity of 119 mAh/g and an F-P distance of 0.908 Å. The fit for stage 2 is no better, see Figure 7.4.12. Although the (001) peak seems to have been fit better, the (003) and (004) peaks are much worse. The best goodness of fit for stage 2 was found to be 0.8132 with a specific capacity of 70 mAh/g, a C-C distance of 3.36 Å and a F-P distance of 1.355 Å. It is clear to say that F-P+4F-F is not the orientation of the intercalated PF_6 atom.

The last possible orientation is a rotating PF_6 molecule. The X-ray diffraction patterns for stage 1 and stage 2 fits are shown in Figures 7.4.13 and 7.4.14, respectively. It is easily seen that the fit for stage 1 is better than for stage 2. In fact stage 1 has a goodness of fit of 0.3408 with 1.492 Å for the F-P distance and a specific capacity of 184.5 mAh/g. The fit for stage 2 has an F-P distance of 2.196 Å and a C-C distance of 3.182 Å and a specific capacity of 115 mAh/g with a goodness of fit of 0.5985. In both cases the (003) is really the only peak with a major problem. For stage 1 this peak is too small but for stage 2 it is too large and by a larger amount. Also for stage 2, the (005) peak is too large as well. Since the F-P distance for stage 2 is so large and the specific

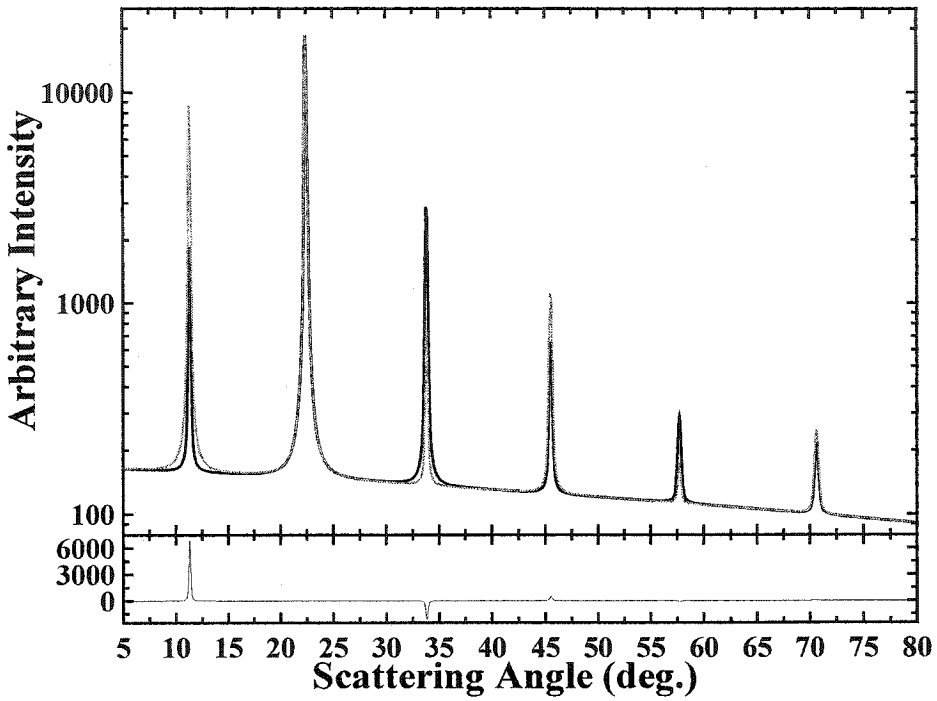

Figure 7.4.11 (top panel) Intensity versus scattering angle for calibrated experimental data, black line, and normalized calculated data, gray line, and (bottom panel) the difference between the experimental and calculated data, for F-P+4F-F, stage 1 as stage 1.

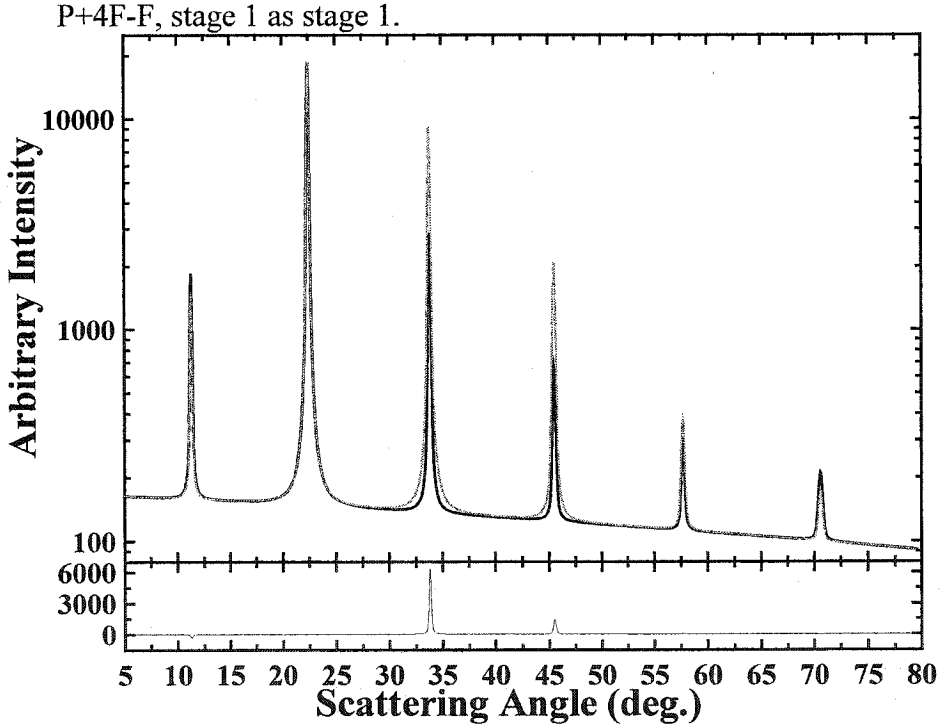

Figure 7.4.12 (top panel) Intensity versus scattering angle for calibrated experimental data, black line, and normalized calculated data, gray line, and (bottom panel) the difference between the experimental and calculated data, for F-P+4F-F, stage 1 as stage 2.

capacity so low, the possibility that this stage is stage 2 is not very likely. If rotating PF_6 is a possible orientation the stage 1 is the more likely possibility.

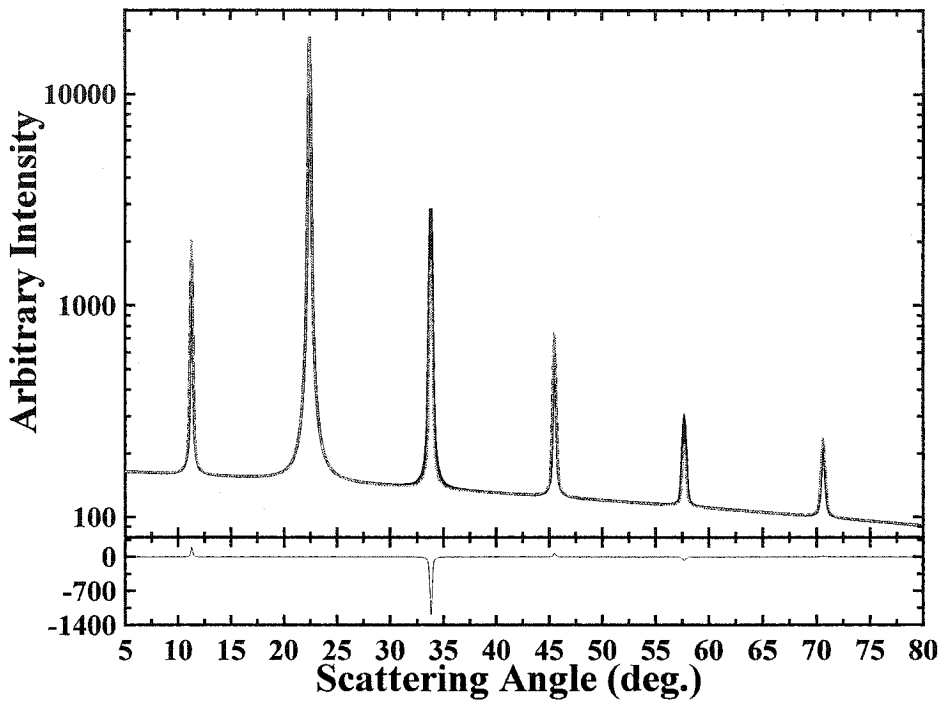

Figure 7.4.13 (top panel) Intensity versus scattering angle for calibrated experimental data, black line, and normalized calculated data, gray line, and (bottom panel) the difference between the experimental and calculated data, for rotating PF_6, stage 1 as stage 1.

Table 7.8 summarizes the results for stage 1 calculations and Table 7.9 summarizes the results for stage 2 calculations. It is not definite that the sample is indeed stage 1 and not stage 2, although stage 1 is more likely. For the two calculations with a goodness of fit <0.5, the specific capacities are larger than the experimental specific capacity. This can be an artifact of co-intercalation of the solvent. This is something that needs to be investigated further. For stage 2 all orientations, except the 3F-P-3F orientation, have specific capacities lower than the experimental capacity. A lower value is possible but not by such a large amount, nearly 30%. The 3F-P-3F sample has a goodness of fit <0.5 and a specific capacity higher than the experimental value but since

the C-C distance is so small this stage 2 orientation is not very likely. It cannot be stated conclusively which orientation fluorophosphate assumes within the carbon layers.

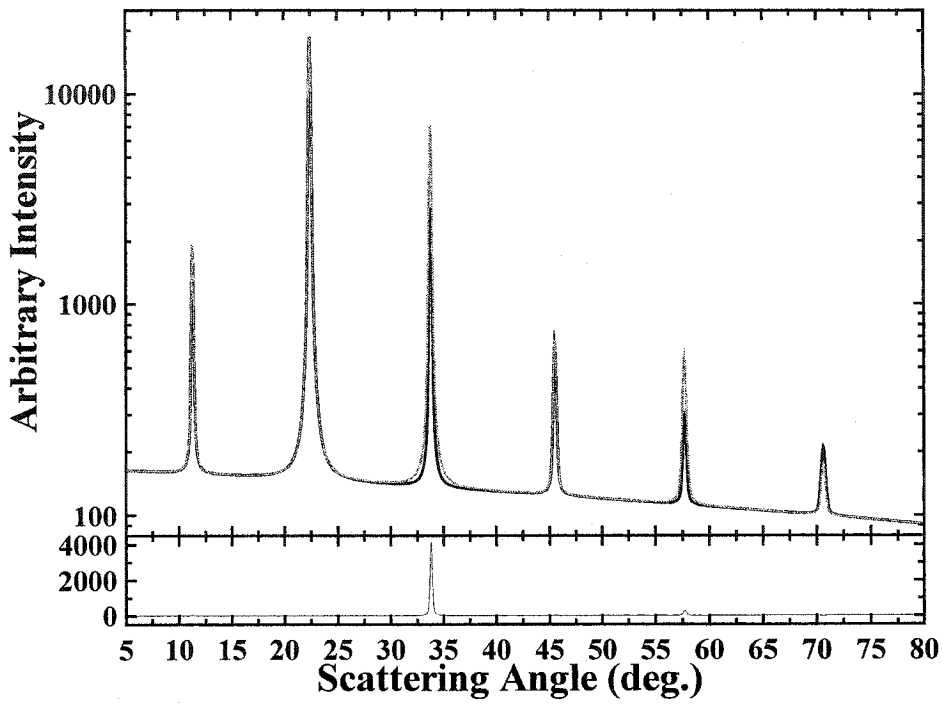

Figure 7.4.14 (top panel) Intensity versus scattering angle for calibrated experimental data, black line, and normalized calculated data, gray line, and (bottom panel) the difference between the experimental and calculated data, for rotating PF_6, stage 1 as stage 2.

Orientation	Fit	Capacity (mAh/g)	F-P distance (Å)
3F-P-3F	1.001	135	0.857
2F-P+2F-2F	0.3213	178.5	0.968
F-P+4F-F	1.12	119	0.908
rotating PF_6	0.3408	184.5	1.492

Table 7.8 Results of stage 1 as stage 1 calculations for PF_6 for the various orientations tested.

Orientation	Fit	Capacity (mAh/g)	C-C distance (Å)	F-P distance (Å)
3F-P-3F	0.2936	200	2.661	1.779
2F-P+2F-2F	0.2070	90	3.331	1.326
F-P+4F-F	0.8132	70	3.36	1.355
rotating PF_6	0.5985	115	3.182	2.196

Table 7.9 Results of stage 1 as stage 2 calculations for PF_6 for the various orientations tested.

The two possible orientations are 2F-P+2F-2F and a rotating PF_6 ion. Since in both of these fits, for stage 1 as stage 1, the specific capacity is higher than the actual experimental value, these two orientations need to be investigated further by considering co-intercalation of EMS.

A diagram of the solvent, EMS, is shown in Figure 7.4.15. This molecule was treated as if it was rotating about the sulfur atom and the hydrogen atoms were ignored in the calculations. Three different spheres for the carbon atoms were used and one was used for the oxygen atoms.

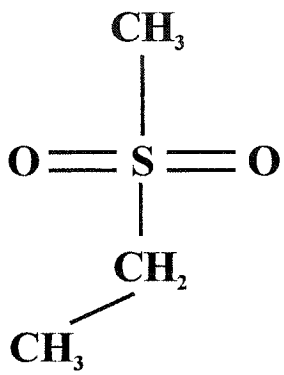

Figure 7.4.15 Diagram of EMS.

The X-ray diffraction patterns for 2F-P+2F-2F and rotating PF_6 are shown in Figures 7.4.16 and 7.4.17, respectively. The best goodness of fits obtained were actually with an EMS fraction of zero, i.e., the results without any co-intercalation of the solvent. However, comparable goodness of fits were obtained at the experimental specific capacity of 140 mAh/g. These results are really not very different from the results without EMS. The goodness of fit for 2F-P+2F-2F is 0.3628 with an F-P distance of 0.962 Å and an EMS fraction of 0.370 per PF_6 molecule. The goodness of fit for the rotating PF_6 is 0.4047 with an F-P distance of 1.465 Å and an EMS fraction of 0.401. In both cases the (003) peak is too small and the (001) peak is too large. Again, it is inconclusive as to which orientation the PF_6 assumes.

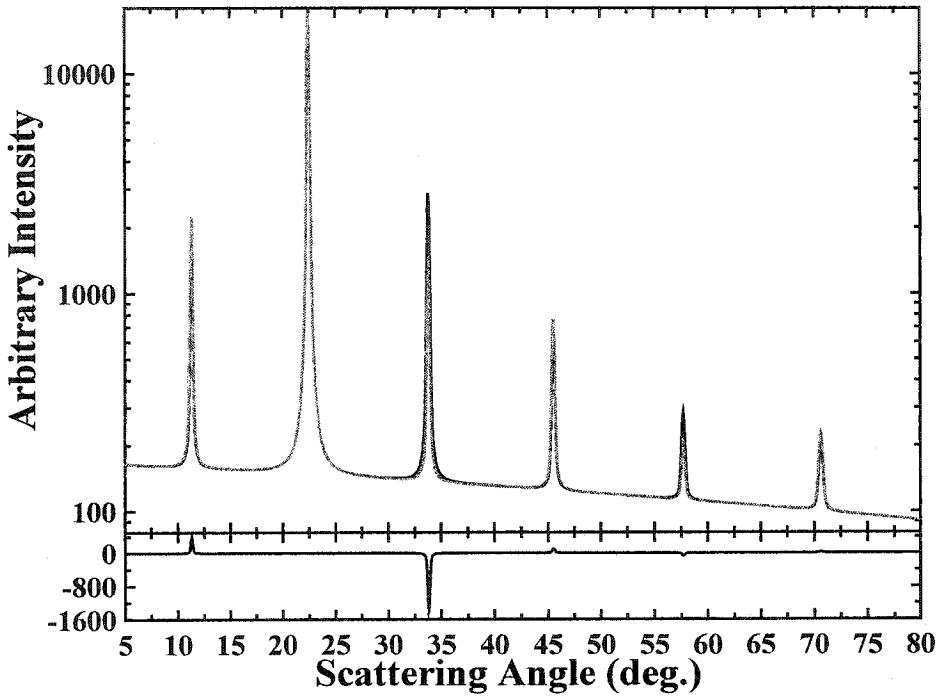

Figure 7.4.16 (top panel) Intensity versus scattering angle for calibrated experimental data, black line, and normalized calculated data, gray line, and (bottom panel) the difference between the experimental and calculated data, for addition of EMS for 2F-P+2F-2F, stage 1 as stage 1.

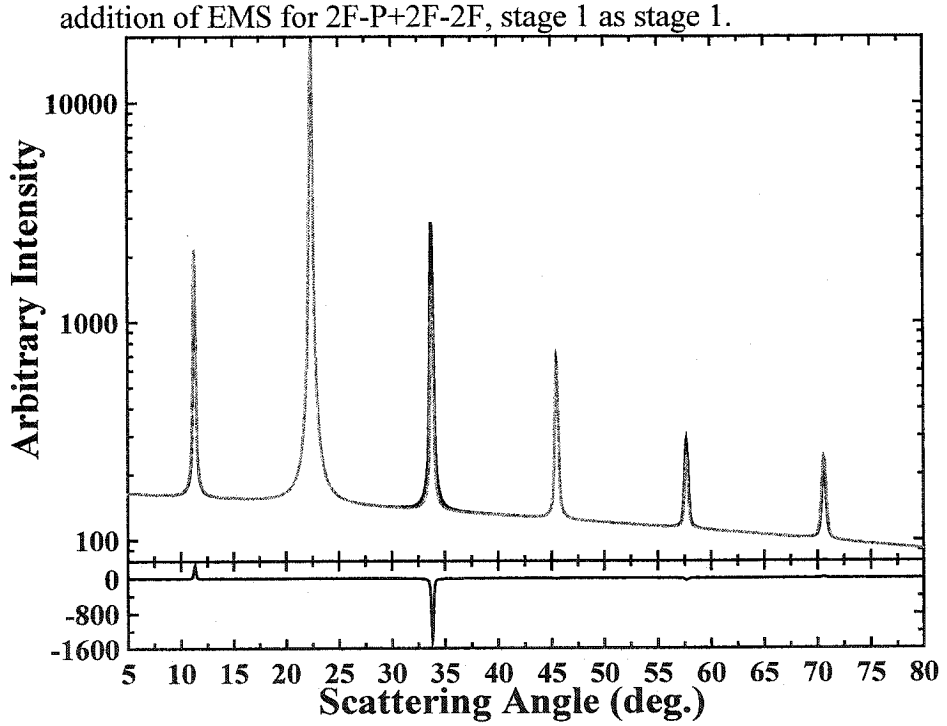

Figure 7.4.17 (top panel) Intensity versus scattering angle for calibrated experimental data, black line, and normalized calculated data, gray line, and (bottom panel) the difference between the experimental and calculated data, for addition of EMS for rotating PF_6, stage 1 as stage 1.

The results for the EMS calculations can be found in Table 7.10. Since the F-P distance for the rotating PF_6 is closer to the bond length of P-F, it is believed that this orientation is more likely. To investigate this possibility further stage 2, or at least what is believed to be stage 2, will be investigated next.

Orientation	Fit	Capacity (mAh/g)	F-P distance (Å)	EMS fraction
2F-P+2F-2F	0.3628	140	0.962	0.370
rotating PF_6	0.4047	140	1.465	0.401

Table 7.10 Results of stage 1 as stage 1 calculations with EMS for PF_6 for the various orientations tested.

For stage 2, the carbon electrode was composed of XP3 Coke 2600°C, the electrolyte was 2M $LiPF_6$/EMS and the counter/reference electrode was lithium metal. The electrochemical coin cell was charged to 5.14 V before being removed and placed in an *ex-situ* holder. Potential versus specific capacity is shown in Figure 7.4.18(a). The specific capacity obtained was 67 mAh/g. The resulting X-ray diffraction pattern is shown in Figure 7.4.18(b). Seven distinct (00ℓ) peaks are visible. The positions and $d_{00\ell}$ spacing of these peaks that are given in Table 7.11 have been corrected for off-axis discrepancies, about 170 microns. The average c-axis spacing is 11.433 ± 0.005 Å. It is interesting to note that the (002) and (005) peaks are not visible. These peaks must be very weak.

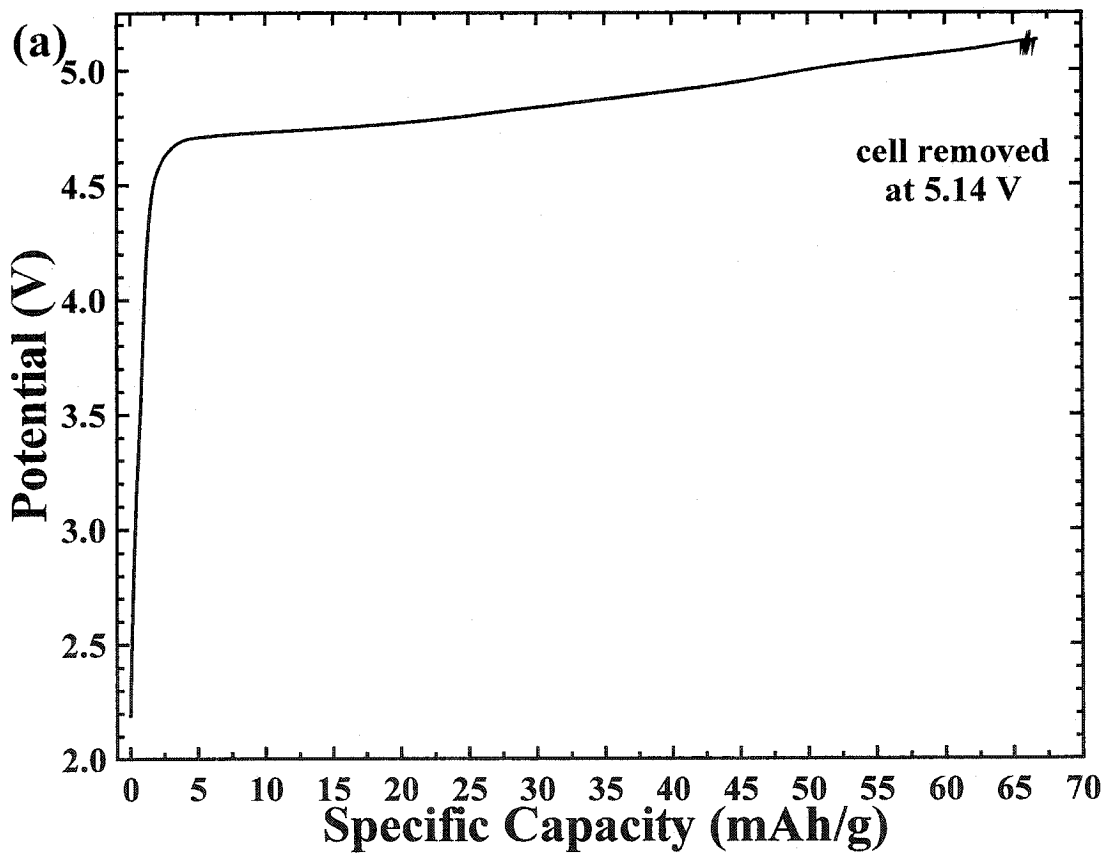

Figure 7.4.18 (a) Potential versus specific capacity for *ex-situ* X-ray diffraction experiment of XP3 Coke heated to 2600°C removed at 5.15 V.

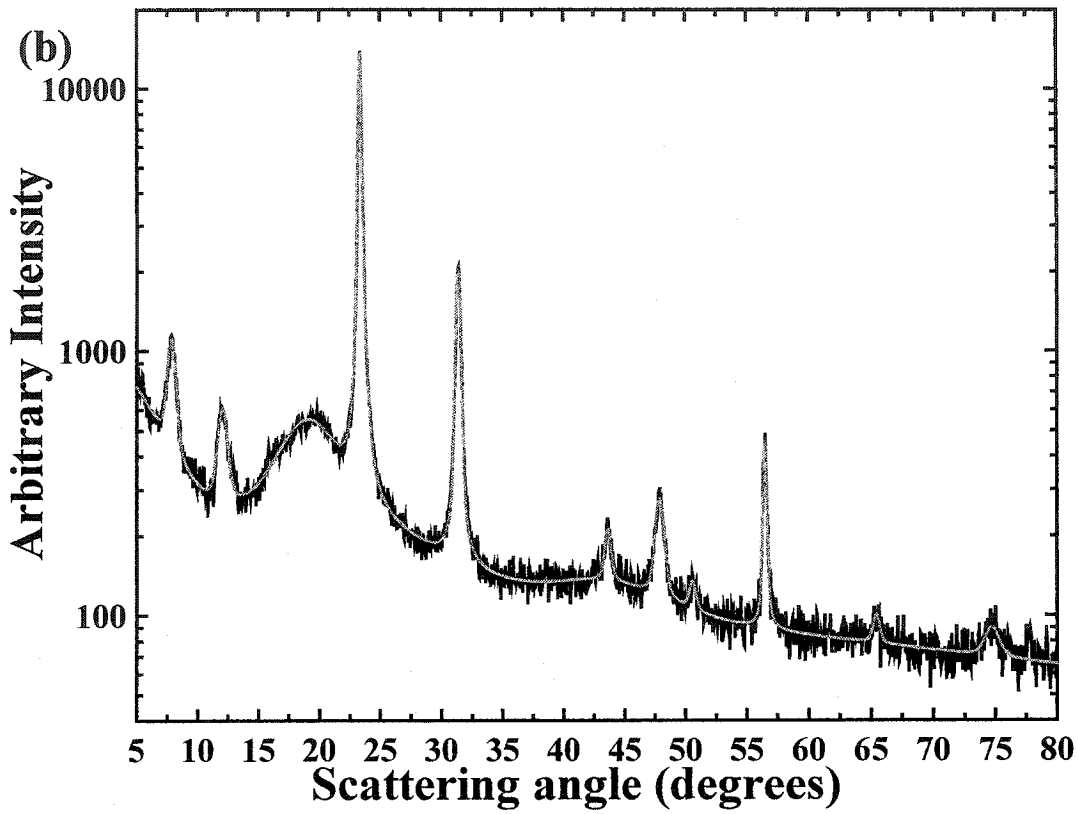

Figure 7.4.18 (b) X-ray diffraction pattern for *ex-situ* X-ray diffraction experiment of XP3 Coke heated to 2600°C removed at 5.15 V.

Peak	Position	$d_{00\ell}$ spacing (Å)	$d_{00\ell}$ x ℓ (Å)
(001)	7.733°	11.432	11.4321
(003)	23.341°	3.8256	11.4328
(004)	31.294°	2.8592	11.4329
(006)	47.728°	1.9032	11.4328
(007)	56.328°	1.6316	11.4328
(008)	65.289°	1.4284	11.4328
(009)	74.725°	1.2715	11.4327

Table 7.11 (00ℓ) peaks information from the *ex-situ* X-ray diffraction pattern for the data shown in Figure 7.4.17

As with the stage 1 sample, four different orientations have been investigated. The first orientation used was 3F-P-3F. The X-ray diffraction pattern obtained from the best goodness of fit for this particular orientation is shown in Figure 7.4.19. It is easily seen that the fit is not that great. The (001) peak is substantially larger than the experimental

one, as are the (004) and the (007) peaks, also the (009) peak is too small. The goodness of fit obtained was 1.327 with a specific capacity of 68 mAh/g with a C-C z-axis distance of 3.326 Å and an F-P z-axis distance of 0.837 Å. Although the specific capacity is about that of the experiment and the C-C and F-P distances are reasonable the fit is very poor. Since the fit is so poor this particular orientation is definitely not the orientation PF_6 assumes once it is intercalated into the carbon electrode if this stage is indeed stage 2.

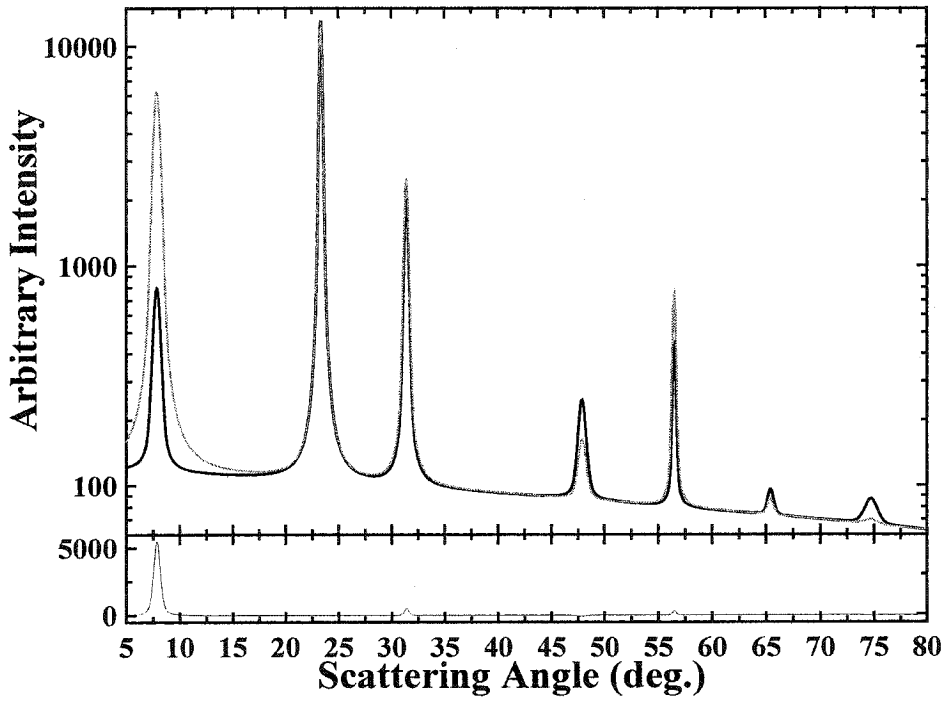

Figure 7.4.19 (top panel) Intensity versus scattering angle for calibrated experimental data, black line, and normalized calculated data, gray line, and (bottom panel) the difference between the experimental and calculated data, for 3F-P-3F, stage 2 as stage 2.

Figure 7.4.20 shows two X-ray diffraction patterns obtained from two very similar fits for the 2F-P+2F-2F orientation. The two goodness of fits are 0.710 and 0.659. The first fit, shown in Figure 7.4.20(a), has a specific capacity of 80 mAh/g, a C-C distance of 3.418 Å and an F-P distance of 1.030 Å. Figure 7.4.20(b) shows the second fit which has a similar specific capacity of 78 mAh/g, a C-C distance of 3.434 Å and an F-P distance of 0.952 Å. The worst fitting peak is the (001) peak. As with "stage 1"

experiments, the specific capacity is higher than the experimental value suggesting that EMS is intercalating along with the PF_6 molecule.

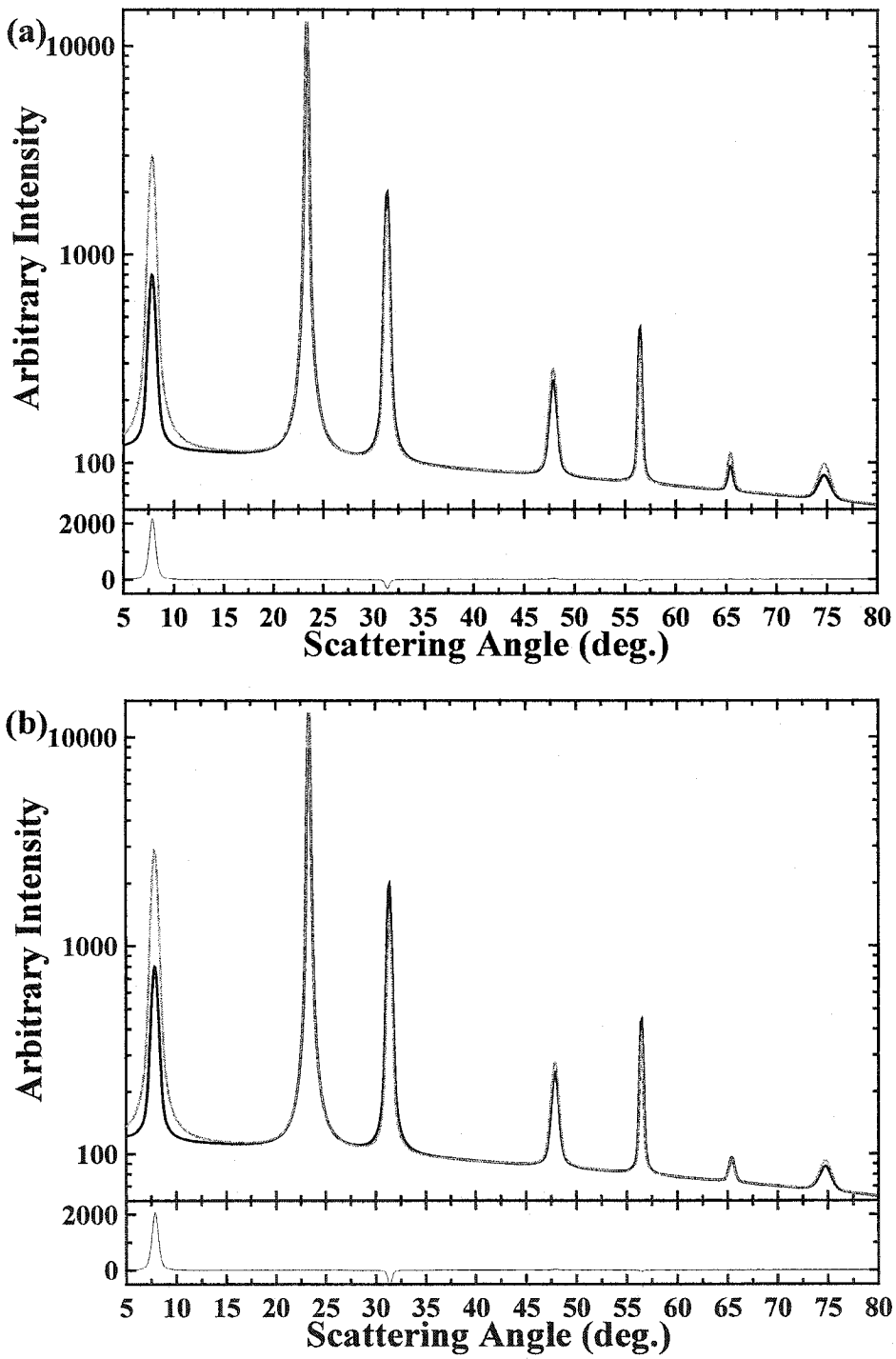

Figure 7.4.20 (top panels) Intensity versus scattering angle for calibrated experimental data, black line, and normalized calculated data, gray line, and (bottom panels) the difference between the experimental and calculated data, for 2F-P+2F-2F, stage 2 as stage 2.

The next orientation, F-P+4F-F, achieved a poor goodness of fit of 1.511, which is easily seen in the X-ray diffraction pattern shown in Figure 7.4.21. The (001), (004) and (007) and quite a bit smaller than they should be and the (006) and (009) peaks are too large. The specific capacity obtained was 90 mAh/g with a C-C distance of 3.638 Å and an F-P distance of 1.209 Å. This orientation is definitely not the correct one.

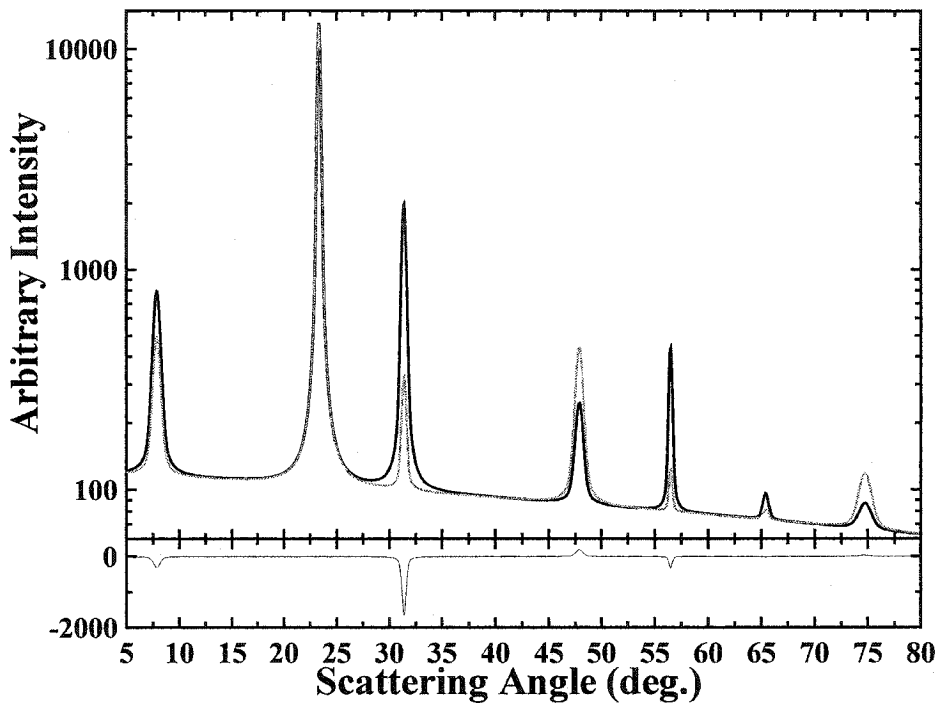

Figure 7.4.21 (top panel) Intensity versus scattering angle for calibrated experimental data, black line, and normalized calculated data, gray line, and (bottom panel) the difference between the experimental and calculated data, for F-P+4F-F, stage 2 as stage 2.

The final orientation, a rotating PF_6, had two somewhat reasonable goodness of fits of 0.515 and 0.590. The X-ray diffraction patterns for these fits are shown in Figure 7.4.22(a) and (b), respectively. Both fits have a (001) peak that is too large and a (004) peak that is too small. The resulting specific capacities were 92 mAh/g and 90 mAh/g. The C-C distance, for the first fit, was determined to be 3.445Å and the F-P distance was

1.646 Å. The second fit had a C-C distance of 3.446 Å and an F-P distance of 1.611 Å. Again, the specific capacity is higher than the experimental value.

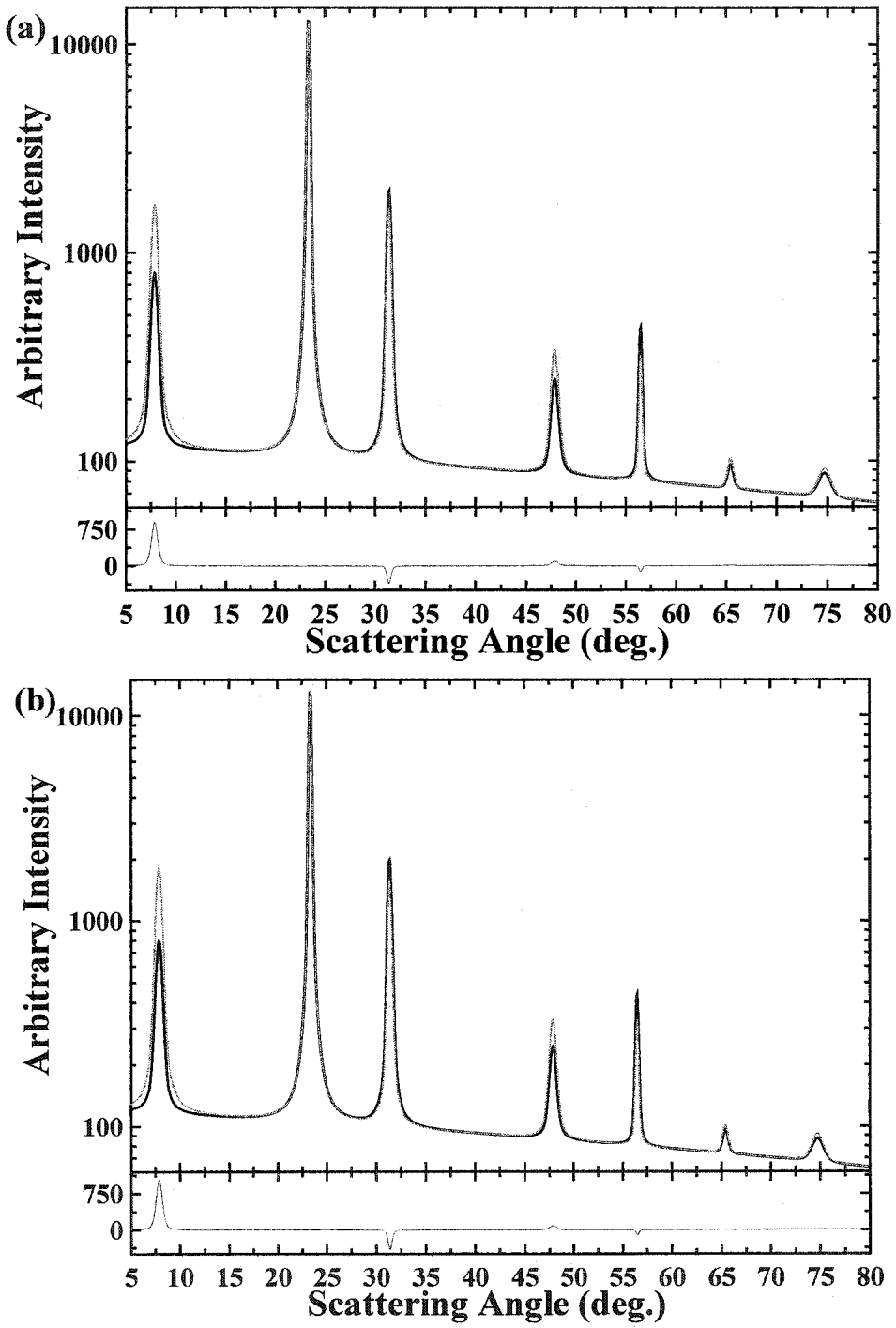

Figure 7.4.22 (top panels) Intensity versus scattering angle for calibrated experimental data, black line, and normalized calculated data, gray line, and (bottom panels) the difference between the experimental and calculated data, for rotating PF_6, stage 2 as stage 2.

The results for these four orientations are shown in Table 7.12. Since the specific capacities are higher than the experimental capacity, as with stage 1, calculations that include EMS should be performed.

Orientation	fit	capacity (mAh/g)	C-C distance (Å)	F-P distance (Å)
3F-P-3F	1.327	68	3.326	0.837
2F-P+2F-2F	0.710	80	3.418	1.030
	0.659	78	3.434	0.952
F-P+4F-F	1.511	90	3.638	1.09
Rotating PF_6	0.515	92	3.445	1.646
	0.590	90	3.446	1.611

Table 7.12 The results of the stage 2 as stage 2 calculations for PF_6 for the various orientations tested.

The X-ray diffraction patterns, for the calculations with EMS, are shown in Figures 7.4.23 and 7.4.24 for the 2F-P+2F-2F and rotating PF_6, respectively. Qualitatively, the rotating PF_6 orientation has a better fit since the (001) peak has a better fit. For both orientations the (004) has a poor fit. For 2F-P+2F-2F, better goodness of fits were obtained with smaller specific capacities, for example a goodness of fit of 0.5895 was obtained with a specific capacity of 50 mAh/g, a C-C distance of 3.422 Å, an F-P distance of 0.939 Å, and an EMS fraction of 0.104. This and lower capacities are not that realistic. A comparable goodness of fit was obtained with the actual experimental specific capacity of 67 mAh/g. This calculation, shown in Figure 7.4.23(b), had a goodness of fit of 0.6391 with a C-C distance of 3.423, an F-P distance of 0.978 and an EMS fraction of 0.041. These goodness of fits are only slightly better than the ones obtained without EMS. For the rotating PF_6, the goodness of fit was much better at 0.3084 with a specific capacity of 67 mAh/g, a C-C distance of 3.446 Å, and F-P distance

of 1.975 Å, and an EMS fraction of 0.128. Both specific capacities are much closer to the experimental value of 67 mAh/g. These results are summarized in Table 7.13.

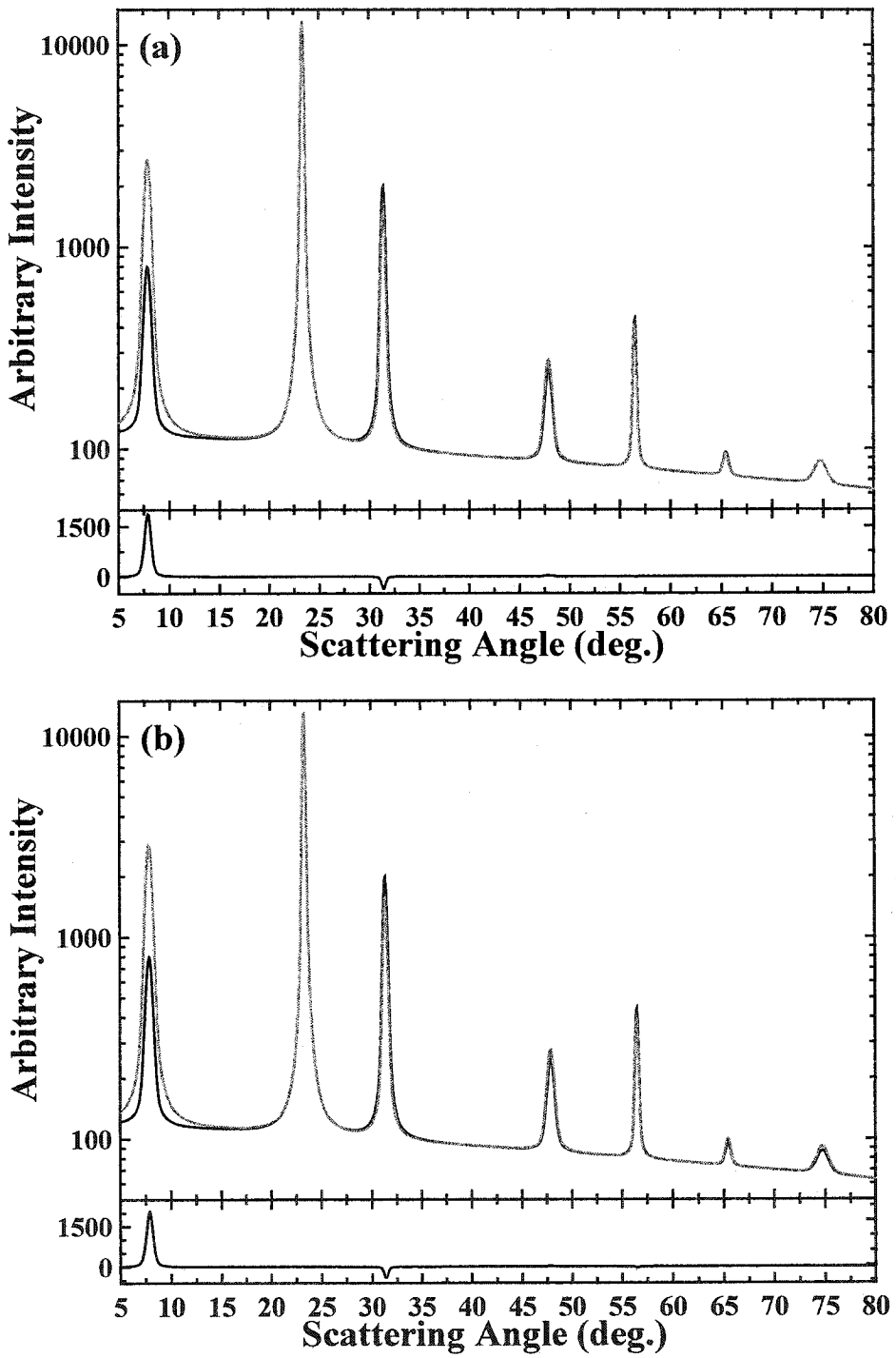

Figure 7.4.23 (top panels) Intensity versus scattering angle for calibrated experimental data, black line, and normalized calculated data, gray line, and (bottom panels) the difference between the experimental and calculated data, for 2F-P+2F-2F, stage 2 as stage 2 with EMS.

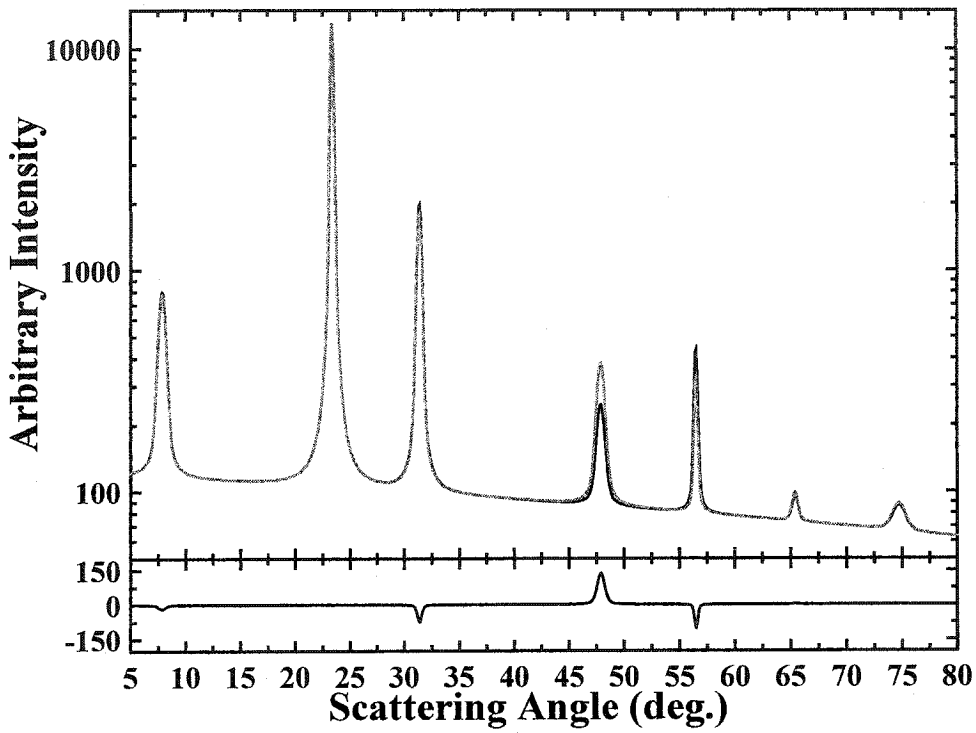

Figure 7.4.24 (top panel) Intensity versus scattering angle for calibrated experimental data, black line, and normalized calculated data, gray line, and (bottom panel) the difference between the experimental and calculated data, for rotating PF_6 as stage 2 with EMS.

Orientation	fit	capacity (mAh/g)	C-C distance (Å)	F-P distance (Å)	EMS fraction
2F-P+2F-2F	0.5895	50	3.422	0.939	0.104
	0.6391	67	3.423	0.978	0.041
Rotating PF_6	0.3084	67	3.446	1.975	0.128

Table 7.13 Results of the EMS calculations for stage 2 as stage 2 for PF_6 for the various orientations tested.

The next step was to determine whether stage 3 would result in better fits than stage 2 for this particular stage with a d-spacing of about 11.4 Å. This would result in PF_6 being situated in between carbon layers that are closer together, see Figure 7.4.25.

In all cases the best fits obtained was greater than 1.5. The best fit that was obtained, out of all four orientations was for 3F-P-3F, which had a fit of 1.6. This

particular fit had a C-C distance of 3.448 Å and an F-P distance of 1.192 Å at a specific capacity of 88 mAh/g. Since no reasonable fits were obtained, it is safe to say that the stage with a c-axis spacing of 11.433 ± 0.005 Å is definitely stage 2.

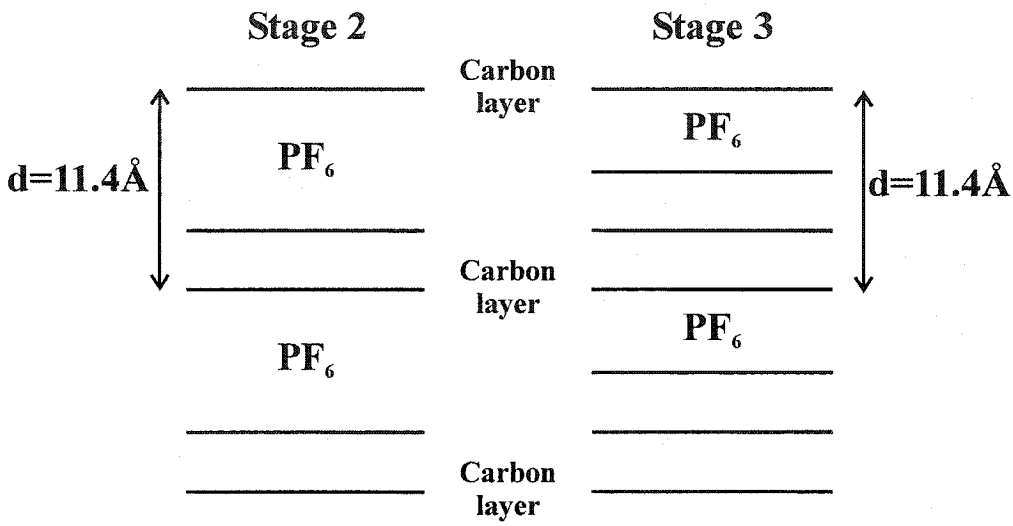

Figure 7.4.25. Illustrating the difference between stage 2 and stage 3 with the same c-axis spacing.

Since in both cases, stage 1 and stage 2, the best fits were obtained from the same two orientations, one of these orientations is most likely the correct one that fluorophosphate assumes when intercalated into graphite. These two orientations are 2F-P+2F-2F and the rotating PF_6. These two orientations and their results are compared in Table 7.14.

By comparing the results from the different stages, overall a rotating PF_6 has better fits. From this it might be concluded that this is the preferred orientation. However, the F-P distance varies from 1.448 Å to 1.975 Å, a range of about 0.5 Å or about 25% for the rotating PF_6. The F-P distances for the 2F-P+2F-2F orientation range from 0.952 Å to 0.978 Å a variation of 0.026 Å or about 3%. If one considers this fact then it would suggest that perhaps this orientation is the more likely one.

With a P-F bond length of 1.598 Å, the F-P distance for the 2F-P+2F-2F orientation would be ~1.13 Å. The values given by the best fits are about 20% lower. The F-P distance for the rotating PF_6 orientation would be same as the bond length. The values given by the best fits differ by about 10% rather than 20%. Some compression of these distances is quite possible although a smaller compression is more likely.

orientation	stage	d-spacing (Å)	fit	cap. (mAh/g)	F-P dist. (Å)	C-C dist. (Å)	EMS frac.	Anion layer spacing
2F-P+2F-2F	1	8.024	0.3213	178.5	0.968	N/A	N/A	N/A
			0.3628	140	0.962	N/A	0.370	N/A
	2	11.433	0.659	78	0.952	3.434	N/A	7.999 Å
			0.6391	67	0.978	3.423	0.041	8.010 Å
rotating PF_6	1	8.024	0.3408	184.5	1.492	N/A	N/A	N/A
			0.4047	140	1.465	N/A	0.401	N/A
	2	11.433	0.515	92	1.646	3.445	N/A	7.988 Å
			0.3084	67	1.975	3.446	0.128	7.987 Å

Table 7.14 Comparing the results for 2F-P+2F-2F and rotating PF_6.

A rotating PF_6 ion may seem a little strange but there is lots of room between the carbon layers for this to occur. In fact, the rotational energy barrier for PF_6 is quite low, <20 meV [60]. This would correspond to a temperature of ~200 K where PF_6 would freely rotate. Since these experiments were performed at room temperature, ~300 K, rotation of fluorophosphate is very likely.

Since the specific capacities of the fits with EMS are closer to the specific experimental capacities, it is most likely that EMS is co-intercalating with the fluorophosphate. The only unfortunate thing is that the ratio of the EMS present is not the same for both stage 1 and stage 2. The fraction for stage 2 is about one third that of stage 1. At this point no explanation can be given for this difference.

From these experiments the stage with a layer spacing of ~8 Å is stage 1 and the stage with a layer spacing of ~11.4 Å is stage 2. Also it can be said with relative certainty that the intercalated hexafluorophosphate is rotating between the carbon layers and perhaps co-intercalation of the solvent ethyl methyl sulfone occurs.

Chapter 8 Other Anions

Since PF_6 intercalates into graphitic carbon materials, it would be interesting to see if other anions also intercalate into the same materials. Two such anions were investigated. These were the perchlorate ion, ClO_4^-, and the tetrafluoroborate ion, BF_4^-. In both cases XP3 Coke heated to 2600°C, or sometimes 2300°C, was used as the active material and the solvent in the electrolyte was ethyl methyl sulfone, the same as before. The counter/reference electrode for all cells discussed in this chapter was a lithium metal electrode.

Section 8.1 Electrochemical Testing

Data from a typical electrochemical cell that uses $LiClO_4$ as the lithium salt in the electrolyte is shown in Figure 8.1.1. Figure 8.1.1(a) shows the potential versus the specific capacity for a sample with XP3 2600°C as the active carbon material. This particular cell had an upper cutoff potential of 6 V, however this high potential was not reached. Initially the cell potential increased but it started to decrease before the upper cutoff potential was achieved. The cell was switched to discharge after this was discovered. The maximum cell potential reached was 5.144 V. Since there was a decrease in potential before discharge began, the charge capacity of 200 mAh/g is really unrealistic. The discharge capacity reached was about 60 mAh/g.

Another cell was cycled with a current to mass ratio about three times as large as the previous experiment. The potential versus specific capacity plot for this cell is shown

in Figure 8.1.1(b). This particular cell was cycled with various upper cutoff potentials, starting with 4.9 V, then 5.0 V and hopefully 5.1 V. The cell begins to develop problems slightly above 5.0 V. The specific capacities for the cycles with 4.9 V as the upper cutoff potential were 28 mAh/g and 15 mAh/g for charge and discharge, respectively. The cycles with an upper cutoff potential of 5.0 V had specific capacities of 33 and 22 mAh/g for charge and discharge, respectively. These experiments were repeated several times with very similar results. This suggests that perchlorate is not a good candidate for this type of intercalation.

To see if there are any interesting features in these charge and discharge curves, differential capacity versus potential curves were plotted, refer to Figure 8.1.2. These plots are quite featureless during charge until about 4.7 V and there are definite problems occurring around 5.0 V. The value of the differential capacity becomes quite large around 5.0 V. This suggests that the electrolyte is decomposing or there are reactions between the components of the electrolyte and possibly with the electrode itself.

There are peaks and valleys in both the charge and discharge parts of the curve. During discharge these peaks are much broader than in the charge part of the curve. It is interesting to note that these peaks, in discharge, become broader and perhaps shift as the upper cutoff potential is changed, Figure 8.1.2(b). The black lines in Figure 8.1.2(b) have an upper cutoff potential of 4.9 V and the gray lines have an upper cutoff potential of 5.0 V. This suggests that the cutoff potential greatly affects the performance of the cell and perhaps the system is not stable. The features in Figure 8.1.2(a) are better defined than in Figure 8.1.2(b). This is most likely due to the difference in the current to mass ratio, i.e. how fast the cell was cycled.

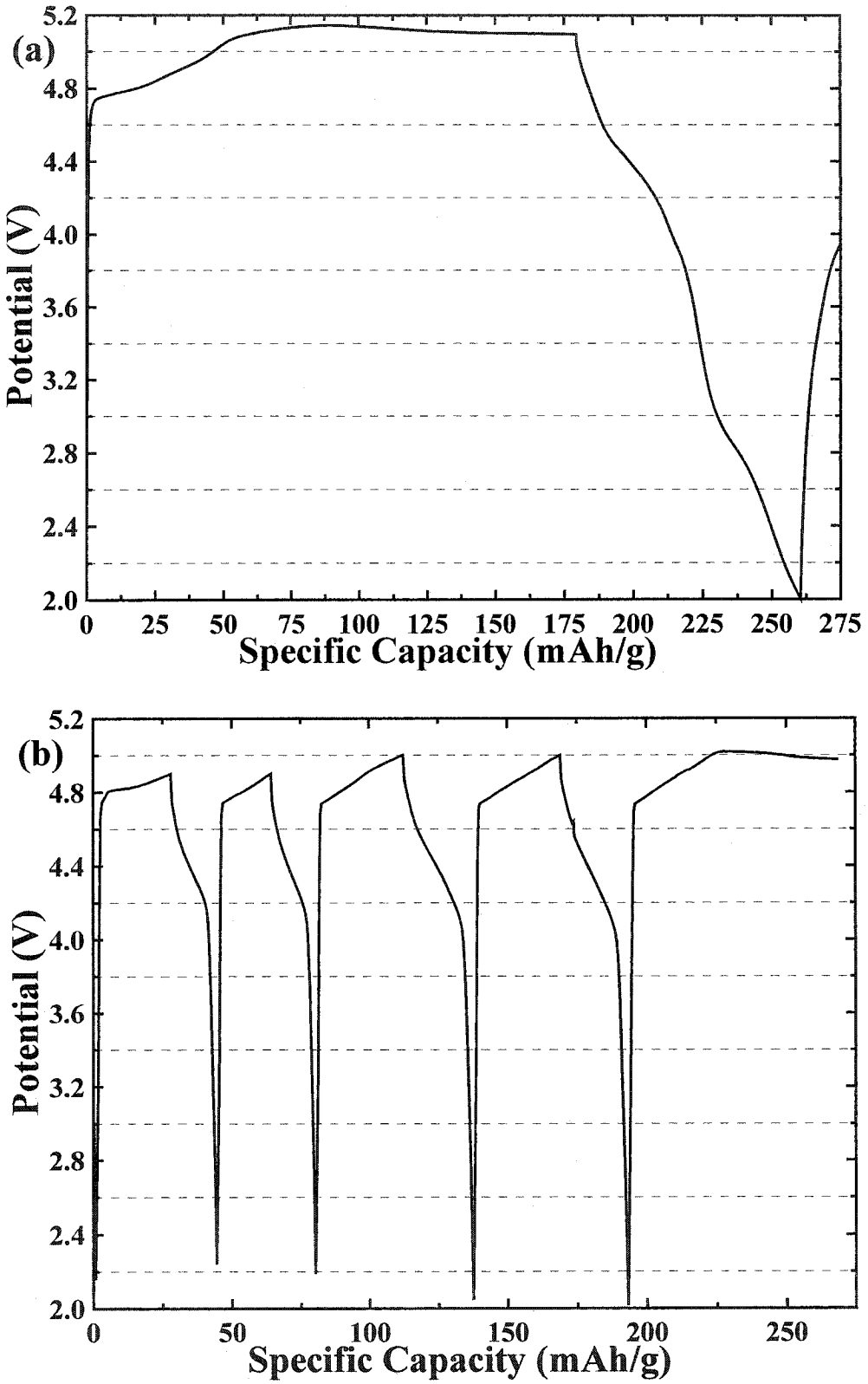

Figure 8.1.1 Potential versus specific capacity for (a) XP3 2600 and (b) XP3 2300 with 2M $LiCLO_4$/EMS as the electrolyte.

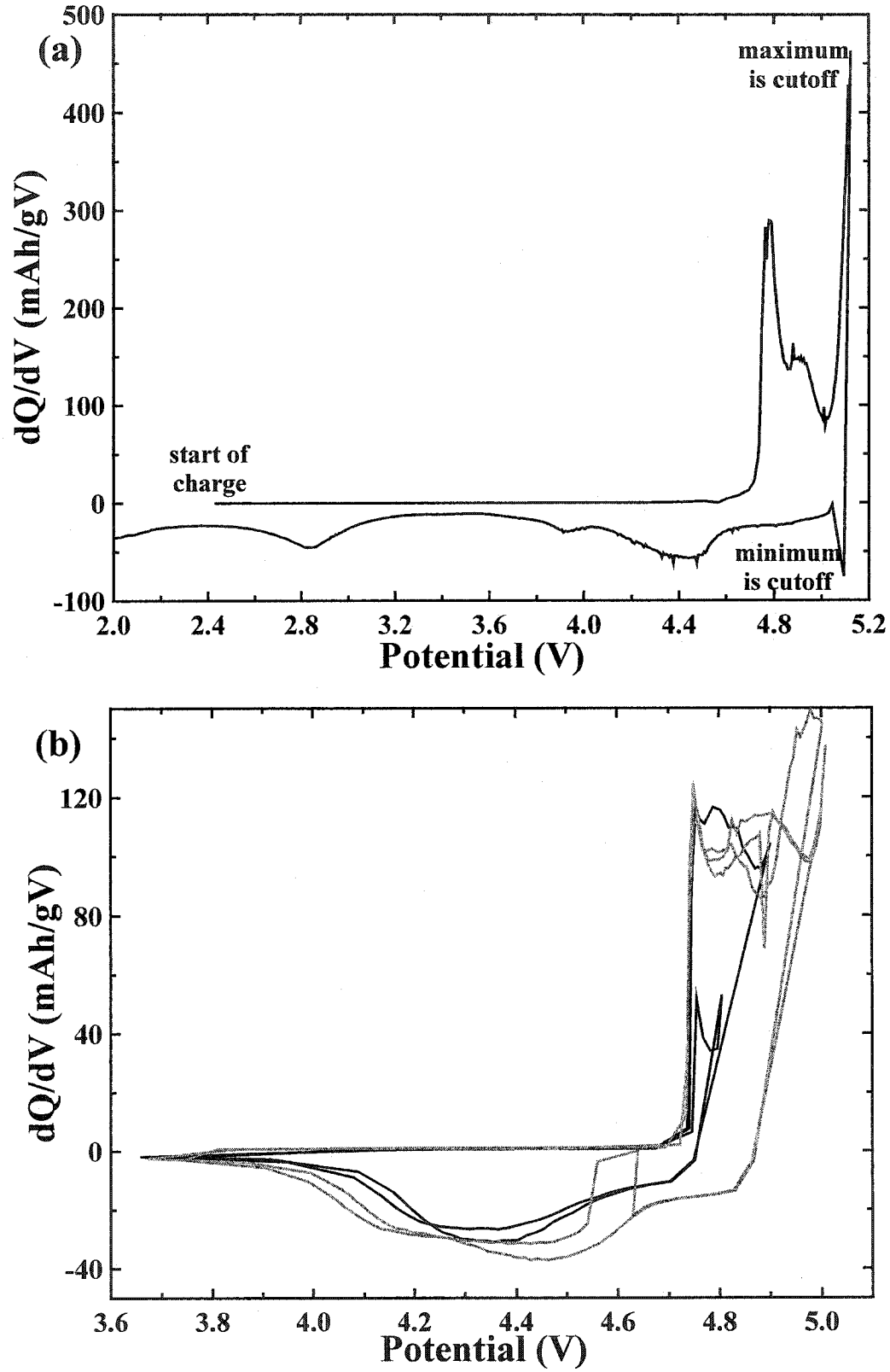

Figure 8.1.2 Differential capacity versus potential for (a) XP3 2600 and (b) XP3 2300 with 2M $LiClO_4$/EMS as the electrolyte, the black and gray lines are for cells that upper cutoff potential of 4.9 V and 5.0 V, respectively.

One of the initial experiments performed with the tetrafluoroborate molecule had a high upper cutoff potential of 5.6 V. The potential versus the specific capacity plot is shown in Figure 8.1.3. It can be easily seen that the upper cutoff potential was not reached. At about 5.46 V the potential begins to decrease. Once this was discovered the cell was switched to discharge. The charge capacity reached at 5.46 V was ~240 mAh/g, and the discharge capacity to 2.0 V was ~90 mAh/g, a substantial loss. The drop in potential suggests that there is a problem with the cell such as electrolyte decomposition. This, perhaps, is more easily seen in a differential capacity versus potential curve, which is shown in Figure 8.1.4. There are several peaks and valleys present in the charge part of the curve, the gray line. These valleys may represent pure stages if tetrafluoroborate intercalates. The very sharp drop and valley in the discharge curve, around 4.8 V, marked by an asterisk, *, in the figure is due to a small power outrage and is not related to the performance of the cell.

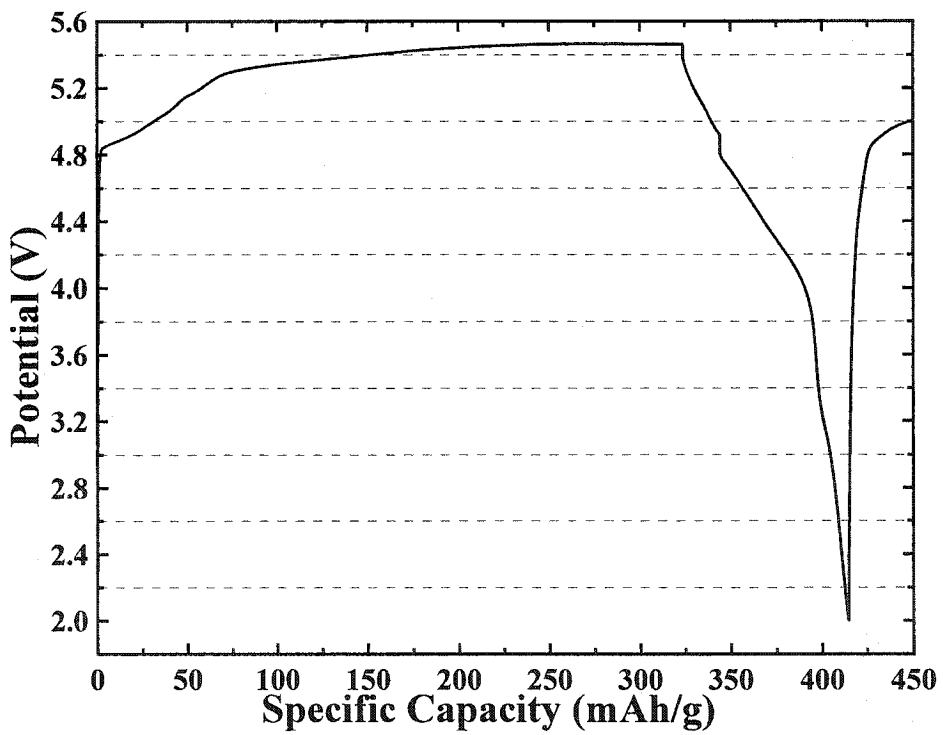

Figure 8.1.3 Potential versus specific capacity for XP3 2600 in 2M $LiBF_4$/EMS.

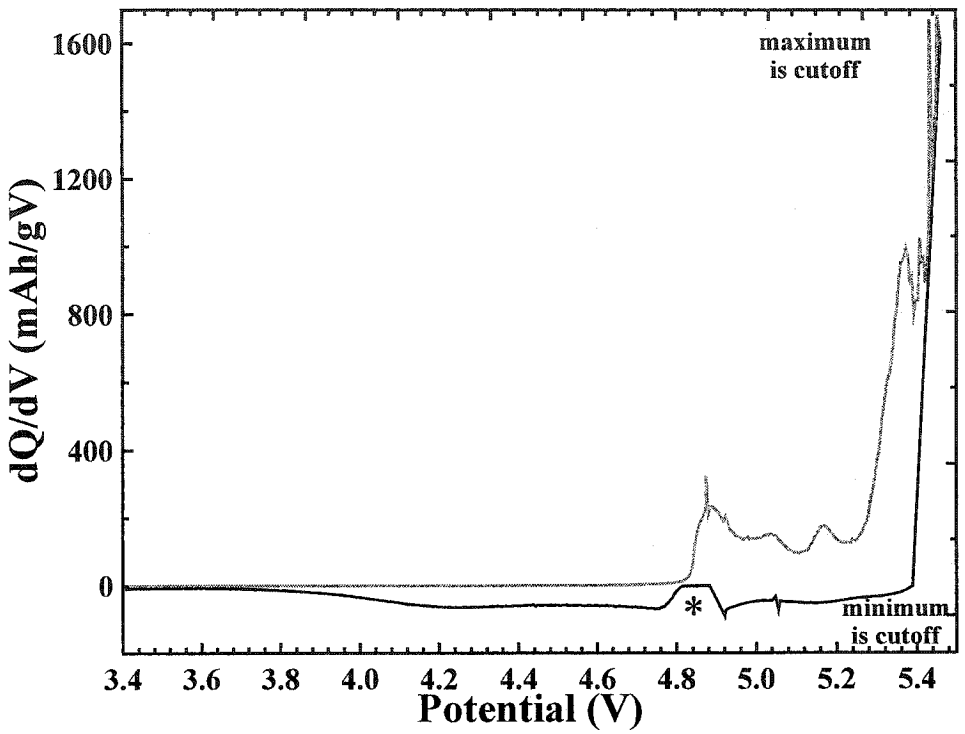

Figure 8.1.4 Differential capacity versus potential for XP3 2600 in 2M $LiBF_4$/EMS.

To see if the differential capacity versus potential curves are dependent on the upper cutoff voltage, an experiment with various upper cutoff potentials was performed. The results for 4.9 V, 5.0 V and 5.1 V are shown in Figure 8.1.5. Figure 8.1.5(a) shows the potential versus the specific capacity whereas Figure 8.1.5(b) shows the differential capacity versus potential for the same cell. Naturally, the charge and discharge capacities increase with increasing upper cutoff potential. All values are fairly small, especially for the cycles with a cutoff potential of 4.9 V, with charge and discharge capacities of about 10 mAh/g each. The charge capacities for upper cutoff potentials of 5.0 V and 5.1 V are about 30 mAh/g and ~45 mAh/g, respectively. The discharge capacities are about 20 mAh/g and 25 mAh/g for 5.0 V and 5.1 V, upper cutoff potentials, respectively. This particular cell developed problems during the second cycle at 5.1 V. This is most likely due to the fact that the cell was cycled relatively slowly.

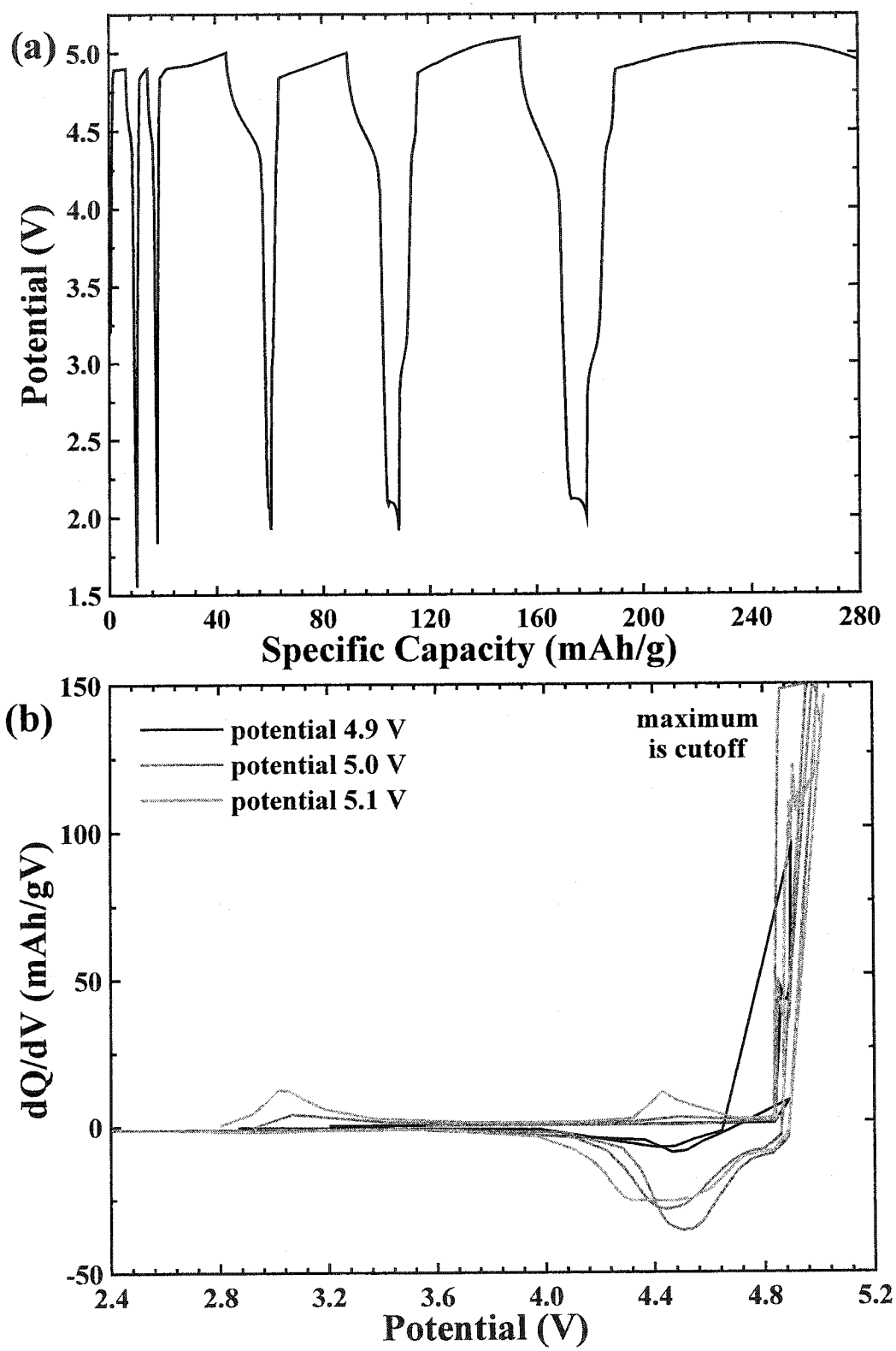

Figure 8.1.5 (a) Potential versus specific capacity and (b) differential capacity versus potential for XP3 2300 in 2M $LiBF_4$/EMS.

The features in the potential versus the specific capacity plot can be seen more easily in the differential capacity versus potential plot shown in Figure 8.1.5(b). It is interesting to note that although the peaks (and valleys) during discharge appear at approximately the same potential, the size of these peaks increases with increases to the cutoff potential. This is not a surprise since the discharge capacities are larger. The charge part of the curve is fairly featureless. There are some peaks and valleys present above 4.8 V but these are hard to distinguish since there is a fair amount of noise present. Tetrafluoroborate seems to perform better and shows more promise than perchlorate as a potential anion for intercalation, however, more research is needed.

So far it has been shown that three different lithium salts, $LiClO_4$, $LiBF_4$ and $LiPF_6$, can be used in electrochemical cells where the anion half of the salt acts as the charge carrier. The differences and similarities shall now be discussed. Figure 8.1.6 shows a potential versus specific capacity plot of three representative curves of PF_6, BF_4 and ClO_4. It can be seen easily that ClO_4 does not perform as well as the other two molecules. The cell only achieves a specific capacity of approximately 80 mAh/g before the potential decreases during charge and the discharge capacity is also quite small, 60 mAh/g, which is close to the charge capacity. The BF_4 cell appears to have a very large specific capacity, ~325 mAh/g, but as with ClO_4, it actually is decreasing in potential before the cell was switched to discharge. The specific capacity reached before this decrease in potential was approximately 240 mAh/g but it is thought that this may include some electrolyte decomposition. If the cell had been switched to discharge at 5.4 V, a potential slightly below where the decrease occurs, then the specific capacity would have

been about 150 mAh/g. The discharge capacity is quite small in comparison, only ~90 mAh/g. The specific capacity balance between charge and discharge with PF_6 is much better: the charge capacity was ~130 mAh/g, the discharge capacity was 90 mAh/g. Although the charge capacity is larger for BF_4 and since the capacity loss is smaller for PF_6, PF_6 would be a better candidate for electrochemical cycling for cells that use EMS as the solvent. These results are summarized in Table 8.1.

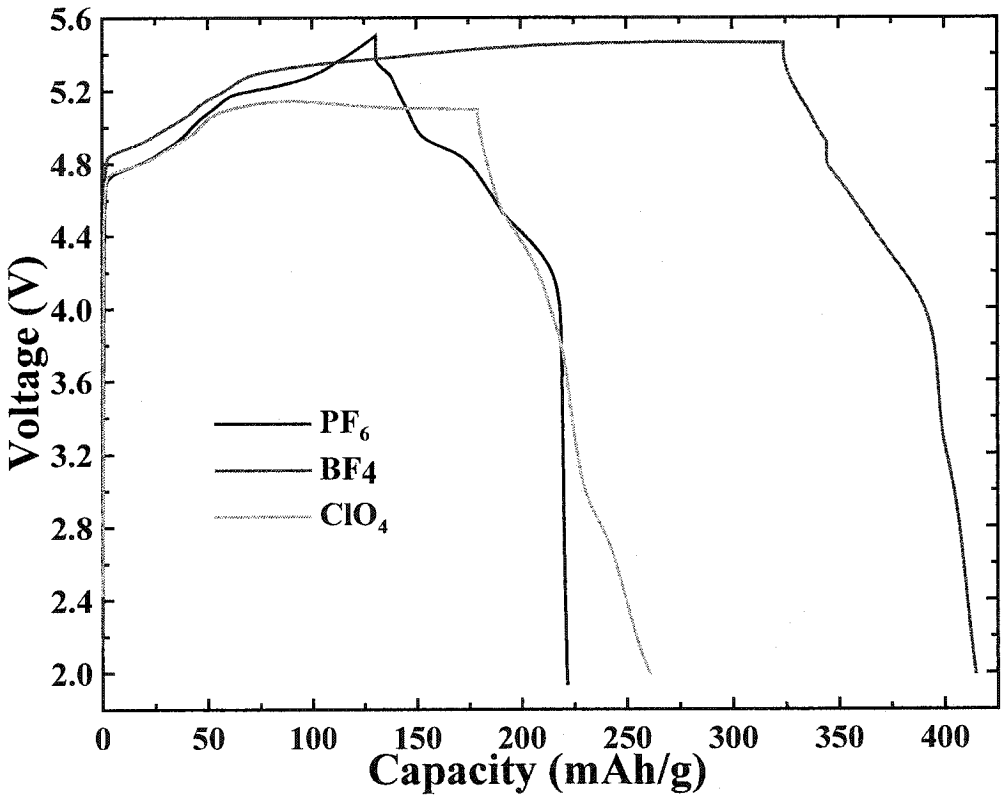

Figure 8.1.6 Potential versus specific capacity plots for PF_6, BF_4 and ClO_4 for XP3 Coke heated to 2600°C.

Anion	Charge Capacity (mAh/g)	Discharge Capacity (mAh/g)	Capacity Loss
ClO_4	80	60	25%
BF_4	150	90	40%
PF_6	130	90	31%

Table 8.1 Comparing charge and discharge capacities for ClO_4, BF_4 and PF_6 in XP3 Coke sample heated to 2600°C.

To compare the cyclability of these anions, their differential capacities versus potential curves were plotted for various cutoff potentials. Figure 8.1.7 shows the differential capacity versus the potential for PF_6 and ClO_4 with a cutoff potential of 4.8 V whereas the BF_4 curve has a cutoff potential of 4.9 V. From this plot it can be easily seen that both PF_6 and ClO_4 start to intercalate into the carbon material at about 4.75 V where as BF_4 does not start to intercalate until 4.85 V. A higher potential is required for BF_4 intercalation.

The curves shown in Figure 8.1.8 all have an upper cutoff potential of 5.0 V. Again it can be seen that BF_4 has a higher potential before things begin to happen and that pure stages may be forming for PF_6 at 4.95 V, for ClO_4 at 4.9 V and just below 5.0 V for BF_4. This would have to be confirmed with *in-situ* X-ray diffraction experiments.

Figure 8.1.9 shows the differential capacity versus potential for all three samples. The bottom panel shows the curve for PF_6. There are several valleys during charge and discharge which represents pure stages at 5 V, 5.15 V and above 5.4 V. The middle panel shows that ClO_4 looks as though it would also intercalate into carbon, especially considering that the shape of the dQ/dV charge part of the curve, is very similar to that of PF_6. However, around 5.1 V electrolyte decomposition becomes too great and the cell no longer cycles well. The discharge part of the curve is almost featureless. By integrating the charge part of the dQ/dV curve an estimate of the capacity and the amount of x in $(ClO_4)_xC$ can be obtained. If this is done up to 5.0 V, i.e. before electrolyte composition becomes too great, the estimated capacity is 52 mAh/g and the resulting x would be 0.023. The top panel in the figure shows that BF_4 should intercalate quite well forming pure stages at perhaps ~5.1 V, 5.25 V and perhaps even at 5.4 V just before major

electrolyte decomposition sets in. Since the estimate of the specific capacity for BF_4 up to 5.4V is 150 mAh/g, there should be 0.067 BF_4 per carbon atom. Again the discharge is featureless suggesting that perhaps pure staging is not occurring during discharge and perhaps there is too much EMS co-intercalation.

The main difference between PF_6, ClO_4 and BF_4 is that PF_6 during discharge gives evidence of pure staging and can be cycled to higher potentials. This may be due to less electrolyte decomposition or reactions of the intercalated molecule with the components of the cell. The shape of the curves during charge is all very similar with BF_4 being offset to a higher potential by about 0.1 V. It will be interesting to see how the *in-situ* X-ray diffraction experiments compare.

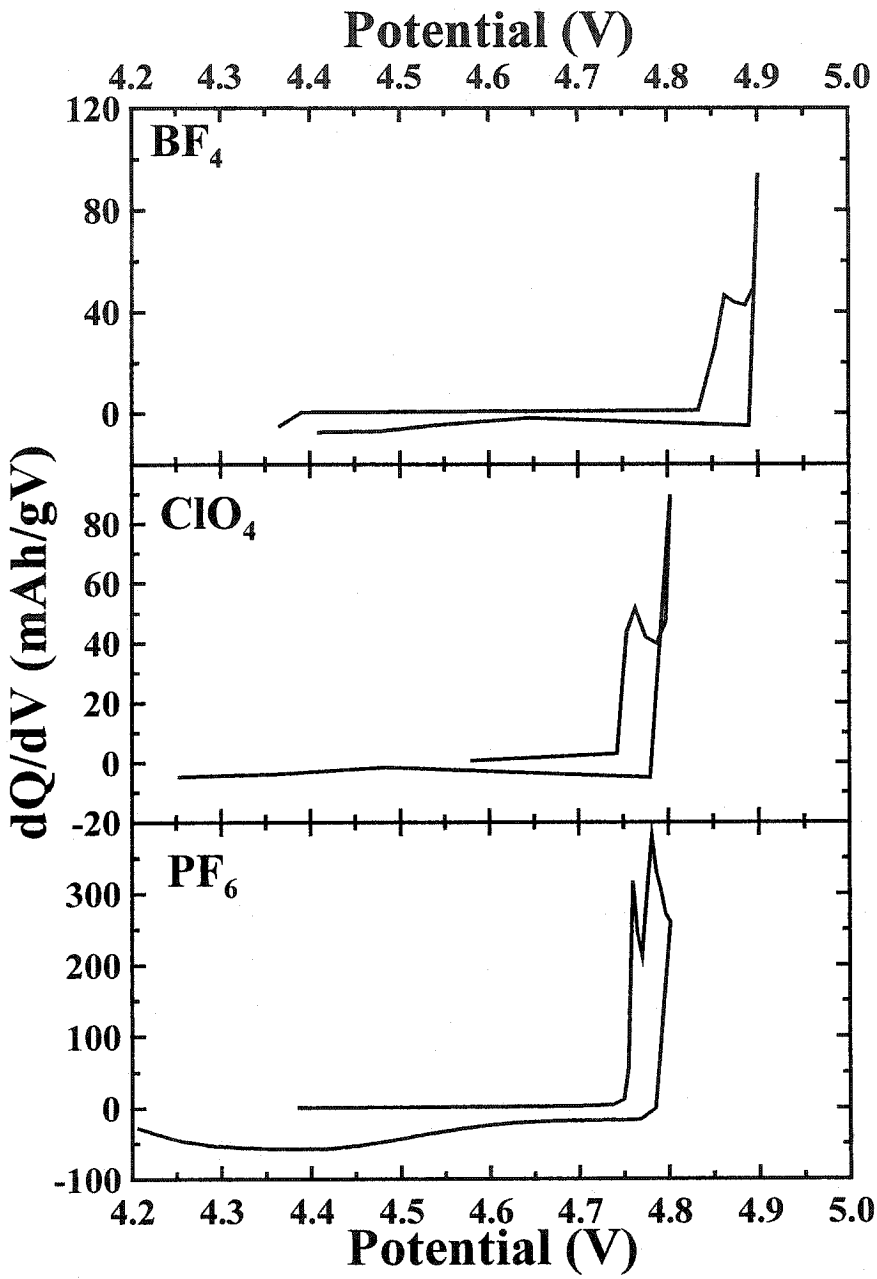

Figure 8.1.7 Differential capacity versus potential for the three molecular anions tested with upper cutoff potentials of 4.8 V for PF_6 and ClO_4 and 4.9 V for BF_4 for XP3 Coke heated to 2300°C.

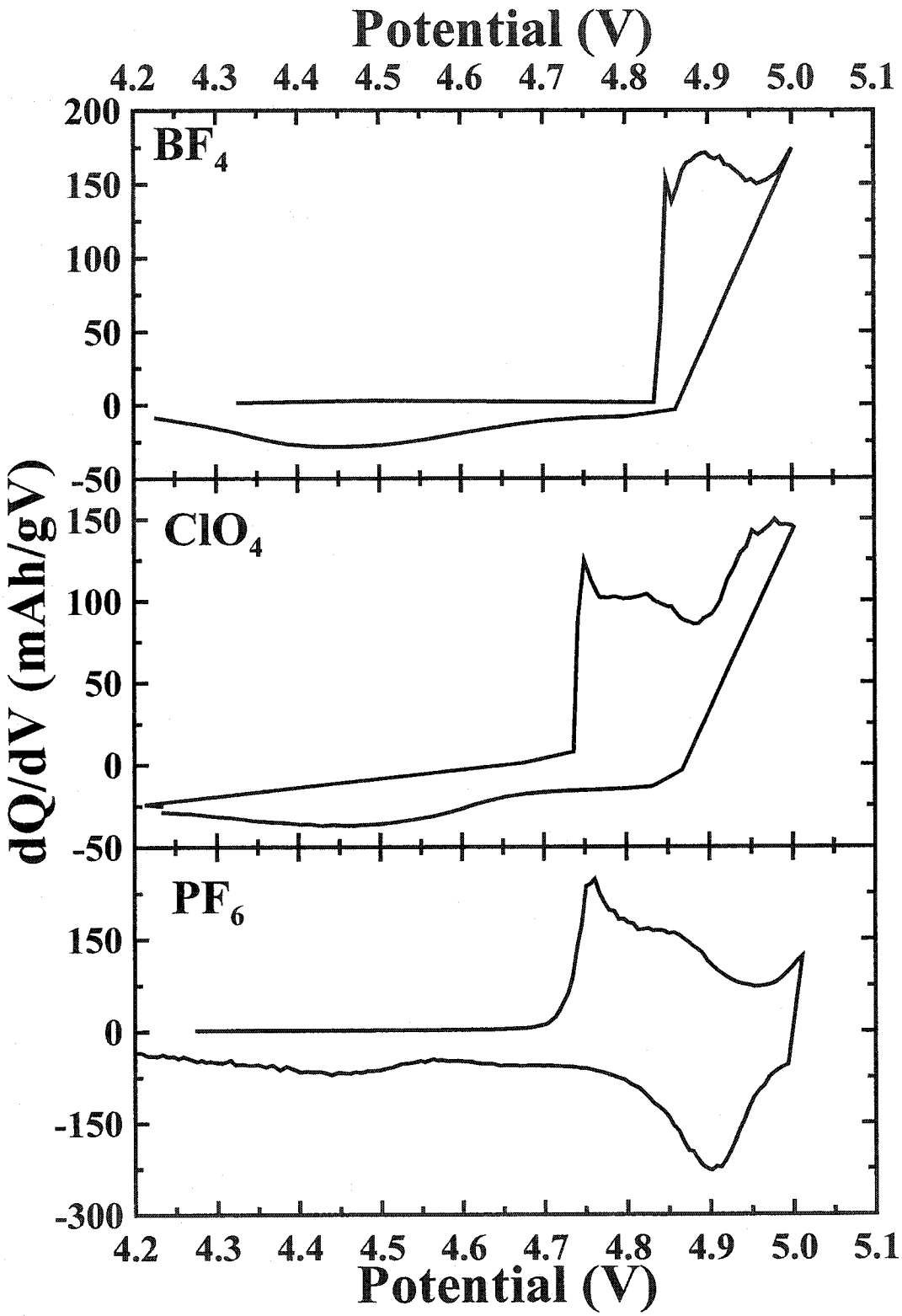

Figure 8.1.8 Differential capacity versus potential for the three molecular anions tested with cutoff potentials of 5.0 V for XP3 Coke heated to 2300°C.

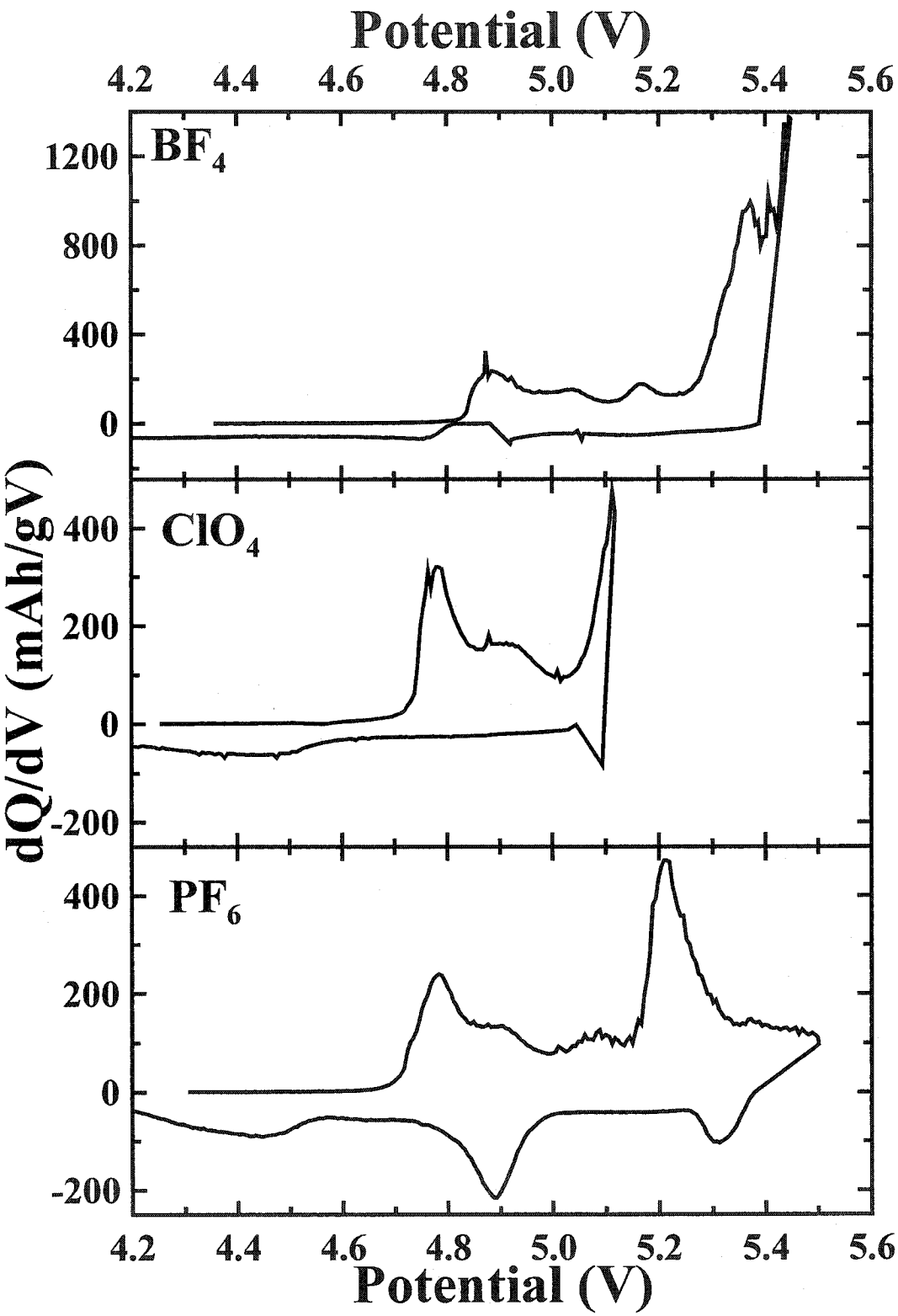

Figure 8.1.9 Differential capacity versus potential for the three molecular anions tested with high cutoff potentials of 5.15 V for ClO_4, 5.45 V for BF_4 and 5.5 V for PF_6 for XP3 Coke heated to 2300°C.

Section 8.2 *In-situ* X-ray Diffraction Experiments

By looking at the electrochemical data presented in the previous section it was thought that ClO_4 would intercalate at least somewhat into XP3 2600°C or 2300°C. However, this was not detected using *in-situ* X-ray diffraction. All *in-situ* X-ray diffraction experiments did not show any evidence of intercalation. The (002) peak of graphite present in the initial X-ray scan of the in-situ X-ray diffraction experiment did diminish in size suggesting that ClO_4 started to intercalate into the carbon electrode but no evidence of new peak formation on either side of the (002) peak was observed to suggest that staging did occur. There is, perhaps, a substantial amount of electrolyte decomposition and a significant amount of co-intercalation of the solvent at relatively low potentials, slightly above 5.0 V, when compared with PF_6 or BF_4 which appear to be stable to potentials around or above 5.4 V. This would result in the deformation or even the destruction of the layered structure of the graphitic carbon and therefore no intercalation can be seen. This was not the case, fortunately, for BF_4.

The potential versus the specific capacity plot for the *in-situ* X-ray diffraction experiment of XP3 coke 2600°C/2M $LiBF_4$/EMS/Li is shown in Figure 8.2.1. There are two cycles, the first with an upper cutoff potential of 5.3 V and a lower cutoff potential of 2.0 V. The second cycle has an upper cutoff potential of 5.4 V and a lower cutoff potential of 1.5 V. Figure 8.2.2 shows the *in-situ* X-ray diffraction patterns for this experiment. The cutoff potential of the first cycle is just below the point where a new stage begins to form.

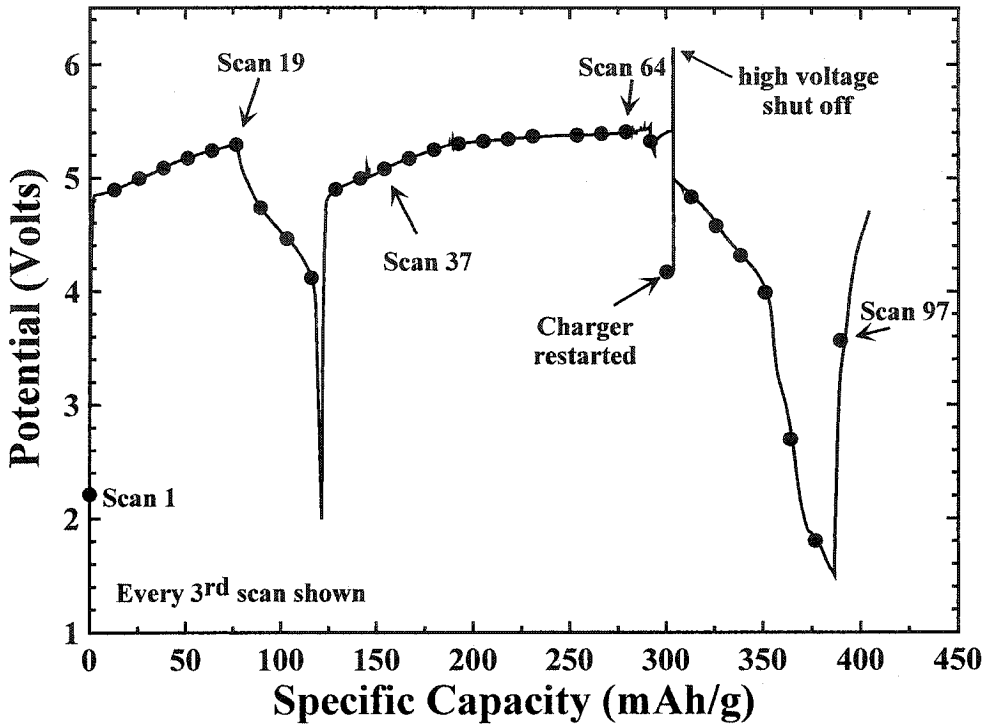

Figure 8.2.1 Potential versus specific capacity for an *in-situ* X-ray diffraction experiment for XP3 2600 in 2M $LiBF_4$/EMS.

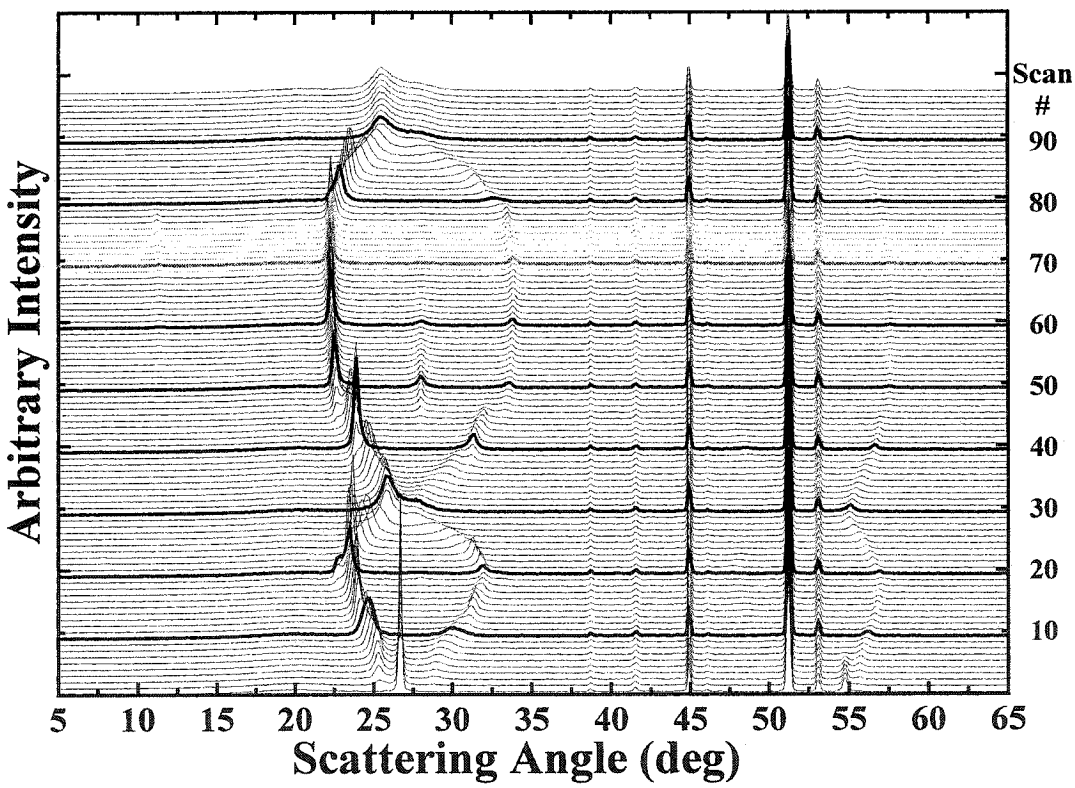

Figure 8.2.2 X-ray diffraction patterns for the *in-situ* X-ray diffraction experiment for XP3 2600°C in 2M $LiBF_4$/EMS. Every 10^{th} scan is shown by a bold line. The gray scans are the scans taken without current being supplied to the cell.

The X-ray diffraction patterns of the second charge are very similar to that of the first charge up to 5.3 V. After this point, the cell continues to charge and the peaks that began to form just before discharge started during the first cycle form completely and no longer shift by scan 59 or 5.38 V. However, there is one peak in particular, at about 28° which diminishes in size and is almost completely gone by scan 68, or 5.4 V. It is thought that this scan represents an almost pure stage. Just after scan 68 there was a power failure in the charging system and the next several scans, scan 69 to 76, were taken as the cell received no current and there was no change in the X-ray diffraction patterns. After that point the cell was switched to discharge. The transitions occur much more rapidly and in fact it appears that the peaks simply shift in angle rather than a clear transition between two sets of peaks. This is most likely due to the fact that the discharge part of the cycle occurs more quickly than the charge part of the cycle. If the current was decreased during charge, separate phases would most likely be present. These shifts and transitions can be more easily seen in Figure 8.2.3.

During charge the (002) peak of graphite diminishes as new peaks begin to form on either side of this peak. These peaks continually shift away from the position of the (002) peak of graphite until scan 11 or 5.12 V. At this point the low angle peak begins to develop a low angle shoulder, a new peak is forming. Over the next couple of scans, the old peak diminishes and this new peak shifts to lower angles. By scan 16, 5.24 V, a new peak, at a lower angle begins to form as the old peak diminishes. Just before discharge, scan 19 or 5.29 V, another lower angle peak begins to form. Similarly, the high angle peaks develop high angle shoulders, although this is harder to see since the intensities of the peaks are much smaller. Another peak above 55° also forms shortly after charging

begins and continuously shifts towards higher angles as charging continues. The charge capacity reached is almost 80 mAh/g. During discharge the peaks simply shift back towards the position of that (002) peak which does not reform completely by 1.5 V. The discharge capacity of the first cycle is about 45 mAh/g.

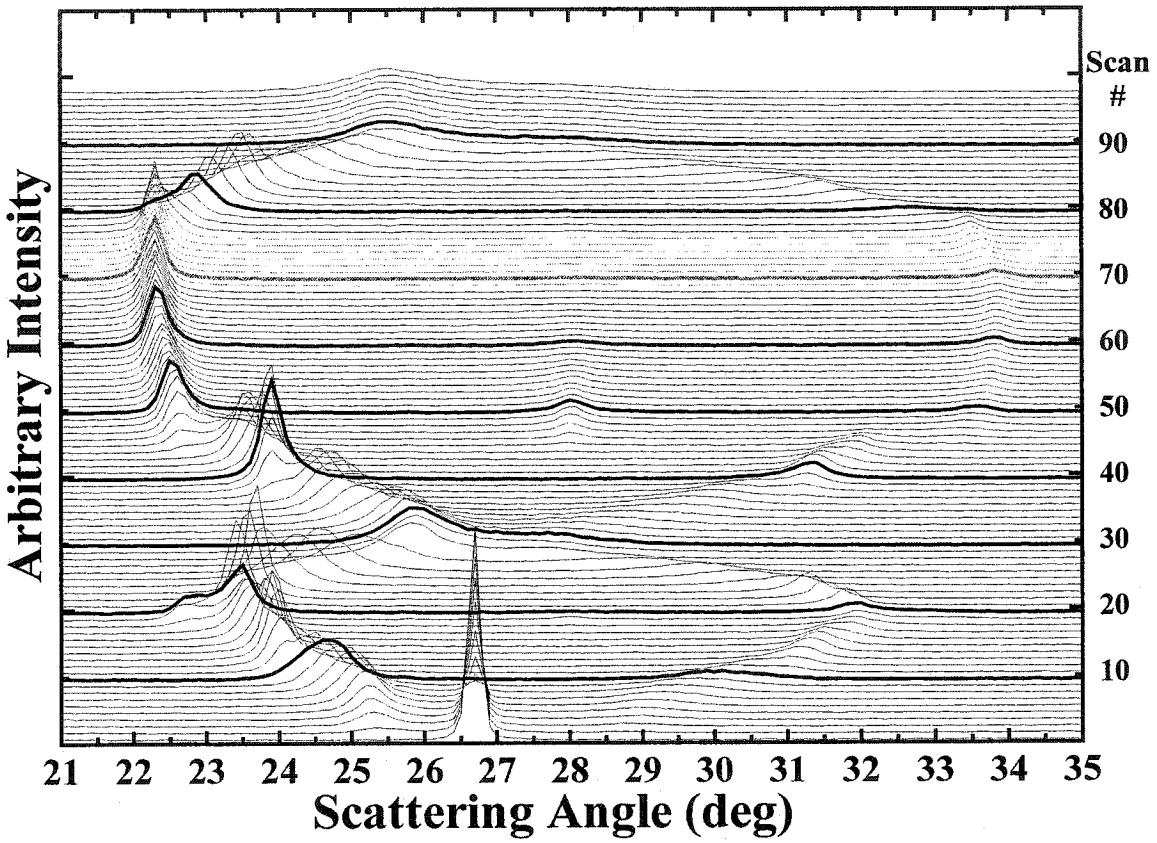

Figure 8.2.3 The same patterns as in Figure 8.2.2 but isolating the peaks in the 20° to 35° range. Every 10^{th} scan is shown by a bold line. The gray scans are the scans taken without current being supplied to the cell.

In order to determine the stage number and c-axis spacings, the scans were fit with gfit. Three of these fitted scans are shown in Figure 8.2.4. Figure 8.2.4(a) shows scan 41 which occurs at 5.2 V, (b) shows scan 54 which occurs at 5.35 V and (c) shows scan 68 which occurs at 5.4 V. It can be seen easily that there are different (00ℓ) peaks for each scan. The positions of these peaks are shown in Table 8.2.

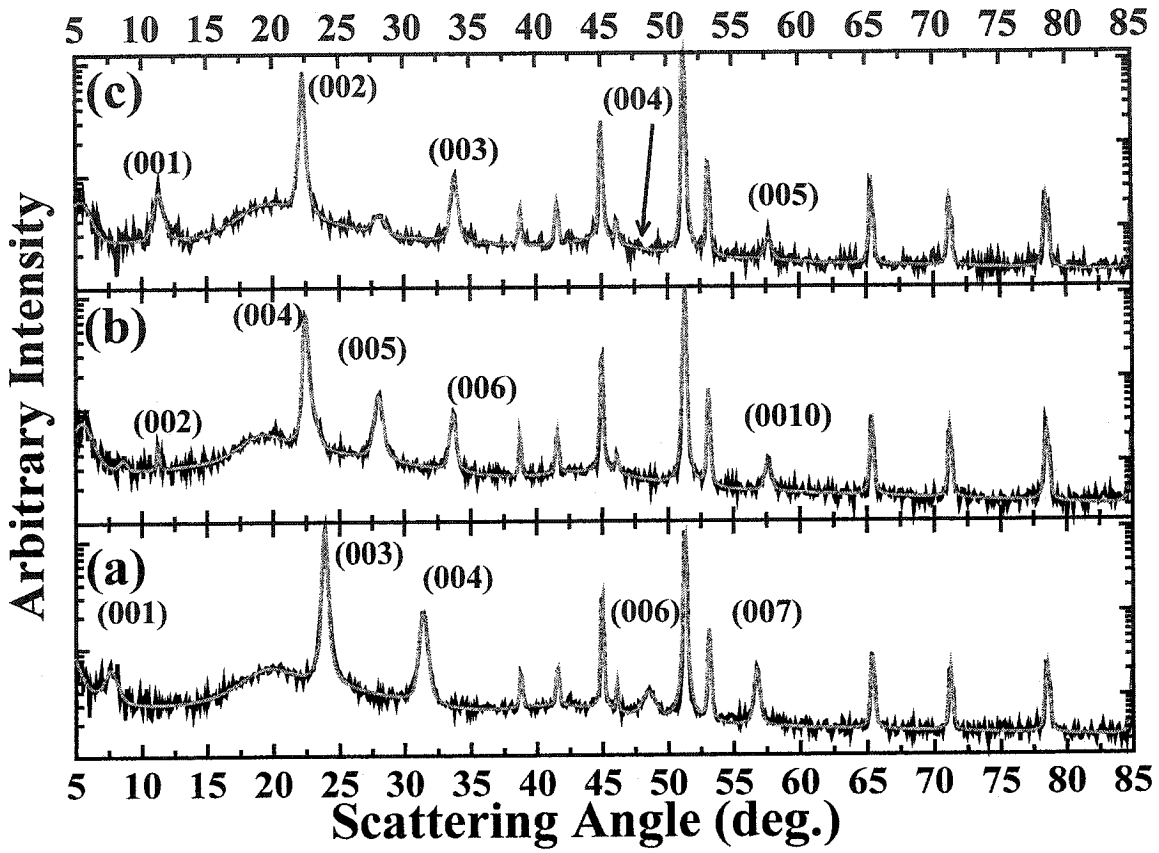

Figure 8.2.4 (a) Scan 41 (b) Scan 54 and (c) Scan 68 from the *in-situ* X-ray diffraction patterns shown in Figure 8.2.3.

Scan 41	Scan 54	Scan 68
7.765°	11.023°	11.056°
23.868°	22.149°	22.120°
31.375°	27.786°	33.676°
48.489°	33.492°	45.209°
56.716°	57.407°	57.530°

Table 8.2 Positions of (00ℓ) peaks of the scans shown in Figure 8.2.4.

There are a few possible combinations for the values of ℓ in (00ℓ) for the three scans shown. One possible combination for the ℓ's are described below. The peaks in scan 41 may be the (001), (003), (004), (006), and (007) peaks. The peaks in scan 68 may be the (001), (002), (003), and (005) peaks. The peaks in scan 54 are very similar to

those present in scan 68 with the exception that the peak at about 28° is stronger and the peak at 11° is much weaker. The main peaks are most likely the (002), (004), (005), (006) and (00,10).

The c-axis spacings for these possibilities are shown in Table 8.3. Since scan 68 represents the lowest possible stage reached, it should have the lowest c-axis spacing. This suggests that the possible ℓ's listed in Table 8.3 along with the corresponding c-axis spacings are correct. This would mean that the c-axis spacings for scans 68, 54, and 41, are 8.011 ± 0.007 Å, 16.053 ± 0.009 Å, and 11.32 ± 0.03 Å, respectively.

scan 41 (Å)		scan 54 (Å)		scan 68 (Å)	
(001)	11.322	(002)	8.026	(001)	8.002
(003)	3.774	(004)	4.013	(002)	4.018
(004)	2.830	(005)	3.211	(003)	2.662
(006)	1.887	(006)	2.676	(004)	2.006
(007)	1.617	(00,10)	1.605	(005)	1.602

Table 8.3 (00ℓ) spacings for various scans from the *in-situ* X-ray diffraction experiment of BF_4 intercalation.

It seems very strange and unlikely to have an average repeat distance along the z-axis that is larger, scan 54, than at lower potentials, scan 41. Scan 54 is in between two possible pure stages. Several of its main peaks are at very similar positions to that of scan 68. It is thought that scan 68 represents stage 1. It is interesting to note that the c-axis spacing for scan 54 is twice that for scan 68. This is a very interesting feature. There is a possible and reasonable explanation for this. To obtain this c-axis spacing of ~16 Å a full layer of intercalated BF_4 would be followed by a partly filled layer, see Figure 8.2.5. As the potential is increased further the partly filled layers become completely filled and a pure stage 1 is achieved.

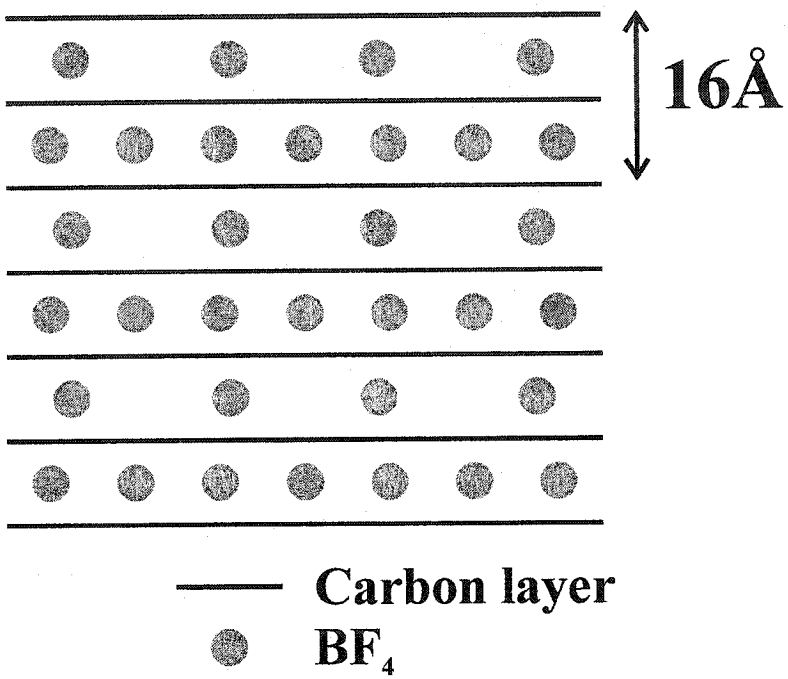

Figure 8.2.5 Illustrating the layered structure that is possibly present in scan 54 and neighboring scans.

If scan 68 represents stage 1, then the c-axis spacing for BF_4 is very similar to that for PF_6, which was about 8.0 Å. Since it has a very similar c-axis spacing, then it is most likely that stage 1 was reached. Work by others, [11,12], has shown that BF_4 has a c-axis spacing of about 11 Å for stage 2 and about 14 Å for stage 3. This suggests that scan 41 represents stage 2 and that stage 1 was achieved through electrochemical insertion of BF_4 into XP3 coke materials with EMS as the solvent.

By comparing the positions of the peaks and valleys of the PF_6 and BF_4 differential capacity versus voltage curves, which were shown in the previous section, the various stages reached should occur at different voltages. It is interesting to note that although the voltages are different, the c-axis spacings for the stage 1 and stage 2 compounds, which were determined through *in-situ* X-ray diffraction experiments, are very similar for both molecules. During charge, stage 2 for PF_6 occurs at 5.07 V whereas

for BF_4 is occurs at 5.20 V. Stage 1 for PF_6 and BF_4 occur at 5.48 V and 5.4 V, respectively. These voltages and the corresponding layer spacings are summarized in Table 8.4.

Anion	Stage 2		Stage 1	
	Potential	c-axis spacing	Potential	c-axis spacing
PF_6	5.07 V	11.43 Å	5.48 V	8.024 Å
BF_4	5.20 V	11.32 Å	5.40 V	8.006 Å

Table 8.4 Comparing staging of PF_6 and BF_4 in XP3 Coke heated to 2600°C.

As with PF_6, the amount of BF_4 that intercalates into the carbon electrode to give the specific capacities in the *in-situ* X-ray diffraction experiment can be determined. The experimental specific capacities for stage 1 and stage 2 for BF_4, in this experiment, were determined to be 215 mAh/g and 85 mAh/g, respectively. For stage 1, this would correspond to 10.4 carbons per BF_4 and hence $(BF_4)_{0.096}C$. For stage 2, there would be 26.3 carbon atoms per BF_4 and hence $(BF_4)_{0.038}C$. The amount of BF_4 present in stage 1 is more than twice of that present in stage 2. This also occurred in the higher temperature XP3 cokes with PF_6.

Section 8.3 Stage Indexing and Orientation of Tetrafluoroborate

In order to determine whether or not scan 68 is really stage 1, a program very similar to that used in Chapter 7, Section 4 and described in Chapter 4, Section 4 was used. Figure 8.3.1 shows scan 68 with the background and the peaks due to the components of the cell removed.

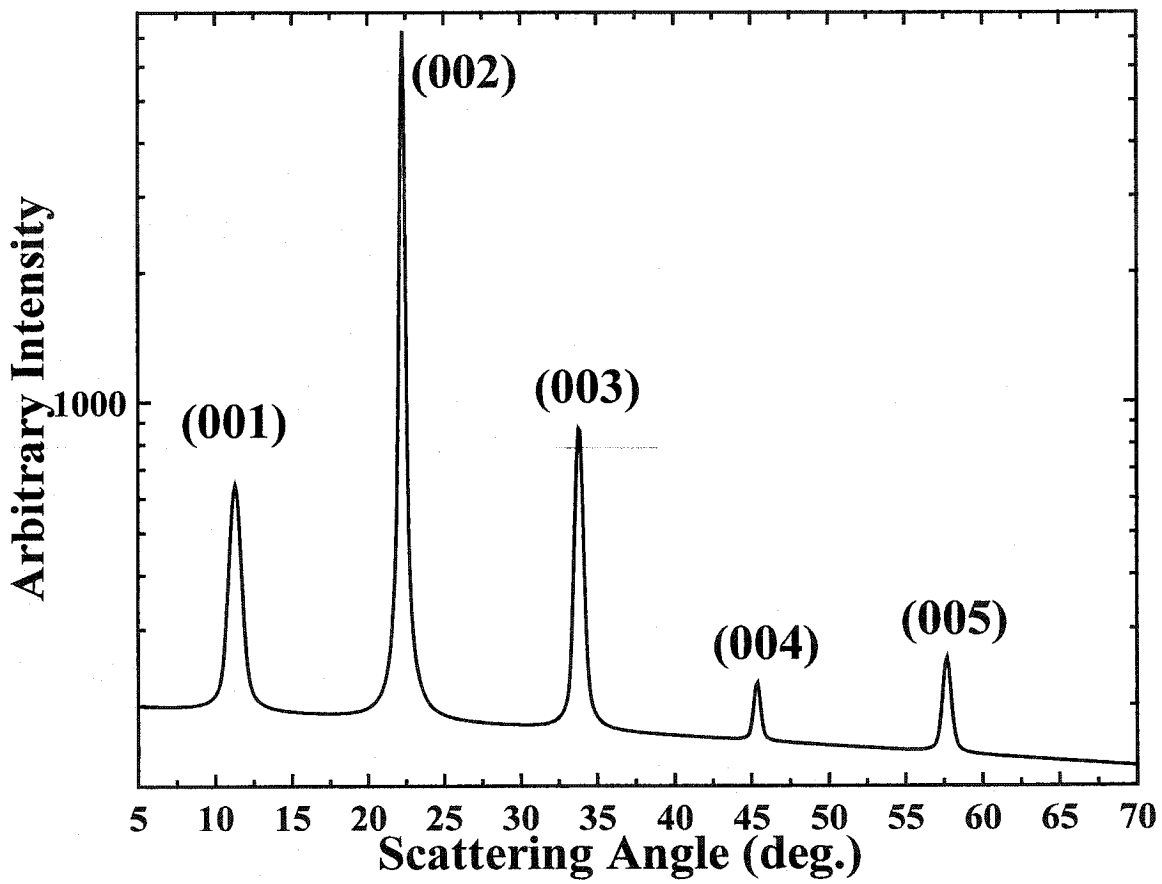

Figure 8.3.1 Scan 68 from the *in-situ* X-ray diffraction patterns shown in Figure 8.2.2.

There are several possible orientations of tetrafluoroborate that are possible. These are illustrated in Figure 8.3.2. The orientation depicted in Figure 8.3.2(a) assumes that the boron atoms are in the center between two carbon sheets. This would result in two layers of fluorine atoms on either side of the boron atoms. It is perhaps a little more

realistic to assume that the fluorine atoms are equidistant from the carbon layers resulting in an offset, from z=0, for the boron atoms, Figure 8.3.2(b). Figure 8.3.2(c) illustrates a possible orientation where there are two fluorine atoms above and another two below the boron atoms, all at the same distance.

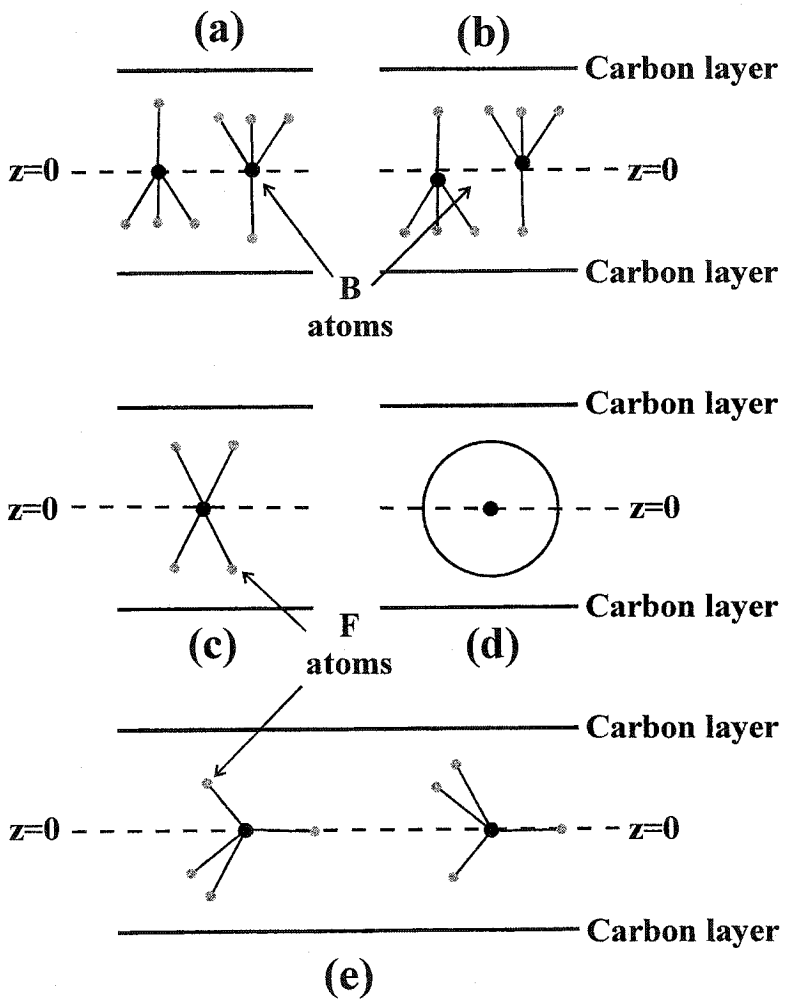

Figure 8.3.2 Illustrating possible orientations of the BF_4 anion between two carbon layers. (a) A central boron atom with two layers of fluorine atoms; (b) An offset boron atom with one layer of fluorine atoms; (c) A central boron atom with two fluorine atoms above and below; (d) A rotating BF_4 atom; and (e) one fluorine atom and the boron atom are centered at z=0 and the other three fluorine atoms are above and below the boron atom at the same distance.

Another possible orientation shown in Figure 8.3.2(d). Here it is assumed that the fluorine atoms are all equidistant from the central boron atom at z = 0. In this case, it is assumed that the atom is rotating between the carbon sheets. A fifth possible orientation for BF_4, shown in Figure 8.3.2(e), is one where one fluorine atom is located at z = 0 along with the boron atom and the other fluorine atoms are located above and below z = 0 at the same distance.

The orientation with two layers of fluorine atoms was used first in the calculations. Two very reasonable goodness of fits were obtained. The goodness of fits were 0.0271 and 0.0947. (Please keep in mind that a goodness of fit of zero is perfect). The X-ray diffraction patterns for the (00ℓ) peaks of these two calculations are shown in Figure 8.3.4. The first calculation, Figure 8.3.3(a), has a specific capacity of 296 mAh/g and the two layers of fluorine atoms were located at 0.970 Å and 0.130 Å. The value of 0.130 Å is ridiculously small. The second calculation, shown in Figure 8.3.3(b), has a specific capacity of 302 mAh/g and the two layers of fluorine atoms were located at 0.654 Å and 1.318 Å which seems a lot more reasonable. If the structure of BF_4 is considered, the two layers of fluorine atoms should occur at ~0.88 Å and 1.43 Å. When this is considered, the second calculation is more likely, however the specific capacity is larger than the experimental specific capacity of 215 mAh/g. The worst fitting peak for the first calculation shown in Figure 8.3.3(a) is the (001) peak which is too large where as in the second calculation the worst fitting peak is the (003) peak which is too small.

The second orientation with offset boron atoms also obtained goodness of fits that were very similar for various offset distances. The best goodness of fit obtained was that with an offset of zero which would make this orientation the same as the one with two

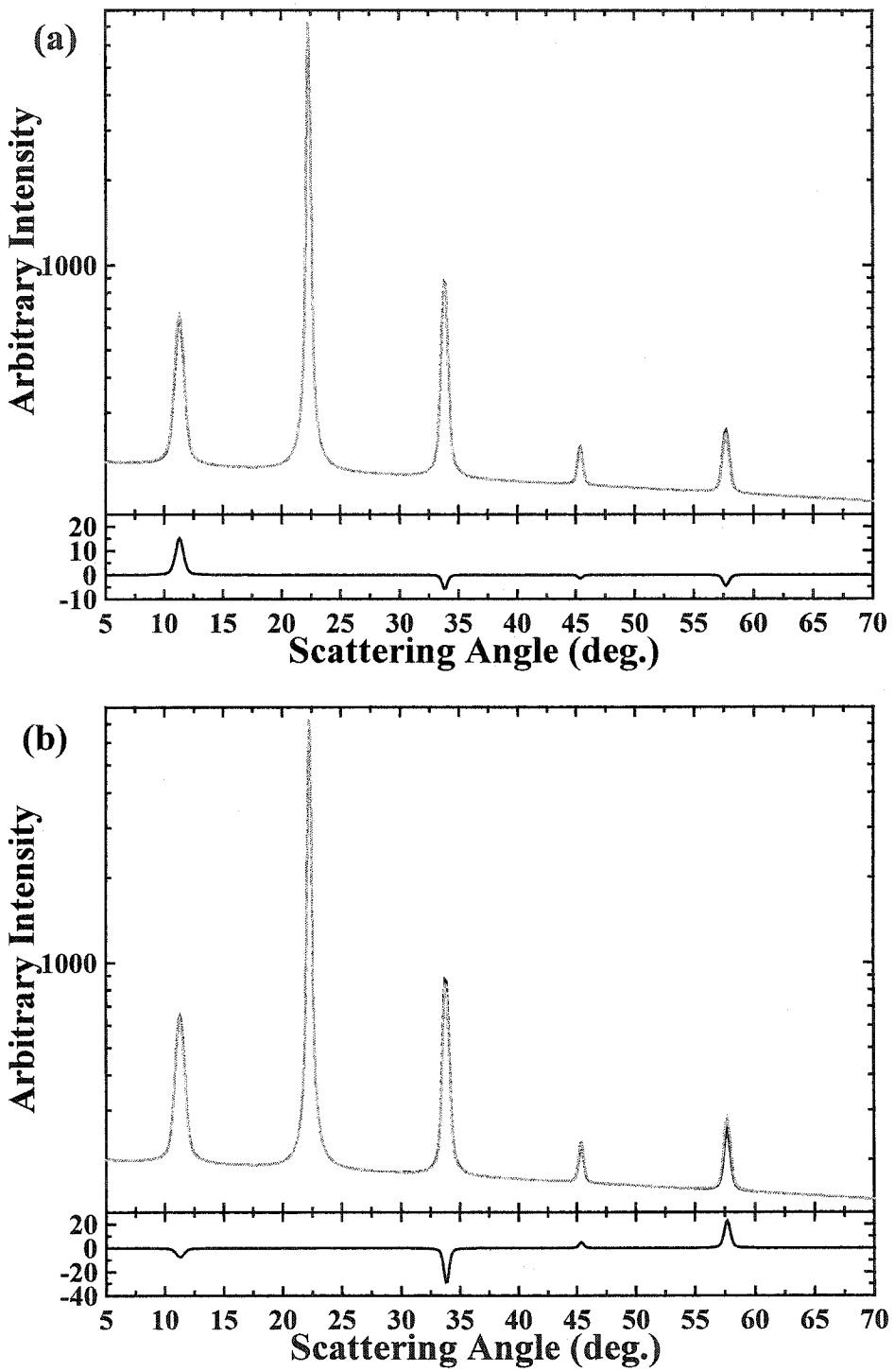

Figure 8.3.3 (top panels) Intensity versus scattering angle for calibrated experimental data, black line, and normalized calculated data, gray line, and (bottom panels) the difference between the experimental and calculated data, for a central boron atom with two layers of fluorine atoms for scan 68 as stage 1.

fluorine atoms above and below the central boron atom. If the offset distance was fixed at the expected value of 0.275 Å then the resulting goodness of fit was 0.3219 with a specific capacity of 263 mAh/g and a fluorine distance of 0.677 Å. The second calculation had a specific capacity of 322 mAh/g, a fluorine distance of 0.906 and offset distance of the boron of 0.160 Å. To obtain a single layer of fluorine atoms they should occur at 1.15 Å. The value obtained with this calculation is too small. The X-ray diffraction pattern obtained for this calculation is shown in Figure 8.3.4. The (003) peak is the worst fitting peak.

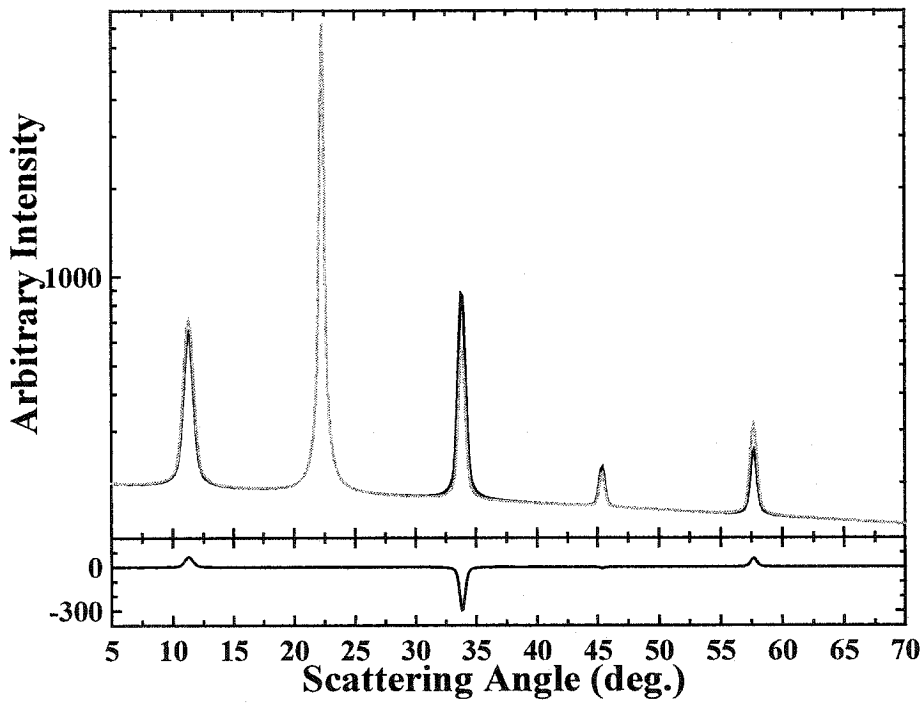

Figure 8.3.4 (top panel) Intensity versus scattering angle for calibrated experimental data, black line, and normalized calculated data, gray line, and (bottom panel) the difference between the experimental and calculated data, for an offset boron atom with one layer of fluorine atoms for scan 68 as stage 1.

The X-ray diffraction pattern for the calculation with the best goodness of fit for the third orientation with two fluorine atoms above and below the central boron atom is given in Figure 8.3.5. The goodness of fit in this case is 0.3084, the specific capacity was

264 mAh/g and the distance of the fluorine atoms from z = 0 was 0.690 Å. The specific capacity is again too high but by only 20%, and the fluorine distance is fairly small, although perhaps possible.

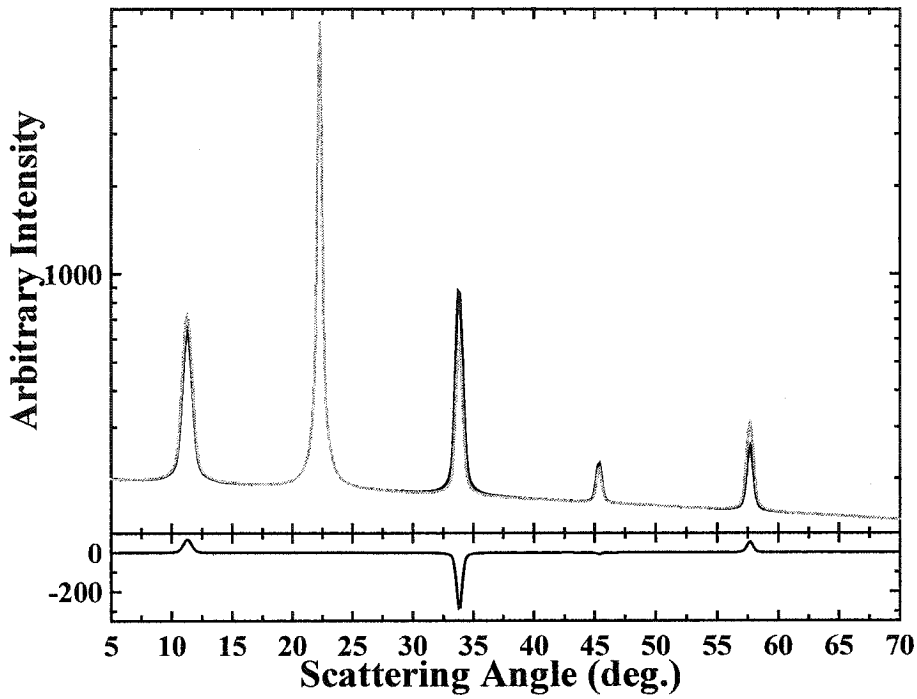

Figure 8.3.5 (top panel) Intensity versus scattering angle for calibrated experimental data, black line, and normalized calculated data, gray line, and (bottom panel) the difference between the experimental and calculated data, for a central boron atom with two fluorine atoms above and below for scan 68 as stage 1.

The next orientation, the rotating BF_4 atom, resulted in two similar goodness of fits of 0.3806 and 0.3943. The X-ray diffraction patterns for these two calculations are shown in Figure 8.3.6. The lower goodness of fit shown in Figure 8.3.6(a) required a specific capacity of 158 mAh/g with a fluorine distance of 1.429 Å. The other calculation, Figure 8.3.6(b), required a specific capacity of 268 mAh/g and a fluorine distance of 1.503 Å. The (003) peak for both calculations is the worst fitting peak.

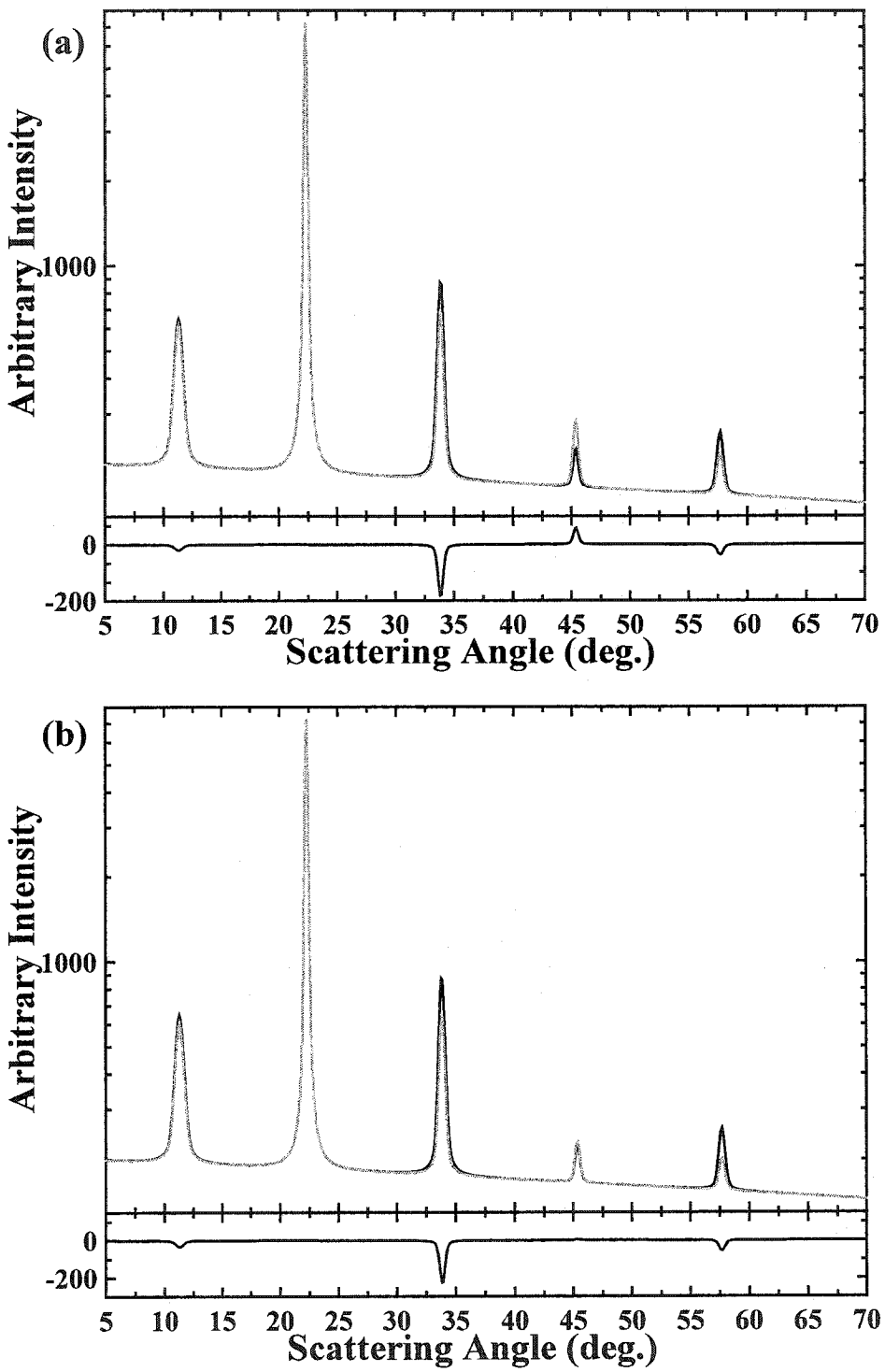

Figure 8.3.6 (top panels) Intensity versus scattering angle for calibrated experimental data, black line, and normalized calculated data, gray line, and (bottom panels) the difference between the experimental and calculated data, for a rotating BF_4 for scan 68 as stage 1.

The final orientation with one fluorine atom at z = 0 along with the boron atom resulted in a very good goodness of fit of 0.0518. The specific capacity required was 297 mAh/g and the resulting fluorine distance was 0.969 Å. The X-ray diffraction pattern for this calculation is shown in Figure 8.3.7. The (003) peak is again too small and it is the worst fitting peak. The goodness of fit is very small even though the specific capacity is about 40% larger than the experimental specific capacity and the fluorine distance is not that far off the expected value of 1.02 Å.

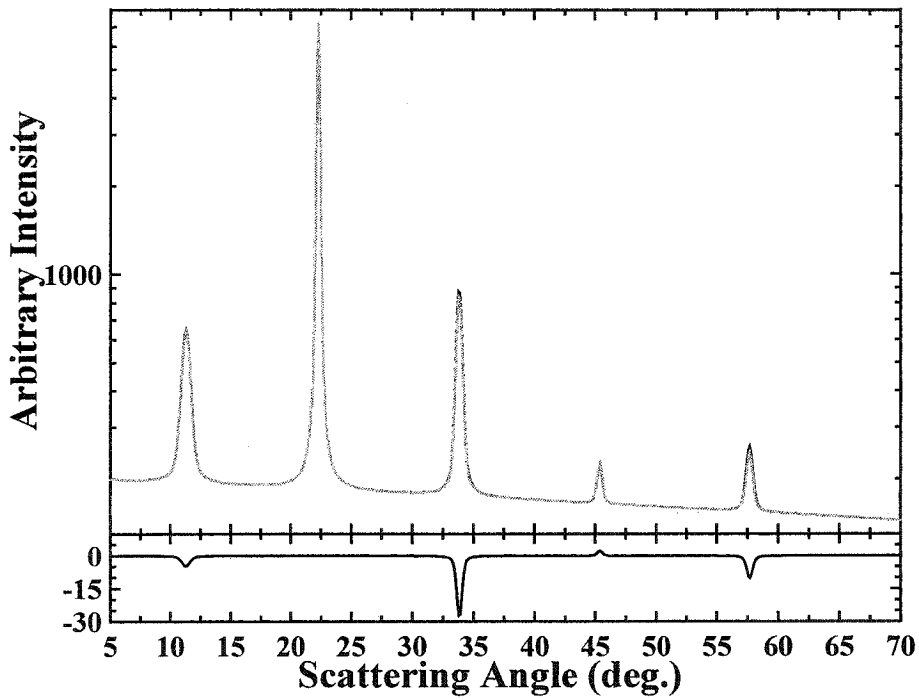

Figure 8.3.7 (top panel) Intensity versus scattering angle for calibrated experimental data, black line, and normalized calculated data, gray line, and (bottom panel) the difference between the experimental and calculated data, for the orientation with one fluorine atom at z = 0 along with the boron atom for scan 68 as stage 1.

To see if scan 68 is stage 2 rather than stage 1 similar calculations were performed assuming that layers were organized as stage 2. All of the calculations with the five orientations tested resulted in fits that were worse than the ones that assumed that scan 68 was stage 1. If similar goodness of fits were obtained the values required for

these calculations were too far off the actual/expected values to be considered valid. For instance, the carbon to carbon empty layer distance for several of the calculations was less than 3.0 Å. Since the C-C distance is really 3.36 Å that amount of compression is not very likely.

From this, it is easy to conclude that this particular stage with a c-axis distance of ~8 Å is definitely stage 1 and not stage 2.

At the moment it looks as though the orientation with two layers of fluorine atoms or the orientation with one fluorine atom at z = 0 are the more likely orientations although the specific capacities are larger than the experimental value. To see if similar results are obtained for stage 2, scan 41 will be analyzed next.

Figure 8.3.8 shows the (00ℓ) peaks with the background removed for scan 41. The c-axis repeat distance was determined to be 11.32 Å.

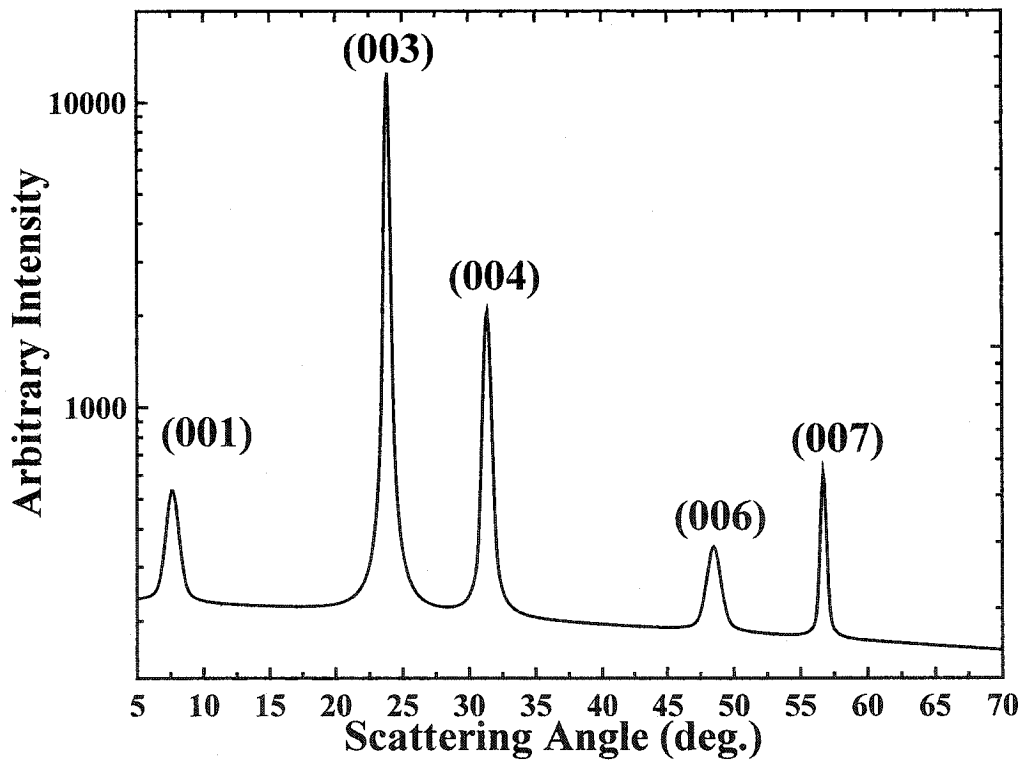

Figure 8.3.8 X-ray diffraction pattern for scan 41 with the background removed.

The first orientation used was the one with two layers of fluorine atoms. The goodness of fit obtained was 0.1143 with a specific capacity of 97 mAh/g, a C-C distance of 3.410 Å and fluorine z-axis distances of 0.652 Å and 1.857 Å. The X-ray diffraction pattern for this fit is shown in Figure 8.3.9. It can be easily seen that the agreement is fairly good except for the (004) peak, which is too small. However, the smaller fluorine z-axis distance is a little too small and the larger fluorine z-axis distance is a little too large. The specific capacity is reasonable since the experimental value was 85 mAh/g.

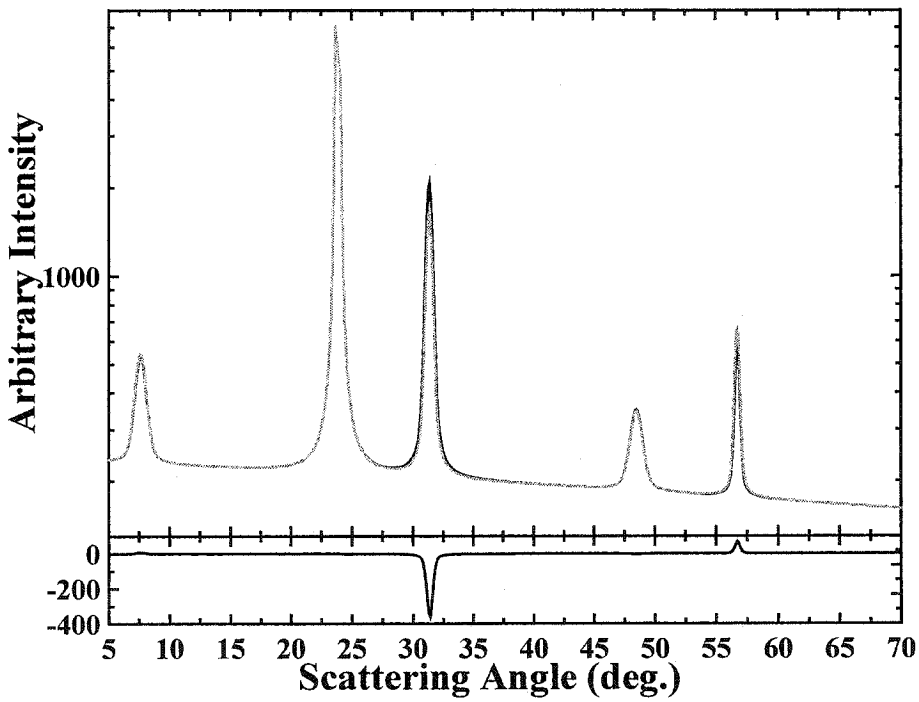

Figure 8.3.9 (top panel) Intensity versus scattering angle for calibrated experimental data, black line, and normalized calculated data, gray line, and (bottom panel) the difference between the experimental and calculated data, for a central boron atom with two layers of fluorine atoms for scan 41 as stage 2.

The next orientation used was the one with the offset boron atom. The smallest goodness of fit obtained was ~2 with a capacity of 100 mAh/g, a C-C distance of 3.15 Å, a fluorine distance of 1.362 Å and an offset distance of 0.256 Å. This calculation has a poor fit although the fluorine and offset distances are reasonable.

The orientation with two fluorine atoms above and below the boron atom has a large goodness of fit. This calculation had a goodness of fit of 0.9, a specific capacity of 63 mAh/g, a C-C distance of 3.471 Å and a B-F distance of 0.516 Å, which is quite small. The specific capacity is also smaller than the experimental value.

The rotating BF_4 orientation has a reasonable goodness of fit of 0.3030. The (004) peak is by far the worst fitting peak, see Figure 8.3.10. This calculation had a specific capacity of 55 mAh/g, which is too small, a C-C distance of 3.345 Å and a B-F distance of 1.946 Å, which is a little large.

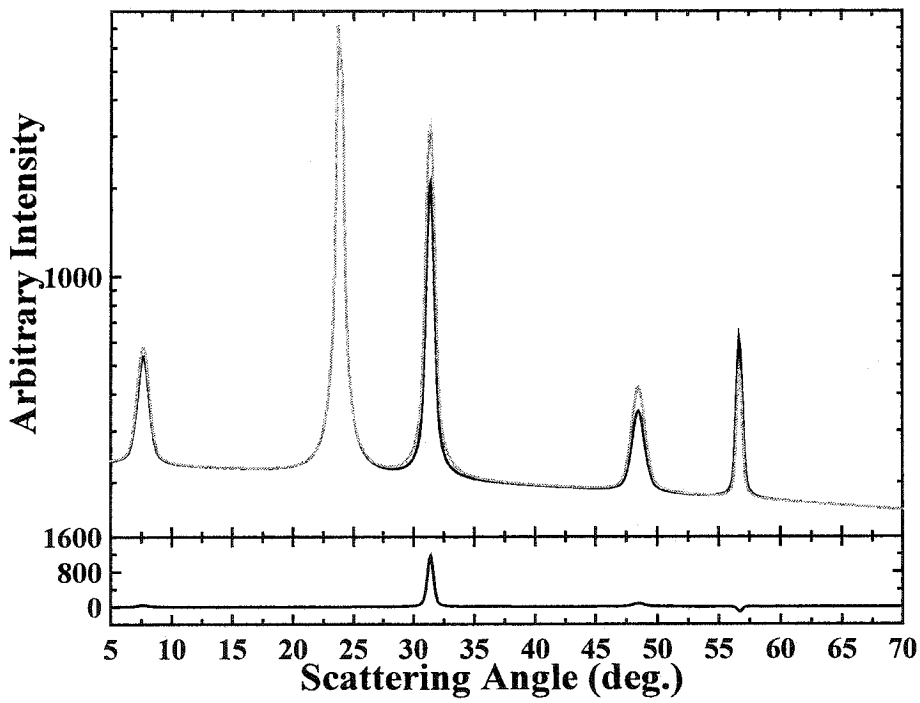

Figure 8.3.10 (top panel) Intensity versus scattering angle for calibrated experimental data, black line, and normalized calculated data, gray line, and (bottom panel) the difference between the experimental and calculated data, for a rotating BF_4 for scan 41 as stage 2.

The final orientation with one fluorine atom at z = 0 along with the boron atom and the other fluorine atoms equidistant from z = 0 resulted in a poor goodness of fit of 0.9. This calculation had a reasonable carbon to carbon empty layer distance of 3.426 Å,

a specific capacity that was too small, 64 mAh/g and a questionable fluorine c-axis distance of 0.614 Å. It is not very likely that this orientation is a possible one.

Of the four orientations used, the orientation with two layers of fluorine atoms has the best fit. This is consistent with stage 1 although the specific capacities obtained are larger than the experimental value of 85 mAh/g.

To be sure that scan 41 is indeed stage 2, similar calculations were performed assuming that the stage was stage 3 rather than stage 2, i.e. that there were two empty carbon layers rather than one and that the anion layer would therefore be smaller. All the best fits obtained were around at 1.5 or higher which is poor. For all cases the (001) peak was too large and the (004) and (006) peaks were too small.

From this it is safe to say that scan 68 represents stage 1 with a c-axis repeat distance of 8.011 Å and that scan 41 is stage 2 with a c-axis distance of 11.32 Å. The best goodness of fits for both stages were obtained with the orientation that assumed that there were two layers of fluorine atoms as in Figure 8.3.2. The specific capacities for these calculations of stage 1 were about 300 mAh/g which is about 40% higher than the experimental value of 215 mAh/g. The stage 2 calculations had specific capacity of 97 mAh/g which is about 15% higher than the experimental value of 85 mAh/g. This suggests that there is co-intercalation of the solvent. The calculations will be repeated with the solvent, EMS, added. The addition of EMS in the stage 1 calculations shall be discussed first.

The goodness of fits obtained for the orientation with two layers of fluorine atoms were comparable to the ones without EMS. The calculation obtained at the experimental specific capacity of 215 mAh/g had a goodness of fit of 0.2088. The two fluorine

distances were determined to be 0.773 Å and 1.233 Å and the EMS fraction was 0.340. The X-ray diffraction pattern for this calculation is shown in Figure 8.3.11.

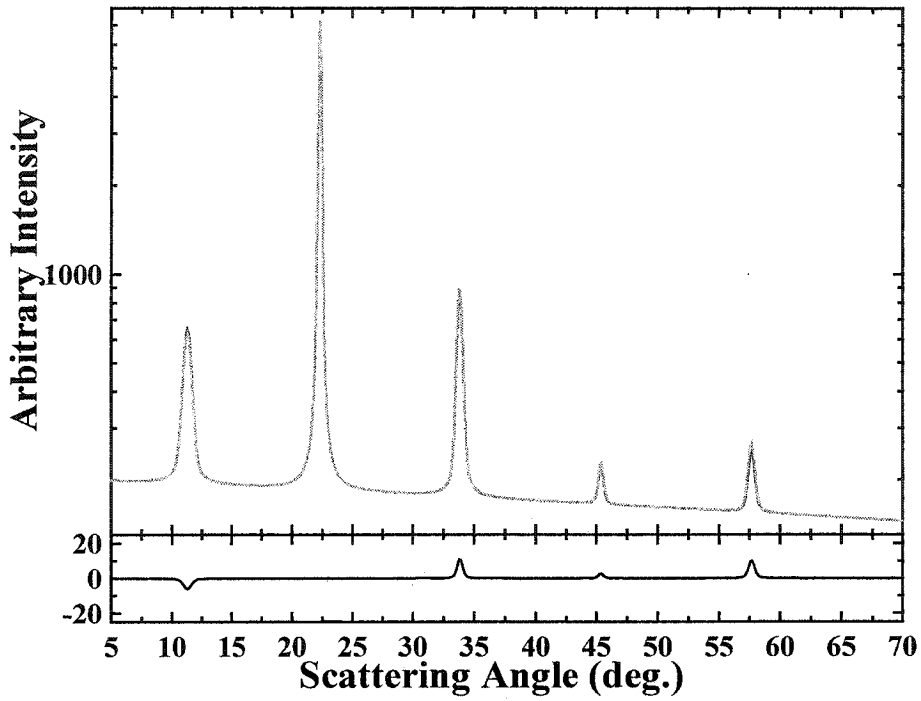

Figure 8.3.11 (top panel) Intensity versus scattering angle for calibrated experimental data, black line, and normalized calculated data, gray line, and (bottom panel) the difference between the experimental and calculated data, for a central boron atom with two layers of fluorine atoms for scan 68 as stage 1 with EMS.

Figure 8.3.12 shows the X-ray diffraction pattern for a calculation with a reasonable goodness of fit for the orientation with an offset boron atom. This calculation has a goodness of fit of 0.3234 at a specific capacity of 215 mAh/g, a fluorine distance of 0.979 Å, an offset distance of 0.291 Å and an EMS fraction of 1.08. This EMS fraction seems rather large and is most likely not very reasonable. The (001), (003) and (005) peaks are too small with the (003) peak being the worst fit peak. This calculation is comparable with those obtained without EMS present.

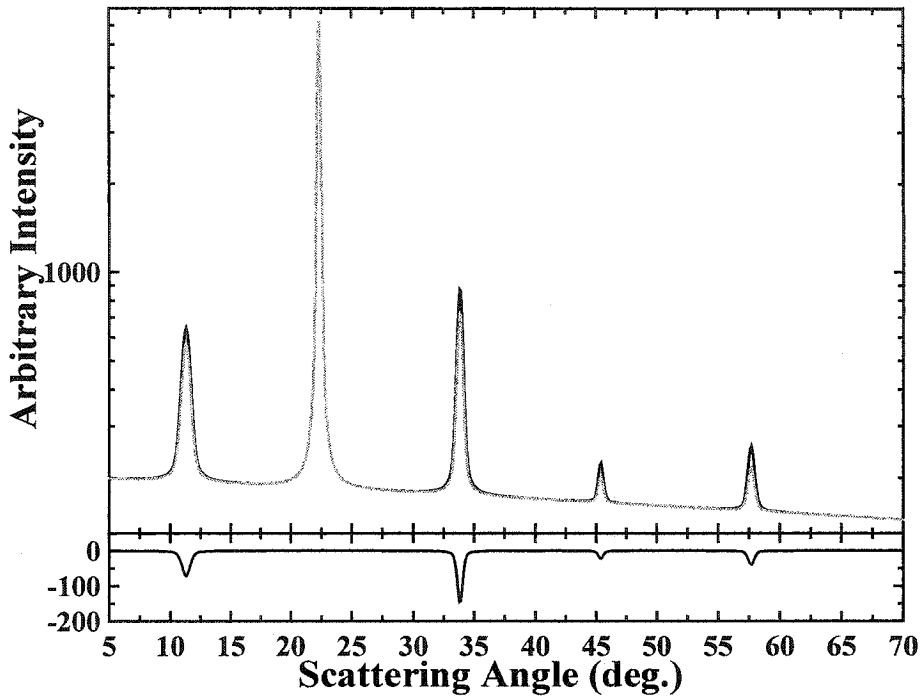

Figure 8.3.12 (top panel) Intensity versus scattering angle for calibrated experimental data, black line, and normalized calculated data, gray line, and (bottom panel) the difference between the experimental and calculated data, for an offset boron atom with one layer of fluorine atoms for scan 68 as stage 1 with EMS.

The next orientation, two fluorine atoms above and below the central boron atom, 2F-B-2F, resulted in a better goodness of fit than without EMS. This calculation had a goodness of fit of 0.1977 at a specific capacity of 215 mAh/g, a fluorine distance of 0.770 Å and an EMS fraction of 0.250. The X-ray diffraction pattern for this calculation is shown in Figure 8.3.13. As with the other calculations the (003) peak is the worst fitting peak.

The rotating BF_4 orientation calculations with EMS did not result in better goodness of fits. The goodness of fit obtained at the experimental specific capacity, 215 mAh/g, was 0.589. The resulting fluorine c-axis distance was 1.484 Å with an EMS fraction of 0.360. The X-ray diffraction pattern is shown in Figure 8.3.14. Again the (003) peak is too small.

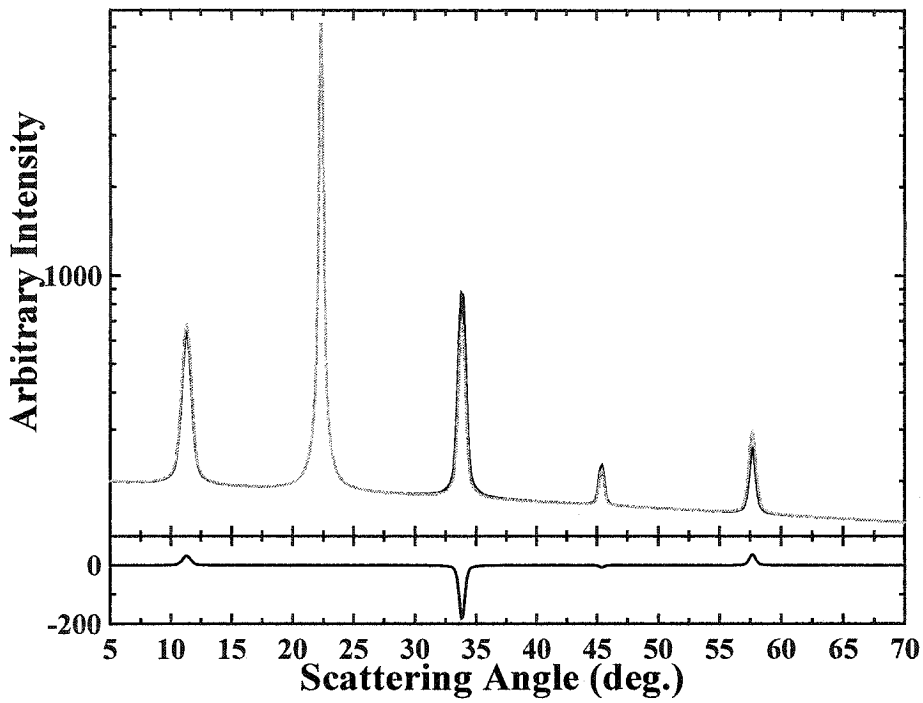

Figure 8.3.13 (top panel) Intensity versus scattering angle for calibrated experimental data, black line, and normalized calculated data, gray line, and (bottom panel) the difference between the experimental and calculated data, for a central boron atom with two fluorine atoms above and below for scan 68 as stage 1 with EMS.

The calculations for the final orientation of one fluorine atom at z =0 obtained a goodness of fit of 0.3254 at the experimental specific capacity. This goodness of fit is much larger than the goodness of fit obtained without EMS. The fluorine distance is 0.969 Å and the EMS fraction is 0.3. The X-ray diffraction pattern obtained for this orientation is shown in Figure 8.3.15. Again the (003) peak is too small.

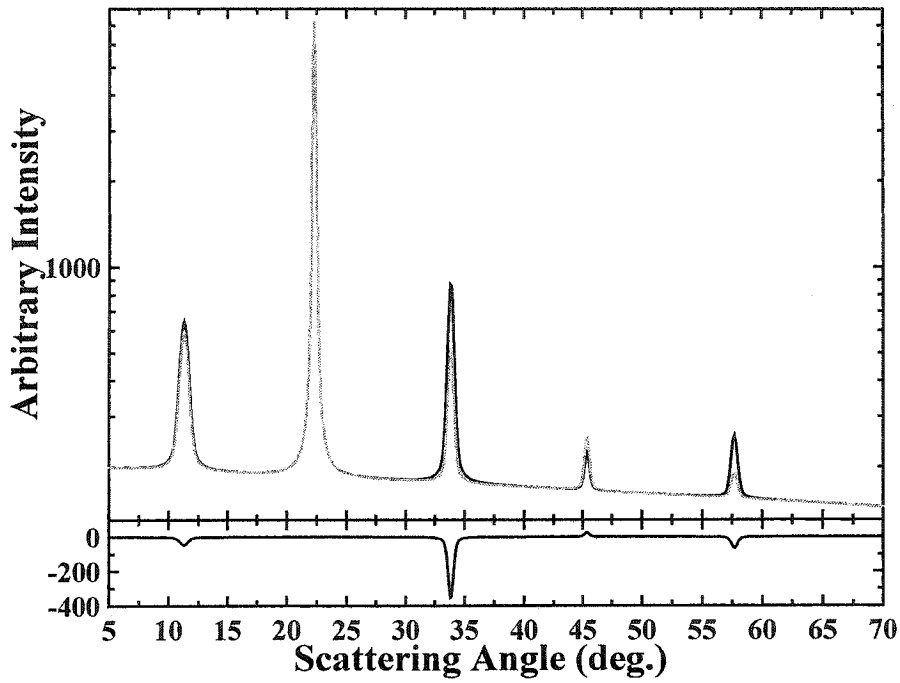

Figure 8.3.14 (top panel) Intensity versus scattering angle for calibrated experimental data, black line, and normalized calculated data, gray line, and (bottom panel) the difference between the experimental and calculated data, for a rotating BF_4 for scan 68 as stage 1 with EMS.

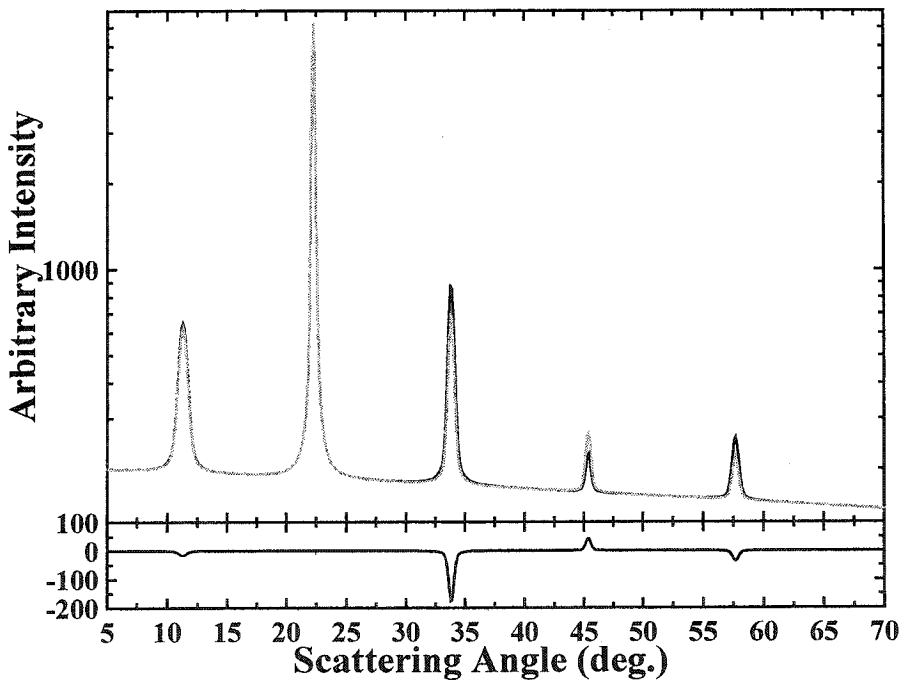

Figure 8.3.15 (top panel) Intensity versus scattering angle for calibrated experimental data, black line, and normalized calculated data, gray line, and (bottom panel) the difference between the experimental and calculated data, for the orientation with one fluorine atom at z = 0 along with the boron atom for scan 68 as stage 1 with EMS.

Next the stage 2 calculations with EMS were performed. The orientation with two layers of fluorine atoms resulted in a low goodness of fit of 0.1238 with a specific capacity of 85 mAh/g which is the experimental value. A reasonable carbon layer distance of 3.411 Å was also obtained. The fluorine distances were 0.681 Å and 1.911 Å and the EMS fraction was 0.114. The X-ray diffraction pattern obtained from this calculation is shown in Figure 8.3.16. The only peak with a real problem is the (004) peak. The distances obtained from the geometry of BF_4 would be 0.8 Å and 1.43 Å. The lower calculated value is too low whereas the higher value is too high. Even though this seems a very likely orientation for BF_4 it may not be possible with such a large fluorine z-axis distance.

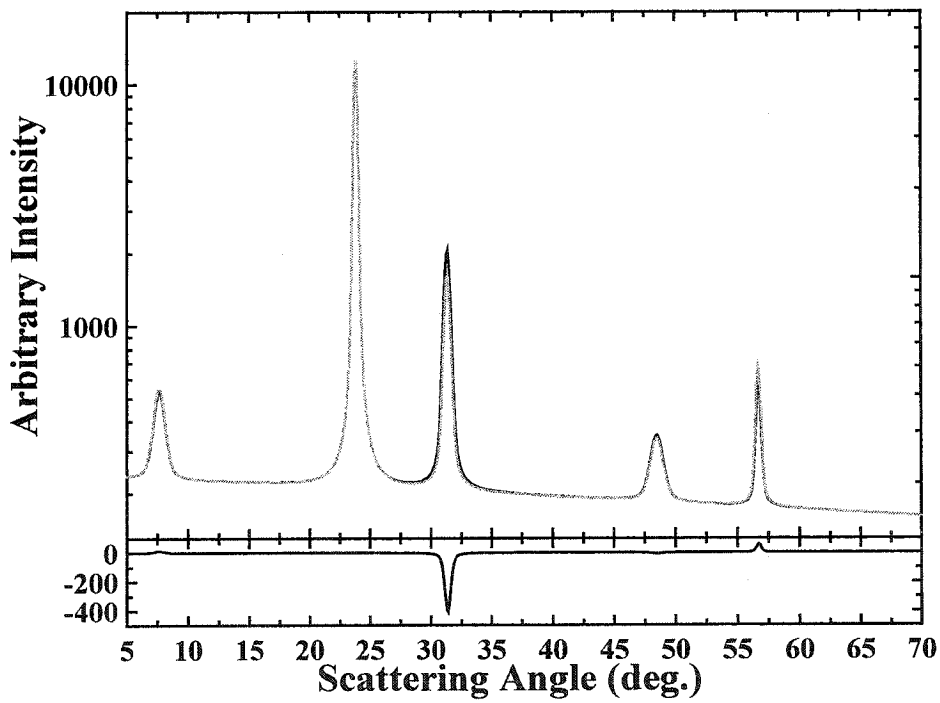

Figure 8.3.16 (top panel) Intensity versus scattering angle for calibrated experimental data, black line, and normalized calculated data, gray line, and (bottom panel) the difference between the experimental and calculated data, for a central boron atom with two layers of fluorine atoms for scan 41 as stage 2 with EMS.

The goodness of fits obtained for the offset boron atom orientation were lower with EMS than without EMS however the values were still very poor. The goodness of fits obtained were greater than one. For instance, at the experimental specific capacity the goodness of fit was 1.2, the C-C distance was 3.152 Å, the fluorine z-axis distance was 1.413 Å, the boron offset distance was 0.247 Å and the EMS fraction was 0.249. This is very likely not the orientation that BF_4 assumes.

The orientation with two fluorine atoms above and below the central boron atom resulted in s slightly better goodness of fit with EMS than without. The goodness of fit was 0.85 with a C-C distance of 3.252 Å, a fluorine distance of 1.444Å, a specific capacity of 70 mAh/g and an EMS fraction of 0.499.

The rotating BF_4 orientation did not result in goodness of fits with specific capacities close enough to the experimental capacity to be considered possible. This is most likely not a possible orientation if EMS co-intercalates along with BF_4.

The orientation that has a fluorine atom at z = 0 obtained a slightly better goodness of fit of 0.834 with EMS than without. The resulting capacity was 85 mAh/g, the C-C distance was 3.318 Å, the fluorine distance was 1.383 Å and an EMS fraction of 0.152. The fit is still quite poor.

The results for the stage 1 and stage 2 calculations with and without EMS co-intercalating along with BF_4 are summarized in Table 8.5 along with the expected values for each orientation.

The stage 1 and stage 2 fits without EMS and the fits for stage 2 with EMS all have one particular orientation that clearly has a better fit than the rest. This orientation is the orientation with two layers of fluorine atoms as shown in Figure 8.3.2(a). The

values for the various parameters are, unfortunately, not consistent suggesting that this, perhaps, is not the correct orientation. In general, the stage 1 values do not agree well with the stage 2 values. Also the fits for stage 1 with EMS does not have a clear best orientation. This is unfortunate and clearly means that further investigation is needed.

It is also unfortunate that the rotating BF_4 orientation did not fare better. Since PF_6 was found to most likely rotate between the carbon layers it was thought that BF_4 would also rotate. It is interesting to note that the fits with EMS for the rotating BF_4 orientation have similar goodness of fits as the calculations without EMS. Also, both the stage 1 and stage 2 calculations without EMS have specific capacities that are too small.

These calculations seem to have raised more questions than provided answers. It is clear that the stage with a c-axis spacing of ~8.0 Å is stage 1 and the stage with a c-axis distance of ~11.3 Å is stage 2. However, it cannot be said conclusively which orientation is the correct one or even if EMS co-intercalates with BF_4 since some of the specific capacities obtained without EMS were not extremely far off the experimental specific capacities.

Although the configurations of PF_6 and BF_4 are different they are similar in size and the fact that the layer spacings are similar is not suprising. Both BF_4 and PF_6 would be possible candidates for anion intercalation into graphitic carbon materials. Since it appears, from section 8.1, that PF_6 has less specific capacity loss; it perhaps is the better choice.

Stage	Orientation	Fit	Cap. (mAh/g)	F dist. (Å)	F dist. #2 (Å)	B offset (Å)	C-C dist. (Å)	EMS frac.
1	2 layers of F	0.0271	296	0.970	0.130			
		0.0947	302	0.654	1.318			
		0.2088	215	0.773	1.233			0.340
	Expected Values		215	0.88	1.43			
	Offset B	0.3219	263	0.677		0.275		
		0.3234	215	0.979		0.291		1.08
	Exp. Values		215	1.155		0.275		
	2F-B-2F	0.3084	264	0.690				
		0.1779	215	0.770				0.250
	Exp. Values		215	~0.6				
	Rotating BF_4	0.3806	158	1.429				
		0.3943	268	1.503				
		0.589	215	1.484				0.360
	Exp. Values		215	1.4				
	1 F at z = 0	0.0518	297	0.969				
		0.3254	215	0.969				0.300
	Exp. values		215	1.02				
2	2 layers of F	0.1143	97	0.652	1.857		3.410	
		0.1238	85	0.681	1.911		3.411	0.114
	Exp. values		85	0.88	1.43		3.36	
	Offset B	2	100	1.362		0.256	3.150	
		1.2	85	1.413		0.247	3.152	0.249
	Exp. values		85	1.155		0.275	3.36	
	2F-B-2F	0.9	63	0.516			3.521	
		0.85	70	1.444			3.252	0.499
			85	~0.6			3.36	
	Rotating BF_4	0.3030	55	1.946			3.345	
		poor	N/A	N/A			N/A	N/A
	Exp. values		85	1.4			3.36	
	1 F at z = 0	0.9	64	0.614			3.426	
		0.834	85	1.383			3.318	0.152
	Exp. values		85	1.02			3.36	

Table 8.5 Summarizing the results for stage 1 and stage 2 calculations for BF_4. The expected values are determined from the orientation of BF_4 and the experimental value of the capacity and experimental distance between the carbon layers.

Chapter 9 Conclusions and Future Work

This chapter will discuss the viability of dual carbon cells, as well as summarizing the important and interesting features discovered during the course of this thesis. As with all research there are always more questions to be answered and future work to be performed, some of which will be discussed.

Section 9.1 Viability of Dual-Carbon Cells

It has been shown that anion intercalation into carbon materials occurs but the question remains whether or not it has a real use in commercial cell. Here, the viability of a commercial cell will be discussed. (This work has been published [61]).

Assume that the cell's geometry is as depicted in Figure 9.1.1. There are two electrodes, both of carbon but of different thicknesses, t_a and t_b. Each will have their own specific capacities, q_a and q_b respectively since one is the positive and the other the negative electrode. Also assume that $LiPF_6$ will be used as the salt in the electrolyte and therefore $q_a = 370$ mAh/g (lithium intercalation) and $q_b = 140$ mAh/g (PF_6 intercalation). Since the salt is the source of the charge the molarity of the electrolyte changes. M_d will be the molarity at the end of discharge and M_c will be the molarity at the end of charge. Naturally, $M_d > M_c$. The porosity, φ, of the graphite electrodes will also come into play. Let ρ_c be the bulk density of the electrolyte and ρ_s the bulk density of the separator which has a porosity given by φ_s and a thickness t_e. The bulk density of graphite is given by $\rho = 2.2$ g/cm^3.

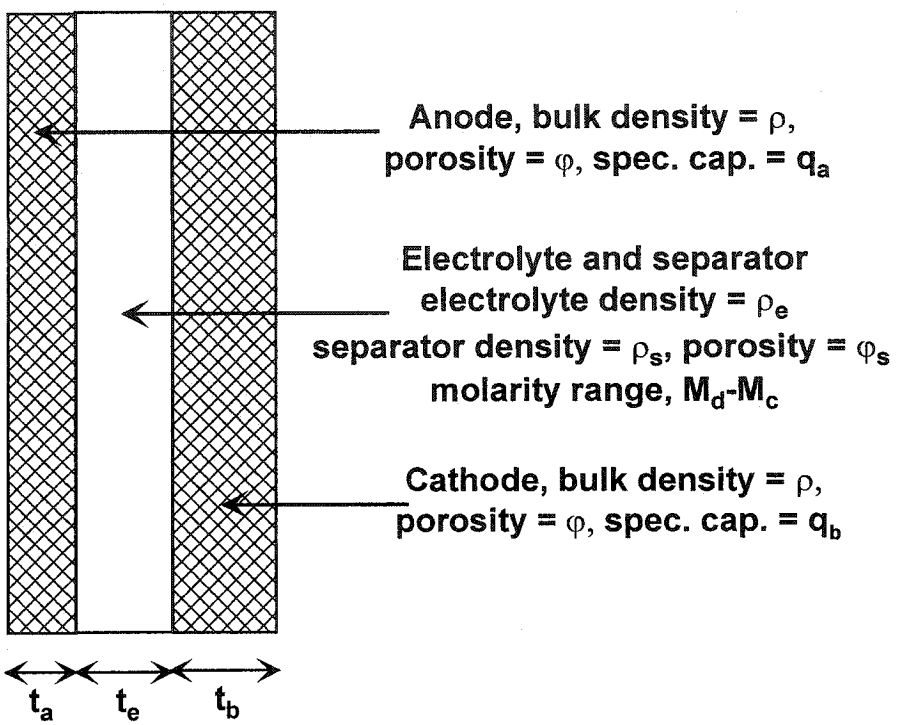

Figure 9.1.1 Schematic of the cell used for the modeling described in the text.

The amount of charge, Q_{total}, that the electrodes can store is given by

$$\begin{aligned} Q_a &= At_a(1-\varphi)q_a\rho \\ Q_b &= At_b(1-\varphi)q_b\rho \end{aligned} \tag{9.1}$$

where A is the cross-sectional area of the electrode. Similarly the amount of charge stored within the electrolyte is given by

$$Q_e = A(M_d - M_c)(t_a\varphi + t_b\varphi + t_s\varphi_s)R \tag{9.2}$$

where R is a conversion factor and is equal to 26.8 AhL/M.

In order for the cell to be charge balanced with V being the volume of the cell

$$\frac{Q_a}{Vol} = \frac{Q_b}{Vol} = \frac{Q_e}{Vol} = \frac{Q}{Vol} \tag{9.3}$$

or

$$\frac{Q}{Vol} = \frac{At_a(1-\varphi)q_a\rho}{A(t_a + t_b + t_s)} \tag{9.4}$$

To limit the number of variables in the above equation, t_b and t_s should be expressed in terms of t_a. By equating Q_a and Q_b from equation (9.1) t_b can be expressed in terms of t_a:

$$t_b = \frac{t_a q_a}{q_b}. \tag{9.5}$$

Similarly, t_e can be found in terms of t_a by equating Q_a with Q_e which results in

$$t_e = \frac{t_a\left[(1-\varphi)q_a\rho - (M_d - M_c)\varphi\left(1+\frac{q_a}{q_c}\right)R\right]}{(M_d - M_c)\varphi_s R} \tag{9.6}$$

Using equations 9.5 and 9.6 in 9.4, results in

$$\frac{Q}{V} = \frac{(1-\varphi)q_a\rho}{1+\frac{q_a}{q_c}+\frac{(1-\varphi)q_a\rho - (M_d - M_c)\varphi\left(1+\frac{q_a}{q_c}\right)R}{(M_d - M_c)\varphi_s R}} \tag{9.7}$$

Assume for the moment that there is no separator, i.e. φ_s=1 then equation (9.7) reduces to

$$\frac{Q}{V} = \frac{q_a\rho}{1+\frac{q_a}{q_b}+\frac{q_a\rho}{(M_d - M_c)R}} \tag{9.8}$$

It is interesting to note that the capacity per unit volume, the volumetric capacity, does not depend on the electrode porosity this resulted from assuming that all the electrolyte can be used in the cell reaction.

Another way of measuring the usefulness and viability of the cell is to consider the gravimetric capacity, Q_{total}/m_{total}. It s given by

$$\frac{Q_{total}}{m_{total}} = \frac{At_a(1-\varphi)q_a\rho}{A\left[(t_a+t_b)\{(1-\varphi)\rho+\varphi\rho_e\}+t_e\{\varphi_s\rho_e+(1-\varphi_s)\rho_s\}\right]} \tag{9.9}$$

By substituting t_b and t_e and again assuming φ_s=1, equation (9.9) reduces to

$$\frac{Q_{total}}{m_{total}} = \frac{q_a}{1 + \frac{q_a}{q_b} + \frac{q_a \rho_e}{(M_d - M_c)R}} \tag{9.10}$$

By multiplying the volumetric and gravimetric capacities by the average cell voltage, which was found to be about 4.5 V, the volumetric and gravimetric energy densities could be determined.

To account for the various components of a commercial cell the following assumptions are made: (1) the total mass of the cell is about 70% electrodes and electrolyte and the other 30% is the current collectors and the cell casing; and (2) the total volume of the cell is about 80% electrodes and electrolyte and the other 20% is the current collectors and the cell casing.

The following parameters will be used to calculate the volumetric and gravimetric capacities (equations 9.8 and 9.10, respectively): q_a = 370 mAh/g, q_b = 140 mAh/g, ρ = 2.2 g/cm^3, ρ_e = 1.4 g/cm^3, φ_s = 1, and R = 26.8 mAh cm^3/M.

Figures 9.1.2 and 9.1.3 show the volumetric and gravimetric capacities versus the electrolyte molarity range, (M_d-M_c) during cycling of the cell. The volumetric capacity increases quickly to a value of about 60 Ah/L and 70 Ah/L for an optimized cell with and without the current collectors and cell case, respectively, at a molarity range of 4 M. The electrolyte concentration operating range is very wide and is most likely unrealistic for liquid electrolytes. For most lithium slats the electrolyte viscosity increases rapidly above concentrations of 2 M. This leads to a severe reduction of ionic conductivity [62]. A practical cell operating at room temperature would have a charge concentration of 2 M and a discharge concentration of 0.5 M. In other words an operating range of 1.5 M. At this range the volumetric capacity for the whole cell would be ~30 Ah/L. In comparison,

the gravimetric capacities for an operating range of 4 M and 1.5 M are 30 Ah/kg and 17 Ah/kg for the whole cell. With discoveries of new electrolytes with high salt concentrations may lead to cells with larger volumetric and gravimetric capacities as long as these are stable at high voltages [63, 64].

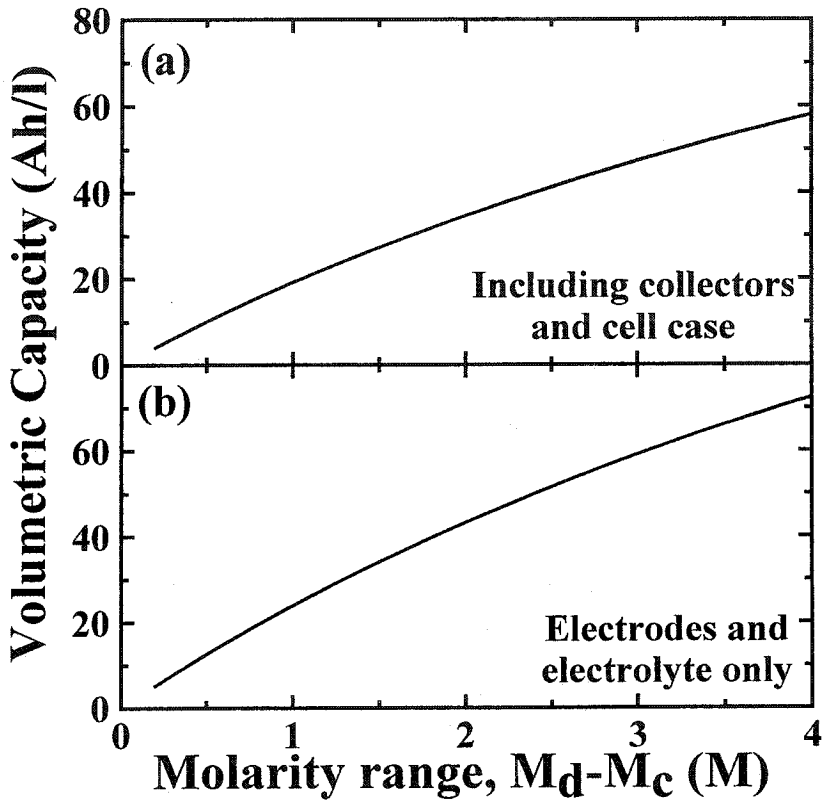

Figure 9.1.2 Volumetric capacity versus the electrolyte concentration operating range for (a) the complete cell and (b) without the current collectors and cell casing.

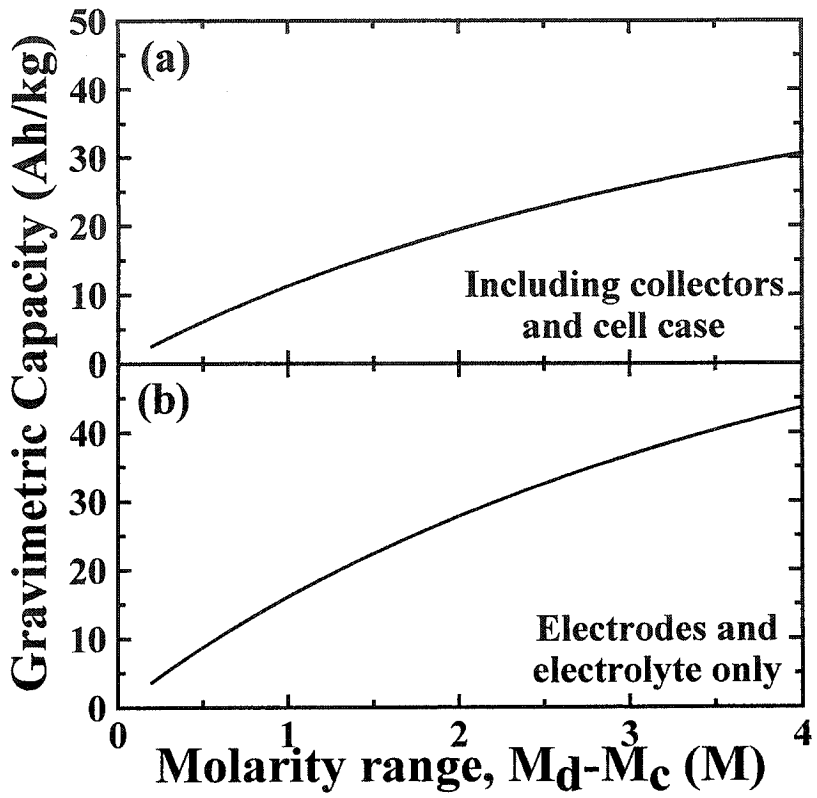

Figure 9.1.3 Gravimetric capacity versus the electrolyte concentration operating range for (a) the complete cell and (b) without the current collectors and cell casing.

Another way to see how viable these cells are is to consider the volumetric and gravimetric energy densities which are shown in Figures 9.1.4 and 9.1.5, respectively. These are shown with respect to the electrolyte concentration operating range. With an operating range of 4 M, energy densities of about 260 Wh/L and 140 Wh/kg for an optimized cell are achieved. If this range is 1.5 M instead, these energy densities are reduced to 130 Wh/L and 70 Wh/kg.

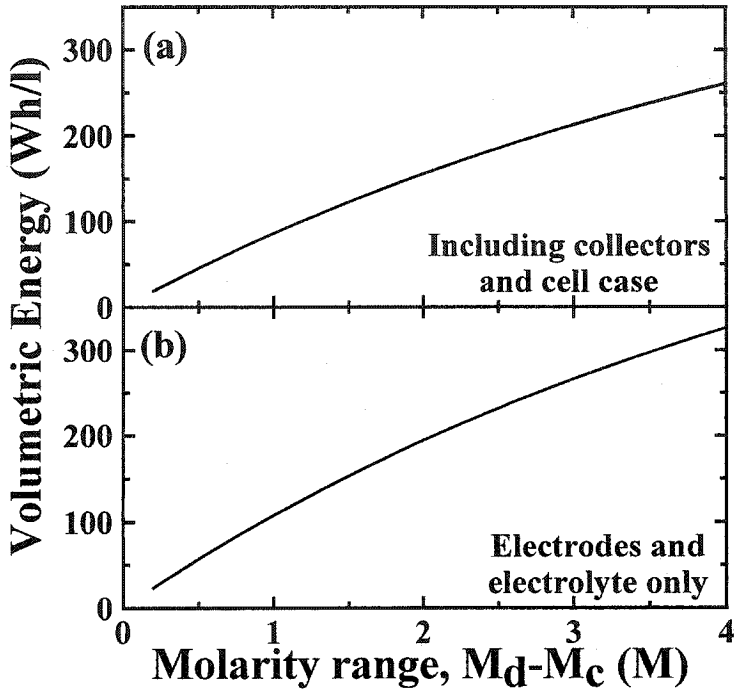

Figure 9.1.4 Volumetric energy density versus the electrolyte concentration operating range for (a) the complete cell and (b) without the current collectors and cell casing.

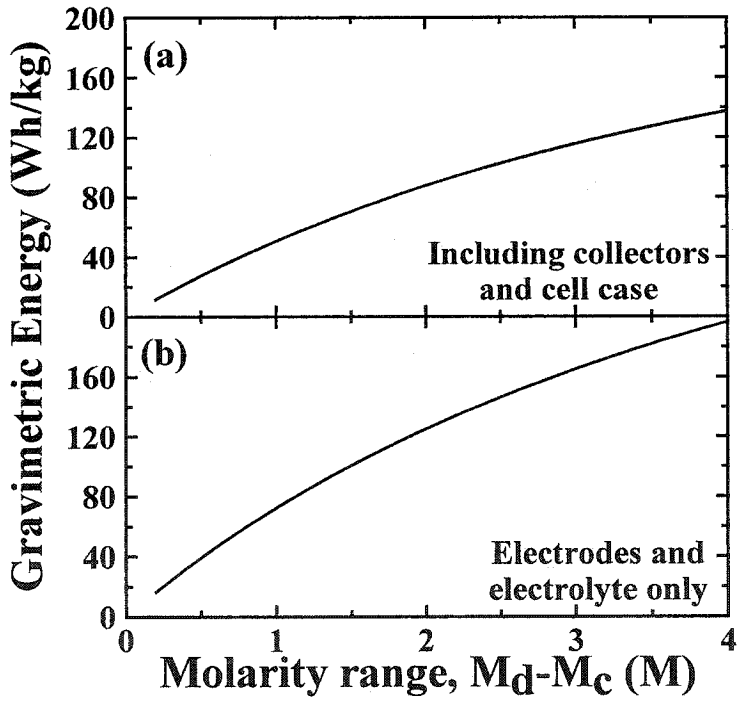

Figure 9.1.5 Gravimetric energy density versus the electrolyte concentration operating range for (a) the complete cell and (b) without the current collectors and cell casing.

A typical lithium-ion cell is the 18650 size which is 18 mm in diameter and 65 mm in length. These cells have capacities of 2400 mAh and a mass of 45 g [65]. This results in energy densities of about 530 Wh/L and 200 Wh/kg. Since the energy densities for dual graphite cells are much lower at the realistic operating range of 1.5 M, they would have difficulty competing with today's lithium ion cells. However, there are possible environmental advantages with dual graphite cell when the fact that these cells have no transition metals is considered. The main problem is that highly concentrated electrolytes are both corrosive and expensive. At the moment, until new inexpensive salts and electrolytes that can operate at high molarities and potentials are discovered, dual graphite cells are not very viable for commercial use.

Section 9.2 Conclusions

As with all research, interesting discoveries happen along the way. By charging rather than discharging a lithium-carbon electrochemical cell, the anions rather than lithium ions, intercalate into the carbon electrode. This occurred not only in graphitic carbons such as Fluka graphite, meso-carbon micro-bead and high temperature cokes but also in fabrics and fibers and low temperature cokes. Anion intercalation into these various carbon materials had varying degrees of success, i.e. some had better capacity retention than others.

Preliminary work showed that different solvents affect the performance of electrochemical cells with anion intercalation into the carbon electrode. It was found that EMS was more stable than EC+DEC at the high potentials (and high salt concentration) that are required in order to insert the anion into the carbon materials.

Once it was discovered that EMS was a more stable choice for the solvent, a range of carbon materials with a different amount of turbostratic disorder were tested. It was found that XP3 cokes heated to higher temperatures were less disordered and performed better electrochemically. The higher temperature cokes have a smaller percentage loss of capacity during cycling.

During the investigation of how turbostratic disorder affected the electrochemical cycling of the carbon materials several interesting things were discovered. It was found that turbostratically disordered carbon layers prefer to remain disordered until PF_6 is inserted between these layers. As a consequence of this it was also found that the more disordered samples become more ordered during the first part of charge as PF_6 began to intercalate into the carbon electrode. At the top of charge, PF_6 remained in stage 1 for an

extended period of time before enough PF_6 was removed to form stage 2. The voltage at which PF_6 no longer remained trapped in stage 1 decreases with an increasing amount of disorder. It was also found during the investigation of the XP3 cokes that during intercalation that co-existence of stage 1 and stage 2 did not occur for a pure stage 2. As the potential was increased and more PF_6 intercalated into the carbon electrode a few of the empty layers in a region of stage 2 were filled with enough PF_6 to change the average stage index to a value slightly lower than 2.

It was also discovered that perhaps not all anions intercalate into ordered XP3 coke. Both PF_6 and BF_4 intercalated into the XP3 coke 2600°C sample. No evidence of ClO_4 intercalation was found through in-situ X-ray diffraction experiments although the differential capacity versus potential curves suggest that some intercalation of ClO_4 did occur. It is thought that a large amount of the solvent co-intercalated with ClO_4 which, most likely, resulted in a large amount of exfoliation which effectively destroyed the layered structure of the carbon material. Electrolyte decomposition most likely also plays a major role. An interesting point is that PF_6 and BF_4 intercalation into XP3 2600°C obtained stage 2 and stage 1 with very similar c-axis spacings, about 11.3 Å for stage 2 and 8 Å for stage 1.

During the BF_4 *in-situ* X–ray diffraction experiments it was discovered that that BF_4 formed an intermediate stage between stage 2 and stage 1 as the potential was increased. This stage has alternating layers that are probably fully and partly filled with intercalated BF_4.

Ex-situ X-ray diffraction experiments have shown that PF_6 most likely rotates about the phosphorous atom between the carbon sheets. The orientation for BF_4 is not as

definite although there may be two separate layers of fluorine atoms about a central boron atom. It was also found that some co-intercalation of the solvent occurred along with hexafluorophosphate. Unfortunately, the EMS fraction was inconsistent between stage 1 and stage 2, something that should be investigated further. It was also not clear if EMS co-intercalates along with tetrafluoroborate.

Section 9.3 Future Work

Since it was not clear which orientation BF_4 assumed during intercalation, further research should be conducted. As with PF_6, *ex-situ* X-ray diffraction experiments should be performed on BF_4 to ensure that the carbon electrode has reached stage 1 or stage 2 fully and completely. This would also allow a wider range of angles to be investigated and therefore in more (00ℓ) peaks could be used in the calculations to determine the anion layer spacing as well as the orientation of BF_4.

The main bulk of this work was performed using soft carbons, carbons that are graphitizable. There are carbon materials that are non-graphtizable which are known as hard carbons. Hard carbons are obtained by heating such precursors such as charcoal, coconut shells and some polymers such as phenol formaldehyde resins. It would be interesting to see if PF_6 and BF_4 would intercalate into these types of carbon materials. It would also be interesting to see if PF_6 would intercalate into TA-1F and PW-03, the fiber and fabric briefly studied in Chapter 5.

Also, perhaps there are better solvents to use, ones that are stable up to high voltages. A few possibilities are trimethylene sulfone, tetramethylene sulfone and trifluoropropylmethyl sulfone, FPMS[46]. Work by Angell et. al. [46] has suggested that FPMS is best suited for lithium ion cells. Whether this is also true for PF_6 or BF_4 intercalation remains to be seen.

Another aspect to investigate is to see if larger species such as $SbClF_4$ and $N(SO_2CF_3)_2^-$ are also good candidates for this type of anion intercalation. In fact, $N(SO_2CF_3)_2^-$ has been studied by others [39] although only pulse charge experiments were reported with EMS as the solvent. It would be interesting to see the behaviour in

constant current cycling as well as using *in-situ* X-ray diffraction experiments to see if such a large molecule would intercalate into carbon. $SbClF_4$ has been studied by heating different amounts $SbClF_4$ along with carbon and studied using X-ray diffraction [15-17]. It was found that it did form stages with slightly larger c-axis spacings than PF_6 and BF_4. It would be interesting to see if similar results would be obtained electrochemically.

These are just some of the many aspects that can be investigated further and there are more likely others. This of course happens with all research and always leads to other ideas and areas to be investigated.

References

[1] F. P. McCullough, A. F. Beale; United States Patent #4,865,931, Sep. 12, 1989

[2] F. P. McCullough; United States Patent, #5,518,836, May 21, 1996

[3] F. P. McCullough; United States Patent, #5,532,083, Jul. 2,1996

[4] F. P. McCullough, A. Levine, R. V. Snelgrove; United States Patent #4,830,938, May 16, 1998

[5] Richard T. Carlin, Hugh C. De Long, Joan Fuller and Paul C. Trulove, *Journal of the Electrochemical Society*, **141**, (1994), L73-L76

[6] R. T. Carlin, H. C. De Long, J. Fuller, W. J. Lauderdale, T. Naughton, P. C. Trulove and C. S. Bahn, *Materials Research Bulletin Symposium Proceedings*, **393,** (1995), 201-206

[7] T. Zheng, J. N. Reimers, and J. R. Dahn, *Physical Review B: Condensed Matter*, **51**, (1995), 734

[8] J. R. Dahn, T. Zheng, Y. Liu, and J. S. Xue, *Science*, **20**, (1995), 590

[9] G. Pistoia (Editor), *Lithium Batteries: New Materials, Developments and Perspectives*, Elsevier Science, The Netherlands, 1994

[10] J. O. Besenhard (Editor), Handbook of Battery Materials, Wiley-VCH, Germany, 1999

[11] H. Zaleski, P. K. Ummat, and W. R. Datars, *Solid State Communications*, **55**, (1985), 401

[12] D. Billaud, A. Pron, F. Lincoln Vogel, and A. Hérold, *Materials Research Bulletin*, **15**, (1980), 1627

[13] G. Wang, P. K. Ummat, W. R. Datars, and Zhibing Hu, *Canadian Journal of Phyiscs*, **73**, (1995), 489

[14] W. R. Datars, J. Palidwar, and P. K. Ummat, *Journal of Physics, Condensed Matter*, 7, (1995), 5967

[15] H. Zaleski, and W. R. Datars, *Phyiscal Review B*, **38**, (1988), 5719

[16] H. Priess, H. Fichtner-Schmittler, *Crystal. Res. technol.*, **21**, (1986), 1047

[17] H. Priess, M Goerlich, and H. Sprenger, *Zeitschrift fur Anorganische und Allgemeine Chemie*, **533**, (1986), 37

[18] J. Melin and A. Herold, *Carbon*, **13**, (1975), 357

[19] H. Homma, and R. Clarke, *Physical Review B*, **31**, (1985), 5865

[20] M. Barati, P.A. Dube, P. K. Ummat, and W. R. Datars, *Solid State Communications*, **107**, (1998), 35

[21] M. S. Dresselhaus and G. Dresselhaus, *Advances in Phyiscs*, **30**, (1981), 139

[22] L. Streifinger, M. P. Boehm, R. Schlögl, and R. Pentenrieder, *Carbon*, **17**, (1979), 195

[23] A. Herold, *Bulletin de la Societe Chimique de France*, (1995), 999

[24] W. Rüdorff, and U. Hoffman, *Zeitschrift fur Anorganische und Allgemeine Chemie*, **238** (1938), 1

[25] J. S. Dunning, W. H. Tiedemann, L. Hsueh and D. N. Bennion, *Journal of the Electrochemical Society*, **118**, (1971), 1886

[26] J. Besenhard and H. P. Fritz, *Journal of the Electrochemical Society*, **119**, (1972), 1697

[27] Von J. O. Besenhard and H. P. Fritz, *Zeitschrift fur Anorganische und Allgemeine Chemie*, **416**, (1975), 106

[28] J. O. Besenhard and H. P. Fritz, *Zeitschrift fur Naturforshung*, **27b**, (1972), 1294

[29] F. Beck, H. Junge, and H. Krohn, *Electrochimica Acta*, **26**, (1981), 797

[30] D. Billaud, A. Chenite,and A.Metrot, *Carbon*, **20**, (1982), 493

[31] D. Billaud and A. Chenite, *Journal of Power Sources*, **13**, (1984), 1

[32] A. Jobert, P. Touzain and L. Bonnetain, *Carbon*, **19**, (1981), 193

[33] P. Touzain, and A. Jobert, *Bulletin de la Societe Chimique de France*, **5-6**, (1982), I110

[34] B. Ruisinger and H. P. Boehm, *Angewandte Chemie International Edition in English*, **26**, (1987), 253

[35] B. Ruisinger and H. P. Boehm, *Carbon*, **31**, (1993), 1131

[36] H. P. Boehm, W. Helle and B. Ruisinger, *Synthetic Metals*, **23**, (1988), 395

[37] R. Sanathanam and M. Noel, *Journal of Power Sources*, **66**, (1997), 47

[38] F. Kang, Y. Leng, and T. Y. Zhang, *Carbon*, **35**, (1997), 1089

[39] W. Yan and M. M. Lerner, *Journal of the Electrochemical Society*, **148**, (2001), D83

[40] Z. Zhang and M. Lerner, *Chemistry of Materials*, **8**, (1996), 257

[41] X. Zhang and M. Lerner, *Chemistry of Materials*, **11**, (1999), 1100

[42] X. Zhang and M. Lerner, *Physical Chemistry Chemical Physics,* **1**, (1999), 5065

[43] W. Yan and M. Lerner, *Journal of the Electrochemical Society*, **151**, (2004), J15

[44] Ph. Depondt, D. A. Neuman, and S. F. Trevion, *Acta Crystallographica*, **B49**, (1993), 153

[45] J. Find, D. Herein, Y. Uchida and R. Schlögl, *Carbon*, **37**, (1999), 143

[46] K. Xu and C. A. Angell, *Journal of the Electrochemical Society*, **149**, (2002), A920

[47] Hang Shi, Ph.D. Thesis, Simon Fraser University, 1988

[48] S. A. Safran, *Physical Review Letters*, **44**, (1980), 937

[49] S. A Safran and D. R. Hoffman, *Physical Review B*, **22**, (1980), 606

[50] J. R. Dahn, D. C. Dahn, and R. R. Haering, *Solid State Communications*, **42**, (1982), 179

[51] S. E. Millman, G. Kirczenow and D. Solenberger, *Journal of Physics C: Solid State Physics*, **15**, (1982), L1269

[52] S. E. Millman and G. Kirczenow, *Physical Review B*, **26**, (1982), 2310

[53] G. E. Stout and L. H. Jenson, *X-ray Structure Determination, A Practical Guide*, John Wiley and Sons, Inc., US, (1989), Second Edition.

[54] *International Tables for X-ray Crystallography*, Vol. 4, Kynoch Press, England, (1974), 71

[55] P. Arora and R. E. White, *Journal of the Electrochemical Society*, **145**, (1998), 3647

[56] T. Tran, B. Yebka, X. Song, G. Nazri, K. Kinoshita, and D.Curtis, *Journal of Power Sources*, **85**, (2000), 269
K. Xu, S. P. Ding and T. R. Jow, *Journal of the Electrochemical Society*, **146**, (1999), 4172

[57] K. Xu and C. A. Angell, *Journal of the Electrochemical Society*, **145**, (1997), L70

[58] J. A. Seel and J. R. Dahn, *Journal of the Electrochemical Society*, **147**, (2000), 892

[59] N. Daumus and A. Hérold, *Comptes Rendus Hebdomadaires des Seances de l'Academie des Sciences Serie C*, **268**, (1969), 373

[60] calculations performed by and conversations with Dr. Jurgen Kreuzer and Richard Wang, Dalhousie University, Halifax, NS, Canada

[61] J. A. Seel and J. R. Dahn, *Journal of the Electrochemical Society*, **147**, (2000), 899

[62] J. T. Dudley, D. P. Wilkinson, G. Thomas, P. Juric, R. LeVue, S. Woo, P. Aghakian, B. Denis, m. W. Juzkow, C. Horvath, and J. R. Dahn, *Journal of Power Sources*, **35**, (1991), 59

[63] C. A. Angell, C. T. Imrie, and M. D. Ingram, *Polym. Int.*, **47**, (1999), 9

[64] K. Xu, S. Zhang, and C. A. Angell, *Journal of the Electrochemical Society*, **143**, (1996), 3558

[65] U. von Sacken, NEC/Moli Energy (Canada) Ltd., Private Communication with J.R. Dahn.